

SPECTROSCOPIC CHARACTERIZATION OF CHARGE  
GENERATION AND TRAPPING IN THIRD-GENERATION  
SOLAR CELL MATERIALS USING WAVELENGTH- AND  
TIME-RESOLVED ELECTRIC FORCE MICROSCOPY

A Dissertation

Presented to the Faculty of the Graduate School

of Cornell University

in Partial Fulfillment of the Requirements for the Degree of

Doctor of Philosophy

by

Justin Luria

August 2011

© 2011 Justin Luria  
ALL RIGHTS RESERVED

SPECTROSCOPIC CHARACTERIZATION OF CHARGE GENERATION AND TRAPPING  
IN THIRD-GENERATION SOLAR CELL MATERIALS USING WAVELENGTH- AND  
TIME-RESOLVED ELECTRIC FORCE MICROSCOPY

Justin Luria, Ph.D.

Cornell University 2011

The mechanism of charge generation and charge trapping are a topic of intense research in many third-generation solar cell materials, such as thin films of organic small-molecules, organic polymers, and nanocrystal quantum dots. We present novel Electric Force Microscopy (EFM) techniques that are able to: (1) determine the chemical identity of charged trap species in polycrystalline pentacene, (2) correlate surface photopotential to the absorption of donor and acceptor materials, (3) detect electron trapping in bulk heterojunction polymer solar cells, (4) calculate exciplex density and charge trapping rates in hexabenzocoronene(HBC)-fullerene(C60) bilayer devices, and (5) confirm that charge generation occurs in the bulk of nanocrystal quantum dot thin films. In pentacene, the direct absorption of stable cations lead to the release of trapped charge. By varying the wavelength of illuminated light, we obtain the trap-clearing action spectrum, from which chemical information of the cation is determined. In addition to the work on pentacene, we report on the first image of photovoltage spectra in bulk heterojunction polymer solar cells, and find that charge trapping from donor-acceptor mixing creates an electric field that opposes geminate-pair splitting. Additionally, we measure fluctuations in the contact potential to provide quantitative information on the vacant trap density. In bilayer films of HBC-C60, we model the vertical distribution of photogenerated charges to determine exciplex density. We further note enhanced degradation in the active material in the absence of an electron-accepting fullerene. Lastly, we demonstrate the generation of free charge in the bulk of highly-coupled lead-salt nanocrystal solar cells in the absence of a chemical gradient or applied electric field.

## BIOGRAPHICAL SKETCH

Justin Louis Luria was born on a Wednesday in 1984 to Cynthia and Robert Luria at a fighting weight of 5 pounds. He was the first of his generation on his father's side, and his grandparents and many others gave him copious amounts of food and love. He weighed 15 pounds within the first few months. The early part of Justin's youth was spent moving progressively westward, until at the age of four, when his family arrived in Goleta, CA. This is where he would attend most of his K-12 education. After twenty years, his first grade teacher still recognizes him.

In high school, Justin participated in a number of extra-curricular activities, including quiz team, math team, debate, e-sports, and wrestling. He was fortunate enough to be able to take community college classes at the Community College of Southern Nevada, earning over 30 credits in two years.

As an undergraduate at the University of Nevada, Reno, Justin studied under Prof. Andrei Derevianko on non-linear equations that model Bose-Einstein Condensation. He graduated with honors earning degrees in Mathematics and Engineering Physics, while maintaining two part-time jobs to pay for his education. Between the various places he lived during this time, he moved through the use of a shopping cart. During this time he also participated in Judo, where he finished a respectable sixth in the collegiate national competition of 2005.

In 2006 Justin moved to Ithaca, NY, by way of FedEx, to attend the chemistry graduate program at Cornell University. There, he joined the group of Prof. John Marohn, developing scanning probe microscopy techniques to study solar cell materials. He intends to graduate by August of 2011. Afterwards, he will sell most of his possessions and relocate to parts unknown.

“...these philosophers, whose hands seem only made to dabble in dirt, and their eyes to pore over the microscope or crucible, have indeed performed miracles. They have acquired new and almost unlimited powers... and even mock the invisible world with its own shadows.”

## ACKNOWLEDGEMENTS

### Colleagues

First and foremost, I would like to thank Professor John Marohn for his tireless effort in ensuring the continued success of this lab. He has fostered an excellent place for work and science. Under his tutelage, I have learned valuable scientific and occupational lessons. His advice was sage and always appreciated. The direction he provided my research, both initially and throughout, showed great foresight. I was allowed intellectual freedom to pursue what I found interesting, while at the same time, was directed in a manner that insured success. My time at Cornell has been engaging, fruitful, and enjoyable, most thanks to the atmosphere within his group. I've always appreciated the back-and-forth I was able to carry on with any member, including el jefe. John, Thank you.

A special thank you to Professor Dave Collum, for giving me an opportunity when I really needed one.

The members of this group have been wonderful to work with. Thank you to the members of the Marohn group: Miguel, Enrique, Nikolai, Andrew, Robert, Joni, Louisa, SangGap, Boyan, Jimmy, Sarah, Vladimir, Showey, True, Steve. There was not one among you who was hesitant to help. Thank you to Michael, who taught me how run the microscope. You ruled the EFM-side with an iron-fist, and remain a good friend. To Nik, my partner-in-crime, thank you. As a theoretical mind, among my peers, I have seldom encountered those who were better equipped. Eric, you have been a terrific foil and straight man. More than that, you've been a great help. I've been dumbfounded on more than one occasion by your great feats of common sense. Joni, what another great foil! Thank you for your help with clean room knowledge, and for being an excellent host. Louisa, you have a top-notch scientific mind and a desire to know. Thank you for carrying on the EFM-side of things, you'll do great. Jimmy, another partner-in-crime, enjoy the TV table. Andrew, thank you for the work that you have put into your projects. Enjoy your time at UCSB, you will rock, vociferously. PS. You should know who the acknowledgement

quote is from.

Thank you to my collaborators, Josh Choi, Katie Schwarz, Alon Gorodotsky, Vladimir Pozdin, Eric Spitler, John DeFranco, Fabio Ciccoira, and those who worked with me as coauthors. Thank you Josh for always being available to help with the evaporations. Thank you Katie for being a careful critic. Thank you Alon, for being a research machine and an ever reliable source of enthusiasm! Thank you Vladimir, for not crushing my skull between your fists when I would make a mistake in the Malliaras lab.

Last of all, I would like to thank all the members of my committee, Professors Tobias Hanrath, Jiwoong Park, Peng Chen, and George Malliaras. I would like to thank Tobias Hanrath and George Malliaras additionally for allowing me the opportunity for a number of successful collaborative efforts.

## **Family**

I would like to thank my family as a whole, for being a constant support for me. Měyh, who endeared me to the classics (of television), and who was the voice in the back of my mind whenever I had the inkling to treat myself. Dàahd, who endeared me to the ancients (of television), and who was the voice in the back of my mind pleading with me desperately to do the reasonable thing. My brother, who despite the difference in our natures, has wished me nothing but success and happiness. And I am happy to say that I wish the same for him. Thank you to the Woogs clan, who often helped with my homework.

To my grandparents, you all have been role models of the highest caliber. As a hero, as a protector, as a matriarch, and as a macher. I have great memories of all of you, and I know that I am lucky to even say that. Thank you for the years and years of birthday cards, letters, and phone calls. I can't pay back what you have given me, I can only pay it forward.

To my extended family, great aunts, great uncles, first cousins, aunts, uncles, second cousins. A special thank you to great aunt Lee, who among a great many other things, took me to the opera. And to my great uncle Eli, for his earnest conversations about science, even if I was only

seven years old at the time.

And lastly, to my partner of nine years, Celia. A constant companion, friend, adviser, and goober, thank you for being with me all of this time. I can not emphasize enough how much I look forward to a life together again.

## **Friends**

My friends from La Patera, my friends from Goleta Valley, my friends from Dos Pueblos, my friends from CCHS. You are simply too numerable to list here. But if you're reading this, bless your hearts.

My Nevada crew, Chris, Dave, Coop, Reid. I will bet even odds that you all will thumb through this thesis to see if you are mentioned. Know that the expectation alone that you all will someday read this implies I believe we will be friends for a long time to come. Thank you guys.

My Tuesdays at Uncle Joe's friend, Kenneth. Thank you for the help. The conversations, the groceries, the movies, thank you man. THOR!

I would like to thank the Tekken community. To Mark Kiley, Tony, Zach, Nicole, Ben, Kyle, Dave, Kayla, Joon, Shaun, Kaluen, Damus, Jason, and all of upstate. There isn't a finer crew in the land. On days when I didn't feel much pride as a scientist, I always felt pride as a Tekkenier. I'm so happy I have had the chance to continue this hobby. Thank you to the members of the broader community, you were my main source of entertainment this whole time.

## **Teachers**

I owe thanks to the teachers that helped me throughout my scholastic days. Too numerous to mention them all, but I appreciate the effort it takes to teach students, and I am grateful. Andrei Derevianko, Roberto Mancini, Will Winn, Fred and Carol Soltysik, Stan Vernoooy, Ryan Sunga, Marc Smereck, Doug Mitchell, Tom Slater, Jeffrey Souther, Judy Hug, Valentin Deaconeu, Birant

Ramazan, Alex Kumjian, thank you all.

Nathan, thank you for all your help in building the microscope. I couldn't have done it without you.

I thank coaches Ethan Woodill and Anthony Califano. The beating I took in wrestling prepared me for any hardship in the academic world.

Coach Earl Upton, never has anyone outside of my family placed as much faith in me as you did. Thank you.

## **Funding**

This work was supported by the U.S. National Science Foundation (DMR-0706508 and DMR-0134956) to study Electric Force Microscopy imaging of fundamental processes in organic electronic materials. Further funding from the NSF was received in collaborative work with Nik Hoepker to study charge trapping and fluctuations in organic semiconductors (DMR-1006633).

## TABLE OF CONTENTS

<b>1</b>	<b>Introduction</b>	<b>1</b>
1.1	The Case for Low-Cost Solar Cell Materials . . . . .	1
1.2	Background - Organic and Nanocrystal Photovoltaics . . . . .	4
1.3	Degradation from Charge Trapping in Small Molecule Solar Cells . . . . .	5
1.4	Metrology in Heterojunction Solar Cells . . . . .	8
1.5	Nanocrystal Quantum Dot Solar Cells . . . . .	11
<b>2</b>	<b>Methods</b>	<b>13</b>
2.1	Electric Force Microscopy . . . . .	13
2.2	EFM Basics . . . . .	14
2.3	Microscope Design . . . . .	18
2.3.1	Cantilever Detection . . . . .	19
2.3.2	XYZ Scanning . . . . .	21
2.3.3	Illumination . . . . .	22
2.3.4	Fiber Optic Alignment . . . . .	24
2.3.5	Machining Mover Piece . . . . .	26
2.3.6	Electrical Control . . . . .	27
2.4	Atomic Force Microscopy . . . . .	28
2.5	Modulated Voltage EFM . . . . .	28
2.6	Cantilever Response Tuning . . . . .	30
2.7	Frequency Noise . . . . .	32
<b>3</b>	<b>Spectroscopic Characterization of Charged Defects in Polycrystalline Pentacene by Time- and Wavelength-Resolved Electric Force Microscopy</b>	<b>34</b>
3.1	Introduction . . . . .	34
3.2	Methods . . . . .	36
3.2.1	Electric Force Microscopy . . . . .	36
3.2.2	Sample Preparation . . . . .	38
3.2.3	DFT and TDDFT Calculations . . . . .	38
3.2.4	Sample Illumination . . . . .	39
3.2.5	Transistor Electrical Characterization and Experimental Control . . . . .	39
3.3	Electric Force Microscopy Results . . . . .	40
3.3.1	Potential and Capacitance Images . . . . .	40
3.3.2	Electrostatic Potential Transients . . . . .	43
3.4	Discussion . . . . .	46
3.5	Identification of Trapping Precursor Molecule . . . . .	48
3.5.1	Time-Dependent Density Functional Theory . . . . .	52
3.5.2	Trap Precursor Codeposition . . . . .	55
3.6	Concluding Remarks . . . . .	58

<b>4</b>	<b>Efficiency Losses in Polymer-Blend Solar Cells Observed by Spectroscopic Photopotential Imaging</b>	<b>60</b>
4.1	Introduction . . . . .	60
4.2	Methods . . . . .	61
4.3	Results . . . . .	63
4.4	Discussion . . . . .	69
4.4.1	PN-Junction Approximation . . . . .	69
4.4.2	Potential Contrast Under Dark Conditions . . . . .	69
4.4.3	ITO/PEDOT:PSS/PFB:F8BT Under Illumination . . . . .	75
4.4.4	Al/PFB:F8BT Under Illumination . . . . .	78
4.5	Concluding Remarks . . . . .	79
<b>5</b>	<b>Electron Trapping in Polymer-Blend Solar Cells Observed by Spectroscopic Photopotential Fluctuations</b>	<b>80</b>
5.1	Introduction . . . . .	80
5.2	Methods . . . . .	81
5.2.1	Noise From Contact Potential Fluctuations . . . . .	82
5.2.2	Noise From Tip-Sample Distance Fluctuations . . . . .	83
5.2.3	Modeling . . . . .	84
5.3	Results . . . . .	84
5.3.1	Material Dependence . . . . .	84
5.3.2	Power Spectral Density . . . . .	86
5.3.3	Tip Voltage Dependence . . . . .	87
5.3.4	Illuminated Wavelength Dependence . . . . .	87
5.3.5	Tip-Sample Distance Dependence . . . . .	91
5.3.6	Jitter over Al/PFB:F8BT . . . . .	93
5.4	Discussion . . . . .	94
5.4.1	Fluctuations from Charge Diffusion . . . . .	94
5.4.2	Fluctuations from Trapping and de-trapping . . . . .	95
5.4.3	ITO/PFB:F8BT films versus Al/PFB:F8BT films . . . . .	98
5.5	Concluding Remarks . . . . .	98
5.6	Supplemental Information . . . . .	99
5.6.1	Wavelength Dependence . . . . .	99
5.6.2	Tip Voltage Dependence . . . . .	100
5.6.3	Tip-Sample Distance Dependence . . . . .	102
5.6.4	Dependence on Light Intensity . . . . .	105
<b>6</b>	<b>Exciplex detetction in Hexabenzocoronene-Fullerene Bilayer Solar Cells by Electric Force Microscopy</b>	<b>107</b>
6.1	Introduction . . . . .	107
6.2	Methods . . . . .	109
6.2.1	Synthesis and Devices Preparation . . . . .	109
6.2.2	Device Characterization . . . . .	110
6.2.3	Scanned Probe Microscopy . . . . .	110
6.3	Results . . . . .	113

6.3.1	Contact Potential Shift under Illumination . . . . .	113
6.3.2	Temporal Response of Contact Potential under Illumination . . . . .	114
6.3.3	Varying DBTTC Layer Thickness . . . . .	117
6.3.4	Degradation of DBTTC on ITO without the Fullerene Layer . . . . .	118
6.4	Discussion . . . . .	120
6.4.1	Temporal Response of Contact Potential . . . . .	120
6.4.2	Variations in ITO/DBTTC . . . . .	124
6.4.3	DBTTC Layer Thickness in ITO/DBTTC/C <sub>60</sub> . . . . .	125
6.4.4	ITO/DBTTC Degradation . . . . .	130
6.5	Concluding Remarks . . . . .	130
<b>7</b>	<b>Charge Generation in Tandem Nanocrystal Quantum Dot Solar Cells</b>	<b>132</b>
7.1	Introduction . . . . .	132
7.2	Methods . . . . .	134
7.3	Results . . . . .	139
7.3.1	Optical Measurements on Nanocrystal Lead Salt Quantum Dot Thin Films	139
7.3.2	Electric Force Microscopy Measurements on Lead Salt Nanocrystal Thin Films . . . . .	145
7.3.3	NC Quantum Dot Tandem Solar Cells . . . . .	149
7.4	Discussion . . . . .	155
7.4.1	Charge Transfer Nanocrystal Lead Salt Quantum Dot Thin Films . . . . .	156
7.4.2	Tandem Quantum Dot Thin Films . . . . .	158
7.5	Concluding Remarks . . . . .	159

## LIST OF FIGURES

1.1	NREL best research cell efficiencies. . . . .	3
1.2	Suspected sources of trapping. . . . .	7
1.3	Charge generation in heterojunction solar cells. . . . .	9
1.4	Cantilever over bulk heterojunction solar cell. . . . .	10
1.5	Nanocrystal transport diagram. . . . .	12
2.1	Parallel plate capacitor model. . . . .	17
2.2	Frequency parabolas. . . . .	17
2.3	Experimental diagram of EFM . . . . .	18
2.4	Vacuum and dry-nitrogen microscopes. . . . .	19
2.5	Cantilever close up. . . . .	20
2.6	Cantilever near surface with illumination. . . . .	22
2.7	Optical fiber diagram. . . . .	25
2.8	Illumination spectrum for LED. . . . .	25
2.9	Schematic of cantilever mover . . . . .	27
2.10	Schematic describing voltage modulated EFM. . . . .	29
3.1	Electrical characterization. . . . .	40
3.2	Topography, Capacitance, and Potential Maps . . . . .	41
3.3	Trap Potential Thermal Decay . . . . .	43
3.4	Contact Potential Decay under Illumination . . . . .	44
3.5	Trap Clearing Action Spectra . . . . .	45
3.6	Trap Clearing Mechanisms . . . . .	47
3.7	Measured and Predicted Spectra . . . . .	49
3.8	Chemical Deptrapping Mechanism 1 . . . . .	50
3.9	Chemical Detrapping Mechanism 2 . . . . .	51
3.10	Defect Orbitals . . . . .	54
3.11	Codeposition Experiment . . . . .	57
4.1	Materials assignment . . . . .	63
4.2	PFB-F8BT Solar Cell . . . . .	64
4.3	SEM of PFB-F8BT Solar Cell . . . . .	65
4.4	Wavelength-resolved surface potentiometry of a PFB/F8BT film. . . . .	66
4.5	Photovoltage vs Absorbance . . . . .	67
4.6	PN Junction . . . . .	70
4.7	PN Junction under Illumination . . . . .	71
4.8	ITO/ PEDOT:PSS/ PFB:F8BT/ Al . . . . .	72
4.9	Contact potential maps . . . . .	73
4.10	Composition Maps . . . . .	76
4.11	Diagram of charge transfer in ITO/PEDOT:PSS/PFB:F8BT . . . . .	77
5.1	Single point measurement sampling locations. . . . .	85
5.2	Power spectral density versus illuminated wavelength. . . . .	85
5.3	Jitter versus tip-voltage. . . . .	86
5.4	Jitter versus illuminated wavelength. . . . .	88

5.5	Jitter fit details versus illuminated wavelength. . . . .	89
5.6	$\alpha$ versus illuminated wavelength. . . . .	90
5.7	$\alpha$ versus distance $d$ . . . . .	91
5.8	Jitter versus tip-sample distance. . . . .	93
5.9	Jitter over Al/PFB:F8BT. . . . .	94
5.10	Jitter: theory versus experiment. . . . .	97
5.11	Jitter versus tip-voltage over F8BT. . . . .	102
5.12	Jitter fit details versus tip-sample distance. . . . .	104
5.13	Potential versus light intensity over F8BT. . . . .	105
5.14	Jitter versus light intensity over F8BT. . . . .	106
6.1	Diagram of HBC-C <sub>60</sub> bilayer devices. . . . .	108
6.2	Molecular structure and solar cell performances of HBC and DBTTC devices. . .	111
6.3	Topography, dark contact potential, and contact potential under illumination of DBTTC films. . . . .	112
6.4	Contact potential versus illuminated wavelength in films of DBTTC. . . . .	113
6.5	Contact potential response of HBC films under white-light illumination. . . . .	114
6.6	Trapping/detrapping rates in HBC films after white-light illumination. . . . .	115
6.7	Contact potential response of DBTTC films under white-light illumination. . . .	116
6.8	Contact potential over ITO/DBTTC/C <sub>60</sub> with varying DBTTC layer thicknesses. .	118
6.9	Contact potential over ITO/DBTTC with varying DBTTC layer thicknesses. . .	119
6.10	ITO/DBTTC sample degradation. . . . .	120
6.11	Contact potential of vertically distributed charges. . . . .	121
6.12	ITO/HBC energy levels and charge distribution model. . . . .	122
6.13	ITO/HBC/C <sub>60</sub> energy levels and charge distribution model. . . . .	122
6.14	ITO/DBTTC/C <sub>60</sub> energy levels and charge distribution model. . . . .	123
6.15	Model of charge density in a film. . . . .	126
6.16	Model charge distribution in a thin film photovoltaic device. . . . .	126
6.17	Fitting of contact potential shift under illumination versus DBTTC layer thickness.	129
7.1	Tandem Solar Cell Schematic . . . . .	135
7.2	FT-IR and GISAXS measurements. . . . .	140
7.3	Transient photoluminescence measurements. . . . .	143
7.4	Transient Photoluminescence in solution vs film. . . . .	144
7.5	EFM measurement of free charge. . . . .	147
7.6	EFM measurements on PbS-nBDT. . . . .	148
7.7	Capacitance signal for PbS-nBDT thin films. . . . .	149
7.8	Device performance for PbS tandem solar cell. . . . .	151
7.9	Scanning Electron Microscopy of metal interlayer. . . . .	153
7.10	Device performance for PbS tandem solar cell. . . . .	154
7.11	Run to run variation in KPFM. . . . .	155
7.12	GISAXS on PbS-nBDT thin films. . . . .	156

## CHAPTER 1

### INTRODUCTION

We will motivate our work by discussing the need for low-cost solar cell materials, specifically organic and nanocrystal photovoltaics. Then, we will discuss a brief history of research done on these materials. And lastly, we will cover three sections providing a background of related research the material studied in each chapter section: degradation from charge trapping in small molecule solar cells, metrology of heterojunction solar cells, and charge generation in nanocrystal solar cells.

#### 1.1 The Case for Low-Cost Solar Cell Materials

In light of the growing demands on energy production, as well as the drive for sustainability, the solar energy industry is likely to be one of the largest growing sectors in the following decades. The amount of solar energy generated in the United States in 2011 is expected to double from 2010 [1]. Despite this growth, solar energy remains a small fraction of the energy production at 0.2%. Global energy use is expected to double to 25-30 TW by 2050. The need for marketable, low-emission energy sources has spurred great interest in creating sustainable alternatives to fossil fuels. The limiting factor in reaching market saturation for photovoltaics is the prohibitive lifetime cost per watt generated for solar cell technology. Current U.S. averaged levelized energy costs, the cost per Watt charged in order to cover total costs, are drastically larger for solar energy than most other forms of energy generation. The projected levelized cost for plants entering service in 2016 for solar photovoltaic power is 210.7 dollars per megaWatt hour, while conventional coal is 94.8 dollars per megaWatt hour [1]. In order to have solar more appealing to the market, there is a great demand for low-cost solar cell materials.

Material and processing costs, a part of capital cost, are related to the technology implemented. Silicon solar cells require large processing costs to make large area photovoltaics (PVs),

as the silicon needs to be purified and evaporated. In addition to processing costs with silicon, there is also a competition for supply of silicon wafers between the PV industry and rest of the semiconductor industry. Solar cells made from transition metals and metalloids, such as cadmium telluride or indium-gallium-arsenide also suffer from poor supply, considering the amount necessary to saturate the global market. These materials are also toxic, and have costs associated with disposal of the hazardous material.

In addition to material and processing costs, there are also costs associated with the usage of land. For niche applications, such as portable power generation and building-integrated photovoltaics, a minimal usage of land is required. These applications require special materials properties, such as mechanical flexibility or infrared absorption. Neither of these properties are obviously available from silicon nor metallic/metalloid photovoltaics.

Low-cost photovoltaic materials such as the ones covered in this thesis offer a pathway to reduced levelized cost in solar cells. Unlike materials used in conventional photovoltaics, these materials are cheap to process and are naturally abundant. In addition, these low cost materials are mechanically flexible and have tunable bandgaps. However, these low-cost materials are also less efficient and have shorter operable lifetimes. Some of these materials, such as organic materials used in Konarka's Power Plastic, are already in the market for use in niche applications. In order to use these materials in utility-scale power plants, effort must be placed on increasing solar cell efficiencies and lifetimes. In order to compete with utilities at  $.07\$/\text{kWh}$ , it is estimated that the efficiency of organic solar must increase to 15% with lifetimes of 15-20 years [3].

Low-cost organic materials have already shown great progress in efficiency over the last decade. See Figure 1.1. Organic electronics have gone from 2% efficient in 2001 to 8.1% in 2010. As of 2011, Konarka is the current record holder is at 8.3% cell efficiency. Elsewhere, the highest efficiency organic solar cells demonstrated to date employ bulk heterojunctions created in phase-separated blends of conjugated polymers [4–6] or in blends of conjugated polymers and small molecules [4, 5, 7]. Also presented in this thesis, nanocrystal solar cells are an exciting

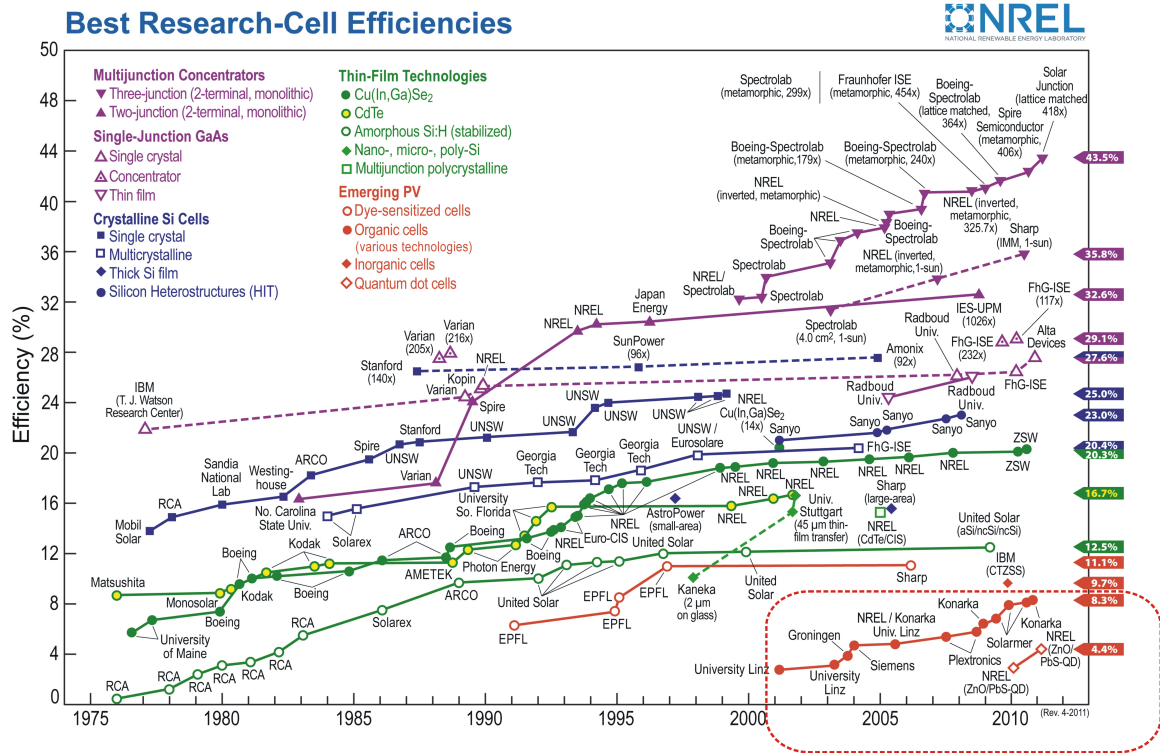


Figure 1.1: NREL best research cell efficiencies.

Best research cell efficiencies for various photovoltaic technologies. Organic and nanocrystal photovoltaic materials are covered in this thesis, are shown in the red dotted outline. Reproduced from NREL report 2011 [2].

new field with efficiencies of between 1.5-3.5%, with record efficiencies of  $\approx 5\%$  [8–14]. These nanocrystals absorb in the infrared, complementing the conjugated polymers studied here which absorb in the visible. Organic and nanocrystal devices have been defined as third-generation solar cells as recently as 2008 [15] by the National Renewable Energy Laboratory, despite not yet having met the condition, set by Green [16] in 2001, that third-generation cells are defined by those that exceed the Shockley-Queisser limit.

## 1.2 Background - Organic and Nanocrystal Photovoltaics

Single crystal silicon based photovoltaic devices have been in the market for some time, and are considered the *first generation* solar cells. These devices suffer from high cost of manufacturing and require delicate installation. *Second generation* devices employ polycrystalline semiconductor thin films. These devices are typically less expensive, but not as efficient, as single crystal silicon devices. Currently in progress is the development of *third generation* solar cells, which involve a number of technologies that can potentially offer high efficiency at a low cost. Among these devices are organic materials and nanocrystal quantum dots.

Organic electronic materials operate through electron transport between  $\pi$ -orbitals, rather than through a crystalline lattice [17–19]. There are three types of organic electronic materials: polymers, small molecule, and molecularly-dispersed polymers. Despite poor initial device performance [20, 21], improvements in chemical purification and synthesis [22, 23] as well as an understanding of intermolecular interactions [24–26] have improved solar cell efficiencies. Organic materials have been shown to be good candidates for light-emitting diodes[27–31], large area displays [17, 27, 32], thin film transistors [17, 27, 31–38], and solar cells[27, 39, 40]. Nanocrystal quantum devices utilize size, shape and material dependencies to tune band gap and optical absorption. Like organic electronic materials, nanocrystals have potential benefits to solar cells [8–11, 41], light-emitting devices [42, 43], photodetectors [44, 45], field effect transistors [46], lasers [47], thermoelectrics [48], and fluorescent biomarkers [10].

The earliest organic solar cells were made from small-molecule organics sandwiched between two metal electrodes, and had conversion efficiencies that were rather unexciting ( $\approx 10^{-3}\%$  to  $10^{-2}\%$ ) [49–52]. Solar cells made from mercantile dyes in a metal-insulator-semiconductor (MIS) architecture managed to reach conversion efficiency of 0.7% [51–53]. The first organic cell made from two organic materials, a phthalocynaine derivative and perylene, was fabricated by Tang et al., with  $\approx 1\%$  conversion efficiency [54].

The first single layer devices based on polymers came about during the mid 1990's [55–58], with conversion efficiencies of less than 0.1%. It was observed that Buckminsterfullerene (C60) greatly enhanced the performance of these cells, and led to polymer-fullerene bilayer heterojunction [59–61] and bulk heterojunction devices with C60 and C60 derivatives [62, 63]. In these cases, the *p*-type polymer (donor) transfers an electron to the *n*-type C60 (acceptor). Bulk heterojunction devices made from two polymers took longer to develop, as *n*-type polymers are difficult to synthesize [64, 65].

Nanocrystal photovoltaic devices are also seen as potential low-cost, abundant alternatives to silicon and metallic/metalloid photovoltaics. This technology arose from the field of dye-sensitized solar cells, with the first nanocrystal quantum dot solar cells made from dye-sensitized colloidal TiO<sub>2</sub> [66]. Solar cells made solely from quantum dot nanocrystals have generated a great deal of interest for potentially being able to break the Shockley-Queisser limit [67] on efficiency, as they have been reported to generate hot carriers [68], and multiple-carriers [69]. In addition, these materials integrate with other materials systems, such as composites with organic polymers [70, 71], and small molecules [72].

### 1.3 Degradation from Charge Trapping in Small Molecule Solar Cells

Pentacene has been an archetypal small-molecule organic semiconductor for research because of its availability and relatively high hole mobility. For comparison, pentacene's performance is similar to hydrogenated amorphous silicon [73]. Pentacene and pentacene derivatives have received attention for use as electron donors [74–78] and acceptors [79] in solar cells. Unfortunately, pentacene devices degrade rather quickly when operated in air. It is noted that the performance of pentacene in solar cells decays on the order of hours [75, 80]. Even under encapsulation, the device lifetime is estimated to be on the order of a few years [81]. This lifetime is well below the lifetime required to be a competitive solar cell.

Great effort has been expended on identifying the sources of degradation in this material. Though it is known from X-ray photoelectron spectroscopy [82] and mass spectroscopy [83] that pentacene oxidizes, the chemical pathway or end product of oxidation has not been identified. Furthermore, even though these techniques prove that oxidation is occurring, they do not prove that oxidation is directly responsible for the loss in solar cell performance. Even if it were shown that oxidization was responsible for degradation, it would remain unclear whether oxidation is removing the molecule from transport or somehow causing charges to trap, i.e. to become an immobile cation.

Charge trapping has been proposed to come from a number of different sources: immobilization of charge at grain boundary defects [84, 85] and dielectric interfaces[85–87], formation of immobile bipolarons [88], molecular sliding [89], stabilization from dipolar fields [90], chemical reactions in the bulk [91–94] and at defect sites [95, 96]. These trapping mechanisms are illustrated in Figure 1.2. For a more detailed exposition of the various forms of charge trapping, consult the Ph.D. thesis of Michael Jaquith [97]. In transistors, these trapped charges result in an increased threshold voltage. In solar cells, trapped charge can impair geminate pair splitting [98], charge transport [99], and charge extraction [100].

The measurement of degradation through characterization of transistor device performance can give details on trapping energetics [78, 84, 88, 102–114], but it is difficult to derive the exact nature of trap formation. Many transistor studies indicate a degradation of device performance following exposure to air, moisture, and/or light [82, 93, 108, 115–119], but whether this degradation arises from physisorption [108, 115, 116, 119] or a chemical reaction [82, 91–93, 117] remains an open question.

In this thesis, in order to study charge traps in pentacene, electric force microscopy (EFM) is combined with variable-wavelength light to follow photochemistry at tens-of-molecule sensitivity and high spatial resolution. Combining light with EFM yields spectroscopic data that can be used, along with *ab initio* calculations of optical spectra, to gain new chemical insights into the

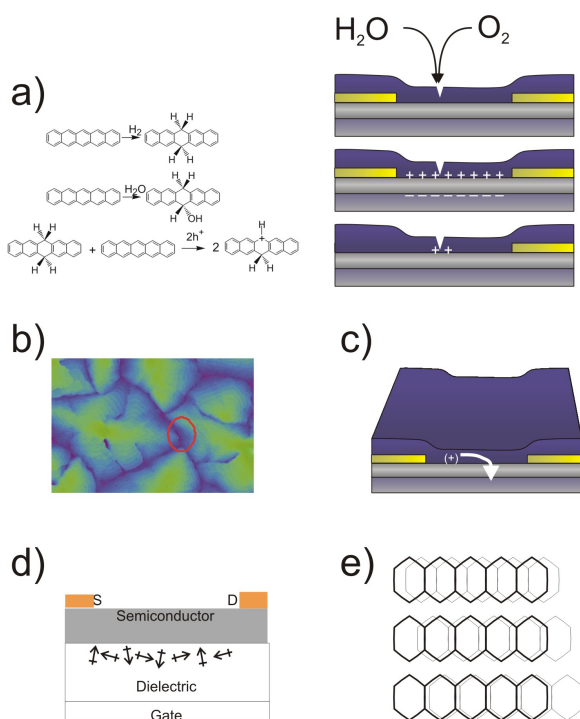


Figure 1.2: Suspected sources of trapping.

In pentacene it is shown that trapping arises from (a) chemical reactions with air and water to form precursors, which react in the presence of holes to form stable cationic species [101]. Additional suspects of trapping include (b) boundary defects, (c) dielectric interfaces, (d) dipolar stabilization, and (e) molecular sliding.

mechanisms of charge trapping and charge clearing in organic semiconductors. In collaboration with the Hennig group, time-dependent density functional theory was used to advance the current knowledge of acenes [120–126]. The result of the work in this thesis shows that at least one significant source of trapping in pentacene is caused by impurities resulting from chemical reactions with air and moisture. These impurities react with mobile holes to form stable charged cations. This work gives the chemical identity of the charge trap species, even for a sub-ppm concentration of charge traps in the thin film. And lastly, it is shown that these charge traps are responsible for the degradation in performance by the observation of depleted free charge concentration. The technique introduced in this work can be applied to a number of other photovoltaic materials to spectroscopically measure differences in the internal electronic energy levels of the molecule on which charge is trapped.

## 1.4 Metrology in Heterojunction Solar Cells

Some of the highest efficiency organic solar cells demonstrated to date employ bulk heterojunctions created in phase-separated blends of conjugated polymers [4–6, 64, 127] or in blends of conjugated polymers and small molecules [4, 5, 7, 62, 128].

In bulk heterojunction cells, materials with different electron affinities (EAs) and ionization potentials (IPs) are blended so that interfaces spread through most of the material. When light is absorbed in a material, a bound electron hole-pair, called an exciton, is created. The exciton is then free to diffuse to an interface, which are plentiful in bulk heterojunction devices. At an interface, electron affinities and ionization potentials between the materials serve to separate the exciton into a geminate pair, with one charge located in each of the materials. The geminate pair is then split by either an external field, thermal energy, or a built-in field. If none of these forces are strong enough to separate the geminate pair, the charges remain bound in a geminate pair and eventually recombine. This bound geminate pair is called an exciplex or a charge-transfer state [129]. The steps in the process of exciton splitting are outlined in Figure 1.3.

While it has been established that optimizing vertical [130] and lateral [131, 132] morphology of the blend is critical to achieving high efficiency, detailed design rules and ultimate efficiency limits for organic solar cells are still being debated and researched [4, 5, 67, 100, 133–147]. Validating solar-cell design principles through independent microscopic measurements of the structure and function of bulk heterojunction films has been challenging [6, 148]. Raman microscopy [149–151], fluorescence microscopy [150], electron microscopy [150, 152, 153], and X-ray spectroscopy [154–157] have been used to image the structure of blends and determine the phase composition. Near-field scanning optical microscopy has been used to image exciton quenching and thereby charge-carrier generation efficiency [158]. Scanned probe microscopy has enabled the imaging of device *function* at submicron resolution [132, 159]. Scanning Kelvin probe microscopy, for example, has been used to image photovoltage [160–168], time-resolved electric force

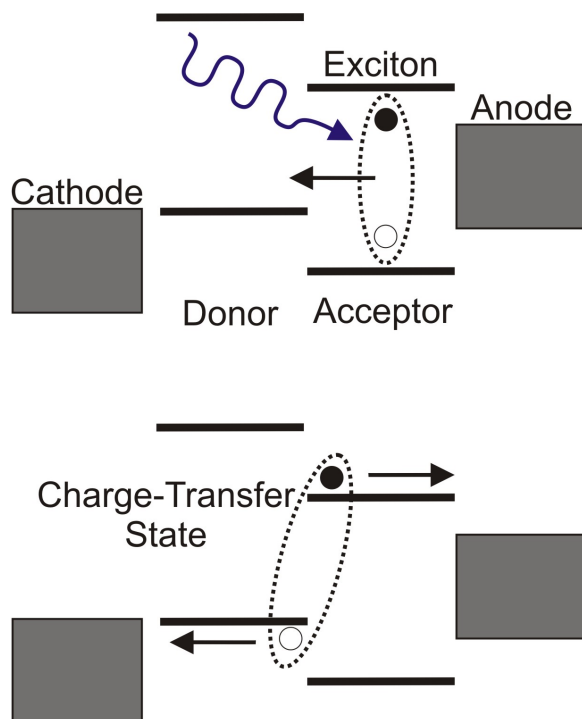


Figure 1.3: Charge generation in heterojunction solar cells.

Widely accepted view of charge generation in heterojunction solar cells. Light creates a bound electron hole pair called an exciton. The exciton diffuses to an interface, where differences in electronic energy levels split the exciton into a geminate bound pair. The geminate bound pair is split, charges migrate to the electrodes and are collected as current.

microscopy to study charge generation [166, 169], and photoconductive atomic force [145, 170–179] and near-field scanning photocurrent microscopy [180, 181] to visualize transport networks.

A number of chapters in this thesis outline the development of novel tools in the metrology of bulk heterojunction solar cells.

In Chapter 4, scanning photovoltage microscopy is introduced and used to show how donor-acceptor intermixing impacts geminate pair splitting in a bulk heterojunction device. In the polymer blend PFB:F8BT, a shift in photovoltage under illumination decreases the contact potential between domains. This decrease serves to reduce the electric field available to split geminate pairs. In conjunction with the work done in chapter 5, it is learned that electron trapping in F8BT is responsible for reduced the reduced electric field across donor-acceptor domain interfaces.

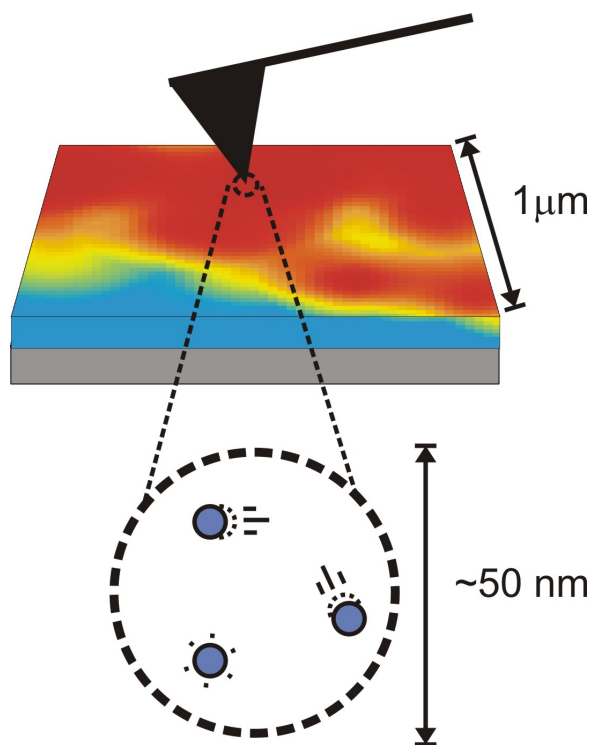


Figure 1.4: Cantilever over bulk heterojunction solar cell.

Charge motion in bulk heterojunction solar cells induces contact potential fluctuations. These fluctuations are observed in electric force microscopy as cantilever frequency noise.

In chapter 5, photovoltage fluctuation microscopy is used to determine the product of vacant trap density and trap-state energy distribution (Figure 1.4). Through a careful series of control experiments, it is learned that noise in the cantilever frequency is due to fluctuations in the contact potential. These fluctuations rise under illumination and are found to have a well-defined dependence on wavelength. In collaboration with the Loring group, we developed a theory that matches the observed dependence of these fluctuations on wavelength of illumination, tip-sample voltage, and tip-sample distance. In films of PFB:F8BT, it is determined that noise is due to trapping/detrapping events, and modeling is used to quantify trap density and trap-state energy distribution. In other samples, the method can conceivably be used to determine mobility.

In chapter 6, photovoltage response versus active-layer thickness is used to calculate *local* exciplex density within a bilayer small molecule organic - fullerene heterojunction device. Hexabenzocoronene (HBC) and derivatives fabricated in the by A. Gorodetsky, in collaboration with

Colin Nuckolls, show promise as air-stable photovoltaic materials. In these samples, photovoltage response is modeled as being the sum of contact potential shifts due to exciplexes, trapped charge, and separated charge. Each of these sources of contact potential shift under illumination vary differently with HBC layer thickness. By fitting contact potential shift as a function of device layer thickness, a value for exciplex density is determined.

## 1.5 Nanocrystal Quantum Dot Solar Cells

Semiconductor nanocrystals can be used as building blocks for a number of applications. The tunability of the nanocrystal bandgap enables their use in a number of applications including solar cells [8–12], light-emitting devices (LEDs) [42, 43], photodetectors [44, 45], field effect transistors [46], lasers [47], thermoelectrics [48], and fluorescent biomarkers [10].

Charge separation in semiconductor nanoparticle systems is usually brought about by coupling between particles with favorable energetics [182], much like donor-acceptor blends that are discussed in the previous section. A number of semiconductors, such as CdS [183], PbS [184], Bi<sub>2</sub>S<sub>3</sub> [184], PbSe [185], CdSe [186], and InP [187] are able absorb visible light and can operate as sensitizers in other devices. These include metal-semiconductor photovoltaic cells, polymer-semiconductor hybrid solar cells, and other quantum dot solar cells.

Devices comprised of a *single* nanocrystal material can also be used in photovoltaics [188]. This observation is curious, since internal or external electric fields are usually invoked to explain exciton splitting. Instead, it is proposed that exciton splitting occurs by spatially confining the exciton to a nanocrystal. If the nanocrystal is smaller than the Bohr radius of the exciton, and the nanocrystal is highly-coupled to a neighboring nanocrystal, charge transfer can take place. This process is optimized by controlling nanocrystal size, shape, and interparticle spacing [185, 188] (Figure 1.5).

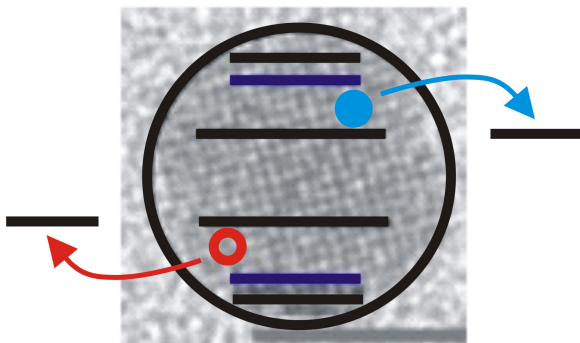


Figure 1.5: Nanocrystal transport diagram.

Figure reproduced from Choi et al. [185]. Films of strongly coupled nanocrystal quantum dots from a single material are shown to generate free charge in the absence of a chemical gradient or externally applied electric field.

The development of single material solar cells has exciting consequences for multijunction solar cells [189]. In a multijunction cell, several solar cells tuned to different parts of the solar spectrum are in contact. Since the size and shape of the quantum dot are responsible for optical and electronic properties, a multijunction cell could now in principle be made from a single active material. However, issues such as current matching and metallic interlayer need to be optimized to improve solar cell performance [189].

In the last chapter of this thesis, electric force microscopy is used to confirm that free carriers are generated in the bulk of lead sulfide nanocrystal quantum dot solar cells fabricated by the Hanrath group at Cornell [188]. Together with photoluminescent and X-ray studies performed by the Wise and Hanrath groups, EFM is able to confirm that excitons are split without the presence of a chemical gradient or external field. In addition, Kelvin probe microscopy is used to characterize metal interlayers in tandem nanocrystal solar cells [189].

## CHAPTER 2

### METHODS

#### 2.1 Electric Force Microscopy

Electric Force Microscopy (EFM) is a technique that is descended from two different technologies. First, the Kelvin probe, eponymously invented by Lord Kelvin, was used as a tool to measure work-function differences between metals [190]. Second, the Atomic Force Microscope (AFM) [191], a scanning probe technique worthy of a Nobel prize, has a plethora of modern uses. Scanning Kelvin Probe Microscopy (SKPM) and Electric Force Microscopy (EFM) are a family of techniques for measuring local surface potential and capacitance. The first Scanning Kelvin Probe Microscope (SKPM) was invented in 1988 [192]. SKPM and EFM utilize a metal coated cantilever to implement the use of a Kelvin probe at the nano-scale. These techniques differ in what quantity is measured, with SKPM measuring force while EFM measures force-gradient.

Scanning probe techniques have been used to study low-cost materials for some time. EFM was used to study inorganic materials [192, 193] and nanocrystals [194] in the years following the development of AFM. Conducting probe AFM was developed to study doped sexithiophene crystals in 1998 [195]. The first surface potential measurements using scanning probe microscopy on monolayer-thick organic films were performed by Kobayashi et al. in 2001 [196]. Scanning probe microscopies such as EFM have been applied to low-cost photovoltaic materials to image surface photovoltage [99, 160–166, 168, 197, 198], charge generation [166, 167, 169], conductivity [145, 170–178, 199–202], morphology [130], trapping [85, 95, 101, 107, 108, 158, 166, 177, 203–206], charge injection [161, 207–211], and photocurrent [102, 179–181]. This thesis work presents the first *images* of photovoltage *spectra*, and develops EFM techniques used to chemically identify charge trap species in polycrystalline pentacene.

This thesis also presents work on fluctuations over bulk heterojunction solar cells due to

trapping-detrapping processes. Fluctuations give rise to stochastic force gradients and cause cantilever frequency noise. Charged AFM cantilevers have been used to observe dissipation due to free and trapped carriers in semiconductors [212–214], and image currents in metals [215–217]. Magnetic-tipped AFM cantilevers have been used to probe dissipation associated with domain wall motion in ferromagnets [218, 219], eddy currents in metals [220], and thermomagnetic fluctuations in submicron magnetic particles [221, 222]. Cantilever frequency noise has been used to study charge blinking in inorganic semiconductor nanoparticles [194] and generation-recombination noise in inorganic semiconductor heterojunctions [223].

## 2.2 EFM Basics

A Kelvin probe operates by detecting the force between two plates of a capacitor [224]. This force is dependent on the contact potential and capacitance. The contact potential difference between the probe and the sample is a function of both the chemical potential and the electrostatic potential differences. Force between the plates is minimized when the contact potential difference is zero. The capacitance between the probe and the sample governs the magnitude of the observed force at a fixed contact potential difference.

Despite EFM experiments operating on a much smaller scale than the original Kelvin probe design, the physics are much the same. A metalized probe is brought in close proximity to a surface capable of electrical conduction. The interaction between the tip and the surface can be modeled as a capacitor. The energy stored in the capacitor is then simply half the capacitance times the potential difference squared.

$$E = \frac{1}{2}C(V_T - \phi_C)^2 \quad (2.1)$$

with  $C$  equal to the capacitance,  $V_T$  equal the potential difference is between the applied tip

potential, and  $\phi_C$  equal to the contact potential. The contact potential has two sources: the chemical potential shift between tip and sample ( $\mu$ ) and the local electrostatic potential (Equation 2.2). The derivation of this result is discussed in Eric Muller's Thesis[225] and by Silveira et al. [226]. To measure the forces and force-gradients acting on the cantilever in our experiments, we make two assumptions. First, that electrical charge equilibrates faster than the cantilever oscillation rate. Second, that the contact potential is independent of tip-sample separation. For the cantilever frequencies discussed in this thesis, these assumptions are reasonable.

$$\phi_C = \phi(x) - \frac{\Delta\mu}{q} \quad (2.2)$$

In other words, EFM detects shifts in Fermi level ( $\Delta\mu/q$ ) as well as static electric fields from the sample( $\phi(x)$ ). For studies of trapping in pentacene, the chemical potential difference is small compared to electrostatic potential, and is often ignored. In EFM studies of solar cells, chemical potential shifts can be on the same order as electrostatic potential.

Since there is a defined energy for this tip-sample capacitor that is a function of position, a potential energy gradient arises for changing tip-sample distances. This gradient creates a force (F) on the cantilever. Because our cantilevers oscillate perpendicular to the sample surface (defined here as z), the force on the cantilever (derived from the grand canonical free energy) [225] is:

$$F_z = \frac{\partial E}{\partial z} \quad (2.3)$$

The change in the cantilever spring constant resulting from this position-dependent force is:

$$\Delta k = \frac{\partial F_z}{\partial z} = \frac{1}{2} \frac{\partial^2 C}{\partial z^2} (V_T + \frac{\Delta\mu}{e} - \phi(x))^2 \quad (2.4)$$

The frequency ( $f$ ) of the cantilever is proportional to the square root of the spring constant ( $k$ ) divided by the mass ( $m$ ). When the tip potential matches the contact potential  $\Delta k \rightarrow 0$

and the frequency and spring constant become the resonant frequency ( $f_0$ ) and resonant spring constant ( $k_0$ ), respectively.

$$f = \frac{1}{2\pi} \sqrt{\frac{k_0 + \Delta k}{m}} \quad (2.5)$$

$$f_0 = \frac{1}{2\pi} \sqrt{\frac{k_0}{m}} \quad (2.6)$$

By expanding equation 2.5 in a Taylor series, and taking the first term only, the observed frequency of the cantilever can be expressed in terms of the capacitance ( $C$ ), applied tip potential ( $V_T$ ), chemical potential ( $\Delta\mu$ ) and the electrostatic potential in the sample ( $\phi(x)$ ) [224, 227].

$$f(V_T) \simeq f_0 - \frac{f_0}{4k_0} \frac{\partial^2 C}{\partial z^2} \left( V_T + \frac{\Delta\mu}{e} - \phi(x) \right)^2 \quad (2.7)$$

The local potential can be measured by recording frequency as a function of tip voltage. As predicted by Eq. 2.7, the frequency is parabolic in applied tip voltage, shown in Fig. 2.2. The width of the parabola depends on the capacitance. The larger the capacitance for a given tip voltage, the greater the frequency shift. The position of the parabola depends on potential. The center of the parabola occurs where the tip voltage matches the local electrostatic potential, corresponding to the case when the capacitor has no potential difference.

The determination of trapped charge density in a bottom-gate transistor from measurements of contact potential are described in Michael Jaquith's thesis [97]. When the chemical potential difference is small compared to the electrostatic potential, trapped charge concentration can be measured. In a bottom-gate transistor with an oxide layer of dielectric constant  $\epsilon$  and thickness  $d$ , by treating the semi-conducting material and the gate as a parallel plate capacitor, trapped charge can be modeled as charge on a plate. In this case, the charge density of trapped charge  $\sigma$  is then:

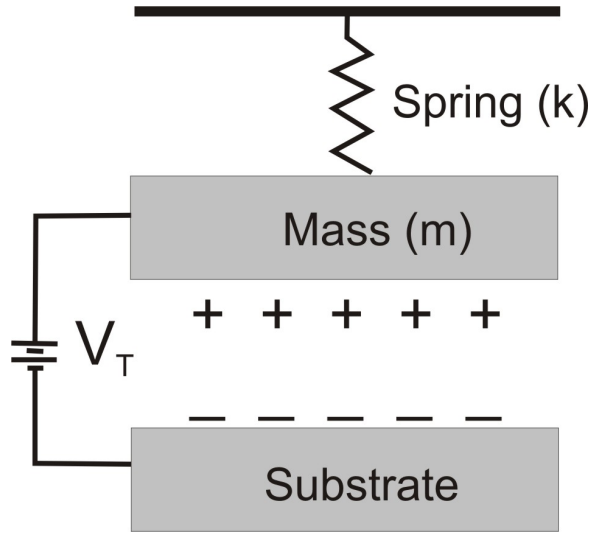


Figure 2.1: Parallel plate capacitor model.

Charged EFM tip over surface is modeled as a parallel plate capacitor in which one side of the capacitor is free to oscillate.

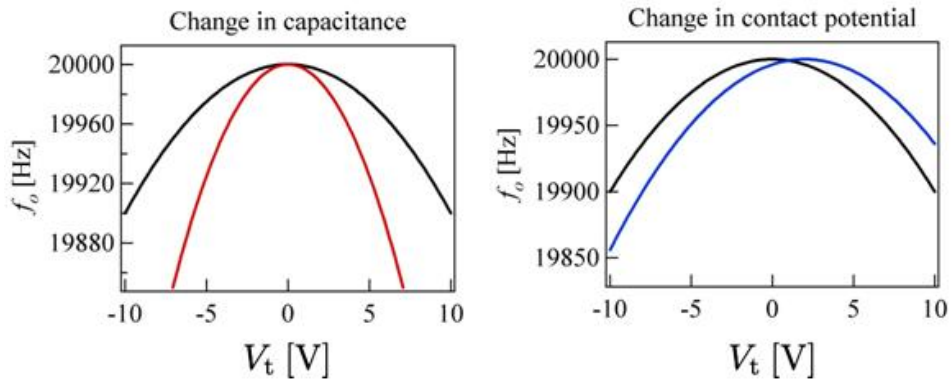


Figure 2.2: Frequency parabolas.

Collected frequency data from Silveira et al. [224] demonstrating the effect of increased capacitance (red) and increased contact potential (blue). This data is fit to Eq. 2.7. For our experiments, the cantilever tip ( $f_0 = 75$  kHz,  $k_0 = 1$  N/m) is about 100 nm over the top a sample of 25 nm pentacene film transistor.

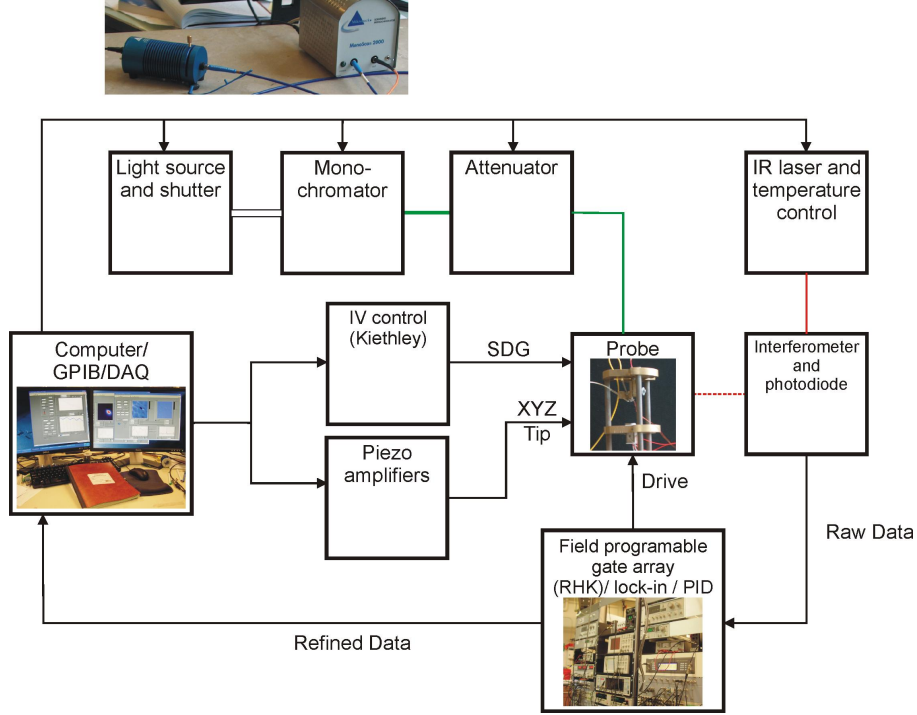


Figure 2.3: Experimental diagram of EFM

Experimental outline of electric force microscope used in this thesis work. A computer controls illumination (source, monochromator, attenuator), cantilever detection (IR laser and temperature control), and voltage sources (source, drain, gate, tip, piezo voltages). Cantilever displacement is detected via optic interferometry. The resulting signal is refined by a field programable gate array (FPGA), an analog PID controller, lock-in amplifiers, and a number of other electronic appliances for processing.

$$\sigma = V\epsilon_0\epsilon/d \quad (2.8)$$

## 2.3 Microscope Design

The description of the microscope itself must be broken into segments: cantilever detection, XYZ scanning, illumination, and electrical control. A block diagram of the electric force microscope is shown in Figure 2.3.

In this thesis, two microscopes were utilized. First, the vacuum microscope (code-named:

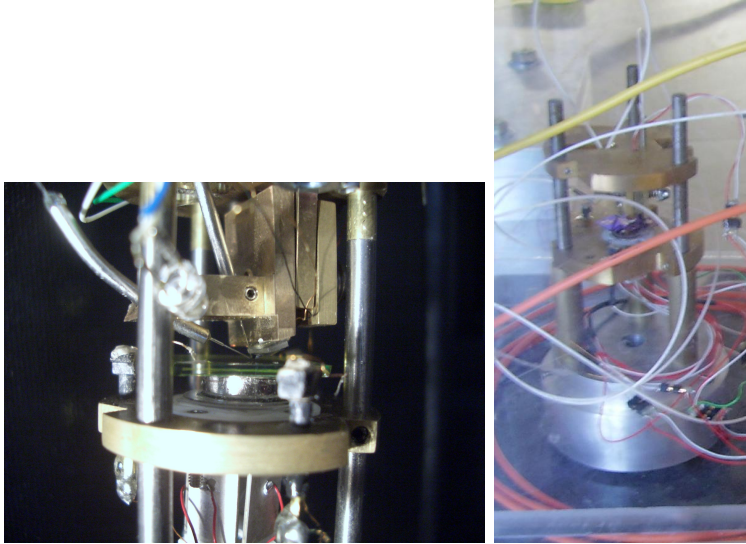


Figure 2.4: Vacuum and dry-nitrogen microscopes.

There are two microscopes used in this thesis. The microscope used in vacuum (left) has higher sensitivities and enhances sample preservation. Sections of the microscope are indicated. In this picture, note there is no visible-light fiber. Also shown is the microscope that is used in a dry-nitrogen environment (right).

THINMAN), which is able to achieve higher sensitivities. Second, the dry-nitrogen microscope (code-named: FATBOY), which is more versatile, easier to fix, but suffers from lower sensitivity. Both microscopes are shown in Figure 2.4. This researcher was responsible for the construction of FATBOY and the dry-nitrogen container. This researcher was also responsible for the modification on THINMAN to illuminate the sample with variable wavelength light.

### 2.3.1 Cantilever Detection

In the experiments presented in this thesis, a commercial cantilever was utilized (MikroMasch NSC18/Ti/Pt) with a spring constant,  $k_0$ , of  $3.5 \text{ Nm}^{-1}$ , a resonance frequency,  $f_0$ , of 75 kHz, and a vacuum quality factor,  $Q$ , of  $10^4$  in high vacuum ( $10^{-5}$  torr). Cantilever quality factors were determined either from the area under the position-fluctuation power spectrum [228] or from fitting the cantilever amplitude versus drive frequency curve. The cantilever block was affixed with epoxy (Hardman double/bubble) to a sapphire plate (Meller optics) in order to electrically

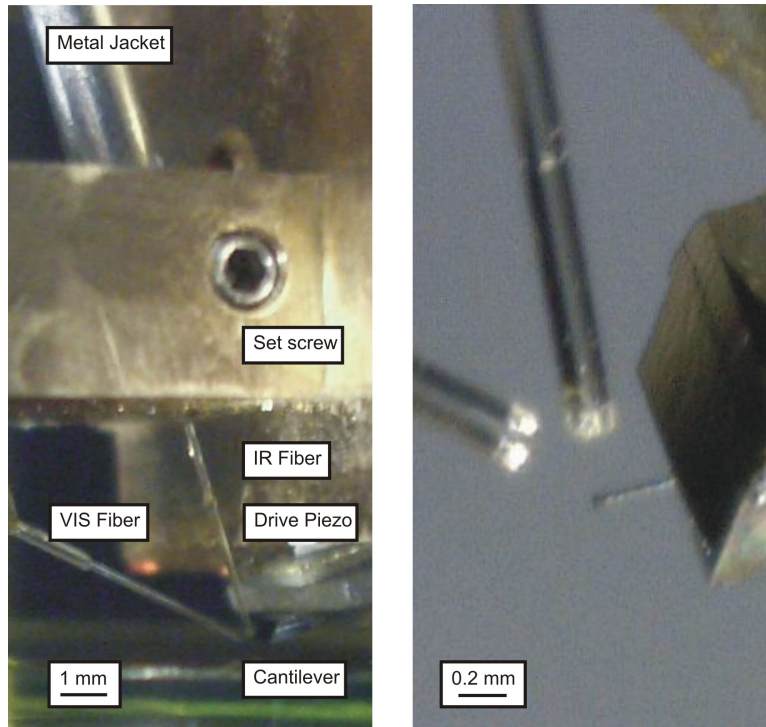


Figure 2.5: Cantilever close up.

Close up of the electric force microscope near the cantilever. Metal jackets house optical fibers which are positioned by set screws so that IR and VIS fibers point directly at the cantilever. The image on the right shows the fiber alignment near the cantilever.

isolate the block from the rest of the probe. Above the sapphire plate was affixed a small piezo sheet (Piezosystems, Inc.), used to drive the piezo. This piezo sheet was also isolated from the rest of the probe with another sapphire plate.

Cantilever displacement is detected by a laser interferometer[229]. The light is generated by a laser diode (Laser Diode Incorporated, model # SCW 1301G-200FC with an FC-APC angle polished connector) operating at 1310 nm and sent down a single mode optical fiber (Corning 9/125 - the core is 9  $\mu\text{m}$  in diameter and the cladding is 125  $\mu\text{m}$  in diameter), shown in Figure 2.5. The laser diode is controlled with an ultra-low noise current source(ILX Lightwave LDT-59108), a temperature controller (ILX Lightwave LDT-59108), a laser-diode mount (ILX Lightwave LDM-4980), and home-built radio frequency (1 Volt, 130 MHz) voltage source. A radio-frequency voltage is applied to the laser diode to prevent mode hopping [229]. An optical coupler is used

which sends ten percent of the light down an optical fiber that is cleaved at ninety degrees and mounted approximately  $50\ \mu\text{m}$  above the cantilever. Infrared light from the interferometer is measured by a photodetector (New Focus 2011 Photoreceiver). Distance between the fibers and the cantilever is estimated from visual inspection under an optical microscope.

### 2.3.2 XYZ Scanning

Scanning in the XY plane is accomplished by the use of a custom built piezoelectric stage [230]. The construction of the stage is outlined in Erik Muller's and Michael Jaquith's theses [97, 225]. The piezos are powered by bipolar amplifiers (PiezoMechanik SVR 350-3-bip) and controlled with a data acquisition and control board (DAQ NI PCI-6259). Lock-in instrumentation is controlled via a GPIB card (NI PCIe-GPIB).

In this thesis, three types of scanning motions are utilized. First, a rastering motion to produce a two dimensional image called a flat scan. Second, a line scan producing only a 1-d array of points. And third, a point scan where data is taken over only one point in space.

Flat scans and line scans vary in speed, depending on several factors. What limits the speed in an AFM image is the ability for the frequency demodulator to track the resonance frequency of the cantilever. For higher quality images, the scan speed is reduced and the PID outputs settings are modified. Surfaces that are flatter and harder can be scanned at a much faster speed than surfaces that are not. If the cantilever is scanned across the surface too quickly, the cantilever will not be driven on resonance, and the PID output will cause the cantilever to bounce. The same rationale applies to linescans.

Pointscans are the last type of scan. A single point on the sample is chosen and the cantilever position is maintained over that point during the scan. To minimize piezo creep, it is advantageous to choose points near the natural resting point of the XY scanner. Point scans in this

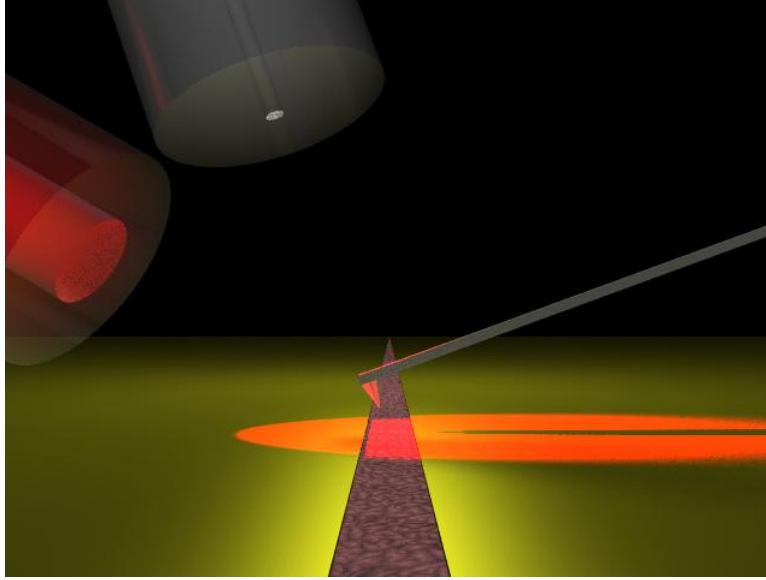


Figure 2.6: Cantilever near surface with illumination.

Artist's rendering of cantilever near the surface of a bottom-contact pentacene transistor with a channel width of 50 microns. Illustration is drawn to scale.

thesis are used when measuring single-point changes in contact potential or capacitance. Point scans are also used in measurements of frequency noise.

Movement in the Z direction is controlled by a home-built slip-stick positioner [231]. A piezo is put under tension by a metal spring, so that extension and retraction can be performed rapidly. The cantilever rests on one of two mover plates resting on sapphire spheres. For more information, read Silveira's thesis [226]. This positioner was modified to allow illumination of the sample by visible light as described in the next section.

### 2.3.3 Illumination

In the experiments discussed in this thesis, a combination of electric force microscopy and variable wavelength illumination is used to probe material properties. The source of the illumination is a Tungsten-Halogen light source (Dolan Jenner MI150 Fiber-lite ). This source is able to provide black-body illumination at a temperature of 3250 Kelvin. A home-built shutter was made from a

model airplane motor. A buffer circuit was also built to provide the proper amount of current to the shutter motor. For applications where a shutter is not needed, an alternate Tungsten-Halogen light source (Mikropack HL-2000 FHSA) is also available.

Light from the source is then coupled to a 600 micron core SMA fiber from ocean optics (QP600-2-UV-VIS). The large fiber core allows for more light to be collected. This fiber is fed into a scanning monochromator (Ocean Optics Monoscan2000). The monochromator is able to continuously scan wavelength from 300 nm to 750 nm. The machine interface to the monochromator is through a serial port, which required composing new labview software to control the device. Light from the monochromator is coupled to a 50 micron core SMA to FC/PC fiber from Thorlabs (M16L01). This coupling provides a 5nm linewidth in illumination. For narrower linewidths, a fiber with a small core must be selected. This modification, however, will make aligning the visible fiber to the cantilever more difficult.

The 50 micron core SMA to FC/PC fiber is coupled to a motor-controlled attenuator (OzOptics DD- 100- 11- 400/700 - 50/125- M- 35- 3A3A- 1- 1- 485:1- 5- DR). Labview software was written to control the attenuator so that light of a constant intensity is applied to the sample. The light to the sample is calibrated using a power meter (Coherent Fieldmate), and a spectrometer (Ocean Optics USB2000). For most experiments in this thesis, the attenuator is calibrated to provide  $.15 \mu\text{W}$  of intensity to the sample across the visible spectrum.

The attenuator output fiber is fed into the vacuum system through a ferrule along with the IR fiber. The end of the visible fiber is cleaved and housed in a metal jacket, in the same process as the IR fiber. The end of the visible fiber is cleaved to reduce the amount of stray light.

Light is illuminated on the sample at a 30 degree incidence, with a tip-to-fiber distance of  $200 \mu\text{m}$ . The numerical aperture of the fiber is rated at  $.22$ , meaning the half angle spread out of the fiber is 12.7 degrees. This produces a spot on the sample with a minor axis of  $120 \mu\text{m}$  and a major axis of  $330 \mu\text{m}$ . The intensity on the surface is calculated to be  $.05 \text{ mW}/\text{cm}^2$ . Since

only a small part of the visible spectrum is accessed, a more relevant number is the spectral irradiance (intensity divided by linewidth) which has a value of .01 mW/cm<sup>2</sup>/nm (compared to .1 mW/cm<sup>2</sup>/nm in the solar spectrum at 500nm). A diagram of EFM microscope near a surface is displayed in Figure 2.6.

In addition to illumination provided by wavelength selected delivery via optical fiber, a InGaN white LED (LiteOn model LTW-1KHC5) is also used in these experiments. The LED was located approximately 1 cm away from the cantilever tip and inclined at a forty five degree angle with respect to the sample surface. This LED provides a luminous intensity of 500 millicandelas on the sample with a spectrum provided in Figure 2.8. To convert into units of intensity, we integrate the optical response spectrum of the human eye multiplied by the LED emission spectrum (approximated in our samples as 100 W/m<sup>2</sup> of one sun).

### 2.3.4 Fiber Optic Alignment

Both fibers are cleaved and housed in metal tubing (Small Parts Inc.) with .02 inch inner diameter and a .0625 inch outer diameter. To cleave the fibers, remove the plastic jacket, buffer, and cladding from the fiber. Place the bare fiber into the fiber optic cleaver. The end of both fibers should stick out about a 1/16th of an inch from the front of the metal casing. To ensure fiber stability, leave the cladding on the fiber everywhere except the cleave. Leave about a half inch of cladding from the end of the metal tube to the fiber jacket. Epoxy the fiber in place at the part of the metal tubing closest to the jacket. To ensure stability of the IR fiber, epoxy both ends of the fiber to the metal tubing.

To align the two fibers containing IR and visible light, set screws are used to adjust the position of each fiber with respect to the cantilever. Alignment with the IR fiber is detected by varying the wavelength of light with the temperature controller described in Erik Muller's thesis [225]. If the fiber is aligned, then photodiode signal should change with varying wavelength.

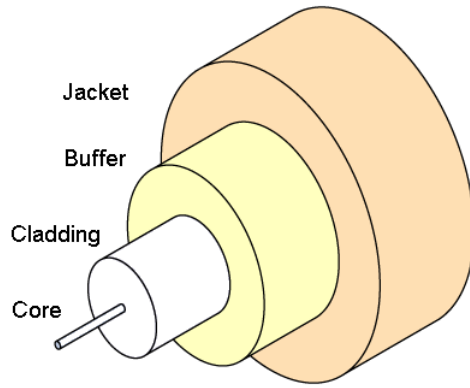


Figure 2.7: Optical fiber diagram.

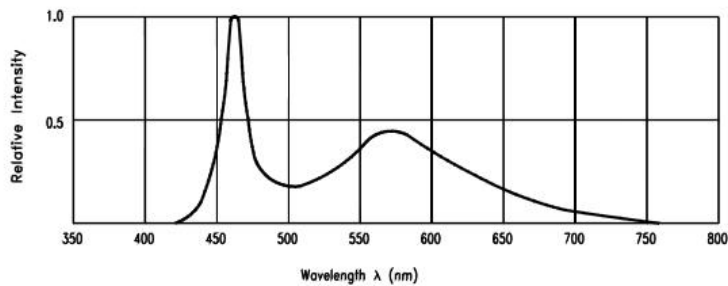


Fig.1 Relative Intensity vs. Wavelength

Figure 2.8: Illumination spectrum for LED.

Spectral density of LED (LiteOn LTW-1KHC5) used for white light illumination. This system is separate from the single wavelength fiber-coupled illumination.

After the IR fiber is in place, illuminate light through the visible fiber and inspect for a reflection off of the cantilever.

Machining the mover piece accurately should allow the two fibers to point reasonably close to the desired point in space. However, some adjustment beyond the set screws might be required. In that case, use two sets of pliers to bend the tube that contains the fiber which contains visible light. By bending and rotating the metal tubing, accurate placement can be achieved.

It should be noted that alignment under the microscope can be a eye-safety hazard. Be sure the laser is off before looking through the eyepiece, and remove the eyepiece whenever the laser is active. However, with IR filters installed on the microscope, the danger is relatively minimal.

### 2.3.5 Machining Mover Piece

In order to have two optical fibers that point at the cantilever, a new mover piece needed to be constructed for FATBOY and THINMAN. This section outlines the general approach to machining a mover piece that can hold the two fibers. The general approach to machining all microscope parts is given in Silveira's thesis [226]

The first step is to mill a block that is .6 by .6 by .46 inches. Mill all opposite sides to be parallel to each other. The hole which will contain the IR fiber is perpendicular to the angle of the cantilever block. In Fat Boy, this hole is 30 degrees from vertical. In thin man, this hole is 15 degrees from vertical. The fiber which illuminates with visible light is 60 degrees off of vertical for both microscopes. Both fibers point to an imaginary spot in space .1 by .1 inches from the base of the part. . Before drilling with 1/16 size drill, mill a small flat area and center-drill. After drilling, ream with size 52. The next step is to mill a flat surface for the cantilever block to rest on, which is a plane perpendicular to the IR fiber. These steps are shown in Figure 2.9a. On the front of the part (the side which will be in contact with sapphire spheres), mill a v-groove .065 inches from the left edge. On the same side as the v-grove, drill and tap a .1 inch deep hole with a 2-56 thread (Figure 2.9b). Next, mill off any excess material. Drill through the part and tap for 0-80 set screws, which will hold the fibers in place. Lastly, remove weight from the part by milling excess material, in order to insure proper coarse movement (Figures 2.9c,d).

A possible improvement on the construction of the part is as follows. In the beginning, instead of relying on trigonometry and the accuracy of the milling tool, start with a block that is 1.4 by 1.4 by 1.4 inches. Then drill holes which are 15 and 60 degrees off of vertical that pass through the center of the part. Then mill the part down to .6 by .6 by .46 inches, and use subsequent steps that are outlined above. This should ensure more accuracy in the fiber placement.

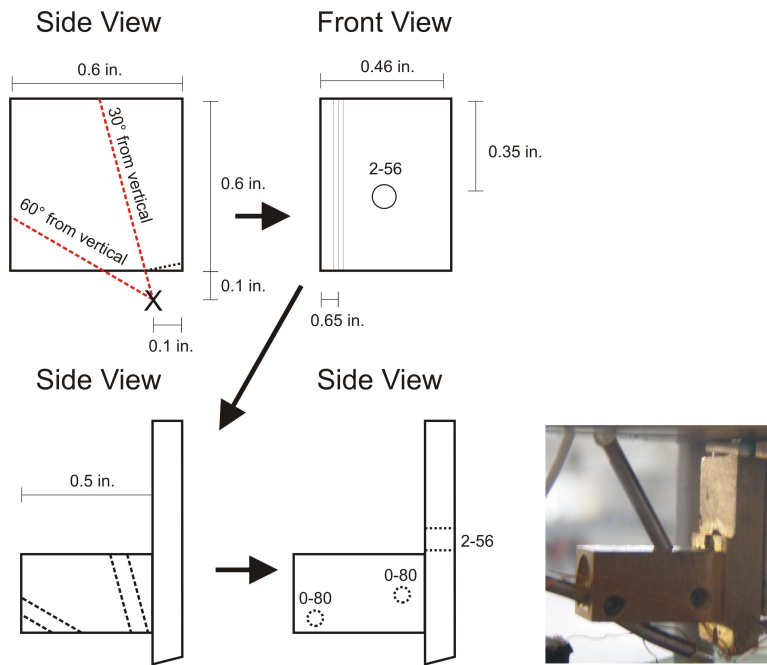


Figure 2.9: Schematic of cantilever mover

Schematic of the mover part for the EFM microscope. This is modified from the Silveira design [231]. Steps are shown from first to last. An image of the part is included to assist in the construction. In Fat Boy, holes containing the optical fibers are drilled at 30 degrees and 60 degrees from vertical. In Thin Man, holes containing the optical fibers are drilled at 15 degrees and 60 degrees from vertical.

### 2.3.6 Electrical Control

In transistor experiments, careful control of source, drain, and gate electrodes must be maintained. In solar cell experiments in this thesis, only one electrode is considered. Control is maintained by a pair of source-meters from Keithley (Keithley 2400 and Keithley 6430). The source-meters are controlled through a GPIB (general purpose interface bus) to a data acquisition and control board.

For delicate current measurements, the Keithley 6430 includes a remote pre-amplifier. This converts measured current from analog to digital near the source, where noise from parasitic capacitance is the least. These instruments are used to measure current from transistor devices, but can also be used in conducting-probe AFM experiments.

## 2.4 Atomic Force Microscopy

Topography is measured in tapping AFM-mode. The cantilever is excited at its resonance frequency with an amplitude of approximately  $50 \text{ mV}_{\text{rms}}$ , applied to piezoelectric element mounted beneath the cantilever. The cantilever amplitude and frequency are determined by a commercial frequency demodulator (RHK PLLPRO). The cantilever amplitude is input into a proportional-integral-derivative (PID) analog feedback controller (Stanford Research SIM960). The PID controls the height of the cantilever above the sample by applying a potential to a home-built slip-stick surface approach [225] referred to as the Z-piezo.

Material contrast can be enhanced in AFM images by operating in ‘phase-mode’ [232]. Typically in phase-mode AFM, the PID controls the height of the cantilever in order to maintain constant cantilever phase, rather than constant cantilever amplitude. Phase-mode AFM images can be taken in two ways. First, by adjusting tip-sample distance to maintain constant cantilever phase at constant drive frequency. Second, by adjusting tip-sample distance to maintain constant amplitude while observing drive frequency. For vacuum systems, the second approach is recommended, as the quality factors are quite high. Phase-mode AFM works best on hard surfaces with surface roughness on the scale of a few nanometers. Scanning speed should be quite slow, with the bandwidth on frequency demodulation never exceeding 400 Hz. In this study, it is easier to collect information on cantilever frequency since cantilever amplitude is fixed. As contrast in a phase-mode AFM is *qualitative*, the two techniques are functionally equivalent.

## 2.5 Modulated Voltage EFM

Modulated voltage EFM, shown in Fig. 2.10, is a fast technique to measure potential and capacitance simultaneously. The potential applied to the tip during modulated-voltage EFM has two components: an AC wave at frequency  $\omega$  generated by a Lock-in Amplifier and a DC value

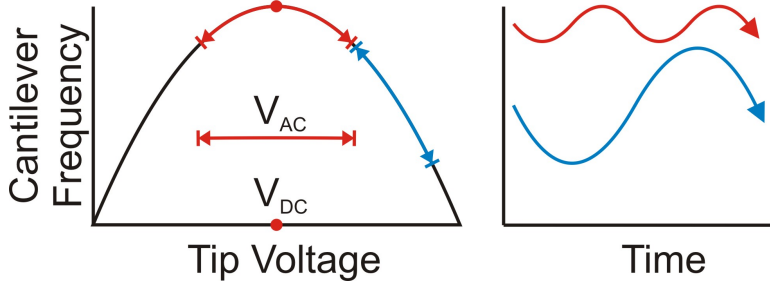


Figure 2.10: Schematic describing voltage modulated EFM.

A voltage with DC and AC components is described by sweeping across regions of the frequency vs voltage curve. Two regions of this curve have the same AC components, but different DC components (red, blue). The red curve is near  $V_{DC} = \phi_C$ . At this point, the cantilever frequency changes at twice the voltage modulation frequency. When  $V_{DC}$  is much larger than  $\phi_C$ , the cantilever frequency response is primarily at the modulation frequency.

generated by a PID controller, shown in Eq. 2.9.

$$V_T(t) = V_{T,DC} + V_{T,AC} \cos(\omega t) \quad (2.9)$$

Fourier components of the cantilever frequency at the first and second harmonics of the modulated-voltage frequency give information on contact potential and capacitance [97, 233]. Near  $V_{T,DC} = \phi$ , the Fourier components are given by

$$\hat{f}(\omega) = \frac{f_0 V_{T,AC}}{2k_0} \frac{\partial^2 C}{\partial z^2} (V_{T,DC} - \phi) \quad (2.10)$$

$$\hat{f}(2\omega) = \frac{f_0 V_{T,AC}^2}{8k_0} \frac{\partial^2 C}{\partial z^2} \quad (2.11)$$

Here,  $\hat{f}(\omega)$  and  $\hat{f}(2\omega)$  are the frequency fourier components created by the modulation of the tip potential. When the cantilever frequency is demodulated and fed into the Lock-in Amplifier, the amplitude of  $\hat{f}(\omega)$  can be measured and input to the PID. When  $V_{T,DC} = \phi$ , the first harmonic Fourier component  $\hat{f}(\omega) = 0$ . The change in the Fourier component near this point is linear in DC tip voltage at this point, and can be input into PID for positive feedback. The lock-in time constant must be on the same order as the scan speed, usually 30 ms.

In modulated voltage EFM, the PID settings must be carefully tuned to produce a high quality image. PID settings must be tuned for each run, depending on the tip-sample capacitance, the frequency-to-voltage scaling factor, and the scanning speed. The Integral term in the PID must integrate over a longer period of time than it takes the Lock-In amplifier monitoring the first harmonic of the modulation frequency to produce a statistically independent point. Typically this is about six time constants. If this condition is not met, then the PID is producing data that is not meaningful. Faster scanning can be achieved with a higher tip-sample capacitance or larger AC tip voltages, as this provides a greater signal to noise.

If a second Lock-in Amplifier is used, the amplitude of  $\hat{f}(2\omega)$  can be measured and used to determine the capacitance second derivative ( $\frac{\partial^2 C}{\partial z^2}$ ) since  $V_{T,AC}$ ,  $f_0$ , and  $k_0$  are known. It is important to note that  $\hat{f}(2\omega)$  is dependent both the frequency-to-voltage scaling factor of the frequency demodulator and the sensitivity factor of the second Lock-in Amplifier.

## 2.6 Cantilever Response Tuning

As the IR fiber is disturbed every time the cantilever is replaced, tuning the system for proper performance is essential. Outlined here are some of the processes for optimizing the EFM for fast scanning.

First, scan for the cantilever resonance frequency, and drive on resonance. Second, adjust the temperature of the laser diode to position the mean cantilever position at the center of a fringe. Typically the temperature is between 5 and 40 degrees Celsius. The cantilever drive amplitude should be such that the cantilever is driven across a full fringe of the interferometer. If the cantilever oscillation looks sinusoidal at all drive amplitudes up to full-fringe, the tuning is complete. If the signal is noisy or lopsided, adjust the frequency of the RF injection and temperature of the laser diode.

In vacuum systems, the cantilever is driven in one of three different modes. The first, Lock-In mode, drives the cantilever at constant drive frequency and measures the amplitude response like a Lock-In amplifier. This mode is typically used in phase-mode AFM and operations performed at ambient pressure. The second, self-oscillation mode, takes the cantilever signal, applies a phase offset and amplification, and applies the signal to the drive. This mode is more sensitive to abrupt changes in the system, and is not recommended for AFM or EFM. The third, phase-locked loop, applies a built in PID to adjust the drive frequency to maintain constant cantilever phase. This mode is most used when performing EFM or AFM in this system. For systems operating at ambient temperature, operating in lock-in mode can also be effective.

To tune the system for AFM, bring the cantilever in close proximity to the surface. Adjust the integral term and setpoint on the PID to slowly approach the sample. Typical numbers for the PID in AFM more are  $P=-0.1$ ,  $I=500$  Hz,  $D=5E-5$  s. Upon touching the surface, the resonance frequency of the cantilever will shift. If this shift is large ( 200 Hz), consider using a setpoint closer to the cantilever amplitude. If the frequency shift is still large, the tip-sample interaction is quite strong. This presents a problem, since abrupt changes in the contact can result in the cantilever not being driven on resonance. To address this problem, widen the bandwidth on the frequency demodulator to (at most) 900Hz.

Tuning the analog PID controller requires observing the oscilloscope in trigger mode. If the cantilever response time is too slow, increase the Integral term (Hz). If the cantilever response is too slow and oscillatory, change settings to allow for faster acquisition of independent points. If the cantilever response time is fast and oscillatory, either decrease the Integral term or increase the Derivative term (seconds). This method of tuning applies to both AFM and modulated EFM schemes.

## 2.7 Frequency Noise

While the cantilever is driven in phase-locked loop mode, the position of the cantilever is measured with the fiber-optic interferometer system and passed through a software 20-th order Butterworth bandpass filter, with a typical high frequency cut-off at a few kHz, to prevent noise folding [228]. A software frequency demodulator is used to convert the cantilever position into a frequency-versus-time signal. Frequency noise spectra,  $P_{\delta f_c}(f)$ , are obtained from the Fourier transform of the autocorrelation function of the cantilever frequency fluctuations,  $\delta f_c(t)$ . Since  $\delta f_c(t)$  is a real-valued function, a one sided Fourier-transform is sufficient.

The correlation function of cantilever frequency fluctuations  $\delta f_c$  defined in the appendix of Seppe Kuehn's thesis [234], is given as

$$\langle \delta f_c(\tau) \delta f_c(0) \rangle = \langle \delta f_c(t + \tau) \delta f_c(t) \rangle = \lim_{T \rightarrow \infty} \frac{1}{2T} \int_{-T}^T f_c(t) f_c(t + \tau) \quad (2.12)$$

where  $2T$  the measurement time and where  $\langle \delta f_c(\tau) \delta f_c(0) \rangle = \langle \delta f_c(t + \tau) \delta f_c(t) \rangle$  holds because the fluctuations are stationary and therefore independent of the starting time. Frequency fluctuation power spectra,  $P_{\delta f_c}(f)$ , are computed as the Fourier transform of the autocorrelation function of cantilever frequency fluctuations as follows:

$$P_{\delta f_c}(f) = 4 \int_0^{\infty} dt \cos(2\pi ft) \langle \delta f_c(t) \delta f_c(0) \rangle. \quad (2.13)$$

Numerical integration and discrete Fourier transforms are used to calculate  $P_{f_c}$ . This puts lower- and upper-bounds on the domain of  $P_{f_c}$ . The highest set by the Butterworth filter cuts out noise at high frequency. The lowest measurable frequency is equal to the inverse of the length of time over which  $f_c$  was measured. This power spectrum is typically averaged several times over the course of several seconds.

Since the effect of noise is dependent on the tip-sample distance, the cantilever amplitude must be carefully chosen. By dropping the cantilever amplitude, the signal-to-noise ratio falls, and the thermal noise-floor on the frequency noise spectra rises [228]. However, the decreased amplitude

allows for the mean position of the cantilever to be closer to the sample. This increases the tip-sample capacitance, and the surface-induced fluctuations. The optimal distance and amplitude to conduct fluctuation experiments is dependent on the sample, and are found empirically.

To quantify  $P_{f_c}(f)$ , it is convenient to report a single number instead of a function of frequency. The term ‘jitter’ is used to express the integral of  $P_{f_c}(f)$  over a range of frequencies.

$$J \equiv \int_L^H P_{f_c}(f)df \quad (2.14)$$

A more detailed description of the equations used in the calculation of jitter are reported in Chapter 5.

CHAPTER 3

**SPECTROSCOPIC CHARACTERIZATION OF CHARGED DEFECTS IN  
POLYCRYSTALLINE PENTACENE BY TIME- AND  
WAVELENGTH-RESOLVED ELECTRIC FORCE MICROSCOPY**

### **3.1 Introduction**

Introduced in this chapter is a new spectroscopic method for microscopically probing the electronic states of long-lived trapped charged species in a  $\pi$ -conjugated film, and the application of this method to record local trap-clearing action spectra in pentacene. Along with codeposition experiments, the identity of charge traps in pentacene are determined. This work was presented in *Advanced Materials* in February of 2011[101]. As a thesis chapter, more details have been provided to assist in the reproduction of the experiment.

Organic semiconductors are attractive materials for microelectronic and photovoltaic applications because their energy levels, optical properties, and solubility can be independently adjusted. While significant progress towards commercialization of organic semiconductor devices has been made, the long-term reliability of most organic semiconductors remains a concern. Charge trapping, for example, causes a wide array of functional problems in organic semiconductor devices including a reduction in mobility, an increase in off current, and an increase in operating voltage. Yet trap formation in these materials remains poorly understood, even in pentacene, the most widely studied organic semiconductor. Proposed trapping mechanisms in pentacene include immobilization of charge at grain boundary defects [84, 85] and dielectric interfaces[85–87], formation of immobile bipolarons [88], and chemical reactions [91–93, 117]. Many transistor studies indicate a degradation of device performance following exposure to air, moisture, and/or light [82, 93, 108, 115–119], but whether this degradation arises from physisorption [108, 115, 116, 119] or a chemical reaction [82, 91–93, 117] remains an open question. Although optical absorption [117] and recent x-ray photoelectron spectroscopy [82, 235] studies have provided more defini-

tive evidence of a chemical transformation in aged transistor films, the relationship between the observed reaction products and trapped species remains unclear.

Despite the large number of organic semiconducting materials, there are only a few systems where the chemical mechanism of degradation is known [236, 237]. This discrepancy is due to the lack of microscopic characterization techniques able to probe trapped charge. Even though techniques such as XPS [238] and UPS [82] have been used to degradation of pentacene thin films after exposure to air, these techniques can only analyze the top few nanometers of a material, and not the active layers of a transistor where charge transport is taking place. While mass spectroscopy techniques, such as MALDI-TOF [83, 239, 240], are capable of micron resolution, they are not able to directly identify the sub-ppm density of charged trap molecules in a thin film amidst isotopic peaks and other decay pathways.

Traps in pentacene and a wide-variety of organic semiconductors exhibit a similar 0.6 eV activation energy and, it has been suggested, may therefore share a common trapping mechanism [108]. Our results provide spectroscopic evidence for pentacen-6(13H)-one as the most likely trap precursor molecule in pentacene. To confirm this identification, pentacen-6(13H)-one was synthesized, intentionally codeposited with pentacene, and analyzed. Because polyacenes like pentacene are promising candidates for field-effect transistors [205, 241–243] and solar cells [75], this finding is of general interest to the organic electronics community.

To study charge traps in pentacene, electric force microscopy (EFM) is combined with variable-wavelength light to follow photochemistry at tens-of-molecule sensitivity and high spatial resolution. Electric force microscopy is a well-established tool for non-pertubatively imaging [210] the spatial distribution of long-lived charge-traps and measuring the kinetics of charge-trap formation in devices [85, 95, 96, 210, 244], but by itself, gives essentially no molecular-level information about the charge-trap species. This study was motivated by recent experiments using EFM to study light-induced trap clearing in polymer transistors [99] and to image photo-response in polymer blends [160, 161, 169]. Combining light with EFM yields spectroscopic data that can

be used, along with *ab initio* calculations of optical spectra, to gain new chemical insights into the mechanisms of charge trapping and charge clearing in organic semiconductors.

Trapping in pentacene has been studied previously by bulk techniques [92, 93] as well as by EFM [85, 95, 96], but the data has led to inconsistent and contradictory conclusions. For example, EFM studies of pentacene transistors have shown charges to trap either in large grain-like regions[95], at isolated defect sites [96], or at intra-grain regions [85]. In some samples, traps are cleared by irradiation with light having an above-bandgap energy [92], while in other samples, light-induced trap clearing is not observed [85].

In an effort to resolve some of these contradictory findings, polycrystalline pentacene transistors were studied using EFM to measure trap-clearing rates during irradiation as a function of the wavelength of the irradiating light. In parallel, the microscope imaged trap density, capacitance, and topography. This work is the first evidence that trapped charge significantly modifies local capacitance, which has implications of lowered local mobility. Additionally, this is the first spatially- and spectrally-resolved action spectrum for trap clearing in polycrystalline pentacene, which is used to identify the chemical mechanism of charge trapping. Measurements were taken in a custom built microscope [95, 96] modified to maintain samples in high-purity dry nitrogen. Tip-voltage modulation and lock-in detection [233] enabled simultaneous imaging of local electrostatic potential and capacitance.

## **3.2 Methods**

### **3.2.1 Electric Force Microscopy**

Transistor source and drain electrodes were grounded during atomic force microscope, electric force microscope, and trap-clearing spectroscopic measurements. Cantilevers were obtained from

SPMTips (spring constant  $k = 1 \text{ N m}^{-1}$ ,  $f_c = 60 \text{ kHz}$ , quality factor  $Q = 300$ ) and were used for both tapping-mode AFM and EFM images. Cantilever displacement was detected with a fiber-optic interferometer operating at 1310 nm. To obtain images of contact potential and capacitance, both a DC and an AC voltage were applied to the cantilever. The AC voltage had a zero-to-peak amplitude of  $V_m = 3 \text{ V}$  and a modulation frequency of  $f_m = 200 \text{ Hz}$ . The cantilever oscillation was analyzed using a commercial frequency demodulator (RHK PLLpro 1.0; output bandwidth of 400 Hz) which produced an output proportional to the deviation in the cantilever frequency  $\delta f_c$ . Fourier components of the cantilever frequency deviation were detected at the first and second harmonics of the modulation frequency using lock-in detectors operating at 1V sensitivity, with time constants of 30 ms (Stanford Research Systems SR830) and 50 ms (Perkin Elmer 7265), respectively. The DC voltage was adjusted, via feedback, to keep the Fourier component  $\mathcal{FT}\{\delta f_c\}(f_m)$  equal to zero; the required tip voltage equals the local electrostatic potential. This feedback was accomplished using a commercial analog feedback controller (Stanford Research Systems SIM960, with  $P = 0.1$ ,  $I = 500 \text{ Hz}$ , and  $D = 0.05 \text{ ms}$ ). The second derivative of tip-sample capacitance  $C$  with respect to tip-sample separation  $z$  was obtained from the measured second harmonic of the cantilever frequency deviation using  $\partial^2 C / \partial z^2 = 8k \mathcal{FT}\{\delta f_c\}(2f_m) / f_c V_m^2$ .

In light clearing experiments where electrostatic potential transients are measured, the cantilever was placed so that the bottom of the oscillation was 400nm above the surface when the gate was being applied and 60 nm above the surface when measurements were being taken. Upon returning the gate bias to zero, the shutter on the light source was opened. Potential and capacitance electric force microscope (EFM) measurements were collected at 1Hz for ten minutes by sweeping tip potential and measuring the parabolic change in frequency.

### 3.2.2 Sample Preparation

Bottom-contact back-gated transistor substrates were prepared by growing 315 nm of SiO<sub>2</sub> on an *n*<sup>+</sup> silicon wafer and depositing gold source/drain electrodes by thermal evaporation (5 μm gap). Substrates were sonicated in detergent, dried, cleaned in UV-Ozone for five minutes, transferred to high vacuum, and heated to 60 °C; pentacene (Sigma-Aldrich; used as received) was thermally evaporated at a rate of ~0.1 Å/s to an average thickness of 15 nm. Completed pentacene field-effect transistors were stored in air, and in the dark, for a few weeks before being transferred for study to a custom scanned probe microscope housed in a dry-nitrogen box. No current was run through the samples while they were stored in air.

Codeposition samples were prepared using the same substrate preparation technique as described above. For the sample evaporation, substrates were heated to 60 °C, with an evaporation rate of ~0.1 Å/s. 60 Å (4 monolayers) of pentacene was deposited followed by 15 Å (1 monolayer) of impurity species.

Trapped charge was generated in samples by applying a  $V_g = -60$  V gate bias stress, unless otherwise noted, for two minutes with the source and drain electrodes grounded.

### 3.2.3 DFT and TDDFT Calculations

Density functional theory (DFT) and time dependent density functional theory (TDDFT) calculations were performed at Cornell by the Hennig group in the Materials Science Department using Gaussian 09 [245, 246] with the B3LYP [247] functional and the 6-311++G(d,p) basis. The basis set was converged using the frequency of pentacene’s first singlet excited state. Changes in this value were less than 4 nm (~ 0.01 eV) for the 6-311++G(d,p) compared to the 6-311+G(d) basis. Defect molecule geometries and ground state energies were found by optimizing single defect molecule geometries with the 6-311++G(d,p) basis and B3LYP. To approximate the chemical

environment of the pentacene molecular solid, DFT and TDDFT calculations were performed with solvation in a dielectric medium, using the Polarizable Continuum Model (PCM) [248] with a dielectric constant of 4.82, as suggested by previous calculations [249]. Dielectric constants from 3 to 6 were examined and the calculated first singlet excitation frequency in pentacene was found to vary by no more than a few nanometers.

### 3.2.4 Sample Illumination

The diagram of sample illumination can be seen in the methods section of this thesis. Light from a tungsten-halogen light source is fiber-coupled to a monochromator. The output of the monochromator is fed to a motor-controlled attenuator so that visible light with a constant intensity of  $0.015 \mu\text{W}$  and a bandwidth of 5 nm was projected down the fiber. The resulting estimate of intensity and spectral irradiance at the sample to be  $0.03 \text{ mW cm}^{-2}$  and  $0.006 \text{ mW cm}^{-2} \text{ nm}^{-1}$ , respectively.

### 3.2.5 Transistor Electrical Characterization and Experimental Control

The transistor's current-voltage characteristics were collected in situ, under nitrogen, and are shown in Figure 3.1. The current-voltage curves in Figure 3.1(a) were analyzed in the saturation regime, Figure 3.1(b), to yield a saturation mobility of  $\mu_{\text{sat}} = 0.013 \text{ cm}^2 \text{ V}^{-1} \text{ s}^{-1}$  and a threshold voltage of  $V_{\text{T}} = -3.7 \text{ V}$ . This data supports the conclusion that experiments were conducted on a working device, and that the studied traps were generated from typical usage of the device.

To populate hole traps within pentacene, a negative gate voltage is applied for a period of time. While there is a negative applied gate voltage, holes are injected in to the film from the

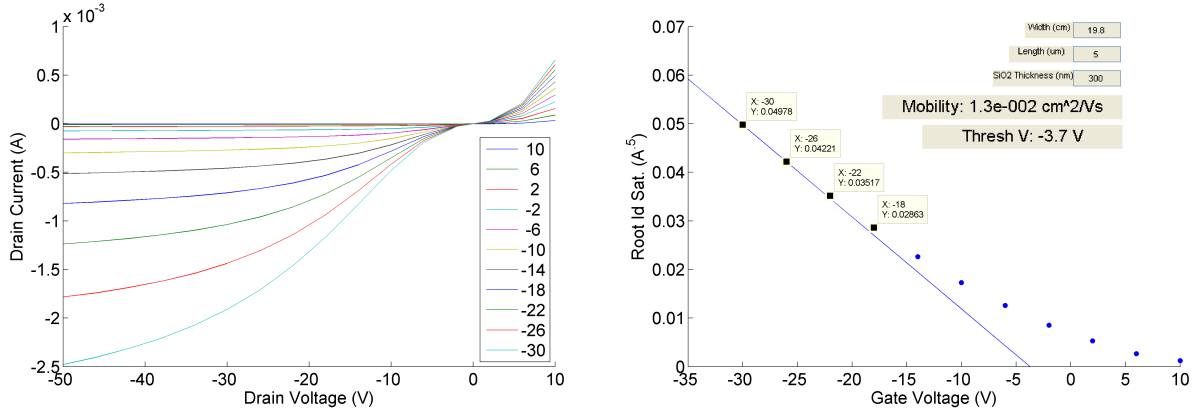


Figure 3.1: Electrical characterization.

(a) Transistor current as a function of drain voltage, for different gate voltages. The current was measured with the source electrode grounded and with the gate voltage set to the values listed in the inset. (b) A plot of the square root of the maximum drain current versus gate voltage. The data was analyzed in the usual way and fit to a line to give the mobility and threshold voltage. Inset indicates the channel width, channel length, and oxide thickness used in the analysis.

source and drain electrodes. Some of those holes become trapped. When the gate voltage is returned to zero, the trapped holes remain in the channel. At this stage, EFM measurements can be conducted to determine the location of trapped charge. In the light clearing experiments, a sample that has had hole traps introduced is illuminated with variable wavelength light. Trap concentration decays over time, or in some cases, under illumination. Between each scan of illumination, traps are re-populated using the same applied gate voltage for the same period of time.

### 3.3 Electric Force Microscopy Results

#### 3.3.1 Potential and Capacitance Images

The topographic data in Figure 3.2(a,d) show regions of low pentacene coverage. Upon bias stress, some of these regions show suppressed capacitance, indicative of depleted mobile charge; see

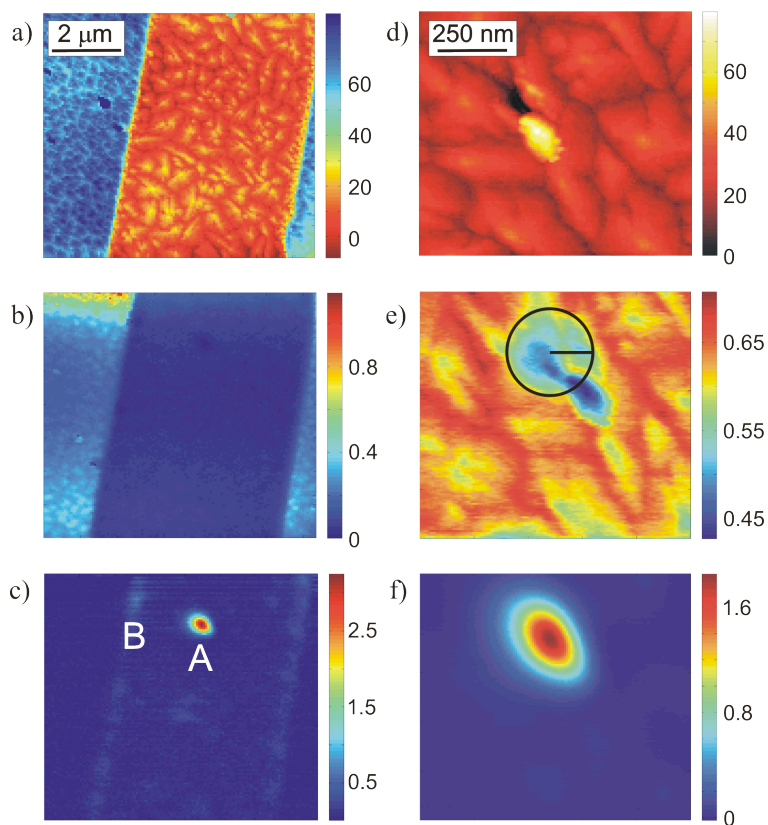


Figure 3.2: Topography, Capacitance, and Potential Maps

Pentacene transistor channel at low (left, a–c) and high (right, d–f) magnification. (a,d) Height in nm; (b,e) second-derivative, with respect to height, of capacitance (arb. units); and (c,f) electrostatic potential (volts). Points A and B in (c) are two locations exhibiting a high density of trapped charge. The images in (d–f) focus on point A.

Figure 3.2(b,e). The same regions also displayed enhanced electrostatic potential due to trapped charge [95, 96, 99, 210], Figure 3.2(c,f). Since the sample had been exposed to air, it is plausible that pentacene molecules near the transistor’s active layer reacted with air to form an impurity [82, 91, 93, 235]. It is proposed that this impurity subsequently reacts, in the presence of holes introduced during bias stress, to form a long-lived cationic species. The observed distribution of trapped charge is also consistent with grain boundary or dielectric trapping. Spectroscopic trap-clearing data can be used to distinguish between these possibilities.

The suppression of local capacitance by trapped charge in a film of  $\pi$ -conjugated molecules is an effect that has not, to current knowledge, been reported before. The suppressed capacitance

highlighted in Figure 3.2(e) is a consequence, possibly, of the Coulombic repulsion of mobile carriers by trapped charge. For simplicity, let us model the trapped charge at position A in Figure 3.2(c,e) as due to  $N_{\text{trap}}$  charges confined to a point and embedded in a material with relative dielectric constant  $\epsilon_r = 3.4$ . Calculating the radius of the depleted-capacitance region as the distance  $R_{kT}$  at which the electrostatic potential from this point charge decays to  $\phi(R_{kT}) = kT/q_e = 0.026$  V, is equal to

$$R_{kT} = \frac{q_e^2 N_{\text{trap}}}{4\pi\epsilon_0\epsilon_r kT}. \quad (3.1)$$

Using Eq. 3.1, it is estimated that  $N_{\text{trap}} \approx 10$  trapped charges lead to the observed  $R_{kT} \approx 160$  nm (the circle indicated in Figure 3.2(e)). As a check, using the same point-charge model to calculate the potential at a height 60 nm above  $N_{\text{trap}}$  charges in vacuum gives  $\phi = 0.24$  V. This potential is a factor of seven smaller than the 1.6 V apparent in Figure 1(f). This order-of-magnitude agreement reasonable given 1) the lack of an independently-validated quantitative theory of the cantilever frequency shift arising from trapped charges [207, 250] and 2) the asymmetry apparent in the Figure 3.2(e) and (f) data near regions of trapped charge which indicates that the trapped charge is not localized at a single point as our simple model assumes. Nevertheless, Coulombic repulsion is a reasonable model of capacitance depletion and that the position A signal arises from approximately ten to only a few hundred trapped charges.

Figure 3.3 shows an image of the capacitance second derivative and electrostatic potential near location A acquired sixteen hours after the bias stress was applied. After the bias stress was applied, the gate, source, and drain electrodes were all grounded while the sample returned to equilibrium in the dark. The electrostatic potential data shown in the upper two panels of the figure show that essentially all of the trapped charge was released after sixteen hours. In this unbiased state, the capacitance derivative at location A is comparatively large; the depleted capacitance seen at location A after bias-stress in Figure 3.3 has clearly recovered. The large capacitance seen in the unbiased state strongly suggests that a thin electrically active layer of pentacene is likely present at location A.

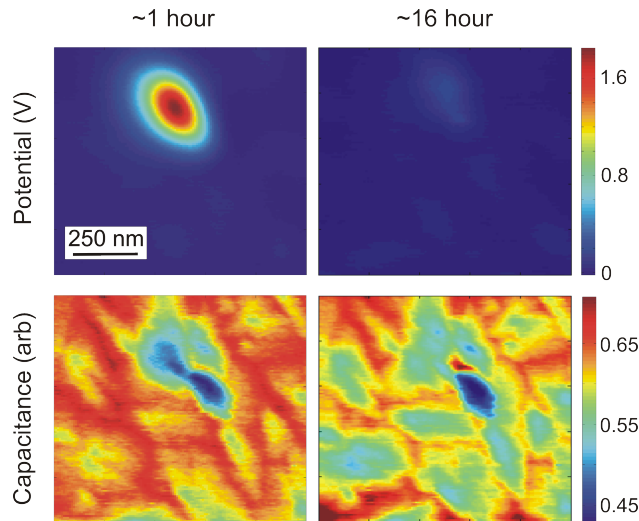


Figure 3.3: Trap Potential Thermal Decay

A comparison of the electrostatic potential (upper) and capacitance second derivative (lower) at 1 hour (left) and 16 hours (right) following the application of a two minute,  $V_g = -60V$  bias stress.

### 3.3.2 Electrostatic Potential Transients

From images of contact potential, areas of trapped charge were able to be identified. The next experiment is to perform a single point measurement at the trapped charge site. In this experiment, the electrostatic potential observed in the trap-clearing experiment is linearly proportional to total number of charges below the tip [95, 250].

Electrostatic potential transients under illumination at three representative wavelengths (400 nm, 500 nm, and 700 nm) are shown in Figure 3.4. For purposes of comparison, the Figure 3.4 transients are normalized by dividing each transient by the electrostatic potential at time zero. The de-trapping rate is clearly fastest at 500 nm. Normalized potential transients were fit to a single exponential decay using MATLAB. Residual plots for the fits are presented in Figure 3.4. Small deviations from a single exponential are apparent at both short and long times. These deviations could be due to gating effects, piezo creep, Coulomb repulsion, or non-linear trap decay kinetics. From these graphs, however, it can be shown that there is a qualitative difference in the trapping time and not simply an error in fitting.

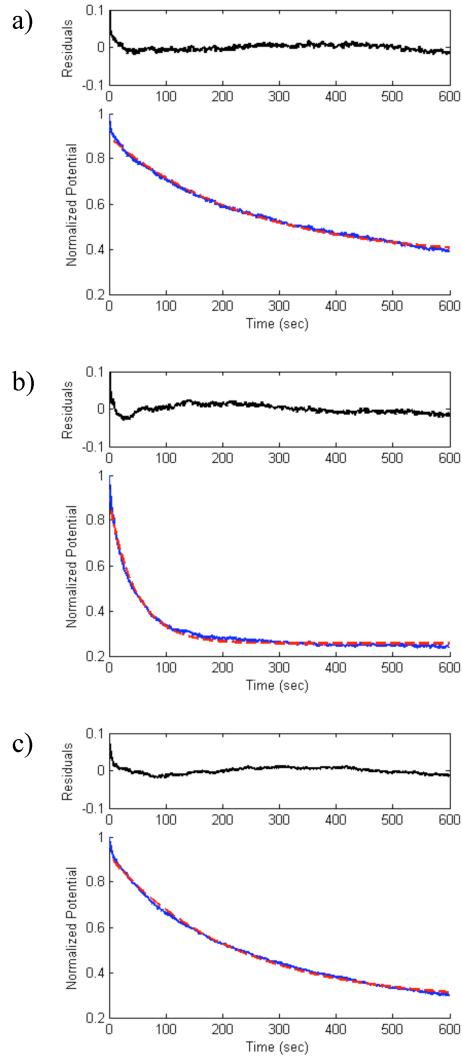


Figure 3.4: Contact Potential Decay under Illumination

First order decay fits (red) to trap voltage transients (blue) under (a) 400, (b) 500, and (c) 700 nm illumination. Residuals are presented above each fit (black).

The decay rate was divided by incident photon energy (eV) to give the constant-incidence action spectrum in units of  $\text{eV}^{-1} \text{s}^{-1}$ . This correction is required because the experiment was performed at constant incident power and not at constant photon flux. The resulting trap clearing rate per photon may be directly compared to the photocurrent-yield spectrum, which has units of free carriers per photon. The absorption and photocurrent-yield [251] spectra are shown in Figure 3.5(a) and (b), respectively. The de-trapping rate is plotted in Figure 3.5 (c) and (d) as a function of irradiated wavelength for points A and B in the sample, respectively.

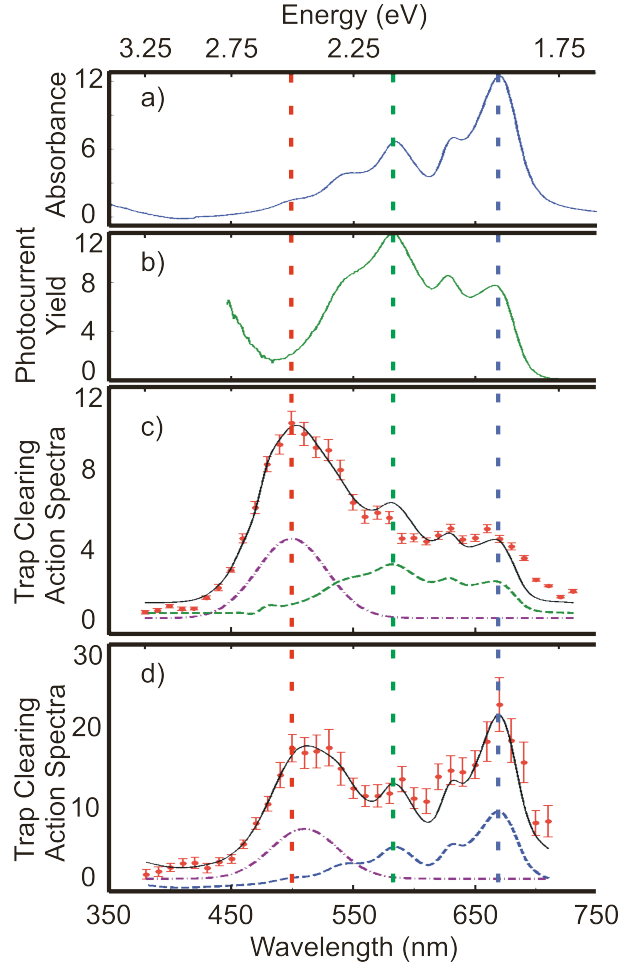


Figure 3.5: Trap Clearing Action Spectra

(a) Absorbance (scale: a.u.) and b) photocurrent yield[251] of bulk pentacene (scale:  $10^{-4}$ ). Trap-clearing action spectrum acquired at (c) location A and (d) location B of Figure 3.2(c) (circles; scale:  $10^{-3} \text{ eV}^{-1} \text{ s}^{-1}$ ). The solid black line in (c) is a fit to a linear combination of the photocurrent spectrum (dashed green line) and a gaussian (dash-dotted purple line; center = 2.48 eV, width = 0.14 eV). The solid black line in (d) is a fit to the absorption spectrum (dashed blue line) plus a gaussian (dash-dotted purple line; center = 2.43 eV, width = 0.13 eV).

The results of the electric force microscopy experiments show that trapping arises from chemical reactions from impurities with charge carriers. The electronic energy levels of these trap molecules can be probed by using light as a spectroscopic tool to clear trapped charges. In the discussion section, theory is used to identify the trap molecule from the electronic energy states associated with the absorption of light. In order to confirm this identification, suspect trap molecules are codeposited with pentacene, and are investigated with electric force microscopy.

### 3.4 Discussion

The clearing of trapped positive charge by light in organic semiconductors is usually attributed to the recombination of trapped holes with excitons[252], free electrons [252], or bipolarons [88]. Observation of light-induced trap clearing is usually taken as evidence against trapping due to migration of charge into the dielectric [85, 253]. In the excitonic trap-clearing mechanism sketched in Figure 3.6(a), light is absorbed to create an exciton (step 1), the excited electron is transferred to an unoccupied state at the trap site (step 2), and the excited hole relaxes and percolates away via electron transfers between adjacent pentacene molecules (step 3). The mid-gap state at the  $T^+$  site in Figure 3.6(a) could be a state associated with a grain boundary [84], sliding defect [89], or a valence orbital in pentacene stabilized by dipoles in the nearby dielectric [86, 87]. Consistent with the mechanism of Figure 3.6(a), observed light-enhanced trap clearing at wavelengths where absorption creates either an exciton localized over a single molecule [254] (at 630 nm and 675 nm) or a charge-transfer exciton with intermolecular character [255] (at 575 nm).

In addition to these expected spectral features, however, the trap-clearing action spectra of Figure 3.5(c,d) exhibits a large peak near  $\lambda = 500$  nm ( $\Delta E = hc/\lambda = 2.5$  eV). This finding is surprising for two reasons. First, the peak energy is well above the bandgap of pentacene — both absorption and photocurrent yield are negligible at this energy, and the widely-accepted

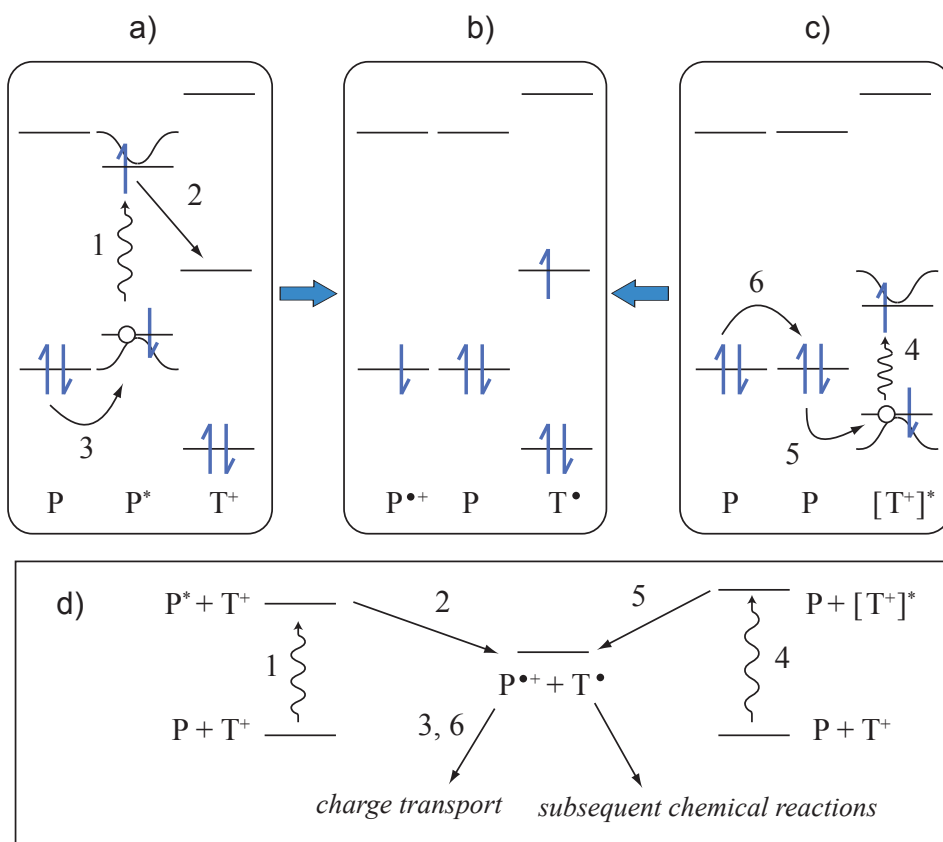


Figure 3.6: Trap Clearing Mechanisms

Here P indicates pentacene, P\* photoexcited pentacene, and P<sup>•+</sup> the pentacene cation radical. The trapped species appears in the figure as a neutral radical, T<sup>•</sup>, charged, T<sup>+</sup>, or photoexcited and charged, [T<sup>+</sup>]<sup>\*</sup>. In (A), a pentacene molecule near a charged trap absorbs light (step 1). Trap-assisted exciton splitting (step 2) populates the trap with an electron and puts a hole on pentacene, which may be converted to a free hole via charge transfer to a distal pentacene (step 3) to yield the charge-liberated configuration shown in (b). In (c), the cationic trap species is photoexcited directly (step 4) and the trapped hole released via electron transfer from an adjacent pentacene (step 5). Charge transfer to a distal pentacene (step 6) yields configuration (b). Both trap-clearing mechanisms are summarized in the state diagram in (d).

mechanism of Figure 3.6(a) is inapplicable. Second, even though the cantilever is detecting signal from many charges in different microstructural and electrostatic environments, there is a comparatively narrow and well defined trap-clearing action spectrum.

To account for these experimental observations, there must be an alternative trap-clearing mechanism. Displayed in Figure 3.6(c), trap clearing by another kind of photoinitiated electron transfer. In step 4 of the figure, a positively charged chemical impurity is optically excited.

The optical excitation does not necessarily have to be the lowest-energy excitation. The trap is cleared in step 5 via backfilling through an electron transfer from a nearby pentacene molecule and the resulting hole is transported away (step 6).

A state diagram summarizing the two mechanisms is shown in Figure 3.6(d). This figure highlights that the neutral, open-shell  $T^\bullet$  species resulting from both trap-clearing mechanisms may undergo further chemical reactions to yield a neutral, closed-shell trap precursor. The chemical mechanism of how these species form are presented in Figures 3.8 and 3.9. This observation supports Lang *et al.*'s conjecture that atomic motion plays a key role in the quenching of charge traps [92].

### 3.5 Identification of Trapping Precursor Molecule

To explain the observed trap-clearing action spectrum by the mechanism of Figure 3.6(c), an impurity or defect in the pentacene solid must be present that exhibits an optical excitation near 500 nm. Time-dependent density functional theory (TDDFT), discussed in the next subsection, was used to calculate the optical spectra for two defects (Figure 3.7). These defects and their predicted spectra are proposed hole traps [91] in pentacene. The two charged defects are the expected products of the reaction of pentacene cation radicals (e.g., holes) with the neutral trap precursors 6,13-dihydropentacene and pentacen-6(13H)-one impurities, respectively [91].

From EFM images, it is likely that trapping arises out of the chemical reaction of trap precursor molecules with positive charge carriers, electron vacancies (holes). These trap precursor molecules form by degradation of pentacene in air, and are more present at the surface of the film. Since trapping only occurs at regions of low coverage, it is not the case that the trap precursor molecules impurities that are present at the time of deposition.

The first impurity species in Figure 3.7(b) was hypothesized by Northrup and Chabinye [91]

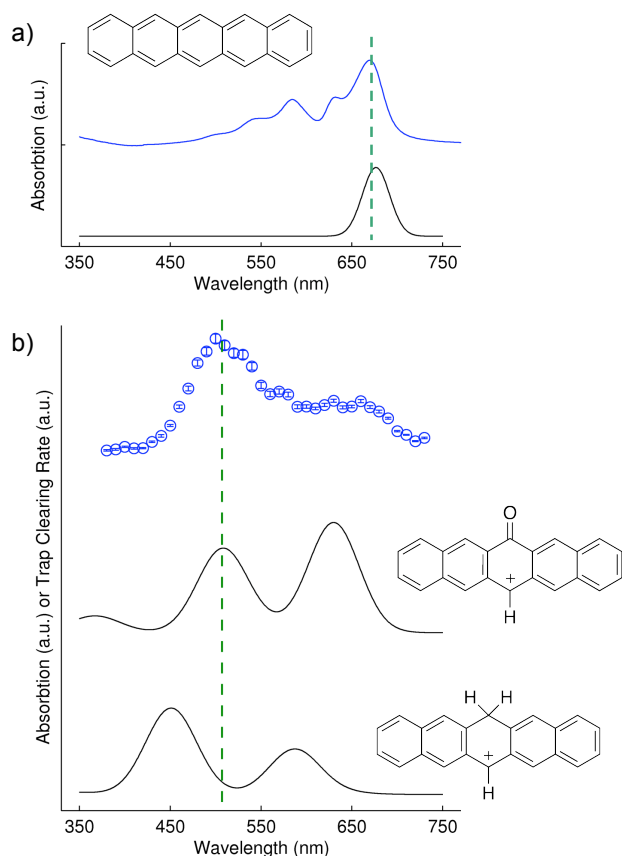


Figure 3.7: Measured and Predicted Spectra

(a) Pentacene absorption spectrum: measured (upper solid blue line) and calculated (lower solid black line). The calculated spectrum was broadened by 15 nm. (b) Measured trap clearing spectrum (upper solid blue circles with error bars) and the calculated absorption spectrum for the charged oxygen defect (middle solid black line) and the charged hydrogen defect (lower solid black line). The middle and lower curves were generated by broadening the calculated absorption spectra by 28 nm. The dotted green vertical lines are a guide to the eye for 500 nm excitation.

to form by the chemical reaction of a 6,13-dihydropentacene impurity with two pentacene cation radicals (e.g., holes). Two proposed mechanisms for this reaction are presented in Figure 3.8. Both mechanisms begin with a hydrogen transfer. The first mechanism proceeds to the trap species via an electron transfer. The second mechanism proceeds to the trap species via a hydrogen atom transfer reaction. Note that both mechanisms result in the same cationic impurity species (the molecules boxed in red in the figure).

The second impurity species in Figure 3.7 is hypothesized (b) to form by a reaction of

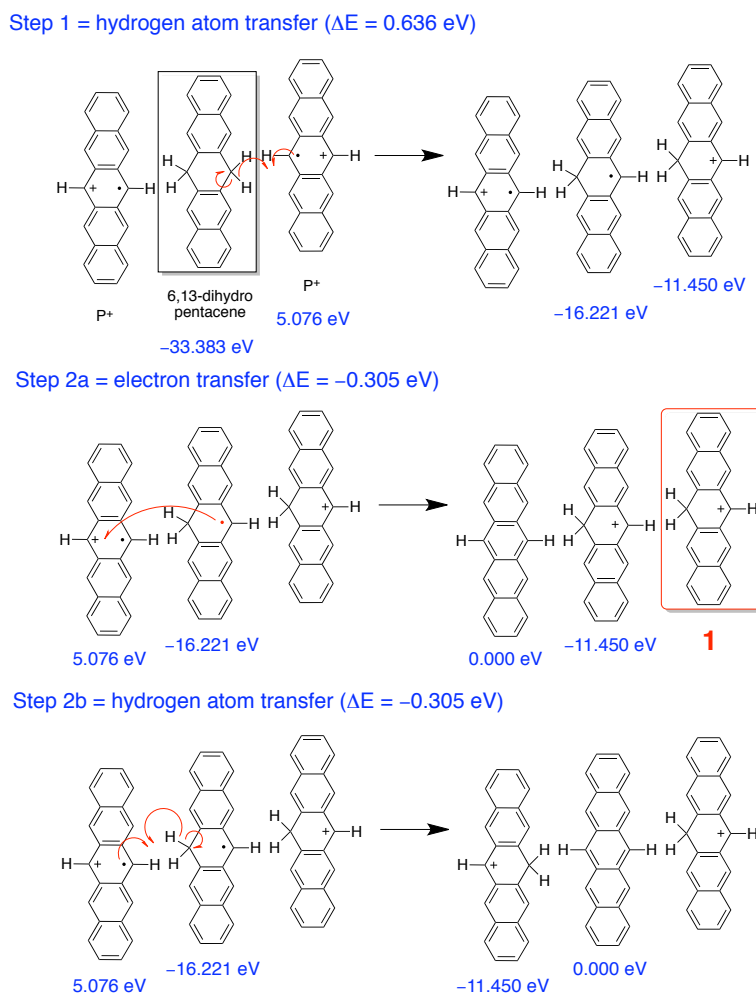


Figure 3.8: Chemical Deptrapping Mechanism 1

Chemical reaction of 6,13-dihydropentacene with two pentacene cations to yield the trap species **1** (red). Energies, shown in blue, were calculated using density functional theory as described in the text. The energies are shown in units of electron volts relative to pentacene's ground state energy ( $-31.1268$  Hartree =  $-847.002$  eV). A reaction energy of  $\Delta E = +0.331$  eV is predicted.

pentacen-6(13*H*)-one with two pentacene cation radicals. A proposed mechanism for this reaction is shown in Figure 3.9. Note that the mechanism leads to the formation of *both* impurities in Figure 3.7(b).

The energies of these two trap-forming reactions are given in the captions of Figure 3.8 and Figure 3.9. The reaction free energies depend also on the concentration of available free holes (e.g., the electron chemical potential or Fermi level), as described by Northrup and Chabynyc

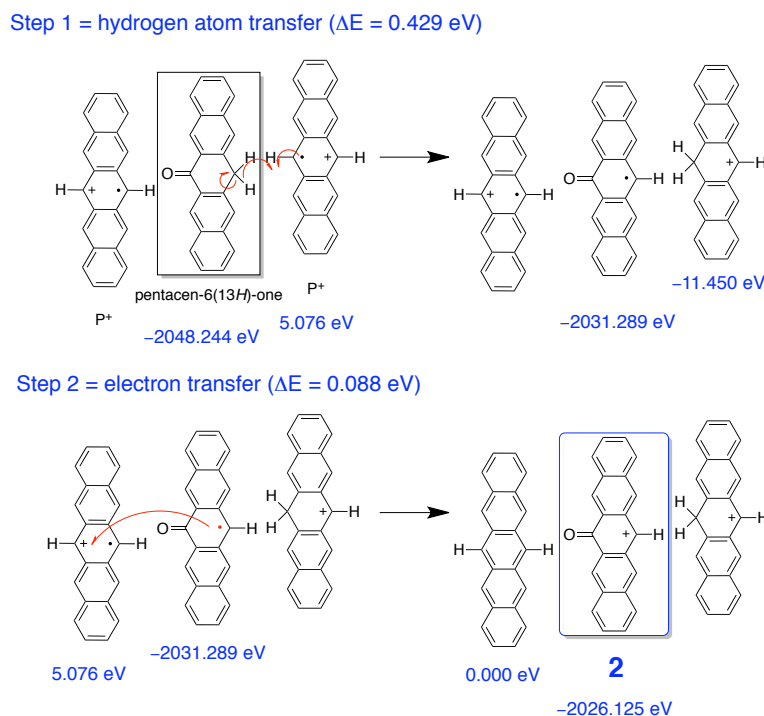


Figure 3.9: Chemical Detrapping Mechanism 2

Chemical reaction of pentacen-6(13H)-one with two pentacene cations to yield the trap species **2** (blue). Energies, shown in blue, were calculated using density functional theory as described in the text. The energies are shown in units of electron volts relative to pentacene's ground state energy ( $-31.1268$  Hartree =  $-847.002$  eV). A reaction energy of  $\Delta E = +0.517$  eV is predicted.

[91]. While the reaction in Figure 3.8 is slightly more energetically favorable than the reaction of Figure 3.9, the activation barrier of the rate determining step in Figure 3.9 is predicted as slightly lower than for the rate determining step in Figure 3.9. If the amount of defect is governed by kinetics and not thermodynamics, then this difference in activation energies might explain why primarily the oxygen-defect cation is observed in the trap-clearing spectra of Figures 3.5 and 3.7.

### 3.5.1 Time-Dependent Density Functional Theory

Time-dependent density functional theory was used to calculate the absorption wavelengths ( $\lambda_j$ ) and oscillator strengths ( $f_j$ ). The absorption spectra is then described using Equation 3.2. These calculations were used in Figure 3.7 to predict the optical spectra and utilized a dielectric continuum model to describe the surrounding pentacene molecules. While TDDFT is less accurate for certain excitations in gas-phase acene molecules [256, 257], using TDDFT to calculate the energies of a molecule embedded in a dielectric continuum has been shown to accurately describe excitations in the bulk acenes [249]. More accurate calculations such as GW-BSE [122] are computationally very expensive for defect calculations, and were not conducted for these experiments.

For the bulk phase acenes, the lowest singlet excitations were investigated, comparing TDDFT results [249] to experimental findings [254]. The normalization constant  $c$  and linewidth  $\Delta\lambda = 15$  nm were varied by hand to maximize agreement between the calculated and observed absorption spectrum.

$$\text{Abs}(\lambda) = c \sum_j f_j \exp\left(-\frac{(\lambda - \lambda_j)^2}{2 \Delta\lambda^2}\right) \quad (3.2)$$

Applying the predicted pentacene absorbance in Table 3.1 to the measured absorbance spectrum Figure 3.7(a), it is shown that the dielectric continuum solvation model employed here correctly predicts the energy of the low-energy Frenkel exciton – localized over a single molecule – at 675 nm in the experimental pentacene absorption spectrum [254]. The peak in the experimental spectrum at 575 nm corresponds to an intermolecular charge transfer exciton [255] and the peak near 630 nm arises from the Davydov crystal-field splitting [254]. To predict the energies of these peaks, one must move beyond a solvation model and explicitly include the neighboring pentacene molecules. Since these types of excitations are not expected to be involved in the observed trap clearing at 500 nm, they are not considered here.

Table 3.1: Singlet excitations of pentacene calculated using TDDFT. The calculated wavelength  $\lambda$  and oscillator strength  $f$  are listed for the three lowest optical excitations indexed by  $j$ .

$j$	$\lambda_j$ [nm]	$f_j$
1	676.6	0.0753
2	422.7	<0.0001
3	394.3	<0.0001

Table 3.2: Singlet excitations calculated using TDDFT for defects **1** and **2** shown in Figure 3.8 and Figure 3.9, respectively. The calculated wavelength  $\lambda$  and oscillator strength  $f$  for the five lowest optical excitations  $j$  is shown.

$j$	Trap species <b>1</b>		Trap species <b>2</b>	
	$\lambda_j$ [nm]	$f_j$	$\lambda_j$ [nm]	$f_j$
1	643	0.02	630	0.72
2	587	0.55	561	0.02
3	451	1.05	526	0.00
4	343	0.02	508	0.55
5	317	0.01	367	0.11

The results of TDDFT calculations carried out for defects **1** and **2** are presented in Table 3.2. The calculated singlet transitions in Table 3.2 were used to compute the absorption spectrum using Equation 3.2, with  $\Delta\lambda = 28$  nm. The calculated spectra are shown as solid black lines in Figure 3.7(b). The oxygen defect **2** has a predicted absorption feature near  $\lambda \sim 500$  nm while hydrogen defect **1** does not, indicating that the oxygen defect and not the hydrogen defect is the source of the unexpected peak in the observed trap-clearing spectrum of Figure 3.5(c,d).

The TDDFT calculation also predicts a  $\lambda = 630$  nm peak in defect **2**'s absorption spectrum which is not apparent in the observed trap-clearing spectrum. What must also be taken into account, however, that the rate of charge-trap clearing at a given wavelength will also depend

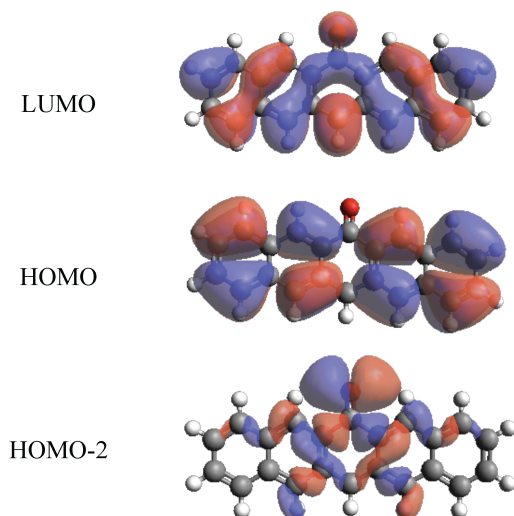


Figure 3.10: Defect Orbitals

Probability density maps of wavefunctions describing HOMO, HOMO-2, and LUMO states in defect **2** .

Table 3.3: Configuration-interaction expansion coefficients for the two dominant excitations of defect **2**. Excitations are a combination of transitions from HOMO-2 to LUMO and HOMO to LUMO.

Excitation 1 (630 nm)			Excitation 4 (508 nm)		
initial	final	coeff.	initial	final	coeff.
HOMO-2	LUMO	-0.14	HOMO-2	LUMO	+0.69
HOMO	LUMO	+0.69	HOMO	LUMO	+0.14

on the probability of inter- and intramolecular electron transfer reactions, as indicated in step 5 of Figure 3.6. Consider, for example, the mechanism shown in Figure 3.6(c). To clear the trap, an electron must be transferred from a neighboring pentacene molecule into the state vacated by the photoexcited electron before the optically excited electron relaxes back to its initial state. Furthermore, in both the mechanisms sketched in Figure 3.6, to regenerate the trap precursor – either 6,13-dihydropentacene or pentacen-6(13*H*)-one – requires the transfer of a proton as well. The rate of electron transfer, proton transfer, and non-radiative decay can be calculated in principle, and provide an excellent pathway for future computational theory.

Nevertheless, the TDDFT results can be used to rationalize why **2**'s  $\lambda = 508$  nm transition might contribute more to the trap-clearing spectrum than its  $\lambda = 630$  nm transition. Table 3.3 shows the configuration-interaction expansion coefficients for the two dominant excitations of defect **2**. The first excitation of **2**, at 630 nm, is predominantly a HOMO  $\rightarrow$  LUMO transition, whereas the fourth excitation, at 508 nm, is dominated by a HOMO-2  $\rightarrow$  LUMO transition. The relevant orbitals are plotted in Figure 3.10. The HOMO - 2 is strongly localized on the oxygen atom while the HOMO is delocalized over the whole defect molecule. Because of this localization, the HOMO - 2 orbital is expected to have greater orbital overlap than would the LUMO orbital with the highest occupied molecular orbital of pentacene. Additionally, the polarization of the excited state is expected to be greater for the fourth singlet excitation. Both of these factors predict that the electron transfer rate should be larger for the 508 nm excitation of **2** than for the 630 nm excitation, in qualitative agreement with what is observed in the trap-clearing spectrum.

### 3.5.2 Trap Precursor Codeposition

The summary of the trap clearing experiment and the TDDFT calculations, shown in Figures 3.5 and 3.7, point to the ketone defect pentacen-6(13*H*)-one as being the precursor to trapped charge. When current is run through the device, the trap precursor reacts in the presence of charge carriers to form a chemically stable charged molecule. To confirm this hypothesis, experiments were conducted where trap precursor molecules were intentionally codeposited in a pentacene thin film.

A single monolayer of impurity molecules, made by novel synthesis from C.A. Lewis, were sequentially deposited on 4 monolayers of pentacene in a bottom-contact transistor by L. Brown and V. Pozdin. Since the active layer is primarily comprised of pentacene, charge transport still occurs. The sequentially deposited impurity molecules should diffuse into the active layer upon evaporation. Then, when the current is run through the device, the impurity molecules

should react to form trapped charge. If the hypothesis that pentacen-6(13*H*)-one is responsible for trapped charge, then the codeposition of that molecule in a pentacene thin film should show trapping. Furthermore, the trapping should have a low onset gating voltage (traps are easily filled), uniform throughout the film (systemic trapping), and have a trap clearing action spectrum similar to what is observed in pentacene. NMR and MALDI-TOF experiments to show the presence of impurity molecules in the film were also conducted, the results of which will be published in the thesis of L. Brown in 2014.

The results of the codeposition experiments are shown in Figure 3.11. Shown in this figure are the chemical structures for the codeposited molecule, images of the topography and contact potential, and graphs of the trap clearing action spectra.

The pentacene control experiment in Figure 3.11(b,c,d) shows topography typical of what has been observed for few monolayer deposition. Trapping, after applying  $-60V$  to the gate electrode for two minutes, has a inhomogeneous spatial distribution. Since these samples are much thinner than the 15nm thick samples in the previous experiment, a larger degree of trapping is expected. The trap clearing action spectrum for the pentacene control sample is also similar to what has perviously been observed. Some peaks in the trap clearing action spectrum correspond to peaks in the absorption spectrum, due to clearing by free charge generation. However, there still remains an observed peak in the trap-clearing spectrum at 500nm that is not correlated with the absorption spectrum, and is attributed to absorption of the trap molecule.

Codeposition of pentacene with 6,13-pentaquinone shown in Figure 3.11(e,f,g) show markedly different results. Traps that were populated by applying  $-40V$  to the gate electrode for two minutes show relatively little trapping compared to the pentacene control sample. Trapping is located near regions of micron-size structural defects. Additionally, the trap clearing action spectrum for this sample appears to be independent of wavelength of illuminated light. While the same mechanism of trap decay might be present, it is obfuscated by another process which is much faster. It is concluded that charge traps are cleared primarily by some other process

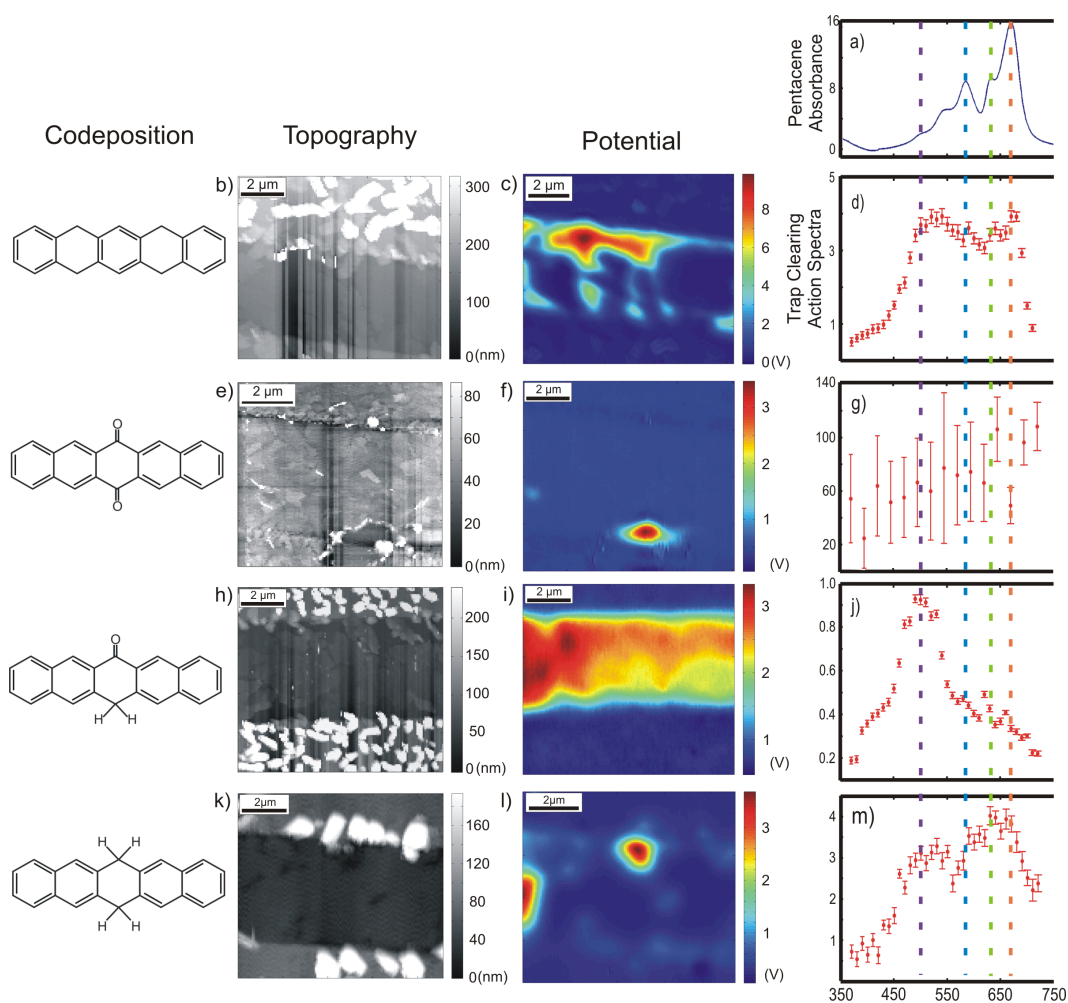


Figure 3.11: Codeposition Experiment

Results of the codeposition experiment. Chemical structure of various trap precursor molecules codeposited with pentacene are shown (left). Images of topography taken by AFM (b,e,h,k) and contact potential taken by EFM (c,f,i,l) show different behavior for each codeposition. Trap clearing action spectra, the rate at which traps clear under illumination, are also shown (d,g,j,m). These spectra are normalized by energy of illuminating light, and have units of ( $10^{-4} \text{ eV}^{-1} \text{ s}^{-1}$ ).

(likely thermal) than absorption of light. These results indicate that 6,13-pentaquinone, a widely studied chemical defect in pentacene [258–261, 261], is not responsible for the trapping observed in pentacene thin films.

In the experiment where the leading trap candidate, pentacene-6(13H)-one, is codeposited with pentacene (Figure 3.11(h,i,j)), our initial hypothesis is confirmed. Traps that were populated by applying  $-5\text{V}$  to the gate, a much lower gate voltage than in other codeposition samples, show

uniform trapping throughout the channel. This indicates that trapping in this film is systemic, due to the ubiquitous presence of the trap precursor molecule. Furthermore, it is observed that there is a large peak in the trap clearing at 500nm, which corresponds to the anomalous trap clearing peak in the pentacene control sample and to those in Figure 3.5. It is also interesting to note that the trap clearing rate in this sample is much less in this sample than in other codeposition samples. This is due to a hinderance in charge transport.

In the last codeposition experiment with the second trap candidate proposed by Northrup and Chabinye [91], 6,13-dihydropentacene (Figure 3.11(k,l,m)), shows spatially inhomogeneous trapping similar to the pentaquinone sample. However, in this sample, the trap clearing action spectrum similar to what was observed in the pentacene control sample. This indicates that the trapping shown is more akin to the natural decay of pentacene, rather than trapping due to the codeposition of 6,13-dihydropentacene.

### 3.6 Concluding Remarks

In summary, time- and wavelength-resolved EFM were used to observe local effects of trapped charge on free carriers, to mechanically detect the electronic spectra of a few hundred molecules in a thin film, and to uncover new mechanisms of light-induced trap clearing in polycrystalline pentacene. Previously-proposed mechanisms of trapping/de-trapping involving mid-gap states at intra-grain regions [84, 85], formation of immobile bipolarons [88], molecular sliding [89], migration of charge into dielectric layers [85], stabilization of charges by dipoles in dielectric layers [86, 87], or chemical reactions in the bulk [91–93, 117] cannot simultaneously explain the spatial distribution of traps and the wavelength dependence of trap clearing observed here. This work suggests a new mechanism of trap clearing via photoexcitation of the trap species followed by electron transfer; our spectroscopic trap-clearing data implicate pentacen-6(13H)-one as the relevant neutral trap precursor. This implication is supported by codeposition experiments that

show codeposited samples of pentacene-6( $^{13}\text{H}$ )-one on pentacene have systemic trapping and a trap clearing action spectra similar to aged pentacene. The experimental technique introduced here opens up exciting possibilities for obtaining electronic spectra of charged trace impurities in films of  $\pi$ -conjugated molecules. Particularly when augmented by *ab initio* theory, this technique is likely to yield much insight into the chemical identity of defects in organic electronic materials.

## EFFICIENCY LOSSES IN POLYMER-BLEND SOLAR CELLS OBSERVED BY SPECTROSCOPIC PHOTOPOTENTIAL IMAGING

### 4.1 Introduction

This chapter presents a study of scanning photopotential spectra over bulk heterojunction solar cells. The conclusion of this chapter is that charge trapping exists solar cells with donor-acceptor intermixing, where trapped charge generates an electric field which that opposes geminate pair splitting. This work is in conjunction with the work done in chapter 5, and is in submission to Nature Materials.

Bulk heterojunction cells offer among the highest efficiencies of all organic photovoltaics. In this work, light-enhanced electric force microscopy and photopotential-fluctuation spectroscopy are used to investigate the ideality of the  $p$ - $n$  heterojunctions present in a polymer-blend solar cell and thereby elucidate the functional consequences of donor-acceptor intermixing in the film. Photopotential spectra acquired over a bulk heterojunction film comprised of phase-separated F8BT and PFB polymers reveal photopotential spectra that (1) do not mirror the polymers' absorption spectra, (2) provide evidence for widespread charge trapping associated with the photoabsorption of F8BT, and (3) show that a photopotential forms across internal  $p$ - $n$  junctions that opposes the separation of geminate pairs. Our findings indicate that the phase boundaries in the F8BT:PFB blend do not behave as a  $p$ - $n$  junction upon illumination and suggest a microscopic mechanism by which intermixing of phases leads to efficiency loss in a bulk heterojunction solar cell.

A key parameter determining the efficiency of any solar cell is the open circuit voltage. In organic bulk heterojunction solar cells, the open-circuit voltage is determined by the energy levels of the constituent molecules [133, 139] but is also thought to depend critically on photoinduced

carrier concentration gradients [135], electric-field and disorder-dependent geminate separation [137, 262] and recombination [100, 138, 141, 144], nanostructure and morphology [145], shunt resistance [136], and reverse saturation current [142]. Scanning probe measurements of contact potential and current have been used to infer the role of morphology in determining open-circuit voltage [145, 161]; however, these studies did not systematically vary the wavelength of the illuminating light.

This work presents 100 nm resolution images of *surface photopotential spectra* of a PFB:F8BT bulk heterojunction film, recorded under 350 nm to 750 nm low-intensity excitation in vacuum using frequency-modulated Kelvin probe microscopy [101]. By comparing surface photopotential to absorption spectra, we are able to determine which molecules are responsible for surface photopotential in the various phases. These spectra reveal new information about charge generation and trapping unobtainable in experiments conducted at only a few wavelengths. The PFB:F8BT system was chosen because it is a nominally well-studied model system in which the role of the heterojunction interface in generating charge nevertheless remains controversial [132, 161, 169]. The surface photopotential spectra reported here reveal that, in the PFB:F8BT blend, photoexcitation of the *minority component* in each phase has a large role in determining the open-circuit voltage. We demonstrate that the minority component leads to photopotential that does not result from transfer of free carriers but rather from trapped charge—a general efficiency-loss mechanism not considered in previous analyses of intermixing [151, 180].

## 4.2 Methods

*Sample Preparation Methods.* Solar cells were fabricated from a 1:1 (unless otherwise noted) solution of PFB (Poly[(9,9-dioctylfluorenyl-2,7-diyl)-co-(N,N-diphenyl)-N,N-di(pbutylphenyl)-1,4-diamino-benzene])) and F8BT (Poly[(9,9-dioctylfluorenyl-2,7-diyl)-alt-co-(1,4-benzo-2,1',3-thiadiazole)]) (American Dye Source, ADS232GE and ADS133YE respectively) dissolved in anhydrous p-xylene

(Sigma-Aldrich), sonicated for 40 minutes, and heated at 50 °C. The 200 nm thick films studied here were made from a solution of 30 mg PFB/ 30 mg F8BT in 2.5 mL of p-xylene. A PEDOT:PSS (Clevios PH500) layer was deposited on bare ITO (KinTec, unpatterned) by spin coating for 60 seconds at 6000 rpm. The PEDOT:PSS layer was annealed at 170 C for 2 min in atmosphere before the substrates were transferred to a glove box, where the PFB:F8BT solution was applied by spin coating for 60 seconds at 2000 rpm (approx. 25 nm thickness). Bilayer devices were fabricated in a method described elsewhere [263]. Samples were transferred under red-light illumination to scanning probe microscope, with approximately ten minutes of air exposure. It is known that exposure to air and light on the order of days does not affect surface photovoltage [166].

*Electric Force Microscopy Methods.* Contact potential maps were collected by scanning a metalized cantilever (SPMTips NSC-18; Ti-Pt coated) at 60 nm peak-to-peak oscillation 90nm (above mean position) across a 6x6 micron area at 4 seconds per line. Tip voltage was modulated at 160 Hz, 3V zero-to-peak while frequency was demodulated by FPGA (RHK PLLpro) with an output at 400 Hz bandwidth. First and second harmonics of the cantilever frequency at the modulation frequency were detected via lock-in (30 ms and 50 ms time constant, respectively). Signal at first harmonic is nullified by applying additional DC tip voltage, through use of a PID controller (P=OFF, I= 80Hz, D= .05 ms). The DC tip voltage required to nullify the first harmonic of the cantilever frequency at the modulation frequency is the contact potential.

*Noise Measurements.* The cantilever was oscillated via positive feedback with a fixed-amplitude drive to a zero-to-peak amplitude of 15 nm. The tip was held, except where noted, at a mean tip-sample distance of  $d = 90$  nm and at a voltage of 5 V above the local electrostatic potential,  $V_{ts} - \phi = 5$  V. The displacement of the cantilever was observed by fiber-optic interferometry, digitally sampled at 260.0 kHz, and sent to a software frequency demodulator[264] which estimated the instantaneous cantilever frequency at an update rate of 11.82 kHz. The frequency demodulator output was passed through a 20<sup>th</sup> order Butterworth bandpass filter centered at  $f_c$

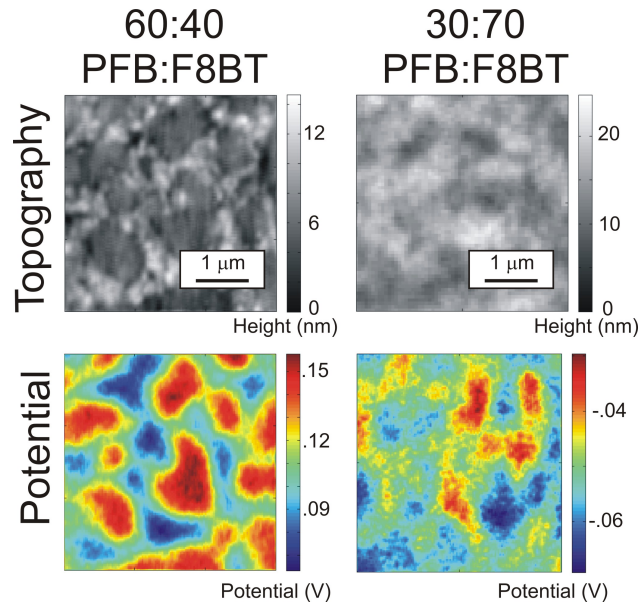


Figure 4.1: Materials assignment

Topography and potential scans of two films with 60:40 and 30:70 concentration of PFB:F8BT. Recessed PFB-rich domains in the 60:40 sample show higher contact potential. 30:70 PFB:F8BT films show now mesoscale morphology, similar to studies done by Ginger [265].

(bandwidth =  $2 \times 1000\text{Hz}$ ). Frequency noise power spectra were obtained by Fourier transforming the autocorrelation function of the frequency fluctuations, recorded for 8-10 seconds typically, and averaging  $N_{\text{avg}} = 30$  spectra together. The resulting one-sided power spectrum of cantilever frequency fluctuations was integrated between  $\approx 0.2\text{-}0.25$  and  $\approx 1.4$  Hz to obtain the jitter. An additional 10 second delay was implemented after any change in the illumination wavelength or tip voltage.

### 4.3 Results

Initial experiments were conducted by spinning two films of PFB:F8BT at different concentrations for the purpose of domain assignment, the results of which are shown in Figure 4.1. The first film, with a concentration of 60:40 PFB to F8BT showed regions of lower topography that corresponded with higher contact potential, while regions of higher topography corresponded

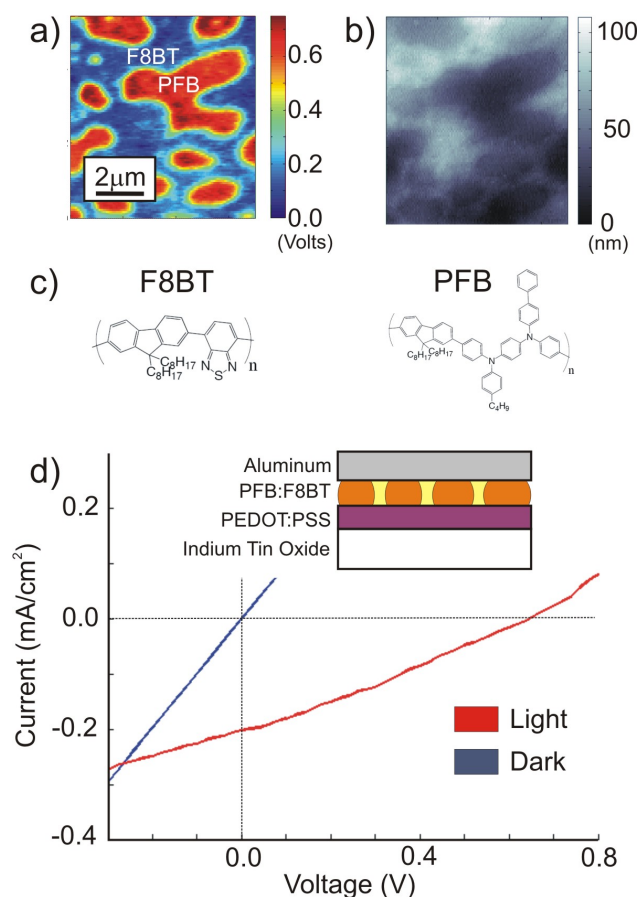


Figure 4.2: PFB-F8BT Solar Cell

(a) Scanning EFM image of contact potential in dark conditions. (b) Tapping mode AFM image of topography on 100-nm thick sample of PFB-F8BT. (c) Chemical structure of F8BT and PFB. (d) Photovoltaic curve Bulk heterojunction of ITO/PEDOT:PSS/PFB-F8BT/Al device under AM1.5. Devices show efficiency of .04%.

with lower potential. By comparing to other studies[265], PFB-rich regions are assigned to lower topography, and F8BT-rich regions correspond to higher topography. The second film, with a concentration of 30:70 PFB to F8BT displayed homogeneity in both topography and contact potential. This assignment is consistent with studies by Coffey[173], but not those of Chiesa[161].

AFM and EFM experiments show polymers phase separate upon spin casting, as seen in Figure 4.2(a-b). PFB-rich regions appear to have high contact potential, as well as recessed topographical features, relative to F8BT regions. The completed solar cells, made from polymers with chemical structure shown in Figure 4.2(c), were tested under AM1.5 conditions with a light

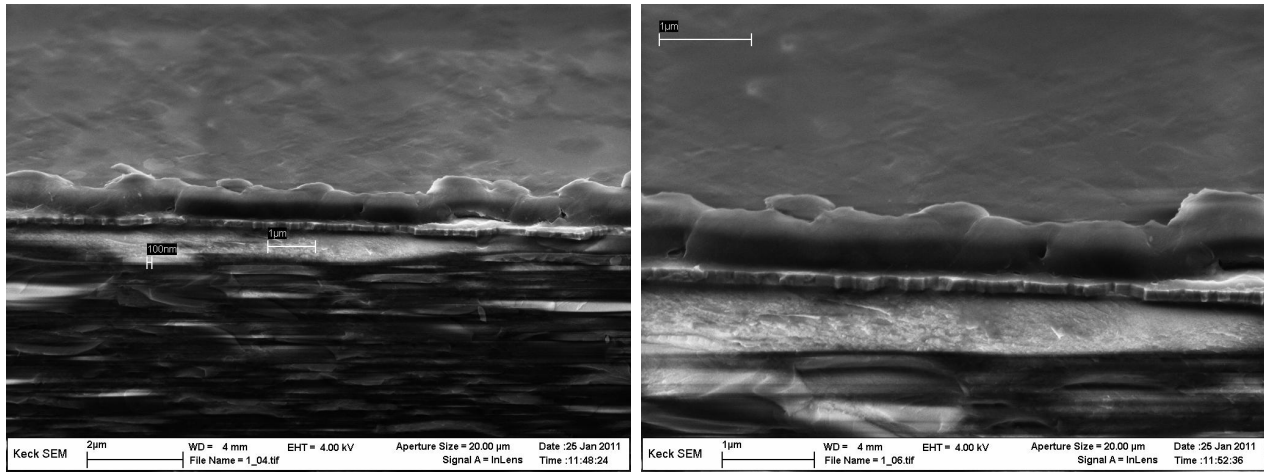


Figure 4.3: SEM of PFB-F8BT Solar Cell

SEM image of 500nm thick PFB:F8BT thin film on ITO/PEDOT:PSS. Domains are difficult to discern.

intensity of  $100\text{mWcm}^{-2}$ . Photovoltaic curves of the bulk heterojunction of ITO/ PEDOT:PSS/ PFB:F8BT/Al device under AM1.5. Devices show efficiency of .04% (Figure 4.2(d)). These device efficiencies are similar to devices made by other groups [266, 267]. While this efficiency is low, this value is not close to peak efficiencies obtained for these materials. PFB:F8BT solar cells spun from different solvents obtain smaller domains, which achieve higher efficiencies. However, cells with smaller domain sizes are more difficult to study with EFM, as the domain sizes are on the order of the resolution achievable with this technique.

In an attempt to gain an idea of vertical morphology in this film, SEM images of a cross section of a thick PFB:F8BT film were taken (Figure 4.3). Although domains are readily apparent in EFM images and somewhat apparent in AFM images, domains in SEM images are difficult to discern. Even though these polymers can conduct, low accelerating voltages are required to avoid charging over time. Though SEM has been used to image other polymers [268], the resolution between different materials at low accelerating voltages is not enough to image films of PFB and F8BT.

A PFB(donor):F8BT(acceptor) blend film with a 50:50 composition ratio was fabricated on a PEDOT:PSS/ITO bottom contact. Images of surface potential were acquired in the dark

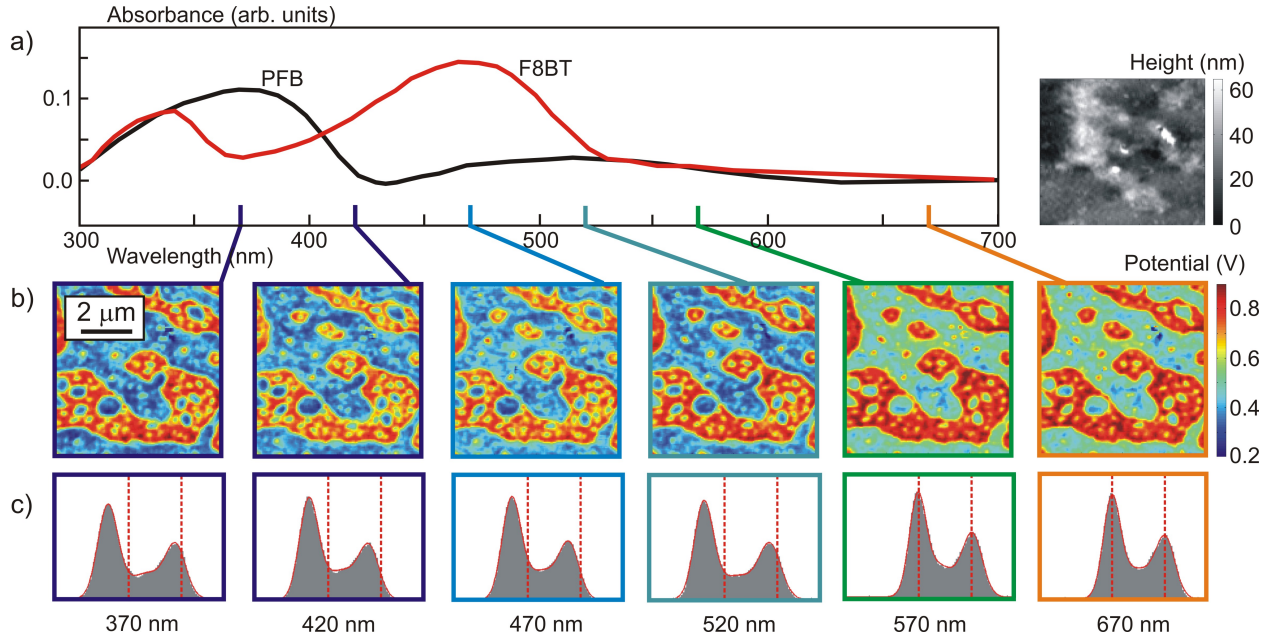


Figure 4.4: Wavelength-resolved surface potentiometry of a PFB/F8BT film.

(a) Normalized absorbance spectra of PFB and F8BT, reproduced from Kietzke [267]. (b) Maps of surface potential  $\phi$  at various wavelengths. The upper inset shows the surface topography of the film. (c) Surface potential histograms at various wavelengths. Each histogram was fit to a sum of three Gaussians. The best-fit line is displayed in red. For comparison, vertical dotted lines have been drawn at the best-fit dark potential for the F8BT-rich regions ( $\phi_{\text{dark}} = 0.48 \text{ V}$ ) and the PFB-rich regions ( $\phi_{\text{dark}} = 0.80 \text{ V}$ ).

and under illumination, with the wavelength of the incident radiation stepped from 350 nm to 750 nm in 10 nm steps. Figure 4.4 displays images of surface potential  $\phi$  at representative irradiation wavelengths  $\lambda$ . A topographic image and bulk optical absorption spectra are shown for comparison.

Histograms of surface potential (Figure 4.4c) show a bimodal distribution corresponding to PFB-rich and F8BT-rich regions. By comparing surface potential images acquired over samples of various PFB:F8BT ratios, we assign the low potential areas in Figure 4.4b to F8BT-rich regions and the high potential areas to PFB-rich regions (Figure 4.1). The left and right vertical lines in Figure 4.4c indicate the potential of the F8BT-rich and PFB-rich regions, respectively, in the dark.

To quantify the change in surface potential with illumination wavelength, the histogram

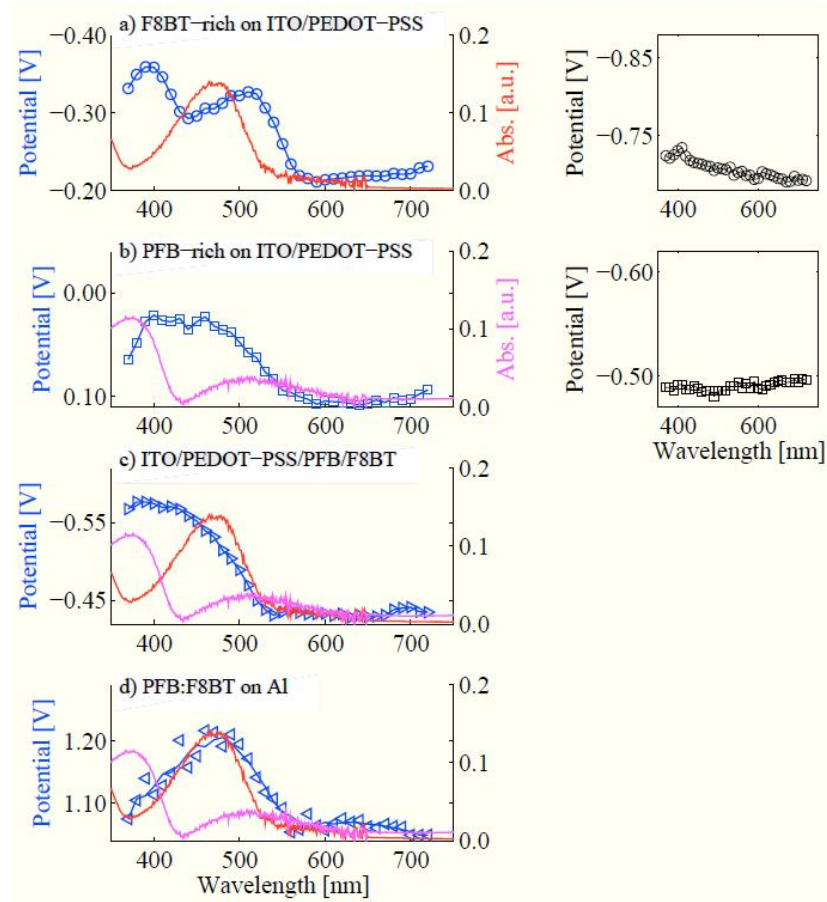


Figure 4.5: Photovoltage vs Absorbance

Surface photovoltage spectra over films prepared on ITO/PEDOT-PSS: (a) photovoltage spectrum of F8BT-rich regions in the bulk heterojunction film (left, blue open circles), absorption spectrum of F8BT (left, red solid line), and photovoltage spectrum over an F8BT control sample (right, black open circles); (b) photovoltage spectrum of PFB-rich regions in the bulk heterojunction film (left, blue open squares), absorption spectrum of PFB (left, magenta solid line), and photovoltage spectrum over a PFB control sample (right, black open squares); and (c) photovoltage spectrum over an F8BT/PFB bilayer film (right-pointing blue triangles), absorption spectrum of F8BT (red solid line) and absorption spectrum of PFB (magenta solid line). (d) Surface photovoltage spectra of a PFB:F8BT bulk heterojunction film prepared on an aluminum substrate (left-pointing blue triangles), with F8BT and PFB absorption spectra shown for comparison. The y-axis has been inverted in (a-c) to facilitate comparing photovoltage and absorption spectra.

data of Figure 4.4c was fit to a sum of three Gaussians to represent F8BT-rich, PFB-rich, and interfacial regions. The extracted mean potential over the F8BT-rich and PFB-rich regions is plotted versus wavelength in Figure 4.5a,b. F8BT and PFB absorption spectra are plotted out for comparison. A bilayer control sample was also prepared via spin coating and lamination. This sample's photopotential decreases upon illumination (Figure 4.5c), consistent with a vertical transfer of electrons from PFB to F8BT, and changes monotonically as  $\lambda$  passes through the F8BT and PFB absorption maxima. Samples of PFB:F8BT on aluminum shows a photopotential spectrum (Figure 4.5d) that only tracks F8BT absorption with a *positive* change in contact potential.

The sign of the surface photopotential over PFB-rich regions is unexpected. The surface photopotential decreases not only over F8BT-rich regions but also over PFB-rich regions as well upon illumination. This observation contradicts the picture of the PFB/F8BT junction as a diode in which electrons are transferred from PFB to F8BT upon dissociation of excitons at the interface; this simple diode model predicts that upon illumination, the potential should increase in PFB-rich regions and decrease in F8BT-rich regions. Instead, our data indicates a net photoinduced transfer of electrons from PEDOT:PSS/ITO into *both* F8BT-rich and PFB-rich regions. Matur-ova and co-workers [165] have observed an analogous net photoinjection of electrons from the substrate into both donor and acceptor phases under single-wavelength illumination in polymer-fullerene bulk heterojunctions. By scanning the wavelength of illuminated light, we find here that the surface photopotential spectrum does not track the absorption spectrum of the majority component in either phase. The photopotential spectrum over PFB-rich regions in fact appears to be dominated by F8BT absorption. The photopotential spectrum over F8BT-rich regions, in contrast, shows an early onset at low  $\lambda$  and a feature at high  $\lambda$  whose wavelength dependence mirrors PFB absorption. Photopotential here is not due to internal photoemission from the PEDOT:PSS/ITO substrate, as control samples of pure F8BT and PFB on the substrate showed no significant surface photopotential in the observed wavelength range (Figure 4.5(a-b)).

## 4.4 Discussion

### 4.4.1 PN-Junction Approximation

The simplest model to describe the operation of these cells is that of a PN-junction. A PN-junction is a type of diode where an n-type material, a material in which electrons are the majority carrier, is brought in contact with a p-type material. Figure 4.6 gives a rudimentary illustration of a PN-junction. The Fermi levels, the chemical potential of electrons, are unaligned before the materials come in contact. After the materials are brought in to contact, mobile charge moves in order to equalize the chemical potential. When the Fermi levels are equalized, charge stops flowing, and the junction is at steady state. The charge that transferred from one material to the other remains in proximity to the interface. This area is called the depletion region. In the n-type material, the depletion region contains holes. From Poisson's equation, where the electric field and potential are functions of spatially distributed charge density, it can be shown that there is an electrical potential installed between the materials. This is called the built-in potential.

In the PN-junction picture under illumination, mobile charges generated in the semiconducting material move under the influence of the potential gradient (electric-field). As described in Figure 4.7, mobile electrons move into the n-type material, while mobile holes move into the p-type material. This reduces the depletion width in the PN-junction. Consequently, this reduces the built-in potential and band bending at the interface between p-type and n-type materials.

### 4.4.2 Potential Contrast Under Dark Conditions

Contrast between two components of bulk heterojunction thin films in the dark contact potential images has been observed before, [160, 161, 163], explained with a detailed description from

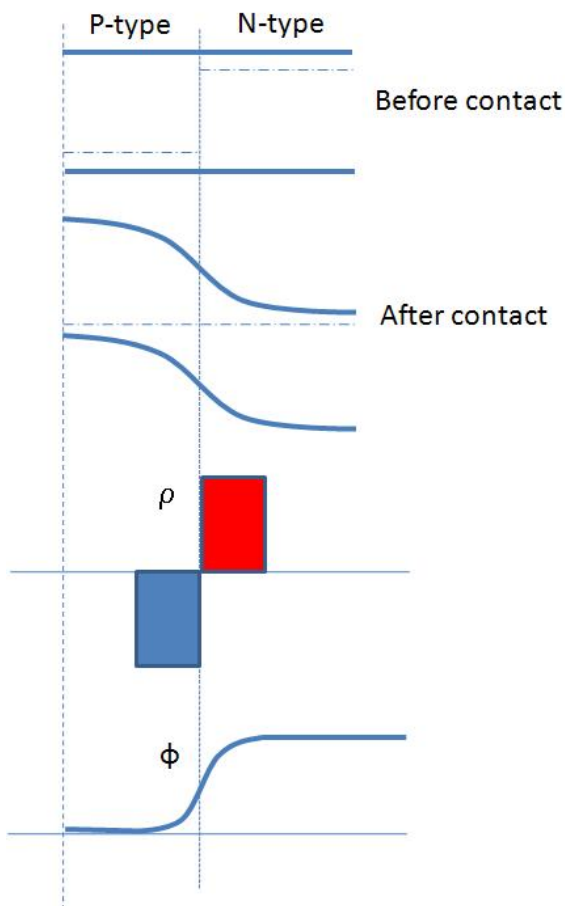


Figure 4.6: PN Junction

Schematic of a PN junction. Before materials are brought into contact, Fermi levels are unaligned (dot-dash lines). After materials are brought into contact, Fermi levels equalize. This establishes a region of charge density ( $\rho$ ) at the interface called the depletion region. It also gives rise to an increase in potential ( $\phi$ ) over the n-type region, known as the built-in potential.

Tengstedt et al. [269]. Contact potential contrast arising from the exchange of charge between active materials has been observed in wide bandgap semiconductors [270], but is thought to be small in fluorinated polymers used in solar cells [271]. The presence of contrast in the dark images is to some extent remarkable, because in the dark charges are thought to be absent in pristine, undoped organic semiconductors. It has been thought that the contact potential should be determined by the work function difference between the tip and the PEDOT:PSS bottom electrode. The crucial point in explaining the dark contrast is the alignment of the donor and acceptor HOMO levels with the work function level of the bottom electrode. Presented here is an

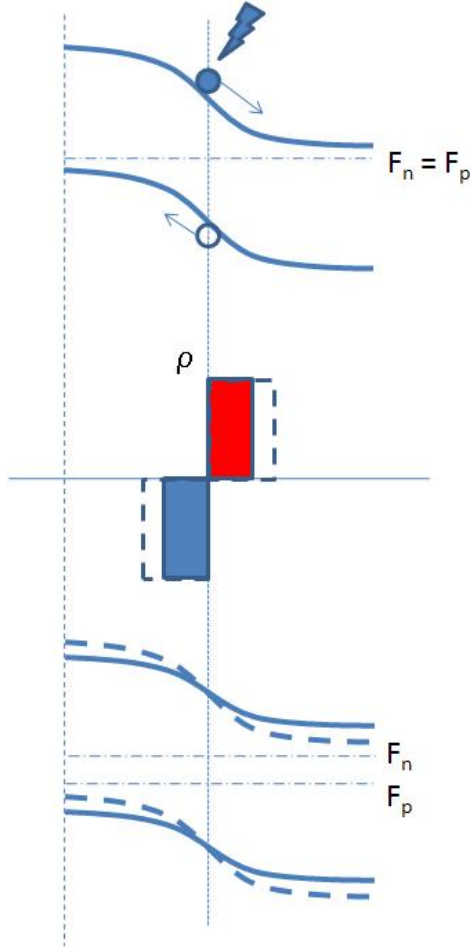


Figure 4.7: PN Junction under Illumination

Under illumination, mobile charges move under the influence of the local electric field at the PN junction interface. This, in turn, narrows the depletion region and lowers the built-in potential.

rough calculation of depletion widths assuming interfaces can be treated as Schottky junctions.

The concentration of holes in the semiconductor at the PEDOT:PSS interface,  $\rho_0$ , depends on the magnitude of the hole injection barrier  $\phi_h$ , and the density of states ( $N_0$ ) at  $E = \mu_m$  in the semiconductor and  $k_B T$  the thermal energy as,

$$\rho_0 = N_0 e^{q\phi_h/k_B T}. \quad (4.1)$$

As a consequence of the small barrier to injection, seen in the energy level diagram for the

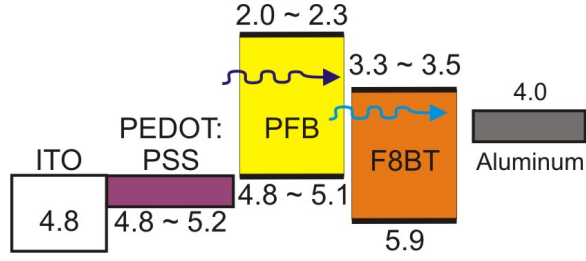


Figure 4.8: ITO/ PEDOT:PSS/ PFB:F8BT/ Al

Energy level diagram of ITO/ PEDOT:PSS/ PFB:F8BT/ Al taken from literature[141, 272–274].

device (Figure 4.8), these carriers will move into the organic layer. This only occurs when the work function of the underlying substrate is near the ionization potential (HOMO level to vacuum level) of the organic polymer, where the barrier to hole injection is small [269, 275, 276]. Since the hole injection barriers  $\phi_h$  of PFB and F8BT with PEDOT:PSS are approximately 0 - 0.1 and 0.7 - 1.1 eV, respectively, holes diffuse into PFB near the ITO/PEDOT:PSS interface. On aluminum, the barrier to hole injection is much larger for both materials. As a consequence, very little positive charge migrates from aluminum into the semiconductor.

To fully understand the dark contrast in these images of contact potential, shown in Figure 4.9, depletion lengths must also be considered. In the case of an intrinsic semiconductor with intrinsic level  $\epsilon_i$  on a metal with work function  $\mu_m$ , the depletion length at the metal-organic interface can be derived from the potential drop across the interface,  $\psi_s = \mu_m - \epsilon_i$ . To estimate the diffusion length, the first step is to derive the intrinsic carrier density  $n_i$ . For an intrinsic semiconductor with a bandgap energy  $\epsilon_g$ ,

$$n_i = \rho_n e^{\sigma^2/4\tau^2} e^{\epsilon_g/2k_bT}. \quad (4.2)$$

Using a molecular number density of  $\rho_n = 10^{27} m^{-3}$ , [277] an energetic disorder of  $\sigma = 0.15 eV$  [278]. Using the estimated bandgap for PFB and F8BT,  $n_i = 1 \times 10^7 m^{-3}$  in PFB and  $n_i = 5 \times 10^9 m^{-3}$  in F8BT. Next, for simplification of the math, it is convenient to write a

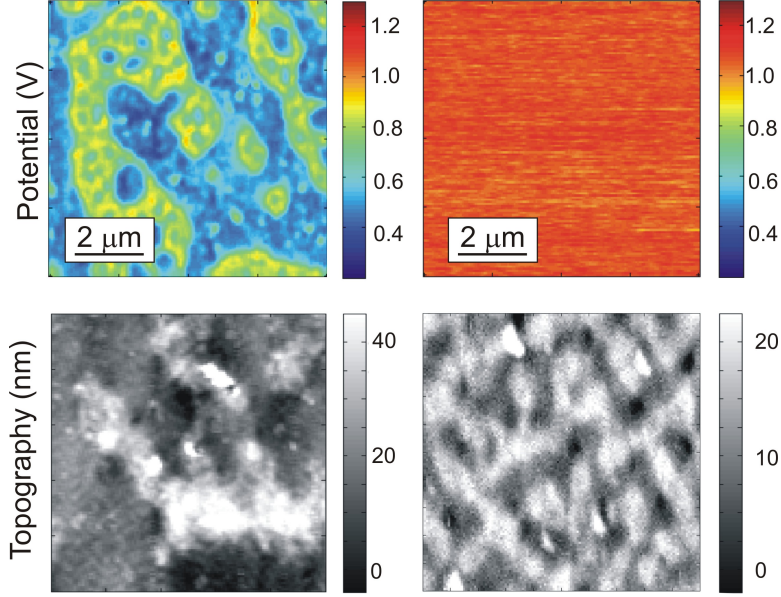


Figure 4.9: Contact potential maps

Contact potential maps of ITO/ PEDOT:PSS/ PFB:F8BT (left) and Aluminum/PFB:F8BT. The film on ITO has a dark potential contrast while the film on Aluminum does not. The difference in contact potential on ITO/ PEDOT:PSS/ PFB:F8BT has a depletion width of  $\sim 100$  nanometers.

characteristic length scale  $x_i$  in terms of the carrier density.

$$x_i = \left( \frac{2k_b T \epsilon}{q^2 n_i} \right)^{1/2}. \quad (4.3)$$

For room temperature, with the estimated intrinsic level, the depletion length for a Schottky diode is a well known function of the built-in potential, and is given by,

$$x_0 = x_i \left( \frac{q V_{bi}}{k_b T} \right)^{1/2}. \quad (4.4)$$

In the Schottky diode model, taking  $V_{bi} = \psi_s$ , depletion lengths on ITO/PEDOT:PSS are estimated to be 7 meters and 12 centimeters in PFB and F8BT, respectively. These depletion lengths are much larger than the thickness of the film. What the Schottky diode model predicts as that little charge is injected into the material at this length scale. As there is an observable

contact potential difference in the EFM experiment, this result is unphysical. What most accurately describes the behavior in this solar cell is Mott-Gurney theory on the injection of carriers from a metal into a semiconductor. This theory, similar to Gouy-Chapman theory in electrochemistry, predicts a build-up of electric potential at the metal interface  $\psi_d$  that affects charges in the bulk of the organic. Mott-Gurney theory mathematically differs from Schottky theory by having non-zero boundary conditions for the local potential at the metal-organic interface. When  $\psi_s = \epsilon_i - \mu_m$  is large,  $\epsilon_i$  estimated here to be in the middle of the band gap (3.5eV and 4.4eV in PFB and F8BT respectively), the depletion length from Schottky theory is significantly modified. Qualitatively, the larger the electric potential buildup at the interface, the shorter the depletion length. With some derivation [279], the depletion length derived from Mott-Gurney theory is

$$x_0 = \frac{x_i}{2\cosh(q\psi_s/2k_bT)}. \quad (4.5)$$

On ITO/PEDOT:PSS, the modified depletion lengths from Equation 4.5 are estimated as 10<sup>-13</sup> meters and 500 nanometers in PFB and F8BT respectively. This is more reasonable given the dark contrast in the contact potential maps. On aluminum,  $\psi_s$  is much smaller in PFB. This gives modified depletion widths as 66 microns and 20 microns in PFB and F8BT respectively. As the depletion widths are much larger than the thickness of the film in this case, no contact potential shift between the metal and organic is expected.

To complete the picture of depletion length, the organic-organic interface must also be investigated. In a derivation by Marohn[280], potential due to interfacial charge density is shown to behave as a kind of lever rule, given by

$$\gamma = \frac{\psi_s^{PFB}}{\psi_s^{F8BT}} = \frac{\epsilon_g^{PFB} - \epsilon_g^{F8BT}}{2k_bT} \approx \text{between 2 and 13}. \quad (4.6)$$

. For this case, most of the potential-drop is expected in PFB. With additional condition

that  $\psi^{PFB} + \psi^{F8BT} = \epsilon_i^{PFB} - \epsilon_i^{F8BT} = 1.1\text{eV}$ , the depletion length is derived to be

$$x_0^{PFB} \approx \frac{x_i}{64} e^{-q\psi_s^{PFB}/2k_bT}; x_0^{F8BT} \approx \frac{x_i}{64} e^{-q\psi_s^{F8BT}/2k_bT} \quad (4.7)$$

Between the organic-organic interface, for  $\gamma = 2$  the calculated depletion length in PFB is 10 nanometers, while F8BT is 600 nanometers. This is within an order of magnitude of the observed organic-organic depletion length in ITO/ PEDOT:PSS/ PFB:F8BT of roughly 100 nanometers. Since these equations are sensitive to small changes in  $\psi_s$ , and that this calculation is an approximation, the result for the depletion length is within reason.

#### 4.4.3 ITO/PEDOT:PSS/PFB:F8BT Under Illumination

Under illumination, the contact potential shown in Figure 4.5 decreases in both regions upon illumination over ITO/ PEDOT:PSS/ PFB:F8BT. This observation contradicts the simple picture demonstrated in Figure 4.7 where the PFB/F8BT junction serves as a diode in which charges are transferred between materials upon dissociation of excitons at the interface. This simple diode model predicts that upon illumination the potential should increase in PFB and decrease in F8BT. Instead, our data indicates a net photoinduced transfer of electrons from ITO/PEDOT:PSS into *both* F8BT and PFB. The sign of contact potential shift in PFB is opposite what is expected in the PN junction approximation.

To explain the photopotential spectra, we must invoke intermixing of the active materials. Both photoluminescence [267] and X-ray spectroscopy [154] studies show the presence of F8BT in the PFB-rich phase and a lack of intermixing of PFB in the F8BT-rich phase. The surface photopotential spectra expected for such an intermixed film are sketched in Figure 4.11. The relevant energy levels of the active materials [141, 273] are sketched in Figure 4.11a. Figures 4.11(b,c) illustrate free charges generated at PFB/F8BT interfaces present in micron-scale and

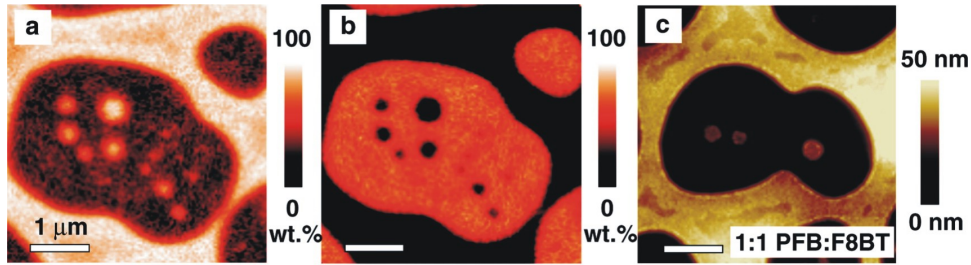
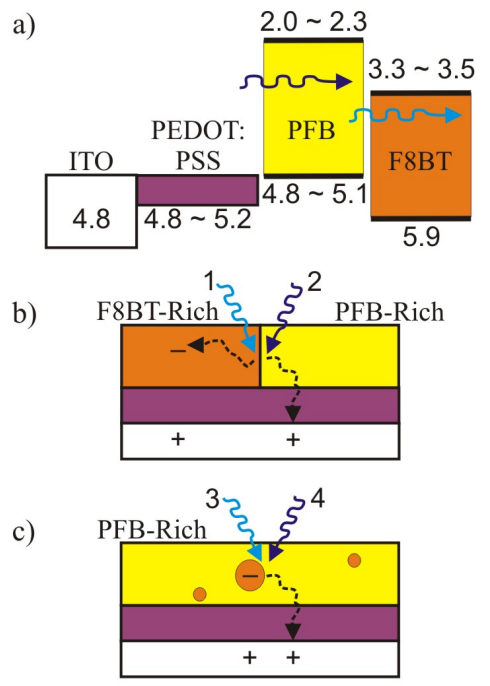


Figure 4.10: Composition Maps

Quantitative F8BT (a) and PFB (b) composition maps and AFM image of 1:1 blend (c) on ITO/PEDOT:PSS obtained by scanning transmission x-ray microscopy (STXM). Reproduced from McNeill et al. [281].

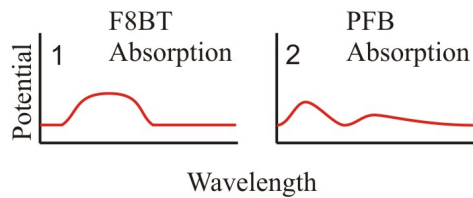
nano-scale domains. At the F8BT/PFB interface in micron-scale domains, free charge can result from optical absorption of either F8BT, 1, or PFB, 2. Analogous optical absorptions, 3 and 4, in nano-scale domains of F8BT present in the PFB-rich phase also result in the creation of free carriers at the F8BT/PFB interface. We would expect holes generated in PFB via processes 1 or 2 to flow to ITO and attract electrons generated in F8BT to the ITO interface. The small charge dipole expected from this process is inconsistent with the comparatively large photopotential apparent in the data of Figure 4.5. The large (negative) surface photopotential observed over F8BT-rich regions can be explained by the presence of trapped electrons in the bulk of F8BT. Consistent with experiment, our model in Figure 4.11 predicts that electrons generated in F8BT via processes 3 or 4 remain trapped in nanoscale domains while holes flow to ITO, likewise generating a large charge dipole. A summary of photopotential spectra expected from processes 1–4 over the two sample regions is presented in Figure 4.11d,e. Comparing the predicted spectra of Figure 4.11d,e to the observed spectra of Figure 4.5a,b, we conclude that the yield of photogenerated charge at the F8BT/PFB interface in the nano-scale domains is much higher following F8BT absorption, 3, than PFB absorption, 4. With this caveat, the phase-composition data of other studies[154, 267] and the model of Figure 4.11 explains the observed photopotential spectra.

The shift in contact potential under illumination can not be attributed to exciton splitting at the metal-semiconductor interface, or intrinsic absorption effects (such as photochemistry), since



Expected shift in contact potential:

d) Over F8BT-rich Region



e) Over PFB-rich Region

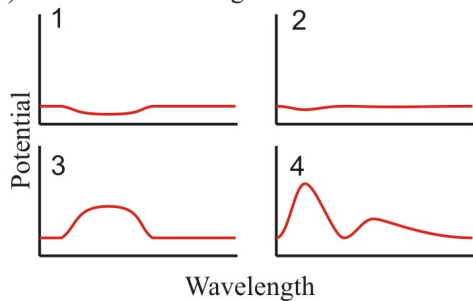


Figure 4.11: Diagram of charge transfer in ITO/PEDOT:PSS/PFB:F8BT

ITO/PEDOT:PSS/PFB:F8BT under illumination: (a) Energy level diagram of ITO/PEDOT:PSS/PFB:F8BT. (b) Light absorption generates free charges at the micron-scale F8BT/PFB interface (processes 1 and 2) or in (c) nano-scale domains in the PFB-rich material (processes 3 and 4). Sketches of the expected photopotential spectra over (d) F8BT-rich regions and (e) PFB-rich regions arising from the photogenerated charges sketched in (b) and (c). The data of Figure 4.5 are consistent with processes 1, 2, and 3 and inconsistent with process 4. Note that the potential scale in (d,e) is negative, in order to compare to Figure 4.5(a-c).

no surface photovoltage is observed in films of ITO/PEDOT:PSS/F8BT nor ITO/PEDOT:PSS/PFB (Figure 4.5(e-f)). Instead, contact potential shifts are attributed to an increase of free carriers in PFB and F8BT [161, 282]. These free carriers can affect contact potential in each material by: (1) modifying the density of carriers, (2) filling trap states, or (3) accumulating in the minority component of the phase-separated polymer.

Absorption can occur near the F8BT-PFB mesoscale interface by the absorption of F8BT (1) or PFB (2). Absorption can also take place in the nanoscale phase interface by the absorption of F8BT (3) or PFB (4). A model of this is shown in Figure 4.11(b). To understand the processes prevalent to the photovoltage, a rough sketch of the response for each process is shown in Figure 4.11(c-d). In processes 1 and 2, the material at the bulk interface is excited, leaving an electron in F8BT-rich phase and a short lived hole in PFB-rich phase. In process 3, F8BT in the nanoscale phase is excited, leaving an electron and a short-lived hole in the PFB-rich region. In process 4, PFB near the nanoscale phase F8BT is excited, with the same result as process 3. A combination of processes 1,2, and 3 best describe our photovoltage spectra. Note that photovoltage has the opposite sign as contact potential. Process 4 could possibly be mitigated by absorption in bulk PFB before reaching the nanoscale interface.

The open circuit potential of the device is approximated as the difference in the contact potential between the two regions[161]. As charge accumulates in the nanoscale region, the electric field throughout the film is greatly affected. This serves to reduce contact potential between PFB-rich and F8BT-rich regions, providing evidence of a reduced open circuit voltage in the device.

#### 4.4.4 Al/PFB:F8BT Under Illumination

Photovoltage measurements over Al/PFB:F8BT shown in Figure 4.9, reveal two curious features. The first of which is that there is no contrast in contact potential between PFB-rich and F8BT-

rich regions. The second, is that the photovoltage spectrum follows the absorption of F8BT, with little effect from PFB absorption.

The lack of contrast, as discussed before, can be explained the long diffusion lengths in Al/PFB:F8BT. Even though charge preferentially tends towards one domain over another, there is not enough difference in charge accumulation between the domains to be observable by EFM. Also observed through EFM is the large positive shift in contact potential when F8BT absorbs light. In this case, free electrons are generated which are extracted through the aluminum substrate. This leaves holes behind, which cause a positive change in contact potential. The fact that this contact potential shift does not occur under PFB absorption suggests that F8BT absorption is primarily responsible for charge generation in films of Al/PFB:F8BT.

## 4.5 Concluding Remarks

Introduced in this work is the first use of surface photovoltage spectroscopy imaging as a tool for probing the fate of photogenerated charges in a bulk heterojunction solar cell film and for investigating mechanisms of open circuit losses in bulk heterojunction solar cells.

Findings in this chapter show the PFB/F8BT mesoscale interface on PEDOT:PSS/ITO does not behave as a  $p$ - $n$  junction under illumination. Our results imply that the presence of the F8BT minority component in the PFB-rich phase has serious functional consequences in a bulk heterojunction solar cell. The nanoscale mixing leads to charge trapping and a surface photopotential that *opposes* exciton splitting at the interphase regions. This finding is in contrast to work done by Chiesa et al. [161], which suggests that disconnected micron-scale capping layers of PFB were responsible for charge trapping. These results suggest that patterned organic solar cells, with regions of a single material, would not suffer from this loss mechanism [268].

# ELECTRON TRAPPING IN POLYMER-BLEND SOLAR CELLS OBSERVED BY SPECTROSCOPIC PHOTOPOTENTIAL FLUCTUATIONS

## 5.1 Introduction

Measurements of contact potential detect electric fields from mobile and trapped carriers. Here we introduce the use of cantilever frequency noise measurements to probe voltage fluctuations arising from photoinduced carriers. We study cantilever frequency noise spectra as a function of irradiation wavelength, height, and tip-voltage. The resulting *voltage-fluctuation spectra* show a wavelength dependence distinct from the surface photopotential data. The spectra mirror the absorption of F8BT in both phases, which indicates that electron trapping occurs in F8BT in *both* PFB-rich and F8BT-rich regions.

This work sets precedent for detection of local contact potential noise measurements in a solar cell. Bulk voltage-noise measurements have been used to study trapping-detrapping fluctuations [283] and percolation transport [284] in organic semiconductor films while cantilever frequency noise has been used to study charge blinking [194], generation-recombination noise in inorganic semiconductor heterojunctions [223], and dielectric fluctuations in thin polymer films [264, 285]. From experiments of photopotential fluctuations versus illumination wavelength, frequency, tip-sample distance, and applied tip voltage, we have approximated a local spatial density of vacant electron traps in F8BT. In samples with less trapping, theory shows photopotential fluctuation spectroscopy can be a tool used to determine the local mobility of free charges.

The work in this chapter establishes that contact potential fluctuations over bulk heterojunction solar cells due to trapping-detrapping processes. Fluctuations give rise to stochastic force gradients and cause cantilever frequency noise. Charged AFM cantilevers have been used to observe dissipation due to free and trapped carriers in semiconductors [212–214], and image

currents in metals [215–217]. Magnetic-tipped AFM cantilevers have been used to probe dissipation associated with domain wall motion in ferromagnets [218, 219], eddy currents in metals [220], and thermomagnetic fluctuations in submicron magnetic particles [221, 222]. Cantilever frequency noise has been used to study charge blinking in inorganic semiconductor nanoparticles [194] and generation-recombination noise in inorganic semiconductor heterojunctions [223]. For more background literature on the applied theory behind cantilever frequency noise, consult Nik Hoepker’s thesis (2012).

## 5.2 Methods

In these experiments, the cantilever is driven into self oscillation via positive feedback, and its instantaneous resonance frequency recorded with sub-millisecond temporal resolution using a software frequency demodulator. An instantaneous cantilever frequency deviation is computed,  $\delta f_c(t) = f_c(t) - f_c$ , and a one-sided power spectrum of cantilever frequency fluctuations calculated from

$$P_{\delta f_c}(f) = 4 \int_0^{\infty} dt \cos(2\pi ft) \langle \delta f_c(t) \delta f_c(0) \rangle. \quad (5.1)$$

See methods section for further details.

To study the dependence of cantilever frequency fluctuations on irradiation wavelength, tip voltage, and distance, it is convenient to display an integrated frequency noise or “jitter”:

$$J \equiv \int_{f_l}^{f_u} P_{\delta f_c}(f) df \quad (5.2)$$

where  $f_l$  and  $f_u$  are the lower and upper frequency cutoffs, respectively. To capture the low-frequency fluctuations in Figure 5.2, the bounds of frequency measurement were set  $f_l = 0.2$  Hz and  $f_u = 1.4$  Hz and call the integrated frequency noise  $J_L$ . To capture the jitter associated with higher-frequency fluctuations,  $J_H$ , the bounds of frequency measurement were set  $f_l = 2.6$  Hz and  $f_u = 4.2$  Hz.

The cantilever was oscillated at 30nm peak to peak amplitude with a mean tip sample distance of 90nm, unless otherwise reported. Tip voltage was maintained at 5 volts above the contact potential, except for the voltage dependent studies. Frequency noise measurements were recorded for 8 seconds, with a 10 second delay after any change in illumination wavelength or tip voltage. Thirty averages (unless otherwise noted) of the cantilever frequency power spectrum was integrated between .25 and 1.25Hz to obtain the value for jitter. Frequency data is sampled at 260kHz with a Nyquist frequency of demodulation at 6kHz. An order 20 filter at 1kHz is imposed on the power spectrum to prevent noise folding.

A number of control experiments in this work are described which elucidate the origin of cantilever frequency noise. Two sources of cantilever frequency noise are fluctuations in the tip-sample distance and fluctuations in the contact potential.

### 5.2.1 Noise From Contact Potential Fluctuations

For frequency noise arising from fluctuating contact potentials ( $\phi_c(t) = \phi_{c0} + \delta\phi(t)$ ), recall the formula for energy stored in a capacitor (see methods section of thesis). To first order, the fluctuation in the energy stored in the tip-sample capacitor and the resulting frequency fluctuations is given by

$$\delta E(t) \equiv (V_T - \delta\phi)C(z)\delta\phi_c(t) \quad (5.3)$$

$$\delta f_c = -\frac{f_c}{4k_c} \frac{\partial^2 C}{\partial z^2} (V_T - \phi_c)^2 \quad (5.4)$$

$$P_{f_c}(f) = \left( \frac{f_c(V_T - \phi_{c0})}{2k_c} \right)^2 \left( \frac{\partial^2 C}{\partial z^2} \right)^2 P_{\delta\phi}(f) \quad (5.5)$$

These equations show that noise in the static frequency fluctuations due to fluctuations in contact potential should follow the square of tip voltage. To first order,  $P_{f_c}$  also follows the square of the tip voltage. The calculation of the source of contact potential noise is not trivial, and is the result of an upcoming publication from N. Hoepker and S. Lekala.

Cantilever frequency noise from contact potential fluctuations can be due to a number of sources, such as diffusion and trapping-detrapping processes. A theory describing the origins of contact potential noise in PFB-F8BT is outlined in the discussion section of this chapter. For a detailed derivation, consult Nik Hoepker's thesis.

### 5.2.2 Noise From Tip-Sample Distance Fluctuations

In addition to noise from fluctuations in the contact potential, noise in the cantilever frequency can also arise from noise in the average tip sample distance. This is attributed to nm-scale vibrations in the XY stage. In order to analyze the contribution to measured probe frequency fluctuations from external mechanical vibrations, the tip-sample separation  $z$  has added a stochastic fluctuation  $\delta z(t)$ . To first order,

$$\delta f_c = -\frac{1}{2} \frac{\partial^3 C}{\partial z^3} (V_T - \phi_c)^2 \delta z(t) \quad (5.6)$$

The effect of the power spectrum of position noise  $P_{\delta z}(f)$  on the power spectrum of cantilever frequency noise  $P_{f_c}$  is then calculated be

$$P_{f_c}(f) = \left( \frac{\partial^3 C}{\partial z^3} (V_T - \phi_c)^2 \frac{f_c}{4k_c} \right)^2 P_{\delta z}(f) \quad (5.7)$$

Here,  $P_{f_c}$  is dependent on tip voltage to the fourth power. This discrepancy with noise from fluctuations in contact potential can be used to differentiate the two sources of noise.

### 5.2.3 Modeling

Stochastic charge motion in the sample will lead to fluctuations in electrostatic potential, electric field, and electric field gradients, all of which can potentially couple to tip charge to yield a cantilever frequency shift. The frequency noise experienced by the tip can be written in terms of  $P_{\phi(z_1),\phi(z_2)}$ , the power spectrum of the time-domain correlation function  $\langle \phi(z_1, t) \phi(z_2, t) \rangle$  of the sample's electrostatic potential at a given height and lateral position. At large tip-sample separations  $d$ , the cantilever tip can be modeled as a cone, whereas at close separations it is better approximated as a sphere [286]. For a sphere, the frequency noise is given by [287]

$$P_{\delta f_c}^{\text{sphere}}(f, d) = \frac{f_c^2 (V_{\text{ts}} - \phi_s)^2}{4k_c^2} \times \partial_{z_1}^2 \partial_{z_2}^2 [C(z_1)C(z_2)P_{\phi(z_1),\phi(z_2)}(f)]|_{d=z_1=z_2}. \quad (5.8)$$

with  $f_c$  and  $k_c$  the cantilever resonance frequency and spring constant, respectively,  $C$  the tip-sample capacitance,  $V_T$  the voltage applied between the tip and the sample, and  $\phi_s$  the sample's local surface potential. From this point in the derivation, it is convenient to write  $(\partial^2 C / \partial z^2) \equiv C_n(z)$ . To treat the case of a cone, we model the cone with capacitance,  $B$ , as having a uniform density of line charge  $\lambda = B(V_T - \phi_s)$ . Within this approximation, the cantilever frequency noise spectrum is given by [287]

$$P_{\delta f}^{\text{cone}}(f, d) = \frac{f_c^2 (V_{\text{ts}} - \phi_s)^2}{4k_c^2} \times B^2 \partial_{z_1} \partial_{z_2} P_{\phi(z_1),\phi(z_2)}(f)|_{d=z_1=z_2}. \quad (5.9)$$

## 5.3 Results

### 5.3.1 Material Dependence

In the bulk heterojunction cell, there are two active materials. Regions rich with electron donating material (PFB), and regions rich with electron accepting material (F8BT). In the previous chapter, it was observed that PFB rich regions had a higher contact potential than F8BT regions. Figure 5.1 gives a contact potential map of the experiments contained in this chapter. Other

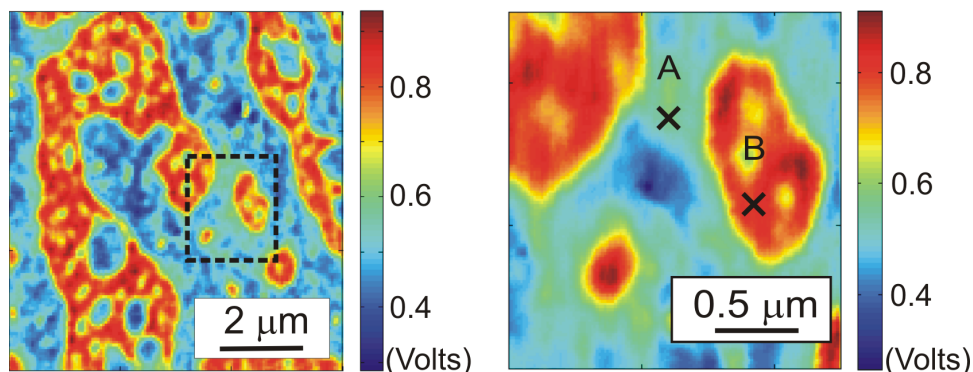


Figure 5.1: Single point measurement sampling locations.

Surface potential images of ITO/ PEDOT:PSS/ PFB:F8BT. Measurements taken over F8BT-rich regions were at location ‘A’ while measurements over PFB-rich regions were taken at ‘B’. Other measurements that corroborated initial findings were conducted at other points within the sample.

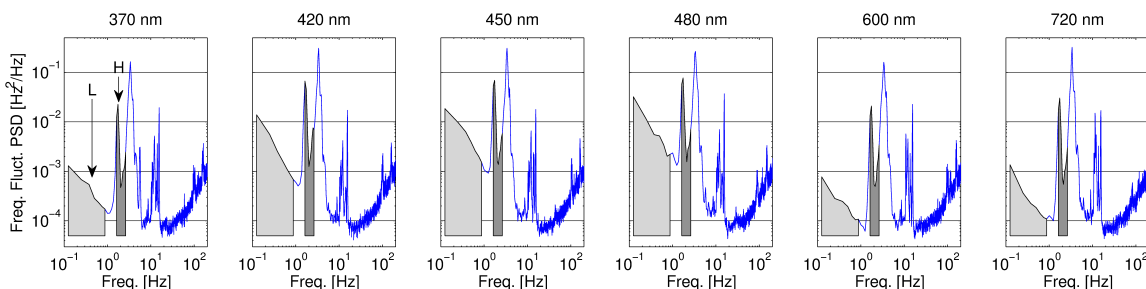


Figure 5.2: Power spectral density versus illuminated wavelength.

Power spectral density (PSD) of cantilever frequency fluctuations,  $P_{\delta f_c}(f)$ , versus frequency,  $f$ , recorded over an F8BT-rich region during illumination at the indicated wavelength. The shaded areas highlight (i) low-frequency fluctuations (labeled “L”, 0.2 to 1.4 Hz) arising from light-dependent processes in the sample and (ii) light-independent high-frequency fluctuations (labeled “H”, 2.6 to 4.2 Hz) arising from relative tip-sample motion.

locations and films were tested on ITO/PEDOT:PSS were tested with similar results. Through the rest of this chapter, F8BT-rich regions refer to location ‘A’, while PFB-rich regions refer to location B. The results from control experiments will be conducted over each region will help determine the origin of cantilever frequency noise.

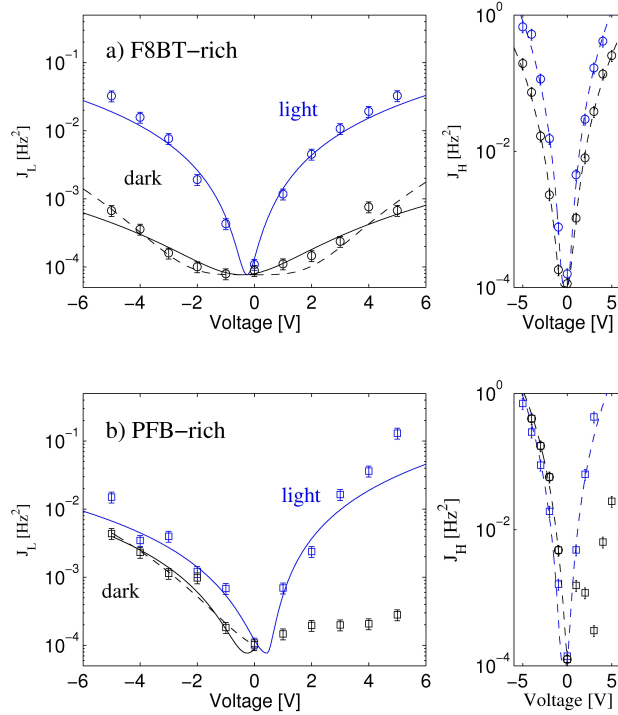


Figure 5.3: Jitter versus tip-voltage.

Cantilever frequency jitter versus tip voltage over (a) an F8BT-rich region (circles) and (b) a PFB-rich region (squares). Jitter at low frequency  $J_L$  and high frequency  $J_H$  is plotted on the left and right, respectively, under both illumination ( $\lambda = 450$  nm; blue, upper curves) and in the dark (black, lower curves). Data was fit to either a  $J \propto V^2$  function (solid lines) or  $J \propto V^4$  function (dashed lines), as discussed in the text.

### 5.3.2 Power Spectral Density

To establish that photoinduced charge leads to measurably large electrostatic potential fluctuations, power spectra of cantilever frequency fluctuations are collected over an F8BT-rich region as a function of irradiation wavelength. The resulting power spectra exhibit low-frequency fluctuations (“L” in Figure 5.2) showing a strong wavelength dependence, and higher-frequency fluctuations (“H” in Figure 5.2) which are essentially wavelength independent.

### 5.3.3 Tip Voltage Dependence

The dependence of cantilever frequency jitter on tip voltage is shown in Figure 5.3. High-frequency jitter shows, under both illumination and in the dark, a clear  $V^4$ -dependence on tip voltage; curve-fitting details and results are given in supporting information at the end of this chapter. This dependence is consistent with Equation 5.7 and proves definitively that the high-frequency jitter,  $J_H$ , is due to environmental vibrations. In the dark, the low-frequency jitter over both PFB-rich and F8BT-rich regions shows a modest dependence on tip voltage. Since  $V^2$  (Equation 5.5) and a  $V^4$  (Equation 5.7) dependence can not be readily distinguished, low-frequency jitter observed in the dark is likely also dominated by environmental vibrations.

Under illumination, however, the low-frequency jitter over F8BT increases by orders of magnitude above the background at modest voltage and clearly follows a  $V^2$  dependence, consistent with Equation 5.5 and the assertion that low-frequency jitter arises from photoinduced electrostatic potential fluctuations in the sample. The fact that  $J_L$  over F8BT strictly follows a  $V^2$  dependence indicates that the tip is passively observing the sample's fluctuating electrostatic potential. Low-frequency jitter over the illuminated PFB-rich region likewise increases by orders of magnitude as the tip voltage is increased by just a few volts. Interestingly, the jitter follows a  $V^2$  law only approximately, with larger fluctuations observed at positive tip bias, suggesting that the tip over PFB is affecting the density of photoinduced charge. The interactions of the cantilever over PFB-rich regions was quite strong when the applied tip voltage was large, so the anomalous effect on noise is not surprising.

### 5.3.4 Illuminated Wavelength Dependence

In Figure 5.4 are graphs of low-frequency and high-frequency cantilever frequency jitter versus wavelength over an F8BT-rich and a PFB-rich region. The high-frequency jitter,  $J_H$ , over both regions is wavelength independent, corroborating the assignment that frequency fluctuations in

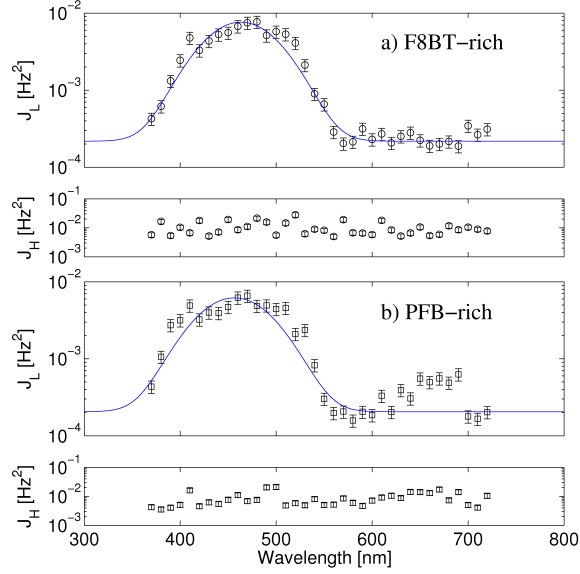


Figure 5.4: Jitter versus illuminated wavelength.

Jitter versus wavelength spectra recorded at two locations over the PFB/F8BT bulk heterojunction film (a) over an F8BT-rich region at low frequency (upper; black open circles) and at high frequency (lower; black open circles) and (b) over a PFB-rich region at low frequency (upper; black open squares) and at high frequency (lower; black open squares). Solid blue lines are fits to a single Gaussian plus a background.

the “H” window of 5.2 are due to environmental vibrations. The low-frequency jitter,  $J_L$ , in contrast, is strongly dependent on wavelength;  $J_L$  is more than a factor of thirty above the background near its peak at 450 nm.

According to the results of the previous chapter, the local electrostatic potential over ITO/PEDOT:PSS/ PFB:F8BT is wavelength dependent. Since jitter is expected to depend on either  $(V_T - \phi)^2$  (Equation 5.5) or  $(V_T - \phi)^4$  (5.7), great care was taken to determine  $\phi$  at each illuminated wavelength in Figure 5.4 and adjust the tip voltage accordingly to keep  $V_T - \phi = 5$  V. The fact that  $J_H$  shows no systematic dependence on  $\lambda$  demonstrates that the wavelength dependence of  $J_L$  is not due to failure to accurately track  $\phi$ . The low-frequency jitter over *both* regions under illumination is well described by a single Gaussian with a width of approximately 35 nm over both regions and a center wavelength over F8BT-rich and PFB-rich regions, respectively, of  $\lambda_c^{\text{F8BT}} = 457 \pm 7$  nm and  $\lambda_c^{\text{PFB}} = 463 \pm 4$  nm. Details in the fitting are given in the supplemental information of this chapter.

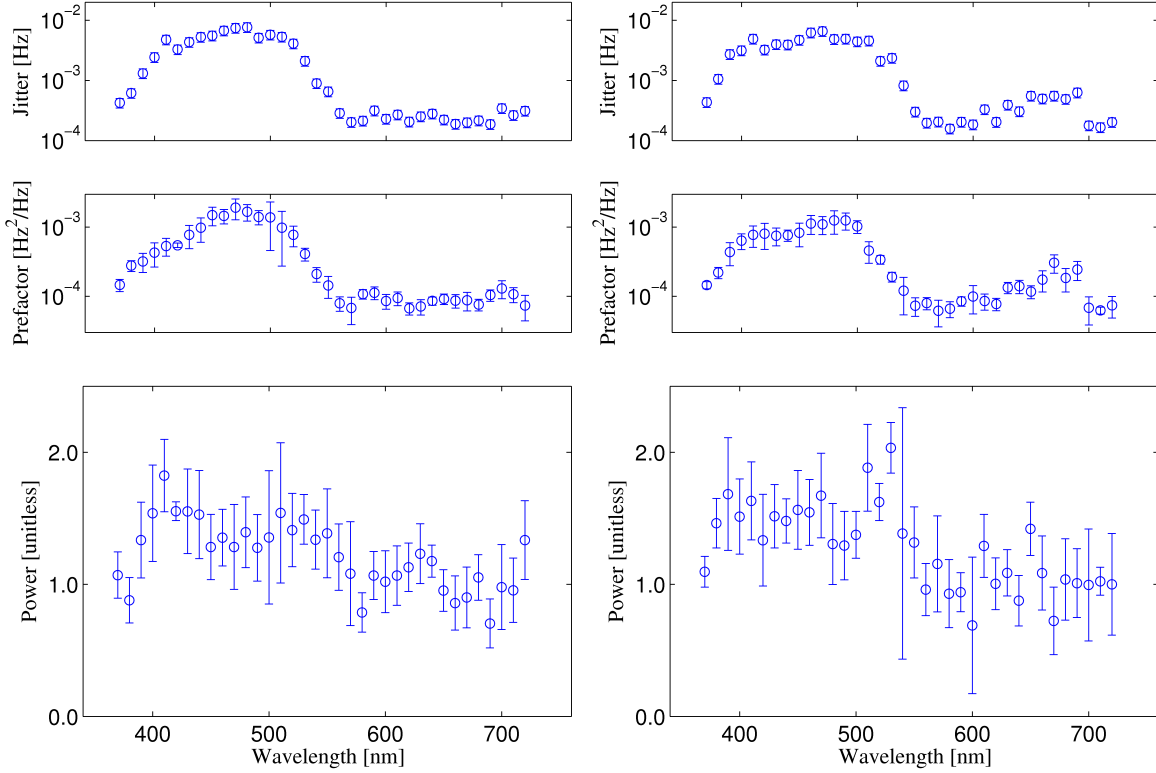


Figure 5.5: Jitter fit details versus illuminated wavelength.

Potential versus light intensity over F8BT(Left) Integrated power spectral density (Jitter), prefactor, and frequency fall off over F8BT versus illuminated wavelength. (Right)Integrated power spectral density (Jitter), prefactor, and frequency fall off over PFB versus illuminated wavelength.

In addition to the integrated power spectral density (jitter) at low frequency being a function of illuminated wavelength, the shape of PSD is also affected by illumination. With a proper theory in place, the shape of the PSD can be used to identify the source of frequency noise. In the same regime where  $J_L$  is measured, the power spectral density of cantilever frequency is described as

$$P_{\delta f_c}(f) \approx P_{\delta f_c}(1\text{Hz})f^n \quad (5.10)$$

with prefactor,  $P_{\delta f_c}(1\text{Hz})$ , and power  $n$ . In Figure 5.5, PSD shape in terms of prefactor and power are given over F8BT (left) and PFB (right). The summary of the fitting is display in

Table 5.1: Mean exponent  $n$ .

sample		power $n$	
		400 to 500 nm	600 to 700 nm
F8BT-rich	light	$1.505 \pm 0.056$	$1.025 \pm 0.057$
PFB-rich	light	$1.466 \pm 0.075$	$1.058 \pm 0.072$

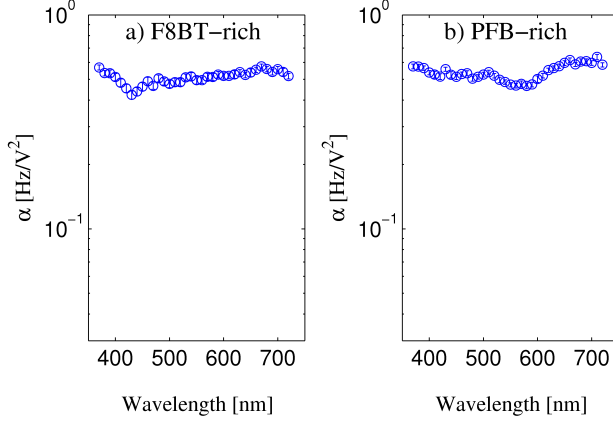


Figure 5.6:  $\alpha$  versus illuminated wavelength.

Curvature of the frequency vs tip-voltage parabola,  $\alpha$ , versus wavelength. Cantilever amplitude 30 nm peak to peak, 75 nm above the bottom of oscillation (90nm from mean position).

Table 5.1. At wavelengths from 400nm to 500nm, where noise from illumination is greatest, the power law best describing PSD is  $n \approx 1.5$ . At wavelengths of illumination where noise level is indistinguishable from dark,  $n \approx 1.0$ . This again suggests that the main source of noise under illumination is different than what is observed in the dark.

Since frequency noise depends greatly on the tip-sample capacitance, it must also be established that light is not serving to increase the capacitance instead of the contact potential noise. In that case, it is simply easier to measure capacitance as a function of wavelength. The  $\Delta f_c$  versus  $V_T$  data was fit to a parabola to obtain the curvature  $\alpha$  in units of  $\text{Hz}/\text{V}^2$  and the local electrostatic potential  $\phi$  in V. As  $\alpha(d) = f_c(\partial^2 C / \partial z^2) / 4k_c$ , this provides a direct measure of the second derivative of capacitance with respect to tip height.

The measured  $\alpha$  as a function of illuminated wavelength is shown in Figure 5.6. There is no large change in  $\alpha$  which can explain the cantilever frequency noise observed in Figure 5.4.

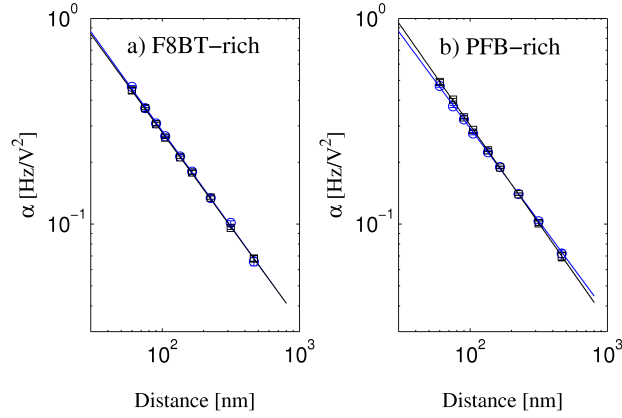


Figure 5.7:  $\alpha$  versus distance  $d$ .

This establishes that increased frequency noise is due to fluctuations in the contact potential, not increased tip-sample capacitance under illumination.

### 5.3.5 Tip-Sample Distance Dependence

In addition to dependencies on tip-sample voltage and illuminated wavelength, tip-sample distance dependence can also serve as a valuable tool in determining the source of cantilever frequency noise.

The curvature  $\alpha$  of the cantilever frequency vs applied tip voltage was studied as a function of distance  $d$ ; the resulting data is shown in Figure 5.7. The curvature data was fit to a power law,

$$\alpha(d) = \alpha_r \left( \frac{d_r}{d} \right)^n, \quad (5.11)$$

with  $n$  the power,  $d_r$  a reference distance, and  $\alpha_r$  the curvature of the parabola at the reference distance. Fits were made with  $d_r = 90$  nm; results are reported in Table 5.2. Since  $\alpha$  and capacitance are related, the power  $n$  is also the best-fit power describing the decay of the

Table 5.2:  $\alpha$  versus height fit results. Error bars represent 95% confidence intervals.

sample		$\alpha_r$ $\times 10^{-3} \text{ Hz}^2$	$n$
F8BT-rich	light	$312.1 \pm 5.4$	$0.926 \pm 0.031$
	dark	$306.4 \pm 3.4$	$0.918 \pm 0.018$
PFB-rich	light	$321.1 \pm 4.0$	$0.903 \pm 0.021$
	dark	$334.2 \pm 2.6$	$0.953 \pm 0.015$

capacitance derivative ( $\partial^2 C / \partial z^2$ ) with distance. Taking an average of the four data sets,

$$\frac{\partial^2 C}{\partial z^2} \propto d^{-0.925 \pm 0.051} \quad (5.12)$$

which is nearly identical to the  $d^{-1}$  power law expected for a cone [286].

Now that the effect of tip-sample distance on capacitance has been established, the focus can now shift on the distance dependence of jitter due to contact potential fluctuations. In Figure 5.8 is the height dependence of light-induced low-frequency jitter, with dark-state jitter and high-frequency jitter plotted for comparison. From measurements of  $\Delta f_c$  versus  $V_T$ , Equation 5.12 shows that  $\partial^2 C / \partial z^2 \propto d^{-n}$  with  $n = 0.925 \pm 0.048$ . Referring to Equation 5.7,  $J_H \propto (\partial^3 C / \partial z^3)^2 = d^{-4}$  for a cone. Fits of  $J_H$  to a power law plus a background are consistent with an  $n = 4$  power law at the 95% confidence level, in agreement with the measured capacitance derivative  $\partial^2 C / \partial z^2$  and Equation 5.7.

Low-frequency jitter can be described by contact potential fluctuations in Equation 5.1. Fitting  $J_L$  to a power law plus a background,  $J_L \propto d^{-n}$  with  $n = 3.43 \pm 0.23$  over the F8BT-rich region and  $n = 2.94 \pm 0.12$  over the PFB-rich region. Considering the measured  $\partial^2 C / \partial z^2$ , the capacitance term in Equation 5.1 to contribute a factor  $(\partial^2 C / \partial z^2)^2 \propto d^{-n}$  with  $n = 1.850 \pm 0.096$  to the height-dependent jitter. Any remaining height dependence can be ascribed to the power spectrum of voltage fluctuations. Thus, the power spectrum of photoinduced voltage fluctuations

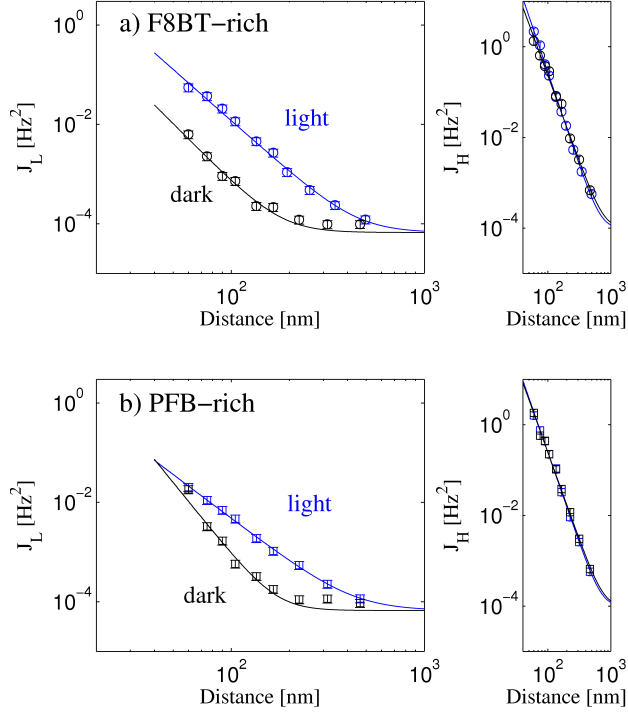


Figure 5.8: Jitter versus tip-sample distance.

Cantilever frequency jitter versus distance over (a) an F8BT-rich region (circles) and (b) a PFB-rich region (squares). Jitter at low frequency  $J_L$  and high frequency  $J_H$  is plotted on the left and right, respectively, under both illumination ( $\lambda = 450$  nm; blue, upper curves) and in the dark (black, lower curves). Data was fit to a power-law (solid curves), as described in the text.

has the following height dependence over the two representative sample regions studied in Figure 5.8:

$$P_{\delta\phi, h\nu}^{\text{F8BT}} \propto d^{-1.58 \pm 0.25} \quad (5.13)$$

$$P_{\delta\phi, h\nu}^{\text{PFB}} \propto d^{-1.09 \pm 0.15} \quad (5.14)$$

### 5.3.6 Jitter over Al/PFB:F8BT

From Figure 5.9, it is shown that jitter under illumination is small compared to jitter observed over ITO/ PEDOT:PSS/ PFB:F8BT over both PFB and F8BT-rich regions. This corresponds

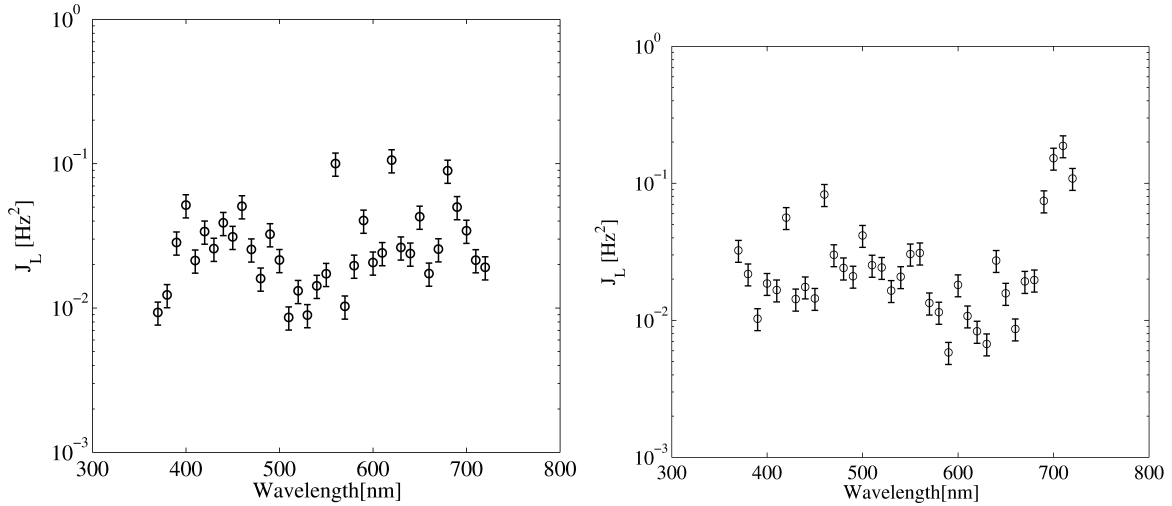


Figure 5.9: Jitter over Al/PFB:F8BT.

Low frequency jitter over Al/PFB:F8BT over F8BT (left) and PFB (right)

well with the idea that jitter is due to electron trapping and detrapping in F8BT. As aluminum is a low work function metal, electrons are thought to be depleted when aluminum is the substrate. When the substrate is ITO, a high workfunction material, electrons are in abundance.

## 5.4 Discussion

Let us now use these charge density estimates and Equations 5.8 and 5.9 to calculate the frequency noise expected in two limiting cases — electrostatic potential fluctuations arising from charge dynamics associated with stochastic trapping and de-trapping at localized sites and from free diffusion.

### 5.4.1 Fluctuations from Charge Diffusion

Consider a sheet of non-interacting charges randomly distributed in the  $xy$ -plane. Fluctuations in the position and number of charges induce fluctuations in the electrostatic potential  $\phi(z, t)$ . The

potential at two heights  $z_1$  and  $z_2$  will be correlated, and described by the correlation function

$$\langle \phi(z_2, t) \phi(z_1, 0) \rangle = c_a \int \int d\mathbf{r}_1 d\mathbf{r}_2 K(\mathbf{r}_2 - \mathbf{r}_1, t) \phi(\mathbf{r}_2, z_2) \phi(\mathbf{r}_1, z_1) \quad (5.15)$$

where  $\mathbf{r} = (x, y)$ ,  $c_a$  is the probability per unit area of finding a charge,  $K(\mathbf{r}_2 - \mathbf{r}_1, t)$  is the function describing charge diffusion, and  $\phi(\mathbf{r}, z)$  is the electric potential at the origin due to a charge located at  $(\mathbf{r}, z)$ . The power spectrum of Equation 5.15 is the term  $P_{\phi(z_1), \phi(z_2)}(f)$  appearing in Equations 5.8 and 5.9. If the charges undergo free diffusion with diffusion constant  $D$ , the spatial Fourier and temporal cosine transform of the charge propagator  $K(\mathbf{r}, t)$  is given by

$$K^{\text{diff}}(\mathbf{r}, t) = \frac{1}{4\pi Dt} e^{-\frac{|\mathbf{r}|^2}{4Dt}} \quad (5.16)$$

where  $\mathbf{k} = (k_x, k_y)$ , and  $k = |\mathbf{k}|$ . Inserting this propagator into Equation 5.15, taking the power spectrum, and inserting the result into Equation 5.8, and after some simplification

$$P_{\delta f_c}^{\text{diffusion}}(f, d) = \frac{2\pi c_a f_c^2 (V_{\text{ts}} - \phi_s)^2 d^2}{D k_c^2} \left( \frac{q}{4\pi\epsilon_0} \right)^2 \times [C''^2 I_0 - 4C' C'' I_1 + 4C'^2 I_2 - 2C C'' I_2 - 4C C' I_3 + C^2 I_4] \quad (5.17)$$

with

$$I_n(\alpha) = d^{-n} \int_0^\infty d\alpha \frac{\alpha^{n+1} e^{-2\alpha}}{\alpha^2 + \theta^4} \quad (5.18)$$

where the shorthand notation  $C = C(d)$  and  $I_n = I_n(2\pi f d^2 / D)$ .

## 5.4.2 Fluctuations from Trapping and de-trapping

Now consider the case where fluctuations in the potential  $\phi(z, t)$  arise from trapping and de-trapping at localized sites. Let us assume that the charge trapping rate  $\lambda_t$  follows the Arrhenius law, i.e.  $\lambda_t \propto \exp(-E/k_b T)$ , and let us further assume that there is not a single energy barrier  $E$  but a flat distribution of barriers between energies  $E_1$  and  $E_2$  whose decay rates bracket the observed frequency range:  $\lambda_1 \ll f \ll \lambda_2$ . With these assumptions, the charge propagator is given by

$$\tilde{K}^{\text{trap}}(\mathbf{k}, f) = \frac{\pi k_B T}{2f(E_2 - E_1)}. \quad (5.19)$$

In the case of a flat trap distribution,  $c_a$  in Equation 5.15 now represents the number of vacant traps per unit area per unit energy. To avoid a divergence of the voltage fluctuations, we find it necessary to modify the potential  $\phi(\mathbf{r}, z)$  in Equation 5.15 to include the image potential associated with counter charges induced in the underlying PEDOT:PSS/ITO substrate. Including effects of image charges and using the propagator in Equation 5.19, the induced frequency noise can be approximated by

$$P_{\delta f_c}^{\text{trapping}}(f, d) = \frac{\pi^2 c_a f_c^2 C^2 (V_{\text{ts}} - \phi_s)^2 k_B T}{k_c^2 (E_2 - E_1) f} \times \left( \frac{q}{4\pi\epsilon_0} \right)^2 J_4\left(d, \frac{2d}{\epsilon_r}\right) \quad (5.20)$$

with

$$J_n(d, \Delta) = (n - 1)! \left[ (2d)^{-n} - 2(2d + \Delta)^{-n} + (2d + 2\Delta)^{-n} \right] \quad (5.21)$$

Similar expressions may be obtained for the cone model.

In Figure 5.10 are plotted jitter versus height and  $P_{\delta f_c}$  versus frequency. The sphere radius and cone angle were taken to be 40 nm and 20 degrees, respectively, and the sphere and cone capacitances taken from literature [264, 286]. For the case of free diffusion, the planar charge density was taken to be  $10^{14} \text{ m}^{-2}$  [288] and computations were carried out using three representative charge mobilities: a fast mobility  $\mu_{\text{fast}}$  taken from field-effect-transistor measurements [289], an intermediate mobility  $\mu_{\text{intermed}}$  drawn from space-charge limited current measurements of diodes [278], and a plausible lower estimate  $\mu_{\text{slow}}$ . From Figure 5.10, the fastest mobility *underestimates* the observed jitter. The intermediate mobility correctly predicts a jitter of the correct order of magnitude, but predicts a jitter frequency dependence which is essentially flat and thus disagrees with experiment. The lower-estimate mobility predicts the correct frequency dependence of the fluctuations, but would require a planar charge density as small as  $\leq 10^{12} \text{ m}^{-2}$  to obtain a jitter whose size agreed with experiment.

Frequency noise due to trapped charge was calculated assuming a density of vacant a trap density of  $8 \times 10^{13} \text{ m}^{-2}$  and a bandwidth of 0.125 eV. Trapping throughout the film volume was also modeled, by integrating Equation 5.20 over the film (thickness  $t = 200 \text{ nm}$ , dielectric constant  $\epsilon = 3.4 \epsilon_0$ ). We can see in Figure 5.10 that both the distance dependence and the

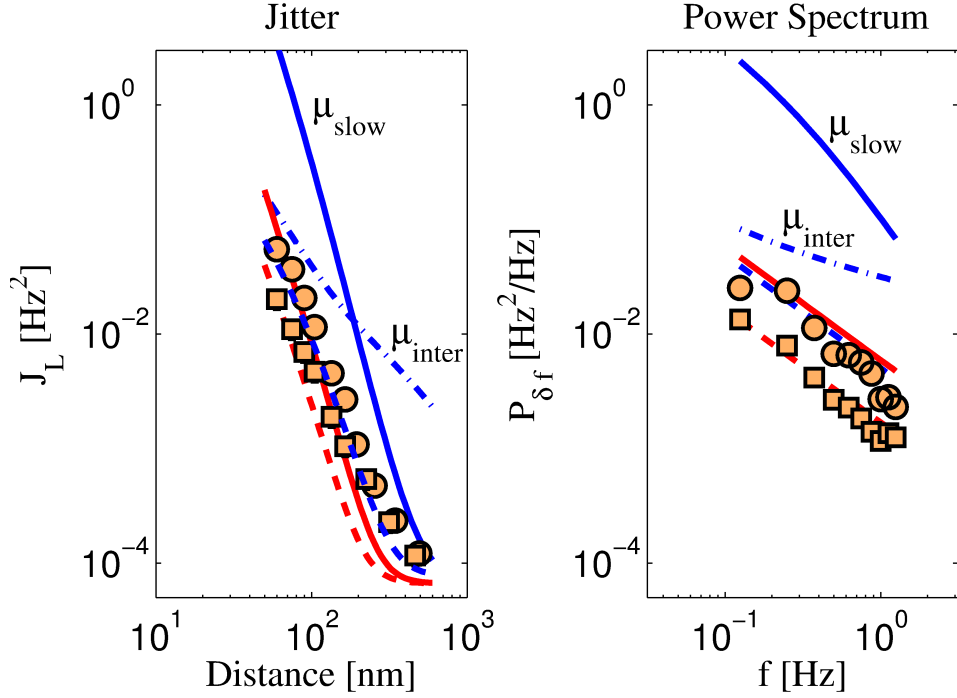


Figure 5.10: Jitter: theory versus experiment.

A comparison of observed and calculated low-frequency jitter  $J_L$  versus  $d$  (left) and the power spectrum  $P_{\delta f_c}$  versus  $f$  at  $d = 90\text{nm}$  (right). The data was acquired over an F8BT-rich region (circles) and a PFB-rich region (squares). For the 2D free diffusion model of equation (5.17), data was calculated for three different charge mobilities:  $\mu_{fast} = 4 \times 10^{-7} \text{ cm}^2/\text{Vs}$  (dashed blue line),  $\mu_{inter} = 10^{-10} \text{ cm}^2/\text{Vs}$  (dot-dashed blue line), and  $\mu_{slow} = 6 \times 10^{-14} \text{ cm}^2/\text{Vs}$  (solid blue line). For the trapping-detrapping model, data was calculated for the case of charges distributed at the top of the film (equation (5.20); solid red line) and throughout the volume of the film (dashed red line). For the diffusion model we used a charge density of  $c_a = 2.5 \times 10^{14} \text{ m}^{-2}$ , whereas for charge trapping we used a vacant trap density per unit energy of  $c_a/(E_{high} - E_{low}) = 10^{13} \text{ m}^{-2} \text{ eV}^{-1}$ .

frequency dependence of the cantilever frequency fluctuations are correctly predicted by the 2D and 3D trapping model.

No increase in frequency fluctuations were seen near  $\lambda = 380 \text{ nm}$ , the peak PFB absorption. Because the jitter spectra are nearly identical over the two regions, we therefore assign the observed photoinduced voltage fluctuations observed here to slow trapping and de-trapping process in F8BT.

### 5.4.3 ITO/PFB:F8BT films versus Al/PFB:F8BT films

In films of ITO/ PEDOT:PSS/ PFB:F8BT, where photogenerated electrons are in abundance, illuminated wavelength dependence shows that jitter signal increases significantly with light absorption in F8BT (Figure 5.4). This increase in jitter is shown to occur over both PFB-rich and F8BT-rich regions. Results from the previous chapter revealed that the F8BT minority component in PFB-rich films contributes significantly to the photovoltage. In films of Al/PFB:F8BT, where photogenerated electrons are transported into aluminum, little change in jitter is observed under illumination (Figure 5.9). Together, these facts explained by an electron trapping in F8BT.

## 5.5 Concluding Remarks

In summary, combined with the previous chapter, this work introduces surface photopotential spectroscopy and photopotential fluctuation spectroscopy as two complimentary tools for probing the fate of photogenerated charges in a bulk heterojunction solar cell film and for investigating mechanisms of open circuit losses in bulk heterojunction solar cells. While surface photopotential spectroscopy has proved a powerful tool for studying sign and carrier dynamics in inorganic semiconductors [282, 290], there is little precedent for acquiring surface photopotential spectra of organic semiconductors [291, 292], and no precedent for acquiring variable wavelength contact potential images of organic semiconductor films. Surface photopotential spectroscopy was used in this work to show that the PFB/F8BT interface on PEDOT:PSS/ITO does not behave as a  $p$ - $n$  junction under illumination.

This work also sets precedent for detection of local contact potential noise measurements in a solar cell. Bulk voltage-noise measurements have been used to study trapping-detrapping fluctuations [283] and percolation transport [284] in organic semiconductor films while cantilever frequency noise has been used to study charge blinking [194], generation-recombination noise

Table 5.3: Jitter versus wavelength fit results. Error bars represent 95% confidence intervals.

parameter	unit	F8BT-rich	PFB-rich
$J_{\text{total}}$	$\text{Hz}^2$	$0.65 \pm 0.09$	$0.53 \pm 0.13$
$\lambda_c$	nm	$463.3 \pm 3.6$	$456.5 \pm 7.0$
$\lambda_w$	nm	$35.1 \pm 2.2$	$35.7 \pm 4.3$
$J_0$	$\times 10^{-4} \text{Hz}^2$	$2.2 \pm 0.3$	$2.1 \pm 0.5$

in inorganic semiconductor heterojunctions [223], and dielectric fluctuations in thin polymer films[264, 285]. From experiments of photopotential fluctuations versus illumination wavelength, frequency, tip-sample distance, and applied tip voltage, we have approximated a local spatial density of vacant electron traps in F8BT. In samples with less trapping, theory shows photopotential fluctuation spectroscopy can be a tool used to determine the local mobility of free charges.

## 5.6 Supplemental Information

### 5.6.1 Wavelength Dependence

The cantilever jitter versus wavelength spectra in Fig. 5.4 were fit to a single Gaussian

$$J(\lambda) = \frac{J_{\text{total}}}{\sqrt{2\pi\lambda_w^2}} \exp\left[-\frac{(\lambda - \lambda_c)^2}{2\lambda_w^2}\right] + J_0 \quad (5.22)$$

where  $J_{\text{total}}$  is the jitter integrated over all illumination wavelengths,  $\lambda_c$  and  $\lambda_w$  are the Gaussian center and width, respectively, and  $J_0$  is a background jitter. Nonlinear least-squares fits were carried out with  $J_{\text{total}}$ ,  $\lambda_c$ ,  $\lambda_w$ , and  $J_0$  as free parameters. Wavelength dependence indicates that jitter is primarily due to the absorption of F8BT, which has a peak absorption at 480nm. No jitter about background noise was detected for absorption in PFB. Fit results are summarized in Table 5.3.

## 5.6.2 Tip Voltage Dependence

The cantilever jitter versus voltage data in Fig. 5.3 was fit as follows. The low-frequency jitter  $J_L$  was fit to either

$$J(V) = J_V^{(2)}(V - \phi)^2 + J_0 \quad (5.23)$$

or

$$J(V) = \begin{cases} J_V^{(2-)}(V - \phi)^2 + J_0 & V < \phi \\ J_V^{(2+)}(V - \phi)^2 + J_0 & V > \phi. \end{cases} \quad (5.24)$$

where  $\phi$  is the contact potential,  $J_0$  is the background jitter, and  $J_V^{(2)}$ ,  $J_V^{(2-)}$ , and  $J_V^{(2+)}$  are parameters that control how steeply the jitter increases with voltage. The F8BT-rich/light, F8BT-rich/dark, and the PFB-rich/dark jitter-versus-voltage data was fit to Equation 5.23. Because the jitter in the PFB-rich/light experiment was not a symmetric function of the applied voltage, the PFB-rich/light jitter versus voltage data was fit instead to Equation 5.24. The results of fitting the low-frequency jitter data  $J_L$  to Equations 5.23 and 5.24 are reported in Table 5.4.

The background jitter  $J_0$  in Equations 5.23 and 5.24 was estimated independently and held fixed during curve fitting. To estimate the background jitter, the power spectrum of cantilever frequency fluctuations,  $P_{\delta f}$ , was examined at zero applied volts over F8BT-rich and PFB-rich regions in both the light-on and light-off state. At zero applied volts, the power spectrum of cantilever frequency fluctuations between 0.2 Hz and 19.8 Hz was identified in all four of these reference spectra as being free of probe vibrations. An average of  $P_{\delta f}$  was computed over this frequency window for each of the four spectra, and the results from light and dark spectra were averaged together to give:

Table 5.4: Jitter versus voltage fit results. In first row of the  $J_V^{(2)}$  column reports  $J_V^{(2-)}$ , while the second column reports  $J_V^{(2+)}$ . Error bars represent 95% confidence intervals.

freq.	sample	$J_V^{(2)}$ $\times 10^{-4} \text{ Hz}^2/\text{V}^2$	$\phi$ [V]	$J_0$ $\times 10^{-4} \text{ Hz}^2$	
$J_L$	F8BT-rich	light	$8.4 \pm 1.8$	$-0.26 \pm 0.11$	0.77
		dark	$0.176 \pm 0.052$	$-0.43 \pm 0.41$	0.77
	PFB-rich	light	$2.2 \pm 1.6$ $14.7 \pm 13.9$	$0.44 \pm 0.50$	0.77
		dark	$1.73 \pm 0.84$	$-0.25 \pm 0.46$	0.77

$$P_{\delta f}^{\text{F8BT floor}} = 63.97 \times 10^{-6} \text{ Hz}^2/\text{Hz} \quad (5.25)$$

$$P_{\delta f}^{\text{PFB floor}} = 63.87 \times 10^{-6} \text{ Hz}^2/\text{Hz}. \quad (5.26)$$

The background jitter was computed from

$$J_0 = P_{\delta f}^{\text{floor}} b, \quad (5.27)$$

with  $P_{\delta f}^{\text{floor}}$  given by either Equations 5.25 or 5.26 and  $b$  the frequency window over which the jitter was computed;  $b = 1.40 - 0.20 = 1.20 \text{ Hz}$  for  $J_L$  and  $b = 4.20 - 2.60 = 1.60 \text{ Hz}$  for  $J_H$  Fig. 5.3, Table 5.4, and Table 5.5 (discussed below). The high-frequency jitter  $J_H$  was fit to

$$J(V) = J_V^{(4)}(V - \phi)^4 + J_0 \quad (5.28)$$

where  $\phi$  is the contact potential,  $J_V^{(4)}$  is a parameter that controls how steeply the jitter increases with voltage, and  $J_0$  is the background jitter, computed from Equations 5.26 and 5.27.

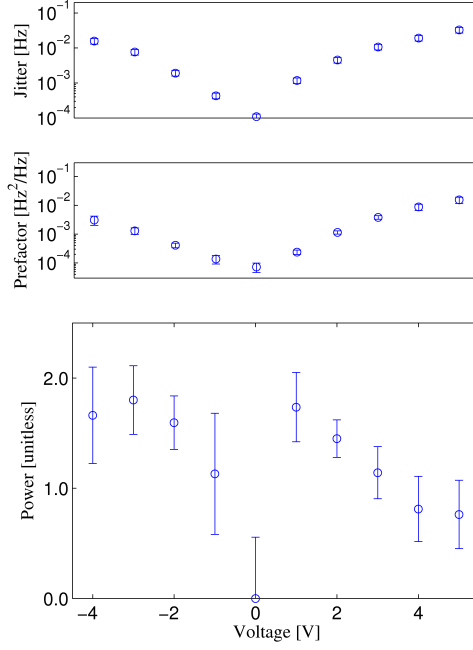


Figure 5.11: Jitter versus tip-voltage over F8BT.

Integrated power spectral density versus applied tip voltage over F8BT.

The low-frequency jitter  $J_L$  in the F8BT-rich dark and PFB-rich dark experiments was also fit to Equation 5.28. The results of these fits are summarized in Table 5.5.

### 5.6.3 Tip-Sample Distance Dependence

The cantilever jitter versus distance data in Fig. 5.8 of the body of the chapter were fit to a power-law

$$J(d) = J_d \left( \frac{d_r}{d} \right)^n + J_\infty \quad (5.29)$$

where  $n$  is the power,  $J_\infty$  is the background jitter at infinite distance,  $d_r$  is a reference distance, and  $J_d$  is the jitter at the reference distance. Fit results are summarized in Table 5.6. For these fits, a reference distance of  $d_r = 90$  nm was used. Non-linear least squares fits were carried out with  $J_d$  and  $n$  as free parameters. The parameter  $J_\infty$  was estimated independently, as follows,

Table 5.5: Jitter versus voltage fit results. The high-frequency jitter data was fit to Equation 5.28. Error bars represent 95% confidence intervals.

freq.	sample		$J_V^{(4)}$ $\times 10^{-4} \text{ Hz}^2/\text{V}^4$	$\phi$ [V]	$J_0$ $\times 10^{-4} \text{ Hz}^2$
$J_H$	F8BT-rich	light	$15.5 \pm 2.9$	$-0.200 \pm 0.091$	1.0
		dark	$3.23 \pm 0.35$	$-0.309 \pm 0.057$	1.0
	PFB-rich	light	$19.2 \pm 7.2$	$-0.32 \pm 0.19$	1.0
		dark	$13.3 \pm 4.2$	$0.39 \pm 0.16$	1.0
$J_L$	F8BT-rich	dark	$0.00115 \pm 0.00035$	$-0.17 \pm 0.32$	0.77
	PFB-rich	dark	$0.0020 \pm 0.0020$	$1.9 \pm 1.2$	0.77

and fixed during the fits. The power spectrum of cantilever frequency fluctuations,  $P_{\delta f}$ , was examined at the the largest tip-sample separation over the F8BT-rich and PFB-rich regions, for both light on and light off spectra. Noise in the frequency region between 5.8 Hz and 9.9 Hz was identified in all four of these reference spectra as being free of probe vibrations. An average of  $P_{\delta f}$  was computed over this frequency window for all four reference spectra, and the results were averaged together to obtain an estimate of the background spectral density of cantilever frequency fluctuations,  $P_{\delta f}^{\text{floor}} = 59.1 \times 10^{-6} \text{ Hz}^2/\text{Hz}$ . The background jitter was computed as

$$J_{\infty} = P_{\delta f}^{\text{floor}} b, \quad (5.30)$$

where  $b$  is the frequency window over which the jitter was computed;  $b = 1.250 - 0.125 = 1.126 \text{ Hz}$  for  $J_L$  and  $b = 4.253 - 2.627 = 1.626 \text{ Hz}$  for  $J_H$  Fig. 5.8 and Table 5.6.

Table 5.6: Jitter versus height fit results. Error bars represent 95% confidence intervals.

freq.	sample	$n$	$J_d$ $\times 10^{-3} \text{ Hz}^2$	$J_\infty$ $\times 10^{-6} \text{ Hz}^2$
$J_L$				
F8BT-rich	light	$3.43 \pm 0.23$	$16.9 \pm 2.6$	67
	dark	$3.90 \pm 0.87$	$1.04 \pm 0.28$	67
PFB-rich	light	$2.94 \pm 0.12$	$6.44 \pm 0.49$	67
	dark	$4.80 \pm 1.35$	$1.49 \pm 0.52$	67
$J_H$				
F8BT-rich	light	$4.11 \pm 0.12$	$422 \pm 38$	96
	dark	$3.79 \pm 0.26$	$344 \pm 74$	96
PFB-rich	light	$4.00 \pm 0.19$	$374 \pm 58$	96
	dark	$3.87 \pm 0.21$	$370 \pm 64$	96

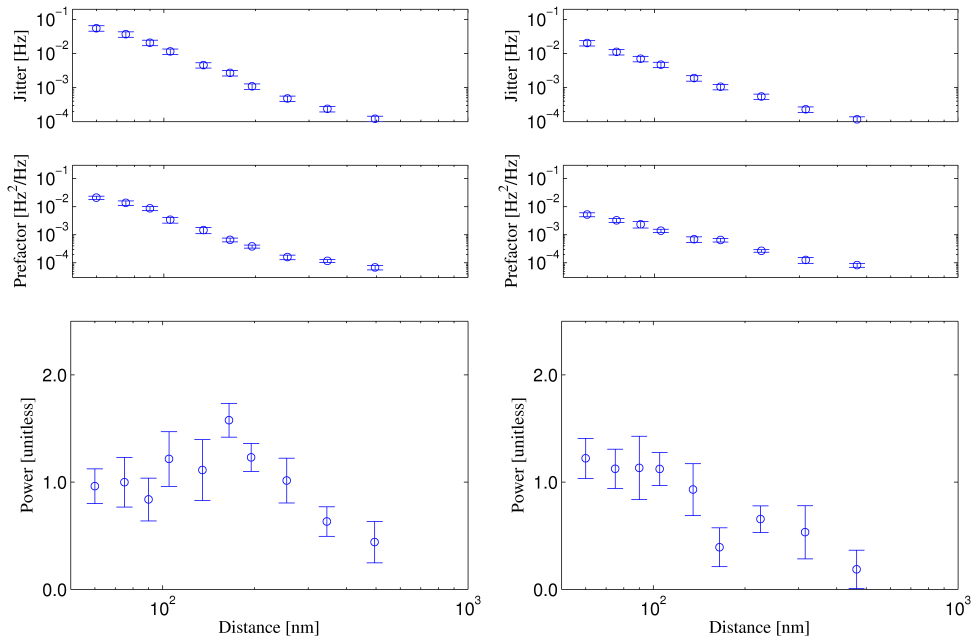


Figure 5.12: Jitter fit details versus tip-sample distance.

Integrated PSD (jitter), prefactor, and frequency fall off for the power spectral densities as a function of top sample distance over F8BT (left) and PFB (right).

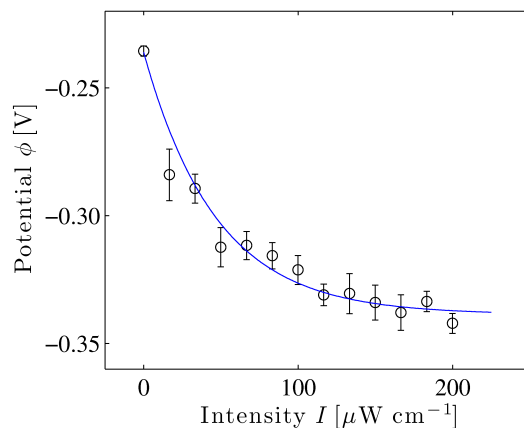


Figure 5.13: Potential versus light intensity over F8BT.

Contact potential as a function of illuminated intensity at 450nm over F8BT.

#### 5.6.4 Dependence on Light Intensity

In addition to applied tip voltage, tip-sample distance, and illuminated wavelength dependence, the effect of light intensity on jitter was also recorded. Again, the intent is to identify the origin of cantilever frequency noise. In a solar cell, photo-generated charge density varies linearly in illuminated light intensity, while open circuit voltage varies logarithmically at high illuminated intensity. From the tip-voltage dependence experiments, it was determined that the cantilever noise experiments are passively observing charges in F8BT. Because of this, light dependence experiments will focus on F8BT. As expected, at low light intensities the observed dependence of contact potential on light intensity is logarithmic (Figure 5.13).

The result of the experiment observing cantilever frequency noise versus light intensity is shown in Figure 5.14. Jitter at high frequency, attributed to mechanical vibrations, does not appear to be correlated with light intensity. A model which predicts jitter from light intensity is challenging and is beyond the scope of this thesis. However, with an accurate model, potentially more information from light intensity can be derived.

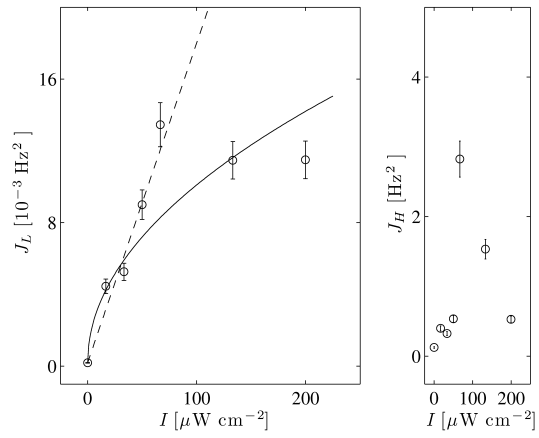


Figure 5.14: Jitter versus light intensity over F8BT.

Jitter versus laser power 90 nm over the surface of a F8BT-rich region. The solid and dashed lines are fits to  $J_0 + aI$  and  $J_0 + b\sqrt{I}$ , respectively, where  $a = 0.18 \text{ Hz}^2/\text{mW cm}^{-2}$  and  $b = 1.0 \text{ Hz}^2\text{W}^{-\frac{1}{2}} \text{ cm}$ .

## EXCIPLEX DETECTION IN HEXABENZOCORONENE-FULLERENE BILAYER SOLAR CELLS BY ELECTRIC FORCE MICROSCOPY

### 6.1 Introduction

This chapter introduces unpublished work done in collaboration with Alon Gorodetsky and Colin Nuckolls at Columbia University. In this study, the charge generation in hexabenzocoronene-family solar cells are observed to be spatially uniform and have multi-exponential photovoltage decay kinetics. This work reports on methods of calculating exciplex and trapped charge density in bilayer solar cells by measuring contact potential shifts under illumination as a function of donor layer thickness. Work on this project was hampered by the degradation of hexabenzocoronene derivative materials under exposure to low-light conditions and air.

Tremblay *et al.* have recently introduced the idea of improving organic solar cell efficiency by increasing the shape complementarity between donor and acceptor molecules [293] (Figure 6.1). To demonstrate the idea of shape complementarity, they chose to work with hexabenzocoronene [294–298] and its derivatives [299–301], which show excellent field-effect mobility [295–298] and photoconductivity [297, 302]. A *contorted* hexabenzocoronene (*c*-HBC) was synthesized which assembled into a ball-and-socket complex with buckminsterfullerene ( $C_{60}$ ), and a *c*-HBC/ $C_{60}$  bilayer solar cell was fabricated which showed notably high efficiency and large open-circuit voltage. Gorodetsky *et al.* prepared a hexyl-substituted dibenzotetrathienocoronene (6-DBTTC) which formed columnar structures upon annealing; the resulting 6-DBTTC/ $C_{60}$  solar cell had a morphology resembling a bulk heterojunction solar cell and exhibited a three- to four-fold improvement in power conversion efficiency compared to the *c*-HBC/ $C_{60}$  bilayer solar cell [300].

To better understand the excellent performance of the hexabenzocoronene-family solar cells, Alon Gorodetsky prepared DBTTC/ $C_{60}$  and *c*-HBC/ $C_{60}$  bilayer cells, along with control samples

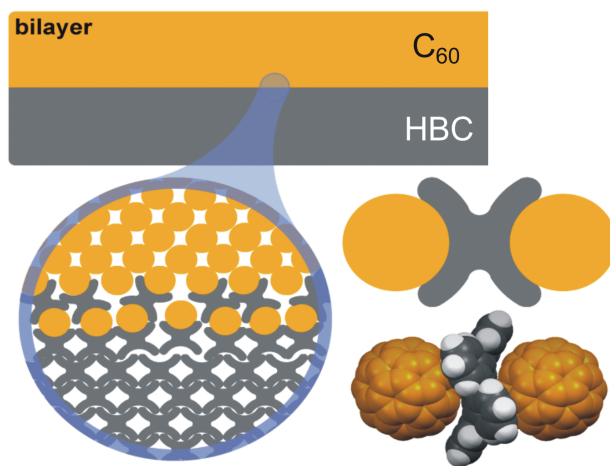


Figure 6.1: Diagram of HBC- $C_{60}$  bilayer devices.

Schematic of a bilayer HBC/ $C_{60}$  device. Contorted HBC molecules fit around Buckminster fullerene molecules to maximize orbital overlap, enhancing charge transfer. Figure reproduced from Tremblay et al. [293].

without the  $C_{60}$  acceptor layer. In this chapter we provide a comparative study of the surface photovoltage [282] of these bilayer cells and control samples using time-resolved light-enhanced electric force microscopy (EFM). These EFM solar-cell sample studies were carried out on samples prepared with the top anode absent. In such reference samples, EFM has been used before to collect non-contact images of surface photovoltage [160, 161, 198] and make time-resolved measurements of local capacitance [169]; however, these studies did not probe photovoltage as a function of active layer thickness. From the data presented in this thesis chapter, we are able to draw conclusions about lateral morphology, the vertical distribution of photogeneration charges, degradation over time, and charge transport rates within the bilayer device [132, 148, 207, 303].

## 6.2 Methods

### 6.2.1 Synthesis and Devices Preparation

DBTTC (Figure 6.2a) synthesis was performed in the Nuckolls lab by A. Gorodetsky [300]. Details of the Gorodetsky synthesis are reported here for completeness. All reactions were run in oven-dried glassware (130 °C), and monitored by TLC using silica gel 60 F254 pre-coated plates (EM Science). Anhydrous and oxygen-free solvents were obtained from a Schlenk manifold system with purification columns packed with activated alumina and supported copper catalyst (Glass Contour). Column chromatography was performed (CombiFlash Rf system) using normal phase silica columns (RediSep™ ISCO, Inc.). <sup>1</sup>H NMR (300 MHz, 400 MHz), and <sup>13</sup>C NMR (75 MHz, 100 MHz) spectra were recorded on Bruker DRX-300 and Bruker DRX-400 spectrometers at room temperature unless otherwise noted. Mass spectrometry was recorded on a JEOL JMS-HX110A/110A tandem mass spectrometer.

*c*-HBC (Figure 6.2b), hereafter called HBC for simplicity, was synthesized as described in Plunket et al. [299]. The process utilizes a double Barton-Kellogg olefination reaction [304] and a subsequent Scholl cyclization from pentacene quinones and double olefin precursors.

Solar cell devices (Figure 6.2) were fabricated on patterned indium-tin oxide (ITO) glass substrates which were cleaned by sonication in acetone and isopropyl alcohol, dried under a stream of nitrogen, and UV-ozone etched for five minutes. PEDOT:PSS (Clevios P, H. C. Starck) was spun onto the cleaned ITO at 5000 rpm for 60 seconds and the film was subsequently baked at 200 °C for 30-45 minutes. For devices with a solution processed donor layer, 6-DBTTC was spuncast from a 3-4 mg/mL toluene solution at 500 rpm; the films were annealed at 150 °C or not annealed at all, depending on the desired aggregation. For devices with a deposited donor layer, 6-DBTTC was thermally evaporated at a rate of  $\approx 2.0$  Å/sec to a thickness of 25 to 30 nm. To complete the active layer, buckminsterfullerene (C<sub>60</sub>, BuckyUSA, Inc.) was thermally evaporated

at a rate of  $\approx 2.0 \text{ \AA}/\text{sec}$  to a thickness of  $\approx 40 \text{ nm}$ . The substrates were taken out of ultra-high vacuum (UHV) and moved to a nitrogen atmosphere where they were masked and placed under UHV again; an aluminum cathode was deposited at a rate of  $\approx 1.0 \text{ \AA}/\text{sec}$  to a thickness of  $\approx 60 \text{ nm}$ . The finished devices had an area of  $0.16 \text{ cm}^2$ .

In order to optimize the photopotential signal in EFM experiments, samples were prepared differently than the completed solar cells described above. The glass/ITO substrates were cleaned in successive acetone (x 3) and isopropanol (x 2) sonications. No PEDOT:PSS was applied for these experiments. HBC and DBTTC samples were thermally evaporated with a thickness of  $25 \text{ nm}$  at a rate of  $1.0 \text{ \AA}/\text{sec}$ . A quartz crystal monitor and atomic force microscope were used to calibrate the thicknesses for the deposited samples. Heat-treated samples were baked at  $150 \text{ }^\circ\text{C}$  for 30-45 minutes. Some devices were capped with a  $5 \text{ nm}$ , thermally evaporated layer of buckminsterfullerene, deposited in high vacuum.

## 6.2.2 Device Characterization

Representative current-voltage curves for two representative solar cells are shown Figure 6.2 (lower). The devices were tested with a Keithley 2602/2400 sourcemeter under both dark conditions and under illumination with either a spectrometer or a solar simulated lightsource (AM1.5) in the Nuckolls lab. All illumination sources were calibrated using a silicon photodiode.

## 6.2.3 Scanned Probe Microscopy

Electric force microscopy measurements were conducted as described in Chapter 2 of this thesis. Typical PID parameters were  $P=.01$ ,  $I=3\text{E}2 \text{ Hz}$ , and  $D=5\text{E}-5 \text{ s}$ . These parameters were chosen to have a response time on the order of tens of milliseconds. In addition, EFM experiments were performed in height-tracking mode, since some of the samples described in this chapter had

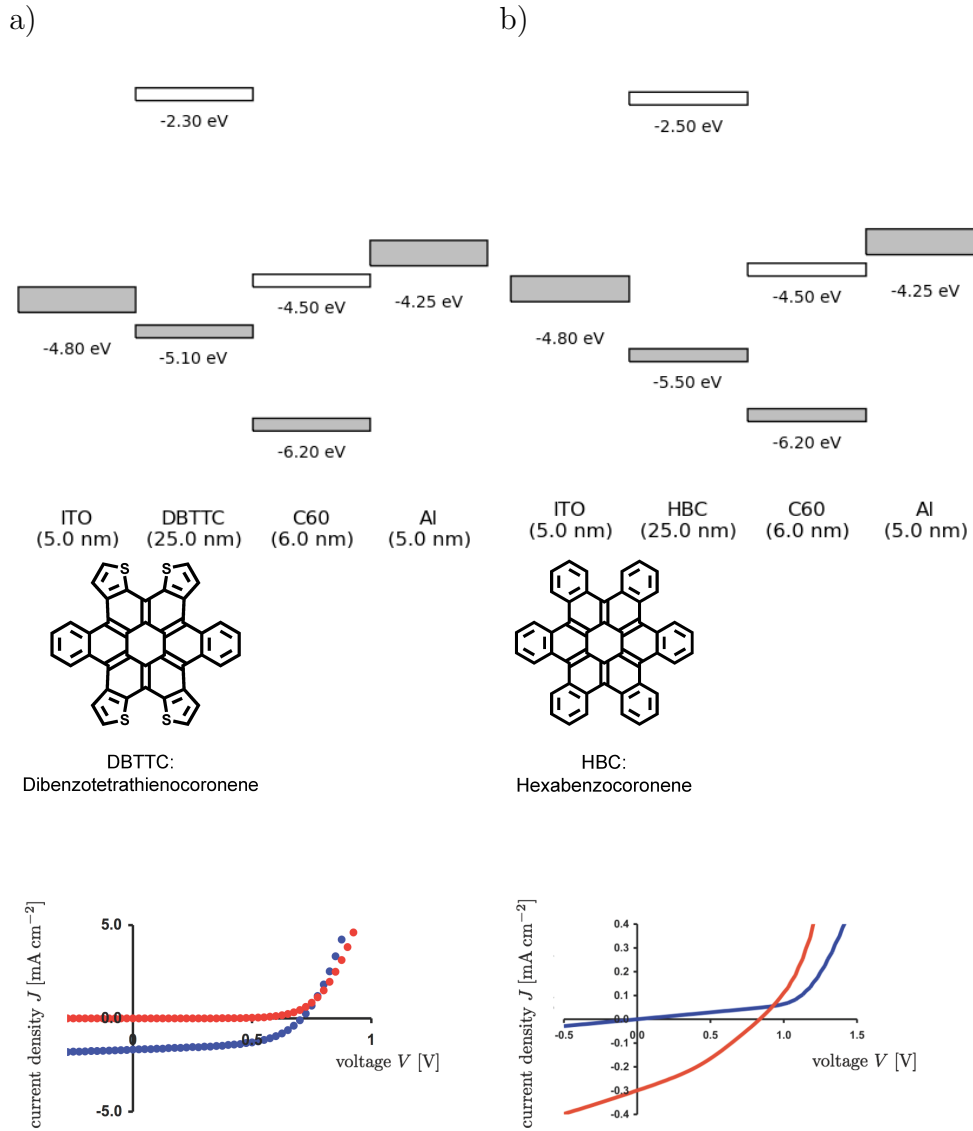


Figure 6.2: Molecular structure and solar cell performances of HBC and DBTTC devices.

The two bilayer solar cells studied here: (upper) energy levels (from Ref. [293]) with approximate device-layer thicknesses, (middle) molecular structure of the donor, (lower) current-voltage curves. (a) DBTTC/ $C_{60}$ , with the lower plot showing the  $J - V$  curve in the dark (red) and under AM1.5 illumination (blue). (b) HBC/ $C_{60}$  with the lower plot showing the  $J - V$  curve in the dark (blue) and under AM1.5 illumination (red). In both (a) and (b) the reported ITO and Al thicknesses are only approximate. Also note that the lower plot in (b), reproduced from Figure 4(B) of Ref. [293] and shown here for comparison, the thickness of the  $C_{60}$  layer was 40 nm and the ITO was coated with 25 nm of PEDOT-PSS.

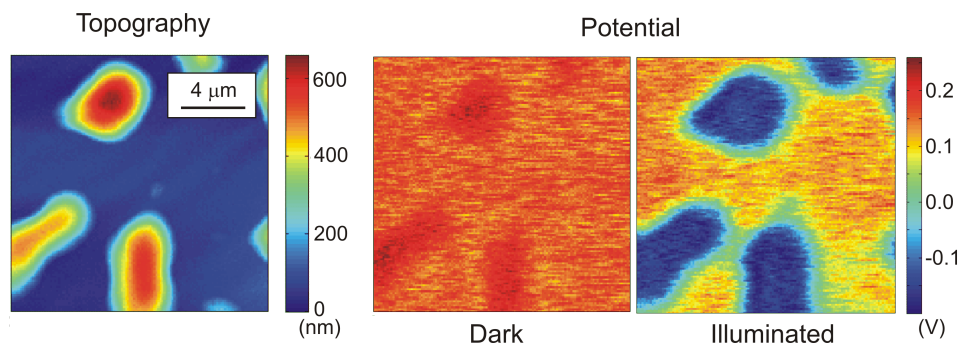


Figure 6.3: Topography, dark contact potential, and contact potential under illumination of DBTTC films.

Topography (left) and electrostatic potential images (right) of ITO/DBTTC/ $C_{60}$  devices. When DBTTC is heat-treated, the film aggregates. Afterwards,  $C_{60}$  is deposited over the whole film. In the dark, there is an observed contrast between ITO/ $C_{60}$  and ITO/DBTTC/ $C_{60}$ . Under illumination, regions of ITO/DBTTC/ $C_{60}$  become (negatively) charged.

topographical features on the order of hundreds of nanometers.

Time-resolved measurements of the change in surface potential upon illumination were made while the cantilever was scanned across the surface, in order to avoid artifacts from trapping due to tip-induced charge. Contact potential was measured over ITO/DBTTC/ $C_{60}$  were collected at an acquisition rate of 32 Hz, with each line scan taking 4.25 seconds to complete. The sample was illuminated with light turned on and off at approximately one-third and two-thirds through image acquisition. Images of contact potential were re-plotted as a function of time and were passed through a 16-point running average smoothing function to produce a 'time response function'. Time response measurements for the degradation of ITO/DBTTC were collected at 16 Hz, with each line scan completing in 8.25 seconds. These time response images were passed through an 8-point running average smoothing function.

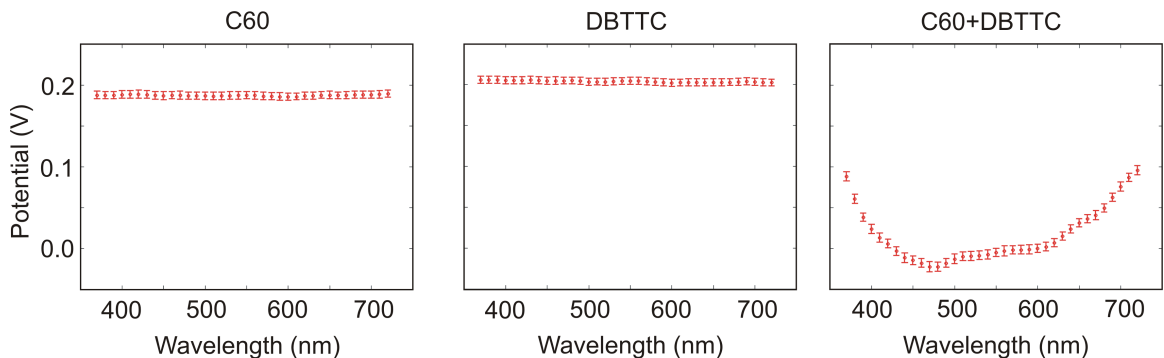


Figure 6.4: Contact potential versus illuminated wavelength in films of DBTTC.

(a) Absorbance spectra for C<sub>60</sub>, shown in black, and DBTTC, shown in blue. Contact potential versus illuminated wavelength for (b) C<sub>60</sub> films, (c) DBTTC films, and (d) DBTTC:C<sub>60</sub> bilayer films on ITO.

## 6.3 Results

### 6.3.1 Contact Potential Shift under Illumination

An interesting feature of DBTTC and HBC as photovoltaic materials is that they form aggregates upon annealing. With the proper control, these films have shown columnar structure which can be advantageous for use in bulk heterojunction solar cells. Contrary to what has been observed in other experiments [300], micron sized topographic domains were observed in our experiments upon annealing (Figure 6.3, left).

A thermally evaporated layer of C<sub>60</sub> on the DBTTC film shows a small amount of contrast in the contact potential image, seen in Figure 6.3 (center). Under white-light illumination (see methods section of thesis), domains of DBTTC+C<sub>60</sub> exhibit a large, negative contact potential shift (Figure 6.3, right). Regions of only C<sub>60</sub> exhibit no contact potential shift under illumination.

To characterize the shift in contact potential, scanning wavelength illumination was used. The results of this experiment are shown in Figure 6.4. Films of ITO/DBTTC and films of ITO/C<sub>60</sub> show no wavelength-dependence in contact potential. However, when the materials are in the

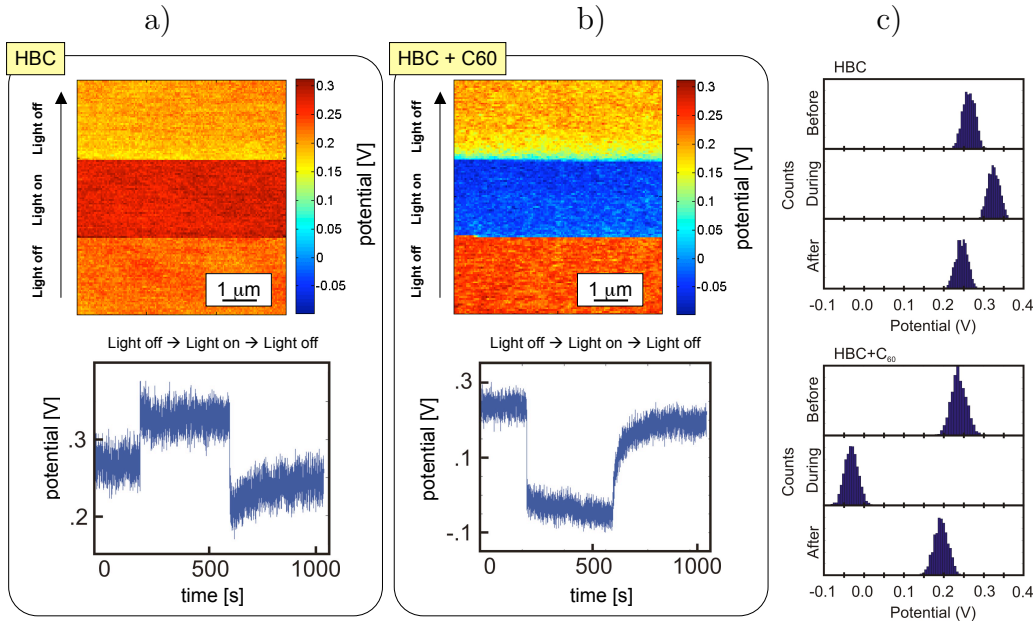


Figure 6.5: Contact potential response of HBC films under white-light illumination.

Contact potential observed with white-light illumination over (a) ITO/HBC and (b) ITO/HBC/C<sub>60</sub>. Under illumination, the trapping rate in ITO/HBC is faster than the 10s of millisecond resolution of our instrument. The trapping rate ITO/HBC/C<sub>60</sub> appears to be very slow. The detrapping rate after illumination is turned off is similar in both samples. Also shown are histograms (c) of contact potential recorded for one minute over ITO/HBC and ITO/HBC/C<sub>60</sub> before, during, and after illumination.

bilayer device configuration, wavelength-dependent features are observed. From the response of the contact potential, it appears as though the bilayer device absorbs across most of the visible spectrum. This unexpected behavior is inconsistent with the absorption spectra of DBTTC and C<sub>60</sub>. However, increased signal has been observed under red light in EQE measurements of many organic solar cell systems. This behavior is generally attributed to mid-gap transitions or inter-material excitation.

### 6.3.2 Temporal Response of Contact Potential under Illumination

Figure 6.5 presents images over a  $5\mu\text{m} \times 5\mu\text{m}$  area of the electrostatic potential of a control sample of 25 nm of HBC on ITO, with and without a 5 nm layer of C<sub>60</sub>. Though the electrostatics inside

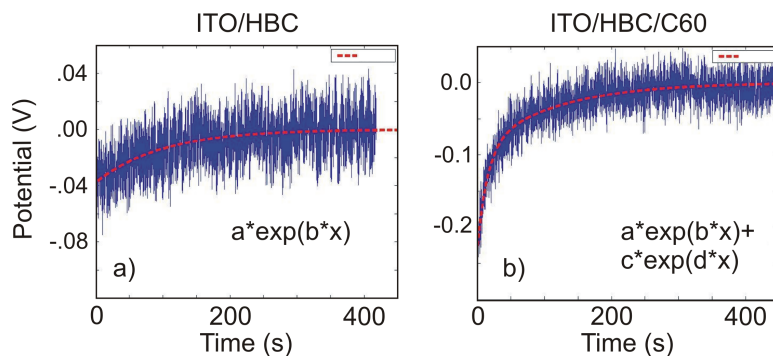


Figure 6.6: Trapping/detrapping rates in HBC films after white-light illumination.

Decay of the contact potential after the white-light illumination was turned off at time  $t = 0$ . (a) Over the ITO/HBC film, for purposes of fitting, the potential was shifted downward by 0.25 V. The shifted potential was fit to  $\Delta\phi(t) = \Delta\phi_1 \exp[-k_1 t]$  to yield best-fit values of  $\Delta\phi_1 = 37.8 \pm 1.6$  mV and  $k_1 = 10.16 \pm 0.63 \times 10^{-3} \text{ s}^{-1}$  for the amplitude and decay rate, respectively, of the shifted electrostatic potential. (b) Over the ITO/HBC/C<sub>60</sub> film, for purposes of fitting, the potential was shifted downward by 0.19 V. The shifted potential was fit to  $\Delta\phi(t) = \Delta\phi_1 \exp[-k_1 t] + \Delta\phi_2 \exp[-k_2 t]$  to obtain best-fit values of  $\Delta\phi_1 = 91.9 \pm 5.2$  mV,  $k_1 = 8.66 \pm 0.43 \times 10^{-3} \text{ s}^{-1}$ ,  $\Delta\phi_2 = 137.1 \pm 6.2$  mV, and  $k_2 = 65.9 \pm 5.9 \times 10^{-3} \text{ s}^{-1}$ . In both (a) and (b), the best-fit line appears as a dashed red line in the upper plot and the fit residuals are shown below.

the cell are different when the electron extracting anode is not in place, these measurements nevertheless give insight to the electron transfer, trapping, and charge generation at play in the working cell. The images of contact potential were acquired scanning from the lower left to the upper right as plotted, with light turned on and off at approximately one-third and two-thirds through image acquisition in Figures 6.5(a,b). From the initial light-off (lower third) and light-on (middle third) images of Figure 6.5, the light-off surface potential and light-on surface potential appear to be spatially homogeneous — down to the  $\sim 100$ nm resolution of the microscope — over both of the HBC samples. Shown in Figure 6.5(c) are histograms of contact potential recorded over ITO/HBC and ITO/HBC/C<sub>60</sub> for sixty seconds (1) just before illumination, (2) halfway through the scanning period, and (3) at the end of the scanning period.

The HBC film on ITO showed an essentially instantaneous increase in electrostatic potential upon applying illumination (Figure 6.5(a)). Surprisingly, turning off the illumination, the electrostatic potential abruptly decreased to a value *below* its initial light-off value; it then slowly

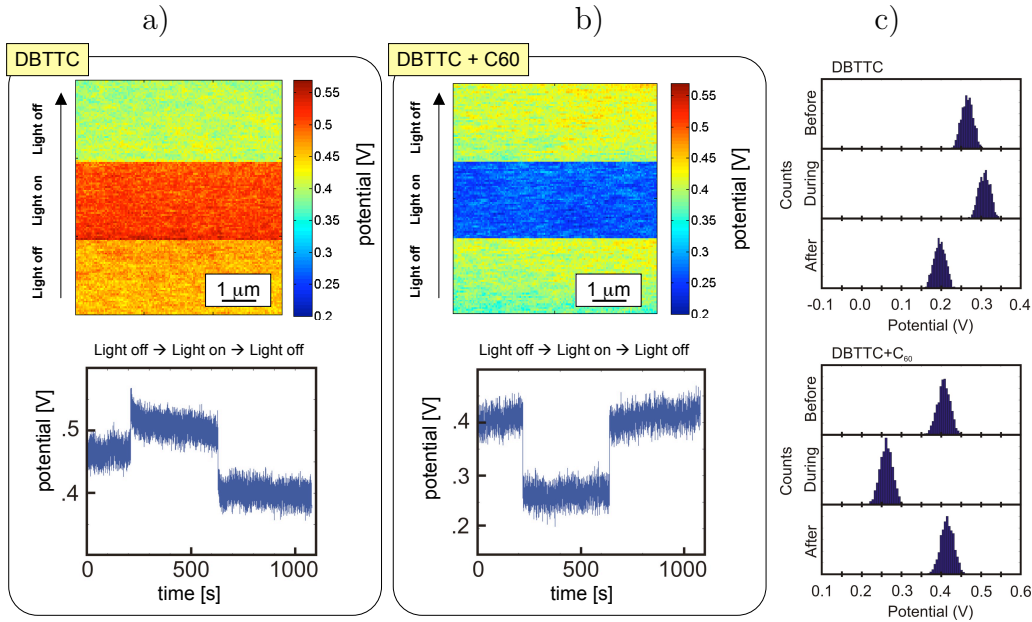


Figure 6.7: Contact potential response of DBTTC films under white-light illumination.

Contact potential observed with white-light illumination over a) ITO/DBTTC and b) ITO/DBTTC/C<sub>60</sub>. Trapping rate under illumination in ITO/DBTTC is slow compared to ITO/HBC, with very little trapping in ITO/DBTTC/C<sub>60</sub>. Detrapping in ITO/DBTTC is very slow compared to ITO/HBC. Also shown are histograms (c) of contact potential recorded for one minute over ITO/DBTTC and ITO/DBTTC/C<sub>60</sub> before, during, and after illumination.

recovered. The HBC/C<sub>60</sub> on ITO film, in contrast, showed an essentially instantaneous decrease in electrostatic potential upon applying illumination; again, the potential slowly recovered to its initial light-off value (Figure 6.5b). The slow recovery of the electrostatic potential in the HBC sample fit well to a single exponential (Figure 6.6(a)), while the slow recovery of the HBC/C<sub>60</sub> was best fit by a double exponential (Figure 6.6(b)).

Figure 6.7 presents images of the electrostatic potential of a control sample of 25 nm of DBTTC on ITO and a bilayer solar-cell sample of DBTTC/C<sub>60</sub> on ITO. Light was turned on and off during the image acquisition, as in Figure 6.5. The light-off and light-on surface potentials were observed to be spatially homogeneous in HBC and DBTTC samples. In the DBTTC sample on ITO, the electrostatic potential increased immediately upon illumination and inverted when the illumination was removed. In contrast with the HBC sample on ITO,

however, the recovery of the potential in the DBTTC on ITO to its initial light-off value was too slow to resolve (with a time constant of hours). The DBTTC/C<sub>60</sub> on ITO film immediately decreased in electrostatic potential upon illumination which, contrary to HBC/C<sub>60</sub>, recovered instantaneously and completely to its initial light-off value.

### 6.3.3 Varying DBTTC Layer Thickness

In an effort to independently determine the contributions of contact potential shift from free carriers, trapped charge, and exciplexes, the thickness of DBTTC in bilayer ITO/DBTTC/C<sub>60</sub> films was varied. The potential response under illumination for each case should depend on the thickness of the DBTTC layer. Displayed in Figure 6.8 are plots of contact potential versus time. At one-third of the way through the scan, the sample was illuminated with white light. At two-thirds through the scan, the white light was turned off. For DBTTC layer thicknesses of 5 nm and 25 nm, Figure 6.8(a,b), the contact potential shift just after initial illumination in both cases was approximately  $\approx -0.2$  V. This finding indicates that charge transfer across the DBTTC/C<sub>60</sub> interface was responsible for the negative shift in contact potential. However, when the thickness of the DBTTC layer was 125 nm, the shift in contact potential was approximately  $\approx -0.3$  V. This indicates that at large film thicknesses, the bulk of DBTTC is adding  $-0.1$  V to the contact potential shift. In addition to the difference in magnitude of the observed contact potential shift, the response after illumination was slower compared to the thinner DBTTC thickness samples. It is also noted that a small but observable shift in the contact potential over time was detected under illumination. In the 5 nm, 25 nm, and 125 nm thicknesses, this potential drop during illumination is roughly 20 mV, 25 mV, and 40 mV respectively.

Measurements were likewise taken over films of ITO/DBTTC, shown in Figure 6.9. Measurements of contact potential response under illumination for the 5 nm sample in Figure 6.9(a) were recorded at a quarter of the speed. To make an better comparison to the 25 nm and 125 nm

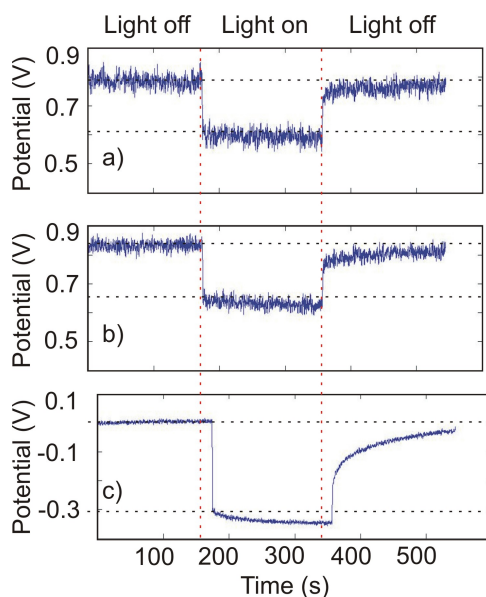


Figure 6.8: Contact potential over ITO/DBTTC/ $C_{60}$  with varying DBTTC layer thicknesses.

Contact potential measurements under illumination over ITO/DBTTC/ $C_{60}$  with DBTTC layer thicknesses of 5 nm (a), 25 nm (b), and 125 nm (c). Red dotted lines indicate when light was turned on (left) and turned off (right). Black lines indicate initial values of contact potential before and after initial illumination.

thick samples in Figure 6.9(c,d), periods of time before and after illumination were concatenated to produce a figure with the same time scale (Figure 6.9b). The shift in contact potential under illumination is *negative*, contrary to the results of Figure 6.7. The 25 nm sample in Figure 6.9(c) is observed to have a longer trapping time than either the 5 nm or the 125 nm sample.

### 6.3.4 Degradation of DBTTC on ITO without the Fullerene Layer

Films of ITO/DBTTC exhibited degradation on the hours time scale after being stored at a pressure of 500 mbar and exposed to low levels of light (approximately  $10^{-4}$  Sun, in the daytime). Samples were exposed to air for several days, in the dark, before testing. After ten minutes of exposure to air and low light levels, shown in Figure 6.10(a), samples respond similarly to those in Figure 6.7. However, after periods of light exposure from one to four days, the contact potential shift under illumination diminishes, as shown in Figure 6.10(b-d). After four days, little or

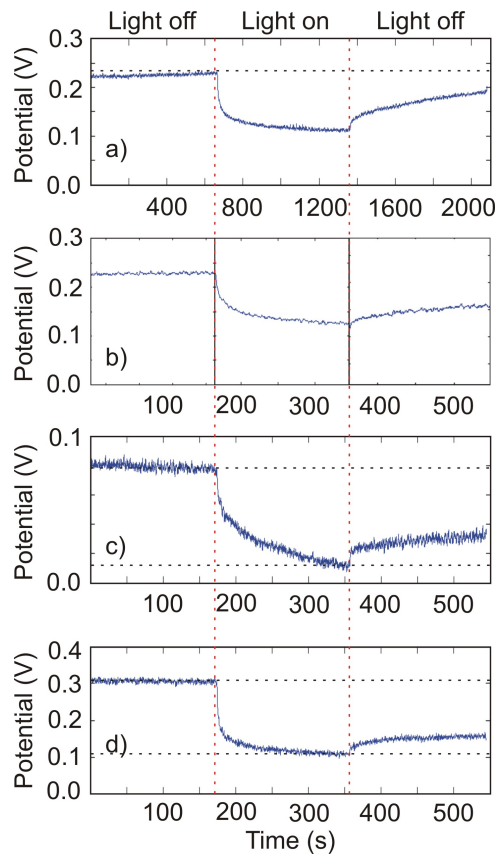


Figure 6.9: Contact potential over ITO/DBTTC with varying DBTTC layer thicknesses.

Contact potential measurements under illumination over ITO/DBTTC with DBTTC layer thicknesses of 5 nm (a,b), 25 nm (c), and 125 nm (d). Time recorded for the 5 nm sample in (a) was recorded at a quarter speed. Periods of measurement in (a) were concatenated together in (b) so that they are on the same time scale as (c) and (d). Red dotted lines indicated when light was turned on (left) and turned off(right). Black lines indicate initial values of contact potential before, and after initial illumination. Figure (c) is slightly offset from (a,b) due to a programming error in the timing of illumination.

no contact potential shift upon illumination was observed. Samples measured in the time decay experiments exhibited a different trapping behavior than the samples of Figure 6.7, suggesting that sample aging is a concern and should be monitored carefully. In future experiments, samples of ITO/DBTTC without the  $C_{60}$  layer should be stored in vacuum without any source of illumination.

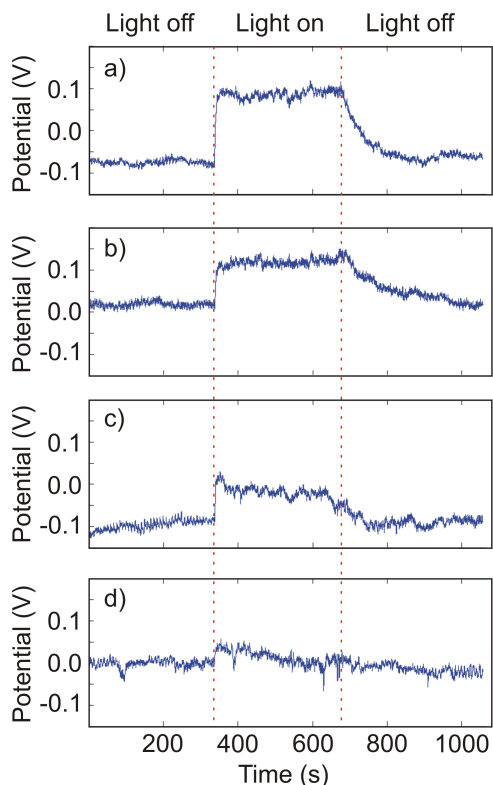


Figure 6.10: ITO/DBTTC sample degradation.

Contact potential observed with white-light illumination under vacuum, after being stored at a pressure of 500 mbar and exposed to low light levels (approximately  $10^{-4}$  sun, daytime) for (a) 10 minutes, (b) one day, (c) two days, and (d) four days. The samples exhibited electron detrapping times much longer than the ITO/DBTTC samples of Figure 6.7.

## 6.4 Discussion

### 6.4.1 Temporal Response of Contact Potential

The high *lateral* spatial homogeneity of electrostatic potential image displayed in Figures 6.5 and 6.7 allows us to model light-induced changes in the *vertical* distribution of charge in the films. The change in the surface potential upon irradiation for a laterally invariant sample is [282],

$$\Delta\phi \approx \frac{\Delta\mathcal{M}_1}{2\epsilon_0} \quad (6.1)$$

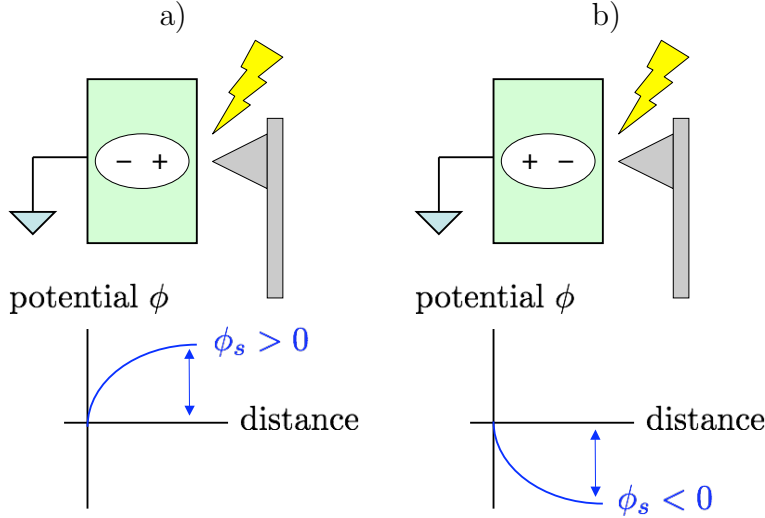


Figure 6.11: Contact potential of vertically distributed charges.

Light-induced charge redistribution, and the resulting change in contact potential, for a net photoinduced transfer of electrons (a) towards the substrate and (b) towards the surface.

with

$$\Delta\mathcal{M}_1 = \int_{-t}^0 \Delta\rho(z') z' dz' \left[ \frac{\text{C}}{\text{m}} \right] \quad (6.2)$$

where  $\Delta\mathcal{M}_1$  is the change in the dipole moment associated with the change in the sample's charge distribution ( $\Delta\rho$ ) upon irradiation. The change in surface potential is sketched in Figure 6.11 (a,b) for a light-induced shift of charge towards and away from the substrate, respectively.

Figure 6.12 is a sketch of light-induced changes in charge density that explains the HBC-on-ITO potential-versus-time data of Figure 6.5. According to Figure 6.11 and Equations 6.1 and 6.2, the increase in electrostatic potential seen upon illumination is consistent with a photoinduced transfer of electrons from HBC towards the ITO substrate (Figure 6.12(left)). The immediate decrease of the electrostatic potential to a value below its initial value requires an instantaneous inversion of the sign of  $\Delta\mathcal{M}_1$  when the light is turned off. The simplest explanation for this inversion is that light has created long-lived trapped electrons in the HBC layer (Figure 6.12(right)). This hypothesis of trapped charge in HBC also explains the slow recovery of the potential, since decay of trapped charge in organic semiconductors typically occurs on the seconds to hours timescale. Referring to the fit of Figure 6.6(a),  $k_1 = 10.16 \pm 0.63 \times 10^{-3} \text{ s}^{-1}$  as

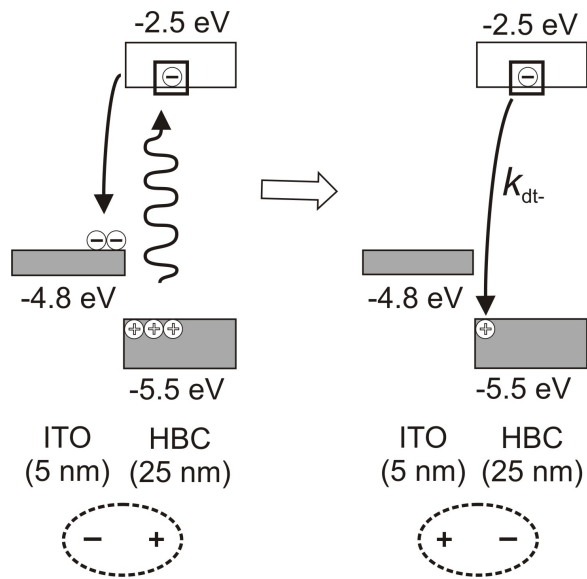


Figure 6.12: ITO/HBC energy levels and charge distribution model.

Energy levels and proposed electron and hole occupancy for the HBC sample on ITO. The dipole moment of the charge distribution is sketched below under light-off and light-on conditions.

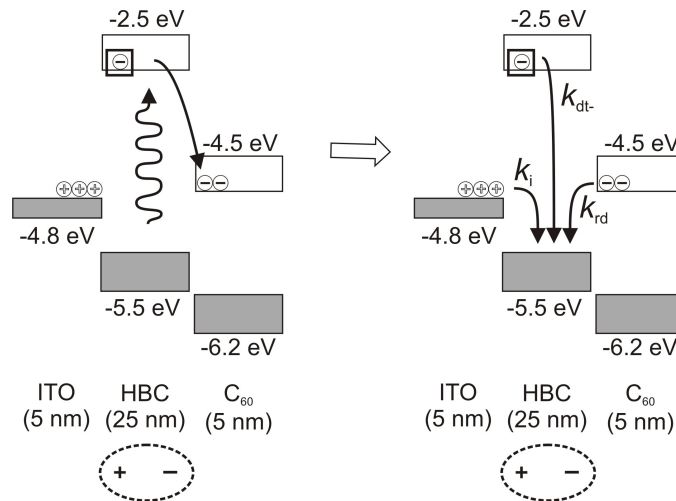


Figure 6.13: ITO/HBC/C<sub>60</sub> energy levels and charge distribution model.

Energy levels and proposed electron and hole occupancy for the HBC/C<sub>60</sub> sample on ITO.

the detrapping rate constant  $k_{dt-}$  of Figure 6.12(right).

The decrease in electrostatic potential seen in the HBC/C<sub>60</sub> sample upon illumination is consistent with a net photoinduced transfer of electrons from HBC towards C<sub>60</sub>. One possible (change in) charge distribution is sketched in Figure 6.13. Because of the long recovery, the data

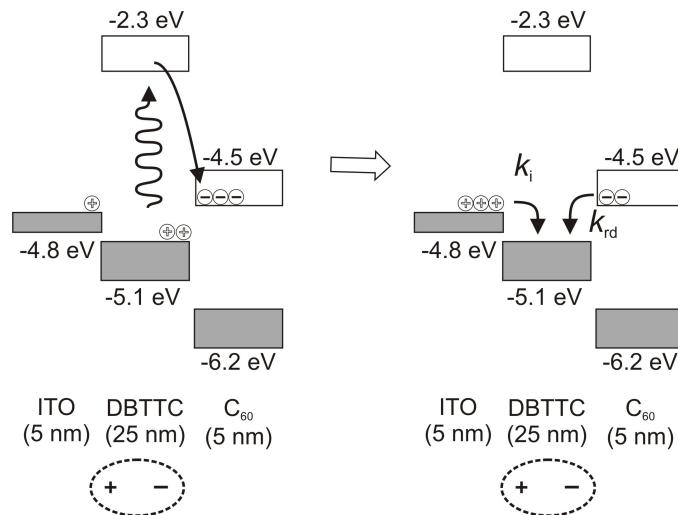


Figure 6.14: ITO/DBTTC/ $C_{60}$  energy levels and charge distribution model.

Energy levels and proposed electron and hole occupancy for the DBTTC/ $C_{60}$  sample on ITO.

again indicates the presence of trapped charge in HBC. Referring to the fit of Figure 6.6(b), the electron-dropping rate constant,  $k_{dt-} = 8.66 \pm 0.43 \times 10^{-3} \text{ s}^{-1}$ , in reasonable agreement with  $10.16 \pm 0.63 \times 10^{-3} \text{ s}^{-1}$  measured in absence of the  $C_{60}$  layer.

In Figure 6.13 is a diagram of the photoexcited holes as concentrated in the ITO HOMO when light is on. Were these holes concentrated in the HBC HOMO instead, we would expect a large and instantaneous change in the electrostatic potential when the light is turned off and electrons in the  $C_{60}$  LUMO to promptly transfer to the HBC HOMO; this was not observed. Instead we observed that the electrostatic potential decay showed a second, faster, but easily resolved component with a rate constant of  $65.9 \pm 5.9 \times 10^{-3} \text{ s}^{-1}$ . It is reasonable to assume that  $k_{rd}$ , the rate of decay of electrons from the  $C_{60}$  LUMO to the HBC HOMO is too fast for us to resolve. We therefore identify the second measured rate,  $k_i = k_2$ , in Figure 6.13 (right) to be associated with injection of electrons from the HBC HOMO to the ITO LUMO. This injection step is required to create empty states in HBC for the electrons in  $C_{60}$  to transfer into.

Comparing the data of Figure 6.5 (a) and Figure 6.7 (a), we conclude that photoinduced charge transfer in the DBTTC sample on ITO is qualitatively similar to that seen in the HBC on ITO sample presented in Figure 6.12. The inversion of the change in surface potential when

illumination is turned off indicates trapped electrons in DBTTC, although now the detrapping is too slow to measure. The complete and essentially instantaneous decay of electrostatic potential in DBTTC/C<sub>60</sub> when light is off is explained by invoking the charge transfer scheme of Figure 6.14 in which most of the photoexcited holes are concentrated in the DBTTC HOMO. As mentioned above,  $k_{rd}$  is expected to be too fast to measure. Holes may or may not be present in ITO as well; if present, the data indicates that the rate of injection  $k_i$  is likewise too fast to resolve by EFM.

The charge transfer scheme of Figure 6.14 also explains the lack of trapped electrons in DBTTC in the DBTTC/C<sub>60</sub> film. If trapping is due to a chemical process, then by Le Chatlier's principle, the rate of conversion of free charge to trapped charge in many organic semiconductors is observed to be a function of the free charge concentration. One possible explanation is that DBTTC remains trap free in the DBTTC/C<sub>60</sub> film, in spite of the ability of DBTTC to trap charge (Figure 6.7(a) and Figure 6.12), because the facile electron transfer to C<sub>60</sub> assures that the steady-state concentration of electrons in DBTTC remains small.

### 6.4.2 Variations in ITO/DBTTC

For the ITO/DBTTC experiments, inconsistency was observed from sample batch to sample batch. The results of Figures 6.7 and 6.10 show that contact potential in ITO/DBTTC shifted *positively* under white light illumination. However, in the thickness dependent experiments highlighted in Figure 6.8, the ITO/DBTTC potential shifted *negatively* under white light illumination. Even where the direction in contact potential shifts agreed (Figures 6.7 and 6.10), the time response appeared to be quite different. For example the detrapping rates in ITO/DBTTC after illumination in Figures 6.7 and 6.10. These differences are attributed to variations in batch preparation, exposure, or contamination.

### 6.4.3 DBTTC Layer Thickness in ITO/DBTTC/C<sub>60</sub>

The surface potential study of Figure 6.8 for ITO/DBTTC/C<sub>60</sub>, which gave data agreeing with subsequent experiments in which the thickness of the DBTTC layer in ITO/DBTTC/C<sub>60</sub> was varied, can be used to provide information on certain processes within the solar cell. For example, since there is little difference in contact potential shift under illumination between DBTTC layer thicknesses of 5 nm and 25 nm, it can be inferred that contact potential drop is occurring across the interface between DBTTC and C<sub>60</sub>.

To quantitatively measure the origin of the contact potential shift under illumination, it is necessary to calculate the how variations in sample thickness contribute to the measured EFM signal. Let us model the system as compromised of planar and volume charge concentrations, shown in Figures 6.15 and 6.16 and consider each of the following: exciplex formation  $\sigma_{\text{ex}}$ , trapped charge  $\rho_{\text{trap}}$ , free charge in DBTTC  $\rho_{\text{free}}$ , and separated charge  $\sigma_{\text{sep}}$ . For exciplex formation, charge is located near the DBTTC/C<sub>60</sub> interface. Trapped charge exists within the bulk of DBTTC, which is apparent from measurements of contact potential versus time. Free charge is also assumed to exist uniformly throughout the thickness of DBTTC, and is observed in illumination experiments on ITO/DBTTC. Separated charge describes the carriers in C<sub>60</sub> that are balanced by opposite charges in ITO. Let us now derive the change in the electrostatic potential above a film due to photo-induced charge rearrangement within the film.

Consider the semi-infinite slab sketched in Figure 6.15. The front surface of the slab is located at  $z' = 0$  and the back surface of the slab is located at  $z' = -t$ . Let  $\rho(x', y', z')$  be the charge density in the slab in units of C m<sup>-3</sup>. The end result of this calculation is the electrostatic potential at distance  $z' = z$  above the slab. The two key assumptions in the following derivation are that 1) the sample is translationally invariant in the  $(x', y')$  plane and 2) the sample is net neutral, that is, the net charge in the sample is zero.

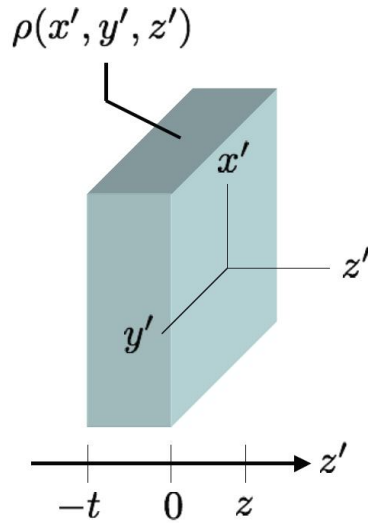


Figure 6.15: Model of charge density in a film.

A thin film photovoltaic device, represented as a semi-infinite slab. Here  $\rho(x', y', z')$  is the charge density in the film.

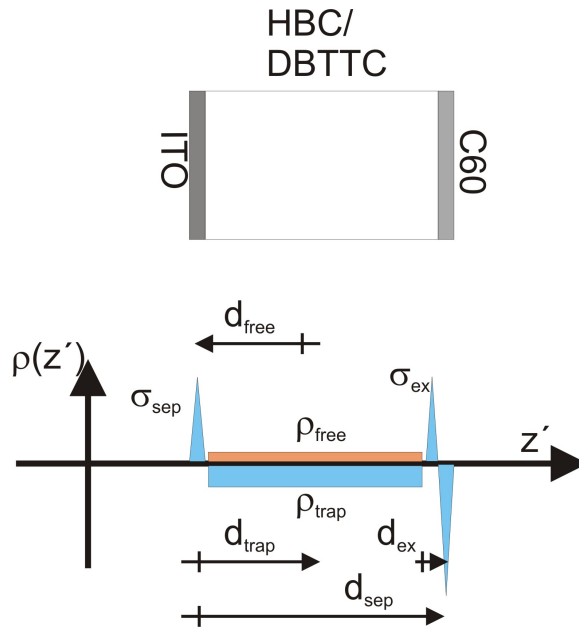


Figure 6.16: Model charge distribution in a thin film photovoltaic device.

Light is absorbed primarily in the HBC/DBTTC layer; excitons diffuse to the interface with C<sub>60</sub> and form bound electron-hole pairs in the form of exciplexes. For convenience, let the electrons of the exciplex be located at  $z' = 0$ . The holes of the exciplex are located at  $z' = -d_{\text{ex}}$  and have a planar charge density of  $\sigma_{\text{ex}}$ . A fraction of the exciplexes dissociate into free charge, giving rise to positive free charge in the ITO (location  $z' = -t$  and planar charge density  $\sigma_{\text{sep}}$ ). Trapped charge of volume density  $\rho_{\text{trap}}$  and free charge volume density  $\rho_{\text{free}}$  are distributed uniformly throughout the HBC/DBTTC layer.

According to Poisson's equation, the potential at location  $(0, 0, z)$  above the film is

$$\phi(0, 0, z) = \frac{1}{4\pi\epsilon_0} \int \int \int \frac{\rho(x', y', z') dx' dy' dz'}{\sqrt{x'^2 + y'^2 + (z - z')^2}} \quad (6.3)$$

where  $\epsilon_0 = 8.8542 \times 10^{-12} \text{ C V}^{-1} \text{ m}^{-1}$  is the free-space permittivity. Assuming that the sample is translationally invariant in the  $(x', y')$  plane,  $\rho(x', y', z') \rightarrow \rho(z')$ . Changing to cylindrical coordinates,  $dx' dy' \rightarrow r' dr' d\theta'$  and  $x'^2 + y'^2 \rightarrow r'^2$ . Substituting,

$$\phi(0, 0, z) = \frac{1}{2\epsilon_0} \int_{-t}^0 dz' \int_0^\infty \frac{\rho(z') r' dr'}{\sqrt{r'^2 + (z - z')^2}} \quad (6.4)$$

where the integral becomes  $\int_0^{2\pi} d\theta' = 2\pi$ . Seeking an approximate expression for  $\phi$  by expanding the denominator in the integrand in powers of  $z'$ ,

$$\frac{1}{\sqrt{r'^2 + (z - z')^2}} \approx \frac{1}{(r'^2 + z^2)^{1/2}} + \frac{z z'}{(r'^2 + z^2)^{3/2}} + \frac{(-r'^2 + 2z^2) z'^2}{2(r'^2 + z^2)^{5/2}} + \mathcal{O}(z'^3) \quad (6.5)$$

Substituting,

$$\begin{aligned} \phi(0, 0, z) \approx & \frac{1}{2\epsilon_0} \underbrace{\int_{-t}^0 \rho(z') dz'}_{\mathcal{M}_0=0} \underbrace{\int_0^\infty \frac{r' dr'}{(r'^2 + z^2)^{1/2}}}_{\text{diverges}} \\ & + \frac{1}{2\epsilon_0} \underbrace{\int_{-t}^0 \rho(z') z' dz'}_{\mathcal{M}_1 \neq 0} \underbrace{\int_0^\infty \frac{r' dr'}{(r'^2 + z^2)^{3/2}}}_{=z^{-1}} \times z \\ & + \frac{1}{2\epsilon_0} \underbrace{\int_{-t}^0 \rho(z') z'^2 dz'}_{\mathcal{M}_2 \neq 0} \underbrace{\int_0^\infty \frac{(-r'^2 + 2z^2) r' dr'}{(r'^2 + z^2)^{5/2}}}_{=0} \times z^2 + \dots \quad (6.6) \end{aligned}$$

The divergence of the integral in the first term can be eliminated by redefining the potential with respect to the potential at  $z = \infty$ ; then the first term drops out because of charge neutrality,  $\int_{-t}^0 \rho(z') dz' = \mathcal{M}_0 = 0$ . The integral over  $r'$  in the third term vanishes. This leaves, to leading order,

$$\phi(0, 0, z) \approx \frac{\mathcal{M}_1}{2\epsilon_0} \quad (6.7)$$

with

$$\mathcal{M}_1 = \int_{-t}^0 \rho(z') z' dz' \left[ \frac{\text{C}}{\text{m}} \right] \quad (6.8)$$

the dipole moment of the charge distribution in the slab.

We use the charge distribution sketched in Figure 6.16 to mathematically model the expected change in contact potential under illumination. We approximate the exciplex at the interface between HBC/DBTTC and C<sub>60</sub> as a delta-function  $+/-$  charge distribution with the electrons located at  $z' = 0$  and the holes located at  $z' = -d_{\text{ex}}$ . Likewise, we approximate any free charge in the ITO layer as a delta-function located at  $z' = -t$  and any trapped charge as uniformly distributed between  $z' = -t$  and  $z' = 0$ . Carrying out the integral in Equation 6.8,

$$\mathcal{M}_1 = -t \sigma_{\text{sep}} + \int_{-t}^0 (\rho_{\text{trap}} - \rho_{\text{free}}) z' dz' - d_{\text{ex}} \sigma_{\text{ex}} \quad (6.9)$$

where the charge distributions are defined pictorially in Figure 6.16. The central integral in Equation 6.9 then simplifies to

$$\int_{-t}^0 (\rho_{\text{trap}} - \rho_{\text{free}}) z' dz' = \left[ \rho_{\text{trap}} \frac{z'^2}{2} \right]_{-t}^0 = -\rho_{\text{trap}} \frac{t^2}{2}$$

We thus determine the potential above the film to be

$$\phi(0, 0, z) \approx -\frac{1}{2\epsilon_0} \left( \sigma_{\text{ex}} d_{\text{ex}} + \sigma_{\text{sep}} t + \frac{\rho_{\text{trap}} - \rho_{\text{free}}}{2} t^2 \right) \quad (6.10)$$

Equation 6.10 is the central finding of our derivation.

Now that the derivation for sources of contact potential as a function of layer thickness is in place, the results of ITO/DBTTC/C<sub>60</sub> samples of Figure 6.8 can be quantitatively approached. Since the contact potential shift after initial illumination is roughly the same ( $\approx -200$  mV) for DBTTC layer thicknesses of 5 nm and 25 nm,  $\sigma_{\text{ex}} d_{\text{ex}}$  is much greater than either  $\sigma_{\text{sep}} t$  or  $\rho_{\text{trap}} t^2/2$  in this regime.

Fitting the parabola to each of the parameters of contact potential shift under illumination versus DBTTC layer thickness (Figure 6.17), adding a gaussian distribution of noise with a width of 10 mV, produces (with 95% confidence intervals)  $\sigma_{\text{ex}} d_{\text{ex}}/(2\epsilon_0) = 0.20V \pm 0.01V$ ,  $\sigma_{\text{sep}}/(2\epsilon_0) = -0.25 \pm 0.45V/\mu\text{m}$ , and  $(\rho_{\text{trap}} - \rho_{\text{free}})/(4\epsilon_0) = 8.3 \pm 3.4V/\mu\text{m}^2$ . The value for the exciplex density has the least uncertainty, while the values for separated and trapped charge density have

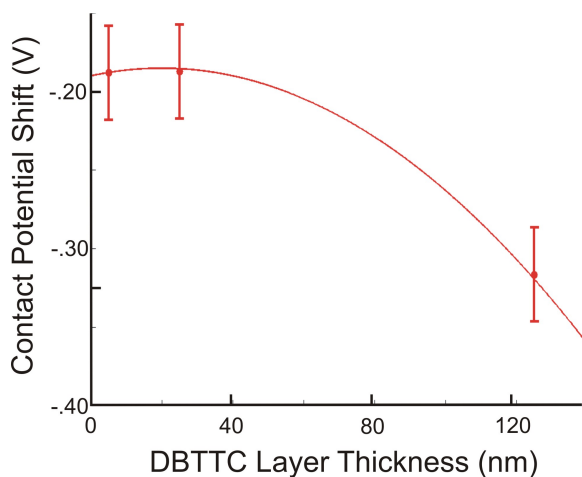


Figure 6.17: Fitting of contact potential shift under illumination versus DBTTC layer thickness.

Plot of contact potential shift under illumination versus DBTTC layer thickness of 5, 25, and 125 nm. Noise of .01 V was added to each point in order to estimate errors on the fitting parameters. Displayed error bars represent  $3\sigma=0.3V$ .

large uncertainties. The value for separated charge density is indistinguishable from zero in this experiment. Plugging in reasonable numbers for the exciplex separation distance  $d_{ex} \approx 5 \text{ \AA}$ , the planar charge concentration is then calculated within ten percent error to be,  $\sigma_{ex} \approx 4 \times 10^4 \text{ q}_e/\mu\text{m}^2$ . Within fifty percent error, the trapped charge volume density is calculated to be,  $\rho_{\text{trap}} \approx 2 \times 10^{21}/\text{m}^3$ . For a film thickness of 25 nm, this corresponds to a planar charge density of  $\rho_{\text{trap}} \approx 4.5 \times 10^{19}/\mu\text{m}^2$ . In order to more accurately derive the trap density, more data must be collected.

After 185 seconds of illumination, the contact potential in the 5 nm, 25 nm, and 125 nm drops roughly 20 mV, 25 mV, and 40 mV respectively. We propose this effect is due to traps that operate under slow (order of several hours) trapping/detrapping kinetics. These values do not appear to scale as the square of the DBBTC layer thickness. From this observation, it can be concluded the approximation of homogeneous trapping used above is not valid for slow traps in DBTTC.

#### 6.4.4 ITO/DBTTC Degradation

The sample degradation observed in Figure 6.10 agrees with the picture that the  $C_{60}$  layer reduces the free electron density in DBTTC, thus reducing trapping. Without the  $C_{60}$  layer, even under low light conditions, contact potential response under illumination significantly decreased on the order of days of exposure to air and light. This result is somewhat curious, considering that ITO/DBTTC/ $C_{60}$ /Al solar cells operate well in air on the order of weeks [300]. There are two possible explanations for this behavior. First, that the  $C_{60}$  and aluminum layers act as a sufficient encapsulation layer as to prevent the DBTTC layer from being exposed to air. In this case, DBTTC under exposure of light and air undergoes photo-oxidation. The second possibility is that, with  $C_{60}$  and aluminum, electrons never build up a sufficiently large concentration in DBTTC. From the DBTTC time decay experiments, summarized in Figure 6.7, it is observed that long-lived electron traps form in these materials, even in high vacuum. This observation supports the second explanation for the decreased contact potential shift. Without an electron accepting material in contact with DBTTC, a sufficiently large electron concentration builds up as to cause trapping and degradation. We thus conclude that photoinduced electron transfer into  $C_{60}$  not only leads to photocurrent in the working device, but also suppresses electron trap formation in DBTTC.

### 6.5 Concluding Remarks

Charge generation in HBC, HBC/ $C_{60}$ , DBTTC, and DBTTC/ $C_{60}$  films is noted to be spatially uniform. This spatial uniformity allows us to draw conclusions about photoinduced changes in the vertical distribution of charges in these films. Multiexponential photovoltage decay kinetics were observed and we interpreted these kinetics in terms of charge trapping and slow recombination processes in these materials. By varying thickness, values for planar exciplex density were determined. Slow trapping was observed in ITO/DBTTC/ $C_{60}$ , and does not appear to

be homogeneously distributed throughout the DBTTC layer. Experiments show that electron trapping occurs in DBTTC when there was no contact with the electron accepting material, C<sub>60</sub>. We conclude that there is facile electron trap formation in DBTTC without C<sub>60</sub>. Even under low-light conditions, samples of ITO/DBTTC show marked decreased shifts in contact potential under illumination. When the C<sub>60</sub> layer is present, DBTTC devices perform better than HBC devices, despite less facile electron trap formation in HBC. We conclude that when evaluating materials for solar cell operation, the trap forming ability of the bulk is not an overriding concern for thin samples.

## CHARGE GENERATION IN TANDEM NANOCRYSTAL QUANTUM DOT SOLAR CELLS

### 7.1 Introduction

Presented in this chapter are studies of exciton dissociation in strongly coupled nanocrystal (NC) films and the role of metallic interlayers in NC tandem solar cells. In combination with transient photoluminescence (tPL) and grazing incidence small-angle X-ray scattering (GISAXS), time-resolved electric force microscopy (tr-EFM) was used to mechanically detect the presence of free charge due to inter-NC coupling and photogenerated exciton dissociation in close packed lead salt NC films. In the first ever reported tandem solar cells made from nanocrystal quantum dots (NQDs), Kelvin Probe Force Microscopy (KPFM) was utilized to observe how metallic interlayers affect device performance. This work was done in collaboration with the Hanrath and Wise groups at Cornell. Electric force microscopy measurements were the sole product of the Marohn group. Synthesis, as well as GISAXS, tPL, FT-IR measurements were performed by others. The work on photogenerated exciton dissociation was published in Nano Letters in 2010 [188], while the work on tandem solar cells is due to be published in Advanced Materials in 2011. The bulk of these papers have been reproduced here. The Methods and Discussion sections have been expanded.

Recent advances in synthesis and characterization of individual semiconductor nanocrystals have greatly improved understanding of their size-, shape-, and composition-dependent properties. The performance of most of these proposed technologies depends not only on the properties of the individual NCs but equally on the properties arising from interactions between the NCs in the assembly where NCs can be regarded as “artificial atoms”, which assemble to form “artificial solids” [305].

Colloidal semiconductor nanocrystal quantum dots (NQDs) have garnered immense interest as materials for next-generation photovoltaics[306–308]. The high absorption cross section and size-tunable energy gaps of NQDs enable efficient capture of solar emission while solution-based processing of NQD films is advantageous for the fabrication of low-cost thin film structures. The fundamental understanding and performance of prototype colloidal NQD-photovoltaics has advanced remarkably in recent years and record conversion efficiencies now exceed 5%, compared to 8% in leading organic solar cells [8–11, 13, 14]. NQDs also offer exciting prospects for the realization of third-generation photovoltaics with conversion efficiencies beyond the Shockley-Queisser limit[67, 306]. Recent reports of hot carrier [68] and multiple carrier [69] extraction from photoexcited NQDs highlight the potential of NQDs in high-performance solar cells.

In contrast to the rapidly growing knowledge of the properties of individual NCs, the understanding of the coupling between NCs is far less developed. NC solar cells provide an illustrative example of this knowledge gap. The surge of interest in NC photovoltaics has led to many encouraging results with size-tunable voltages and remarkably high current densities. However, the complex subprocesses of exciton dissociation and free carrier transport at the level of an individual NC and macroscopic charge transfer through the NC film to the external electrodes are still not fully understood. While analogies to charge separation at bulk semiconductor interfaces [8–11] have provided important initial insights, these models do not capture the physics governing charge transfer across NC nanostructured interfaces.

To understand exciton dissociation in an NC assembly at the microscopic level warrants consideration of the inter-NC electronic coupling and exciton binding energies, which govern exciton energy transfer,[309, 310] exciton dissociation, exciton formation, and charge transport [46] in the NC assembly. Exciton binding energy can be tuned by changing NC size but is largely an intrinsic property of the NC itself [311, 312] whereas inter-NC coupling energy can be tuned by altering the inter-NC separation distance. To tune the inter-NC binding energy, variable length bi-linker dithiol ligands such as 1,2-ethanedithiol (EDT), 1,4-benzenedithiol (BDT), 4,4'-

dibenzenedithiol (DBDT) and 4,4'-tribenzenedithiol (TBDT) were used in this study.

In addition to understanding charge generation in a thin film NC assembly, this work covers NC in a complex photovoltaic architecture. In addition to hot carrier and multiple carrier extraction, tandem solar cells offer an additional method of breaking the Shockley-Queisser limit. Tandem solar cells are comprised of distinct absorber layers with cascaded energy gaps, a schematic of which is shown in Figure 7.1. In the tandem solar cell described, absorption in the large bandgap NC material produces holes, while the narrow bandgap material produces electrons. Electrons from large bandgap NC layer and holes from narrow bandgap NC layer recombine at a metallic interlayer. Despite the ability to absorb over a larger portion of the solar spectrum in tandem solar cells, many daunting constraints, in particular regarding the charge extraction dynamics, need to be resolved before these discoveries can be translated to prototype photovoltaic devices.

## 7.2 Methods

*PbS Nanocrystal Synthesis* — The procedure for 2.7 nm PbS NCs was as follows. PbO (0.66g) and oleic acid (1.9mL) were dissolved in 28 ml of 1-octadecene (ODE). The solution was then degassed and heated to 150 °C for 1 hour under flowing nitrogen to form a lead oleate precursor solution. In a glovebox, 380  $\mu$ L of bis(trimethylsilyl)sulfide (TMS) was dissolved in 18 mL of ODE and stirred thoroughly. The lead oleate precursor solution was cooled to 90 oC prior to TMS solution injection. 15 mL of the TMS solution was rapidly injected into the vigorously stirred lead oleate solution. PbS NCs formed immediately after injection and they were collected after 1 minute of reaction at 90 °C. Following the synthesis, the NCs were washed several times by sequential precipitation with ethanol and redispersion in anhydrous hexane.

*Close packed NC Assembly Preparation* — The samples were prepared inside a glovebox. As-synthesized NCs were dissolved in hexane to make a 10 mg/mL solution. 100  $\mu$ L of the

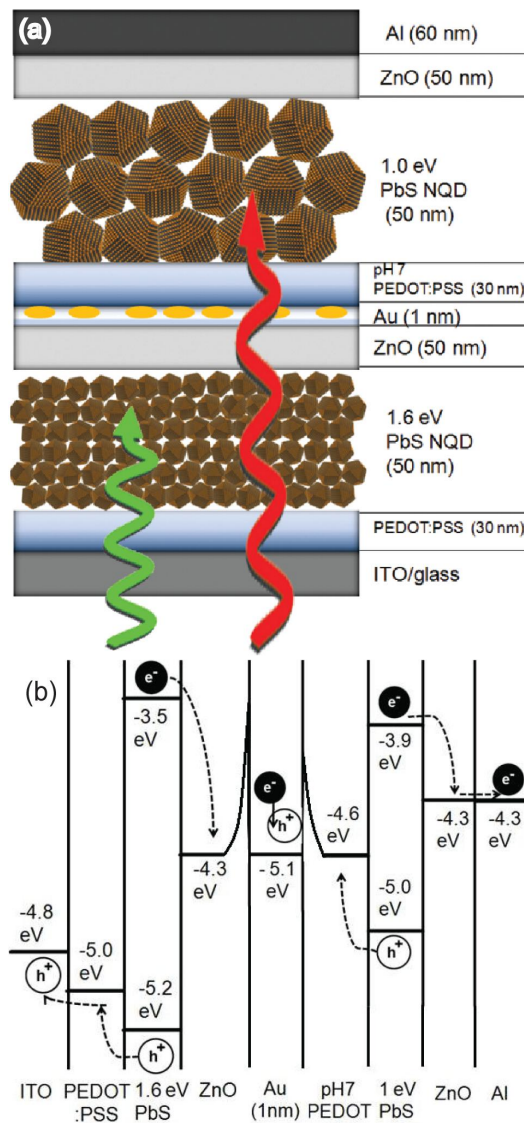


Figure 7.1: Tandem Solar Cell Schematic

(a) Schematic of the proposed tandem cell with optimal combination of PbS NQD bandgaps.  
 (b) Energy level diagram of the tandem device stack. The PbS NQD layers in the subcells are electrically connected by ZnO/Au (1 nm)/PEDOT:PSS interlayer where efficient recombination occurs.

NC solution was drop-cast on a cleaned 25 mm by 25 mm by 1 mm glass slide. The glass slide with deposited NC film was then put on a spin-coater. For EDT ligand treatment, 300  $\mu\text{L}$  of 0.1 M EDT in acetonitrile solution was dispensed on top of the NC film, and after a delay of 1 minute, was spun at 1000 rpm for 1 minute. The treated film was rinsed with pure acetonitrile and chlorobenzene. Cross-linking of NCs by EDT prevents the NC from dissolving into chlorobenzene. For BDT, DBDT and TBDT treatment, 0.01M of nBDT in a toluene solution was dispensed on top of the NC film. After 1 minute, the nBDT solution was spun away at 1000 rpm for 1 minute. The treated films were rinsed with pure toluene. Crosslinking of NCs by nBDT prevents the NC from dissolving into toluene. The prepared PbS-nBDT and PbS-EDT films were then sealed by putting another cleaned 25 mm by 25 mm by 1 mm glass slide on top and sealing the sides with epoxy. Encapsulated samples were stable against oxidation for several months.

*FT-IR and GISAXS Measurements* — A Bruker Optics - Vertex80v FT-IR spectrometer was used for FTIR characterization of PbS-nBDT samples. GISAXS measurements were performed on beam line D1 of the Cornell High Energy Synchrotron Source (CHESS) using monochromatic radiation of wavelength  $\lambda = 1.2373 \text{ \AA}$  with a bandwidth  $\Delta\lambda/\lambda$  of 1.5%. The X-ray beam was produced by a hardbent dipole magnet of the Cornell storage ring and monochromatized with Mo-B4C synthetic multilayers with a period of 30  $\text{\AA}$ . The D1 area detector (MedOptics) is a fiber-coupled CCD camera with a pixel size of 46.9  $\text{\AA}$  by 46.9  $\text{\AA}$  and a total of 1024 by 1024 pixels with a 14-bit dynamical range per pixel. Typical read-out time per image was below 5 s. The images were dark-current corrected, distortion-corrected, and flat-field corrected by the acquisition software. The sample-to-detector distance was 660.2 mm, as determined using a silver behenate powder standard. The incident angle of the X-ray beam was at 0.25 degree. Typical exposure times ranged from 0.1 to 1.0 s. Scattering images were calibrated and integrated using the Fit2D software package.

*Transient Photoluminescence Measurements* — For tPL measurements, the samples were

excited at a repetition rate of 1 kHz by frequency doubled (400 nm) femtosecond pulses of a Ti:sapphire laser system with a regenerative amplifier. The pump fluence was kept low so that the average number of exciton per NC was 0.1. Fluorescence was monitored with a Si avalanche photodiode single photon counting module (PerkinElmer, SPCM-AQRH-44-FC). For PbS-OA samples, the output was fed into a multichannel scalar (Stanford Research Systems, SR430), which provides an instrument response of a 5.2 nanoseconds, and adequate dynamic range to monitor decay times in the microsecond range. For PbS-nBDT samples with lifetimes in the sub-microsecond range, tPL measurements were performed in the time-correlated single photon counting (TCSPC) mode with a TCSPC board (PicoQuant, TimeHarp 200) and a digital delay generator (Stanford Research Systems, DG645) under right-angle sample geometry. The tPL curves were analyzed by means of iterative re-convolution using the FluoFit software package (version.4.4).

*Tandem Cell Fabrication* — Pre-patterned ITO-coated glass substrates were cleaned and treated with UV-ozone for 10 minutes. PEDOT:PSS (Product No. AI4083 , H.C. Starck) was filtered through 0.45  $\mu\text{m}$  PVDF syringe filter and spin-cast onto the cleaned ITO substrate at 6000 rpm for 1 minute and baked on a hot plate at 170 oC for 4 minutes. PbS NQDs for the front cell were spin-cast from a 30 mg/mL chlorobenzene solution at 1000 rpm for 30 seconds. The NQD film was then treated with a 0.1M solution of (EDT) in acetonitrile and rinsed with pure acetonitrile and chlorobenzene by dispensing the solution on top of film and spin-casting at 1000 rpm for 30 seconds. This protocol constituted one cycle of the PbS NQD layer deposition. Typically, three cycles of depositions were performed. After deposition of the PbS NQD film, 20 mg/mL of a ZnO nanoparticle solution was spin-cast at 1000 rpm for 1 minute. Three such depositions of ZnO nanoparticles were carried out to ensure complete coverage. Following ZnO deposition, 10 Å of Au, Ag or Al was thermally evaporated in ultrahigh vacuum (  $10^{-6}$  Torr) at a rate of 0.1 Å/second. The pH 7 PEDOT:PSS layer for the interlayer was spin-cast on top to complete the interlayer. Subsequently, a PbS NQDs layer and a ZnO layer were deposited with identical methods mentioned above. For the top electrode, 600 Å of aluminum was deposited via

thermal evaporation in ultrahigh vacuum ( $10^{-6}$  Torr). The entire device fabrication sequence, except for the metal evaporation step, was performed in ambient air. The completed devices were tested after 3 hours of air exposure.

*Electric Force Microscopy on NQD Thin Films* — Electric force microscope measurements were carried out in vacuum at room temperature. A Pt-Au coated cantilever (SPMtips model NSC18-Pt/Au) was employed with a spring constant of  $k = 1$  N/m, resonance frequency of  $f_0 = 80$  kHz, and a quality factor of  $Q = 8000$  (at a pressure of  $10^{-6}$  mbar). Cantilever displacement was detected with a fiber-optic interferometer operating at 1310 nm. Measurements were carried out using a cantilever peak-to-peak oscillation amplitude of 325 nm and a tip-sample separation of 60 nm. Simultaneous imaging of local electrostatic potential and capacitance was accomplished as follows. The tip voltage was modulated at frequency  $f_m = 200$  Hz, deviations in cantilever frequency were detected using a commercial frequency demodulator (RHK PLLpro 1.0; bandwidth = 400 Hz), and lock-in detection was used to measure the Fourier components of the cantilever frequency deviation. The zero-to-peak amplitude of the voltage modulation  $V_m$  was between 1 and 3 V. A dc voltage was also applied to the tip and it was adjusted, via feedback, to zero the Fourier component of the first harmonic. These measurements utilized a lock-in time constant of 30 ms and an analog PID controller with (typical) coefficients  $P = 1$ ,  $I = 2$  Hz, and  $D = 3$  ms. The optimal PID coefficients were sensitive to the absolute capacitance, so the coefficients were adjusted for each sample to ensure a critically-damped response of the photo-potential; the measured capacitance was insensitive to the exact PID coefficients. Sample illumination was provided by an InGaN white LED (LiteOn model LTW-1KHC5). The LED was located approximately 1 cm away from the cantilever tip and inclined at a forty five degree angle with respect to the sample surface. For further details, see the methods section of this thesis.

*Kelvin Probe Force Microscopy on Tandem Solar Cells* — KPFM measurements used similar equipment as described for the electric force microscopy experiments on NQD thin films. The tip-

sample separation in this experiment was 30 nm. For imaging of local electrostatic potential, tip voltage was modulated with a 100 mV zero-to-peak sine wave applied at the cantilever resonance frequency. Cantilever motion was demodulated using a commercial FPGA (RHK PLLpro 1.0; bandwidth = 400 Hz). During imaging, a DC voltage to cantilever tip was adjusted via feedback to zero the cantilever amplitude zero at the cantilever resonance frequency,  $f_c = 80$  kHz, using an analog PID controller with (typical) coefficients (P=-.01, I= 2 Hz, D=.5 ms).

## 7.3 Results

### 7.3.1 Optical Measurements on Nanocrystal Lead Salt Quantum Dot Thin Films

As one of the most strongly quantum confined systems[313], lead salt NCs naturally provide an ideal experimental testbed for the study of the relationship between inter-NC coupling and exciton separation mechanism. Inter-NC coupling energy between close packed lead salt NCs has previously been measured to be in the range of tens of milli-electronVolts[314, 315], which is comparable to the exciton binding energy of around  $\sim 100$  meV[311]. The high coupling energy and low exciton binding energy in lead salt NCs, compared to other materials, originate from their strong quantum confinement that allows significant leakage of the electronic wave function out of the NC. In contrast, in other NC systems, e.g., cadmium salts, the coupling energy is much smaller than the exciton binding energy and consequently resonant energy transfer acts as the dominant pathway for photogenerated excitons without involving exciton dissociation[310]. Whether the fate of photogenerated excitons is charge dissociation or energy transfer has major implications on optoelectronic device performance. These findings explain why lead salt Schottky devices give 2 orders of magnitude higher short-circuit currents than similarly prepared cadmium salt Schottky devices,[8, 316] while cadmium salt NCs show high performance in LED devices[42].

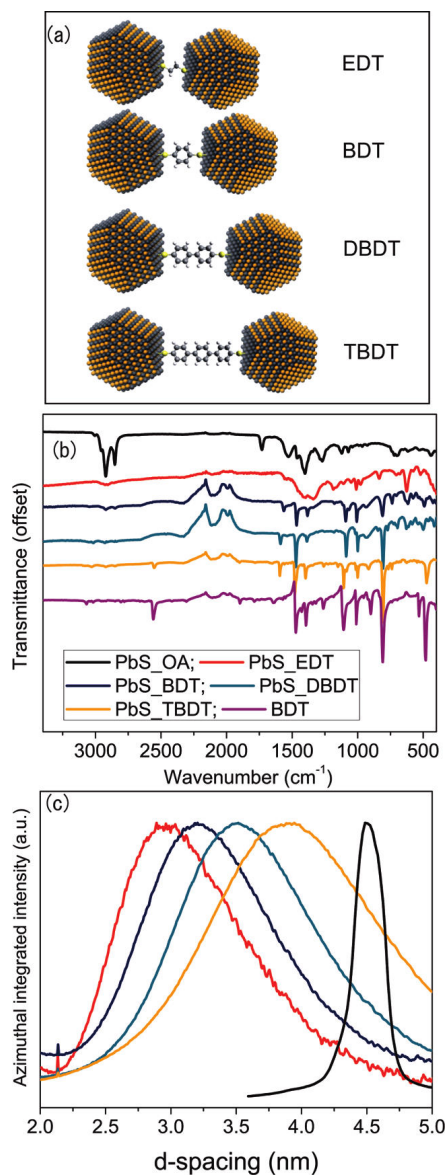


Figure 7.2: FT-IR and GISAXS measurements.

(a) Schematic of NCs linked with various bi-linker molecules. (b) FTIR spectroscopy of the samples showing reduction of the C-H stretch peak near  $2900\text{ cm}^{-1}$  and an aromatic CdC stretch peak near  $1500\text{ cm}^{-1}$  after treatment with the bi-linker molecules. (c) GISAXS shows a trend of longer inter-NC distance with NC assemblies treated with longer bi-linker molecule (same color legend as (b)).

Synthesis and optical experiments were conducted by members of the Hanrath and Wise groups.

PbS NCs were synthesized via the hot injection method[317] were deposited on cleaned glass substrates via spin-coating or drop-casting to form close-packed NC assemblies. Inter-NC separation distance was adjusted using variable length bi-linker dithiol ligands such as 1,2-ethanedithiol (EDT), (BDT), (DBDT), and (TBDT) (Figure 7.2(a). NC assemblies treated with the bi-linker molecules as PbS-nBDT where n identifies the number of benzene rings (n = 0 for EDT, n = 1 for BDT, n = 2 for DBDT, n = 3 for TBDT). Bi-linker molecules were comprised of phenyl rings since they possess only a torsional degree of freedom, to first approximation[318]; their rigidity allows to precise control over the inter-NC separation distance. Moreover, the bi-linker nBDT molecules used in this study have HOMO-LUMO levels that are energetically unfavorable for direct NC-to-ligand charge transfer[319].

FTIR spectroscopy was used to monitor NC surface chemistry before and after the ligand exchange. The data in Figure 7.2(b) illustrate the extent of replacement of oleic acid ligands with dithiol ligands. The most prominent feature is the reduction of aliphatic C-H stretching peaks near  $2900\text{ cm}^{-1}$  and emergence of aromatic C=C stretching peaks near  $1500\text{ cm}^{-1}$ . These results show that bi-linker molecules with thiol functional groups readily replace the long chain alkyl ligands with carboxylic acid group. The absence of an S-H peak at  $\sim 2600\text{ cm}^{-1}$  in dithiol-treated samples and the stiffness of the linker molecule supports the hypothesis that the molecule is bound to the surface of two neighboring NCs. An FTIR spectrum taken from pure BDT is included in Figure 7.2(b) for comparison.

The structure and inter-NC distance of the NC assemblies were characterized with synchrotron-based GISAXS[320]. Azimuthally integrated GISAXS intensity profiles of the NC assemblies, shown in Figure 7.2(c) show a direct correlation between inter-NC separation and the length of the bi-linker molecule. The PbS-OA film shows a narrow scattering feature corresponding to a well-ordered film with an average interparticle spacing of 4.5 nm. By contrast, the EDT treated

PbS NC films have an average spacing of 2.95 nm, which, considering the 2.7 nm NC diameter, translates to  $\sim 0.25$  nm separation between the surfaces of proximate NCs. Each additional benzene ring contributes a  $\sim 0.3$  nm increase in average inter-NC distance, which is in reasonable agreement with the expected trend considering that the length of benzene ring is  $\sim 0.4$  nm. The trend observed in GISAXS data validates the approach to tuning the inter-NC separation and provides direct access to the study of distance-coupling relationships. Despite the broad distributions of inter-NC spacing present in the amorphous NC assembly, there is a clear trend in the peaks of the distributions which is correlated with ensemble average measurements such as exciton lifetime measurements, as discussed below.

Optical characterization of the NC assemblies is summarized in Figure 7.3. Absorbance spectra of the samples are shown in the Figure 7.3(a). Compared to the PbS-OA film sample, PbS-nBDT samples exhibit pronounced red-shift and broadened absorption peak. The red-shift is a strong indication of the presence of inter-NC electronic coupling from the reduction of the quantum confinement energy[310, 314]. A trend of larger red-shift from samples with smaller inter-NC spacing is apparent: the biggest red-shift of  $\sim 170$  meV is seen in the PbS-EDT sample while the smallest red-shift of  $\sim 120$  meV is seen in the PbS-TBDT sample. The magnitudes of the red-shift shown in these samples are much greater than the  $\sim 20$  meV red-shift reported earlier in assemblies of larger diameter NCs[8, 321] (inset of Figure 7.3(a)). The greater red-shift in smaller diameter NCs is attributed to the greater electronic wave function overlap between smaller NCs[310]. The red-shift of 120-170 meV seen in PbS-nBDT films is a good indication of high inter-NC coupling energy.

Photoluminescence (PL) measurements, performed by the Hanrath and Wise groups, can provide basic insights into the relaxation of photogenerated excitons. The PL spectra of PbS-nBDT films show red-shifts compared to the spectrum of the PbS-OA film. The slight variation in red-shift across the PbS-nBDT samples is attributed to different degree of Stokes shifts with different surface ligands. The PL intensity of all bi-linker-treated films was quenched by up to

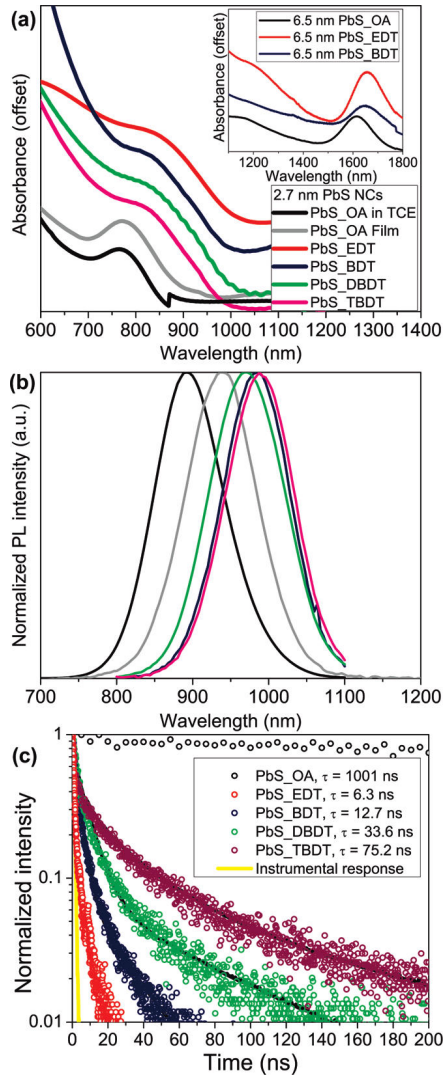


Figure 7.3: Transient photoluminescence measurements.

(a) Absorbance spectra of the NC assemblies. The inset shows a smaller degree ( $\sim 20$  meV) of red-shift observed in bigger (6.5 nm) NCs. (b) Time-integrated photoluminescence spectra (same color legend as (a)). The PL spectra are normalized to account for the quenching and variations in film thickness. (c) Time-resolved photoluminescence data from the NC assemblies show a 2 orders of magnitude quenching of exciton lifetime in NC assemblies treated with bi-linker molecules compared to the untreated NC assembly. Each sample was probed at its peak photoluminescence emission wavelength.

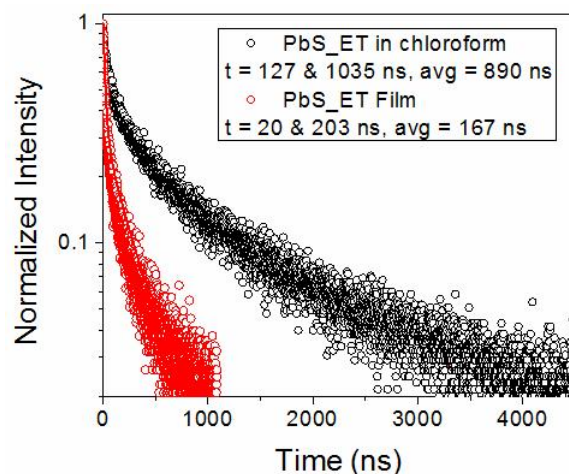


Figure 7.4: Transient Photoluminescence in solution vs film.

The long exciton lifetime of PbS-ethanethiol in colloidal solution form indicates that surface ligands with thiol functional groups do not quench excitons significantly. The drastic lifetime quenching observed in close-packed assembly form, still with same ligand, indicates that the proximity of NCs is the cause of the lifetime quenching.

5 orders of magnitude compared to PbS-OA films. The pronounced PL quenching in NC films treated with bi-linkers can be attributed to several nonradiative mechanisms including charge transfer to the ligands, charge transfer to neighboring NCs, or charge trapping by NC surface states.

To better understand the PL quenching mechanism, transient photoluminescence spectroscopy (tPL) was implemented. Transient PL data of PbS-OA films (Figure 7.3(c)) show a long exciton lifetime of  $\sim 1\mu\text{s}$  with a single exponential decay behavior. In contrast, PbS-nBDT samples show exciton lifetimes on the order of few to tens of nanoseconds, two orders of magnitude less than the PbS-OA film. Because the decay behavior of PbS-nBDT is not well fit by a single exponential, the data was fit to a biexponential decay. The reduced exciton lifetime observed in PbS-nBDT films suggests that the de-excitation dynamics for PbS-nBDT films are fundamentally different from that of the PbS-OA film. This trend can be explained by several mechanisms such as inter-NC exciton dissociation, resonant energy transfer, [309, 310] charge transfer to surface ligands[322], and surface charge trapping [323].

To distinguish between inter-NC energy\charge transfer mechanisms and charge transfer to the surface ligand or surface charge trapping, PbS NCs were treated with ethanethiol, a short ligand molecule, in (1) colloidal solution form and in (2) close-packed film form and compared their exciton lifetimes. The results from this experiment are shown in Figure 7.4. In these experiments, both samples have the same surface thiol functional groups. If charge transfer to the ligand[322] or surface trapping[323] were to occur, the exciton lifetime would be quenched in both colloidal solution and close packed film forms. Instead, the experiment reveals a long lifetime of 890 ns in colloidal PbS-ethanethiol solution in toluene while identical particles in the close-packed film exhibit a shorter lifetime of 167 ns. It can therefore be concluded that the exciton lifetime quenching does not originate from charge transfer to ligand or surface trapping but rather from proximity of NCs to each other. It is important to note that the bi-linker nBDT molecules used in this study have HOMO-LUMO levels that are unsuitable to accept charges from PbS NCs.[319] These findings rule out charge transfer to the surface ligand or surface charge trapping as possible mechanisms of exciton lifetime quenching.

### **7.3.2 Electric Force Microscopy Measurements on Lead Salt Nanocrystal Thin Films**

The summary of the optical measurements on thin films of PbS nanocrystals concluded that transient photoluminescent signal could be due to several mechanisms such as inter-NC exciton dissociation, resonant energy transfer, [309, 310] charge transfer to surface ligands[322], and surface charge trapping [323]. The results of transient photoluminescence experiments comparing transient decay in quantum dot thin films versus colloidal solution show that signal is neither due to charge transfer to surface ligands nor due to surface charge trapping.

To better understand exciton quenching, optical measurements were augmented with time-resolved electrostatic force microscopy to observe light-induced free carrier generation in PbS-

nBDT samples at millisecond time scales. EFM enables direct examination of local capacitance, proportional to free charge density, and local potential.[324, 325] Unlike photoluminescent measurements, local capacitance measured by EFM can only be affected by motion of charges on the several nanometer scale, much larger than the diameter of a single NQD (Figure 7.5). For a given tip voltage  $V_T$ , such as those seen by the cantilever during modulation, a charge ( $Q = CV$ ) is installed in the capacitor (C) that is formed between the tip and the surface. As the cantilever oscillates much faster than the modulation voltage, this voltage can be assumed to be constant over the course of a cantilever cycle. Throughout the oscillation, the cantilever distance to the surface changes, which alters the tip-sample capacitance. Over many cycles, the cantilever is able to measure the second derivative of capacitance with respect to tip height (which is henceforth referred to as capacitance). Photoinduced carriers that are able to charge and discharge the tip-sample capacitor as the cantilever moves are recorded in this measurement.

Measurements of capacitance differ from the measurements of jitter in Chapter 5. While measurements of jitter are sensitive to charges which trap-detrap on the order of hundreds of milliseconds, measurements of capacitance detect charges which move in and out from under a cantilever on the order of tens of microseconds. In addition to the detection of capacitance, shifts in contact potential due to trapped charges[97] provide direct proof of whether the exciton lifetime quenching is due to surface traps or exciton dissociation.

PbS-OA and PbS-nBDT films were prepared on top of interdigitated gold electrodes on glass substrate and loaded into a high vacuum electric force microscope. All measurements were taken at a single location near the midpoint of the channel between electrodes with no source-drain voltage applied during the measurement. Figure 7.6(a) shows that there is no change in the second derivative of capacitance with respect to tip height of the PbS-OA film upon illumination with white light. This result, coupled with the optical characterization of PbS-OA film that showed bright PL with long lifetime, indicates that quenched excitons in PbS-OA film do not lead to free carrier generation. In contrast, Figure 7.6(b) shows that the PbS-EDT film shows

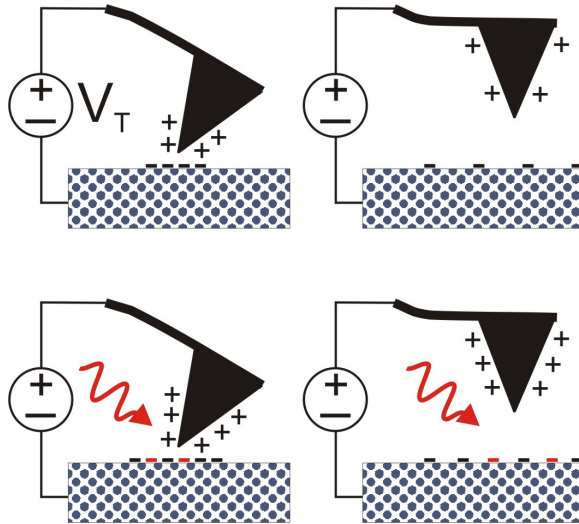


Figure 7.5: EFM measurement of free charge.

Schematic representation of an oscillating cantilever with an applied tip voltage. As the cantilever oscillates, the tip-sample capacitance varies. If more charges are able to charge and discharge the tip-sample capacitor as the cantilever oscillates, this will result in a larger measurement of the second derivative of capacitance with respect to tip height ( $\mu F/m^2$ ).

an increase in capacitance under light illumination with a rise time faster than the instrumental response time of 0.4 ms, indicating increased free carrier density upon light illumination. One possible criticism is that the electric field from the applied tip voltage is responsible for exciton splitting. To disprove this, cantilever frequency was measured at various tip modulation voltages. At each modulation voltage, the capacitance was inferred by taking the ratio of the Fourier component of the cantilever frequency at twice the modulation frequency divided by the square of the tip voltage (see methods section of this thesis). Nearly identical capacitances were measured at tip modulation voltages of 1, 2, and 3 V (Figure 7.6(c)), proving that the EFM measurement was not perturbing charge generation. If exciton splitting was occurring under the influence of the cantilever tip voltage, larger voltages would have resulted in larger measured capacitances.

A similar increase in tip-sample capacitance under illumination was observed in other PbS-nBDT samples (Figure 7.7). The local potential did not show any sign of trapped charges in PbS-nBDT films after the sample returned to darkness.

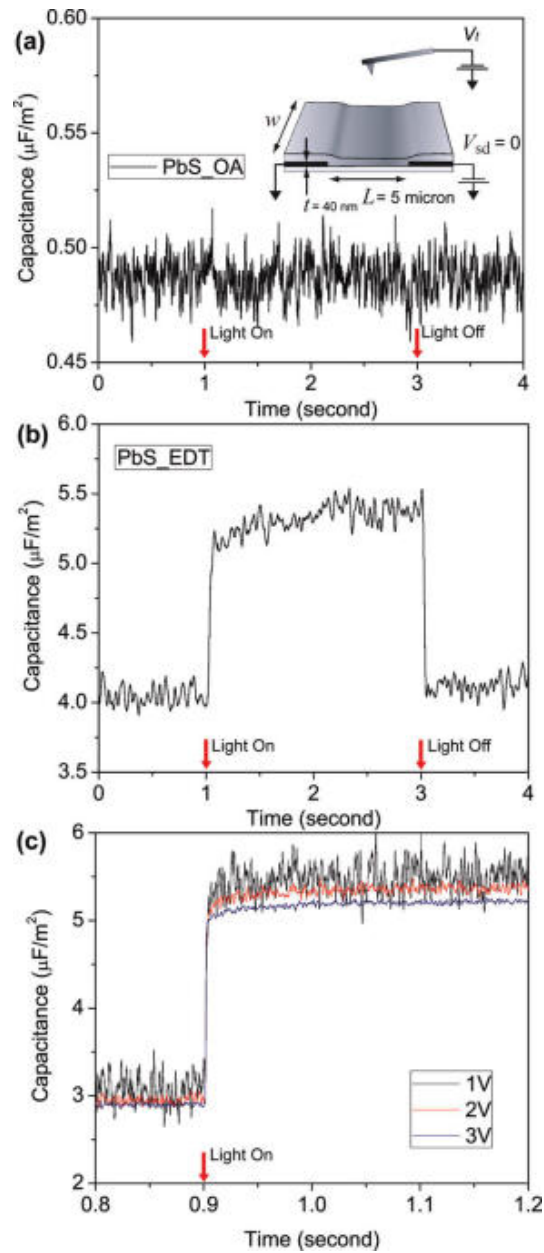


Figure 7.6: EFM measurements on PbS-nBDT.

(a) Inset shows a schematic of the electric force microscope measurement. The PbS-OA film does not show change in capacitance upon white-light illumination, indicating that the photogenerated excitons in this film do not result in free charge generation. (b) In contrast, the PbS-EDT film shows rapid increase in capacitance upon light illumination indicating a photoinduced increase in free carrier density. (c) The independence of the capacitance measurements from the modulation voltage shows that the electric field from cantilever tip does not cause exciton dissociation.

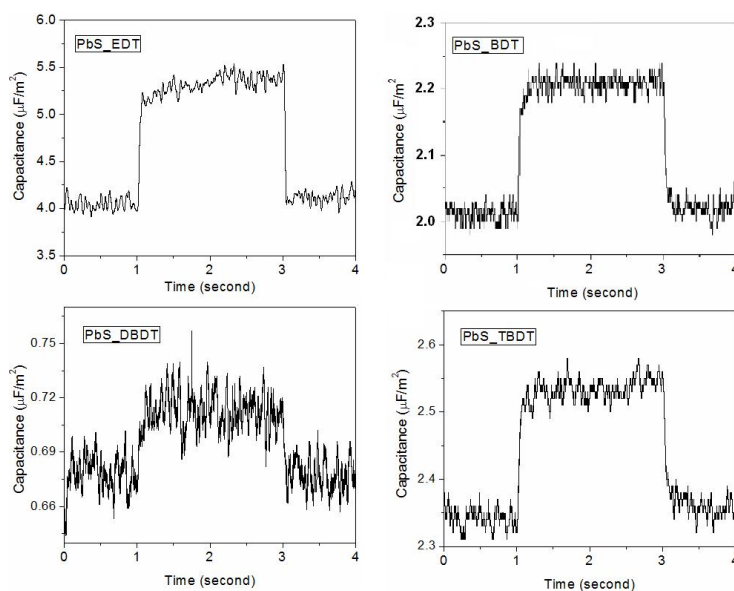


Figure 7.7: Capacitance signal for PbS-nBDT thin films.

Capacitance signals in various PbS-nBDT thin films under illumination. Illumination in each plot is indicated by a rise in capacitance.

### 7.3.3 NC Quantum Dot Tandem Solar Cells

Results from optical and electric force microscopy experiments on NC Lead salt thin films have shown that these materials are capable of generating free charge in the absence of an electrical or chemical potential gradient. The prospect of solution-processed NQD-based multijunction solar cells introduces exciting opportunities for realizing high conversion efficiency in low-cost device structures. In this section we discuss on tandem solar cells produced from colloidal suspensions of size-tuned PbS-EDT NQDs.

Related studies of organic multijunction cells have illustrated the importance of understanding and designing the optical absorption profile throughout the device stack and the charge transport characteristics of the interlayer[326–329]. The interlayer connecting the front and back cell must meet several stringent optical and electrical constraints: first, it should be optically transparent to pass light to the underlying cell and second, it must provide appropriate energy level alignment to accept electrons and holes from the subcells and efficiently recombine them without degrading

the overall photovoltage of the cell. The interlayers in the best performing organic tandem cells reported so far are based on junctions between an n-type metal oxide layer and a p-type poly(3,4- ethylenedioxythiophene):poly(styrenesulfonate) (PEDOT:PSS) layer[328]. This study demonstrates that analogous interlayer structures can be applied to connect NQD-based subcells with specific energy gaps.

The device performance of the NQD tandem cell (Figure 7.8) shows that the  $V_{oc}$  of the tandem cell is the sum of the  $V_{oc}$  of its subcells, which indicates that the interlayer efficiently recombines charges without significant voltage loss. Because the two-terminal tandem cell structure does not allow separate testing of its subcells, corresponding single junction devices were fabricated as controls with NQDs from the same synthesis batch prepared under identical film deposition conditions. Optimized tandem cells and the corresponding control devices of each subcell were fabricated from 1.6 eV (diameter = 3 nm) and 1.0 eV (diameter = 4.8 nm) PbS NQD films; these size-tuned energy gaps correspond to the optimal theoretical value for a two terminal device[330]. Best cell performance had an open-circuit voltage of  $V_{oc} = 0.91 \pm 0.02$  V, a shortcircuit current density  $J_{sc} = 3.7 \pm 0.1$  mA cm<sup>-2</sup>, fill factor  $FF = 0.37 \pm 0.01$ , and a power conversion efficiency  $PCE = 1.27 \pm 0.05\%$ . The control front cell showed  $V_{oc} = 0.58 \pm 0.02$  V,  $J_{sc} = 7.0 \pm 0.7$  mA cm<sup>-2</sup>, a  $FF = 0.44 \pm 0.01$ , and  $PCE = 1.8 \pm 0.2\%$ . The control back cell showed  $V_{oc} = 0.32 \pm 0.02$  V,  $J_{sc} = 9.4 \pm 0.4$  mA cm<sup>-2</sup>,  $FF = 0.42 \pm 0.02$ , and  $PCE = 1.26 \pm 0.07\%$ .

Figure 7.8(b) shows the external quantum efficiency (EQE) of each subcell within the tandem cell device alongside the absorbance spectra of the corresponding NQD films in the device stacks. Absorbance measurements of the device stacks were performed using an integrating sphere to account for light scattering. External quantum efficiency (EQE) measurements were performed with two excitation light sources, an unmodulated optical bias light beam was used to excite only one of the subcells while a modulated monochromatic probe light was used to measure the EQE of the other subcell.[328, 331] The EQE spectra closely follow the EQE spectra of the front and back cells, confirming that the photocurrents are generated from the size-tuned NQDs. It should

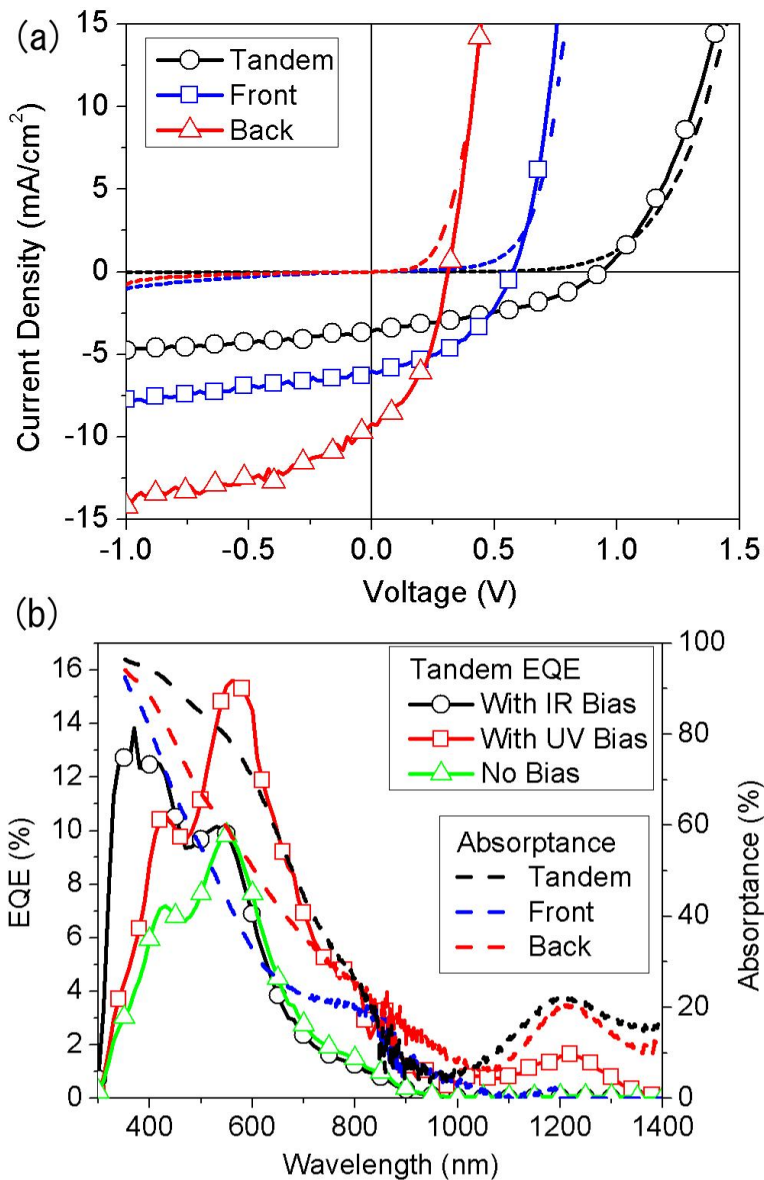


Figure 7.8: Device performance for PbS tandem solar cell.

(a) Current-voltage (JV) characteristic of the tandem cell and corresponding control single junction devices. The tandem cell exhibits a  $V_{oc}$  that is a sum of the open-circuit voltages of the subcells. (b) EQE and absorbance spectra of the devices. Carefully adjusted light bias is required to measure signals from the subcells.

be noted that the overall decrease in EQE for the whole cell is smaller than each of the back cells. This is due to reflection/absorption losses within the solar cell. In order to be efficient, tandem solar cells require high intensity illumination. The decrease in EQE at short wavelengths arises primarily from parasitic absorption in the indium tin oxide (ITO) and ZnO layers.

Efficient recombination in the interlayer is contingent upon proper energy level alignment and sufficient carrier densities. The energy level offset between ZnO and PEDOT can be mitigated by the incorporation of ultrathin metal films; this approach has been successfully demonstrated in organic tandem cells[332]. To create efficient interlayers for the NQD tandem cell shown in Figure 7.1, a thin (1 nm) Au layer was thermally evaporated onto the ZnO film, which was followed by spin-coating a pH neutral PEDOT:PSS layer. Scanning electron microscopy images (Figure 7.9) show that Au forms few-nanometer-sized metal islands instead of a continuous film. Without the Au layer, the current-voltage characteristics of the tandem devices (Figure 7.10(a)) exhibited an S-shaped kink that has previously been attributed to an interfacial barrier for charge transport[333]. Interestingly, the incorporation of either Ag or Al thin films into the interlayers failed to remedy the S-shaped kink in the current-voltage behavior. To delineate the effect of the surface work function and the carrier density, a series of control experiments were conducted.

Kelvin probe force microscopy (KPFM), performed by the Marohn group, was used to understand how the composition of the metal thin film influences the surface Fermi level of ZnO/M (M= Al, Ag, or Au) layers. A platinum coated atomic force microscopy (AFM) tip was used and its workfunction was taken to be 5.65 eV. KPFM results showed that the ZnO surface Fermi level was 4.62 eV and that Au, Ag, and Al raise the Fermi level to 5.11 eV, 5.03 eV, and 4.98 eV respectively (Figure 7.10(b)). The run-to-run variation in the KPFM measurements over different samples of ZnO, shown in Figure 7.11, introduced an experimental error of  $\pm 0.069$  V. The ZnO Fermi level value is consistent with the literature values[334] and the increase in the Fermi level due to Au consistent with the  $\sim 5.1$  to 5.4 eV workfunction of Au[335]. The rise of the surface workfunction of Ag to 5.0 eV has been observed previously and is attributed to oxidation in

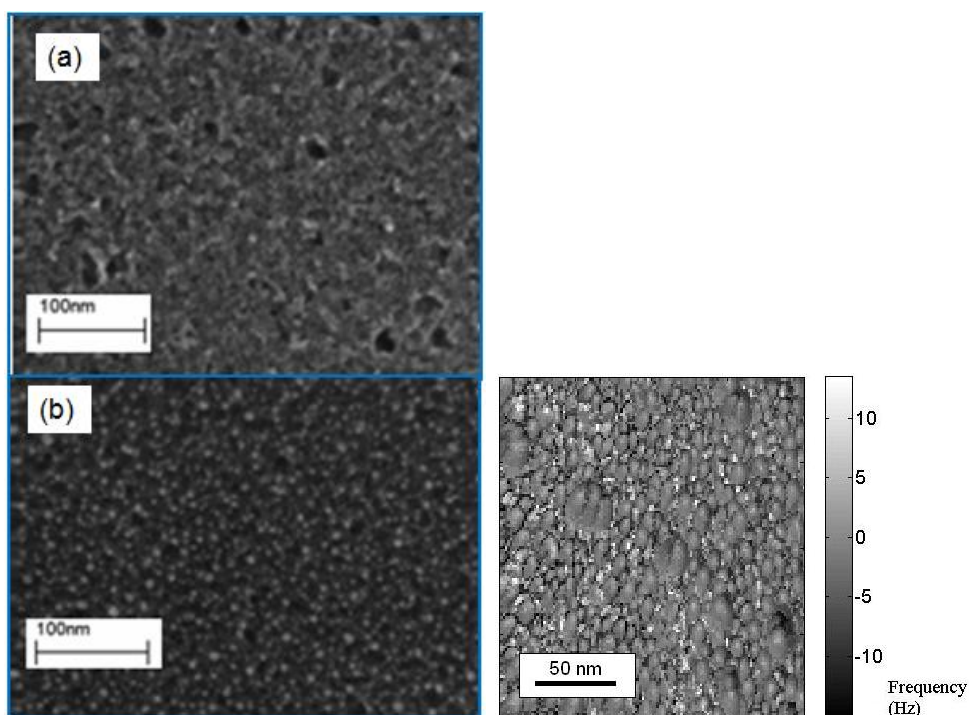


Figure 7.9: Scanning Electron Microscopy of metal interlayer.

Scanning electron microscopy image of the (top-left) ZnO layer surface and (bottom-left) ZnO layer surface with 1 nm of thermally deposited Au. The gold layer forms nanoscale islands instead of continuous layer. Also shown is an atomic force microscopy image in phase mode of ZnO surface with Ag metal layer (right).

air[336]. This feature is tentatively attributed the higher-than-expected workfunction of ZnO/Al to the oxidation of Al and its interaction with the ZnO surface. The lack of a statistically significant difference in the Fermi level of the ZnO/M surfaces suggests that the shift in workfunction due to metal composition alone cannot explain the observed trends in interlayer performance.

The transport characteristics of the interlayer stack were isolated by preparing a series of ITO/ZnO/M/PEDOT:PSS/Ag (M = Al, Ag, Au) control devices. This device configuration allowed insight in to how metal composition and photodoping of the underlying ZnO nanoparticle film influence electrical characteristics of the interlayer. Janssen and co-workers have recently shown that short UV light exposure effectively eliminates S-shaped kinks in organic tandem cell performance[326]; this effect was attributed to increased concentration of mobile electrons[337]. In this study, the combination of ultrathin Au films and UV photodoping yielded interlayers

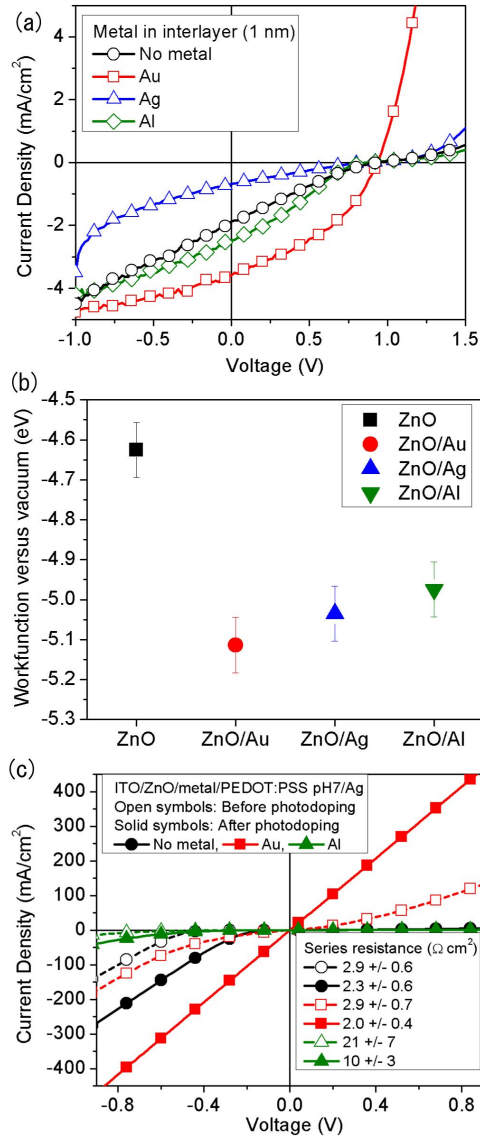


Figure 7.10: Device performance for PbS tandem solar cell.

(a) Effect of a thin (1 nm) metal layer in the interlayer on tandem device performance. The S-shaped kink that is attributed to interfacial barrier for charge transport disappears only when gold layer is inserted. (b) KPFM measurement of the surface workfunction of the bare ZnO layer and various metals on top. The presence of metal layers increases the surface workfunction. (c) Conductance measurements on the interlayer stacks show that inserting a Au layer causes an ohmic tunnel junction, while inserting a Al layer increases the series resistance by a factor of 3.

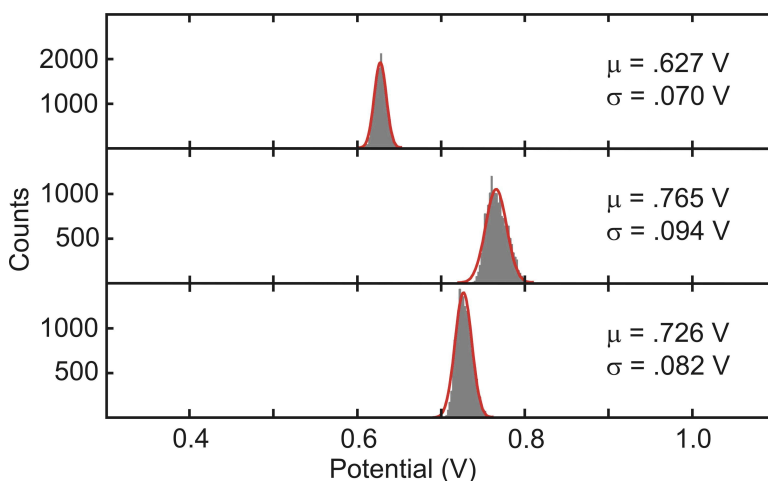


Figure 7.11: Run to run variation in KPFM.

Gaussian distribution of contact potential measurements using KPFM for three samples of ZnO. Sample error of  $\pm 0.069\text{V}$  was observed.

with Ohmic transport characteristics (Figure 7.10(c)). Interlayer control devices with ultrathin Ag or Al films on the other hand exhibit nonlinear transport characteristics even after 1 h of photodoping. Addition of an Al thin film to the interlayer increased the series resistance by a factor of 3 compared to no metal or an Au layer. This observation serves as another indication that the Al layer is likely partially oxidized and thus reduces the conductance of the interlayer stack. These results, combined with KPFM data, suggest that the metal layer serves to provide enough carriers for proper Fermi level tuning and band bending over a short spatial distance while maintaining conductance for successful interlayer operation.

## 7.4 Discussion

It was observed that lead salt nanocrystals generate free carriers upon absorption of light at the bandgap energy. Taking advantage of the bandgap tunability of quantum dots, tandem solar cells were fabricated with various-sized NQDs. These solar cells were able to use different sized quantum dots to absorb light across a larger spectrum. To optimize efficiency of NQD solar cells, it is first necessary to understand the physics of charge separation in PbS-nBDT quantum dots.

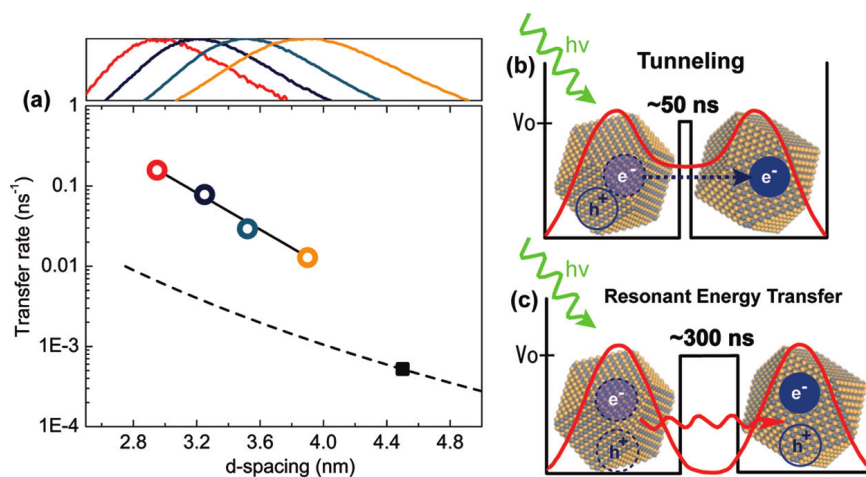


Figure 7.12: GISAXS on PbS-nBDT thin films.

(a) Plot of charge transfer rates (with PbS-EDT, PbS-BDT, PbS-DBDT, and PbS-TBDT corresponding to red, violet, teal, and yellow), calculated from exciton lifetimes (Figure 7.3b), versus inter-NC spacing measured with GISAXS (Figure 7.2(c)). Single exponential decay fit (black solid line) indicates that the charge transfer occurs via tunneling of charge through a potential barrier. Resonant energy transfer is shown in the PbS-OA sample (black rectangle) and the calculated energy transfer rates (dotted line) for corresponding inter-NC spacing using a Förster radius of 5 nm shows an order of magnitude lower rate than the charge transfer rates. This indicates that exciton dissociation via tunneling is the dominant pathway in the regime of short inter-NC distance and high coupling energy (b) whereas resonant energy transfer is dominant in low inter-NC coupling regime (c). All calculated transfer rates have error bars smaller than the symbols. Distributions in d spacing measured with GISAXS are shown on the top of (a).

#### 7.4.1 Charge Transfer Nanocrystal Lead Salt Quantum Dot Thin Films

Figure 7.12 provides a summary of the results from Figures 7.2 and 7.3. Transfer rates from tPL measurements are plotted against inter-NC d-spacing. For decreasing inter-NC spacing, transfer rates increase. To delineate between resonant energy transfer and exciton dissociation de-excitation pathways, the rise times of PL transients were measured. On the basis of the work by Clark et al.[309], the Förster radius was calculated to be  $\sim 5$  nm for PbS NCs used in this study. This translates to a resonant energy transfer lifetime in the PbS-nBDT assemblies on the order of tens to hundreds of nanoseconds. Rise times with such time scales can be clearly resolved with tPL measurements but were not observed in the PbS-nBDT samples. In contrast,

consistent with earlier reports,[309] tPL measurements on the PbS-OA film did exhibit a rise time characteristic of resonant energy transfer (Figure 7.12(a)). These results provide a strong indication that resonant energy transfer is not the dominant de-excitation pathway in PbS-nBDT films.

In light of the corroborating optical and electrical signatures of photogenerated exciton dissociation in PbS-nBDT, more analysis is needed to gain further insight on the precise mechanism underlying the exciton dissociation. Charge transfer time constants were calculated in each of the PbS-nBDT samples from the measured exciton lifetimes (Figure 7.3(c)) via the equation  $k_{et} = 1/\tau(\text{coupled}) - 1/\tau(\text{isolated})$  and plotted them versus the inter-NC distance,  $d$ , obtained from GISAXS measurements (Figure 7.2(c)). The resulting plot shows that the charge transfer rate as a function of inter-NC distance is well described by a single exponential decay function (Figure 7.12a). This behavior can be described with the Marcus theory[338]. In the case of symmetric reorganization energy and Gibbs free energy for the charge transfer reaction, this behavior is explained by a rate-distance relationship of the form  $k_{et} = k_0 \exp(-\beta d)$  in terms of the electron tunneling constant  $\beta$  and the donor-acceptor distance  $d$ . This, in short, describes tunneling of the charge through a potential barrier.

In PbS-nBDT films, the donor and the acceptor in charge transfer reaction are the neighboring PbS NCs. Since all presented PbS-nBDT samples are prepared from the same synthesis batch and have the same narrow NC size distribution and site energy dispersion, identical reorganization energy and Gibbs free energy hold to good approximation. The good fit to single exponential function also indicates that the variation in the potential barrier due to different nBDT bi-linker molecules is small and that the inter-NC distance is the dominant parameter governing the electron transfer. The value of the electron tunneling constant,  $\beta$ , obtained from fitting the data to a single exponential is  $2.6 \pm 0.2 \text{ nm}^{-1}$ . This value of  $\beta$  should be taken as a lower bound; preliminary calculations indicate that modifying the analysis of  $k_{et}$  to account for the different distributions in d-spacing of the PbS-nBDT samples give a slightly larger best-fit  $\beta$ . Note that

the PbS-OA film, in which resonant energy transfer is the dominant pathway for photogenerated excitons, shows an order of magnitude slower rate than the trend from charge transfer rates (Figure 7.12(a)).

Depending on the inter-NC separation distance and associated inter-NC coupling energy, there are two distinct regimes: one in which exciton dissociation via tunneling of charge is dominant (Figure 7.12(b)) and one in which resonant energy transfer is dominant (Figure 7.12(c)). The first insight provides a guideline for maximum performance in targeted optoelectronic device applications by selecting the appropriate NC material, which largely determines the exciton binding energy, and the inter-NC separation distance, which determines the inter-NC coupling energy. Consider solar cells and LEDs, for example. Both cases require high electronic coupling, and thus shorter inter-NC separation distance and lower inter-NC potential barrier, for efficient charge transport across the NC assembly. However, requirements for the dominant pathway for excitons are drastically different. Solar cells require efficient exciton dissociation whereas LEDs require efficient exciton radiative recombination. Thus, for solar cell devices, NC materials with low exciton binding energy would be preferred so that inter-NC coupling energy can be comparable to the exciton binding energy. In contrast, LEDs require NC materials with high exciton binding energy for the NC assembly to be in the regime of dominant radiative recombination. These insights explain why Schottky solar cells based on lead salt NCs[8, 9] generate a short-circuit current that is 2 orders of magnitude higher than similarly prepared cadmium salt devices[8, 316] whereas, in LED devices, cadmium salt NCs have shown promising performance.[42].

### **7.4.2 Tandem Quantum Dot Thin Films**

Performance of lead salt nanocrystal tandem solar cells is promising, given the band-gap tunability of quantum dots. For a single absorbing material with a bandgap of 1.1 eV, the limit of

solar cell efficiency has been predicted to be  $\nu \approx 30\%$  [67, 339]. For two absorbing materials, at band gaps of 1.6 eV and 0.9 eV, the theoretical maximum of efficiency jumps to  $\nu \approx 45\%$  [330, 340]. Despite the high thermodynamic limits of efficiency, engineering limitations specific to tandem solar cells remain prevalent. These include, but are not limited to, light transmission to underlying cells, current matching, and interlayer optimization.

In this tandem solar cell, the metal interlayer serves as a tunnel junction, where recombination can occur without significant loss of open circuit voltage. Tunnel junctions are implemented in tandem solar cells to provide low electrical resistance and a relatively transparent connection between cells. Without the presence of the gold interlayer, semiconductor materials in contact would install a potential that counteracts the flow of charge induced from each cell individually. In order for the tunnel junction to perform properly, the depletion region needs to be sufficiently narrow, so that charge can effectively tunnel across the barrier. Oxidation of metallic layers result in lower maximum current densities, cause S-shaped bends in current voltage curves, as well as lower-than-expected measurements of workfunction seen in Figure 7.10 in the device with the aluminum interlayer.

## 7.5 Concluding Remarks

Taken together, the EFM and optical data show, for the first time to current knowledge, that photogenerated excitons in PbS-nBDT films ultimately results in free carrier generation *without* the aid of a chemical potential gradient or external bias. Optical and scanned-probe measurements showed inter-NC coupling induced dissociation of photogenerated excitons in lead salt NC arrays. Exciton dissociation occurs via tunneling of charge between neighboring NCs. New insights obtained from this work provide guidelines for improving the design of a range of optoelectronic devices based on NC solids. Further work was done to fabricate and characterize a NQD tandem solar cell made from lead salt nanocrystals. Kelvin probe force microscopy,

current-voltage, and conductivity measurements were taken to understand the role of metallic interlayers in the device. It was found that a gold metal provides sufficient charge carrier concentration to maintain energy level alignment, and is thin enough to avoid optical absorption losses, and while maintaining conductance for successful interlayer operation.

## REFERENCES

- [1] 2008 solar technologies market report, Technical report, U.S. Department of Energy, 2010.
- [2] L. Kazmerski, Best research cell efficiencies, 2011.
- [3] J. Kalowekamo and E. Baker, Estimating the manufacturing cost of purely organic solar cells, *Solar Energy* **83**, 1224 (2009).
- [4] M. Scharber et al., Design rules for donors in bulk-heterojunction solar cells—Towards 10% energy-conversion efficiency, *Adv. Mater.* **18**, 789 (2006).
- [5] G. Dennler et al., Design rules for donors in bulk-heterojunction tandem solar cells—towards 15 % energy-conversion efficiency, *Adv. Mater.* **20**, 579 (2008).
- [6] C. R. McNeill and N. C. Greenham, Conjugated-polymer blends for optoelectronics, *Adv. Mater.* **21**, 3840 (2009).
- [7] Y. Liang et al., Highly efficient solar cell polymers developed via fine-tuning of structural and electronic properties, *J. Am. Chem. Soc.* **131**, 7792 (2009).
- [8] J. M. Luther et al., Structural, optical, and electrical properties of self-assembled films of pbse nanocrystals treated with 1,2-ethanedithiol, **2**, 271 (2008).
- [9] G. I. Koleilat et al., Efficient, stable infrared photovoltaics based on solution-cast colloidal quantum dots, **2**, 833 (2008).
- [10] J. J. Choi et al., Pbse nanocrystal excitonic solar cells, **9**, 3749 (2009).
- [11] K. S. Leschkies, T. J. Beatty, M. S. Kang, D. J. Norris, and E. S. Aydil, Solar cells based on junctions between colloidal pbse nanocrystals and thin zno films, **3**, 3638 (2009).
- [12] B.-R. Hyun et al., Role of solvent dielectric properties on charge transfer from pbs nanocrystals to molecules, **10**, 318 (2010).
- [13] J. M. Luther et al., Stability assessment on a 3heterojunction solar cell, **22**, 3704 (2010).
- [14] A. G. Pattantyus-Abraham et al., Depleted-heterojunction colloidal quantum dot solar cells, **4**, 3374 (2010).
- [15] D. Ginley, M. Green, and R. Collins, Solar energy conversion toward 1 terawatt, *MRS Bulletin* **33**, 355 (2008).
- [16] M. Green, Third generation photovoltaics: Ultra-high conversion efficiency at low cost, *Progress in Photovoltaics: Research and Applications* **9**, 123 (2001).
- [17] C. Dimitrakopoulos and P. Malenfant, Organic thin film transistors for large area electronics, *Advanced Materials* **14**, 99 (2002).
- [18] F. Garnier and G. Horowitz, Organic semiconducting polymers as molecular material for electronic devices, *Synthetic Metals* **18**, 693 (1987).

- [19] G. Horowitz, Organic field-effect transistors, *Advanced Materials* **10**, 365 (1998).
- [20] P. M. Borsenberger and D. S. Weiss, *Organic Photoreceptors for Xerography*, Marcel Dekker, Inc., New York, 1998.
- [21] M. Pope and C. Swenberg, *Electronic Processes in Organic Crystals*, volume 39, Oxford University Press, New York, 1982.
- [22] R. D. McCullough et al., Design and control of conducting polymer architectures: Synthesis and properties of regiochemically well-defined poly(3-alkylthiophenes), *Synthetic Metals* **55**, 1198 (1993).
- [23] U. Mitschke and P. Bauerle, The electroluminescence of organic materials, *Journal of Materials Chemistry* **10**, 1471 (2000).
- [24] K. Itaka et al., High-mobility c60 field-effect transistors fabricated on molecular-wetting controlled substrates., *Advanced Materials* **18**, 1713 (2006).
- [25] H. Meng et al., 2,6-bis[2-(4-pentylphenyl)vinyl]anthracene: A stable and high charge mobility organic semiconductor with densely packed crystal structure., *Journal of the American Chemical Society* **128**, 9304 (2006).
- [26] C.-a. Di, G. Yu, Y. Liu, and D. Zhu, High-performance organic field-effect transistors: Molecular design, device fabrication, and physical properties., *Journal of Physical Chemistry B* **111**, 14083 (2007).
- [27] J. Roncali, P. Leriche, and A. Cravino, From one- to three-dimensional organic semiconductors: in search of the organic silicon?., *Advanced Materials* **19**, 2045 (2007).
- [28] J. Burroughes et al., Light-emitting diodes based on conjugated polymers, *Nature* **347**, 539 (1990).
- [29] R. H. Friend et al., Electroluminescence in conjugated polymers, *Nature* **397**, 121 (1999).
- [30] P. Peumans, A. Yakimov, and S. Forrest, Small molecular weight organic thin-film photodetectors and solar cells, *Journal of Applied Physics* **93**, 3693 (2003).
- [31] H. Sirringhaus, N. Tessler, and R. Friend, Integrated optoelectronic devices based on conjugated polymers, *Science* **280**, 1741 (1998).
- [32] M. Mas-Torrent and C. Rovira, Novel small molecules for organic field-effect transistors. towards processability and high performance., *Chemical Society Reviews* **37**, 827 (2008).
- [33] Z. Bao, A. Dodabalapur, and A. Lovinger, Soluble and processable regioregular poly(3-hexylthiophene) for thin film field-effect transistor applications with high mobility, *Applied Physics Letters* **69**, 4108 (1996).
- [34] A. Dodabalapur, H. Katz, L. Torsi, and R. Haddon, Organic heterostructure field-effect transistors, *Science* **269**, 1560 (1995).

- [35] G. Horowitz, X. Peng, D. Fichou, and F. Garnier, The oligothiophene-based field-effect transistor: how it works and how to improve it, *Journal of Applied Physics* **67**, 528 (1990).
- [36] H. Katz and Z. Bao, The physical chemistry of organic field-effect transistors, *Journal of Physical Chemistry B* **104**, 671 (2000).
- [37] S. Nelson, Y.-Y. Lin, D. Gundlach, and T. Jackson, Temperature-independent transport in high-mobility pentacene transistors, *Applied Physics Letters* **72**, 1854 (1998).
- [38] L. Torsi, A. Dodabalapur, L. Rothberg, A. Fung, and H. Katz, Intrinsic transport properties and performance limits of organic field-effect transistors, *Science* **272**, 1462 (1996).
- [39] P. Strohriegl and J. Grazulevicius, Charge-transporting molecular glasses, *Advanced Materials* **14**, 1439 (2002).
- [40] C. Tang, Two-layer organic photovoltaic cell, *Applied Physics Letters* **48**, 183 (1986).
- [41] B.-R. Hyun et al., Electron injection from colloidal pbs quantum dots into titanium dioxide nanoparticles, **2**, 2206 (2008).
- [42] K. S. Cho et al., High-performance crosslinked colloidal quantum-dot light-emitting diodes, **3**, 341 (2009).
- [43] J. S. Steckel et al., 1.3 nm to 1.55 nm tunable electroluminescence from pbse quantum dots embedded within an organic device, **15**, 1862 (2003).
- [44] D. C. Oertel, M. G. Bawendi, A. C. Arango, and V. Bulovic, Photodetectors based on treated cdse quantum-dot films, **87**, 213505 (2005).
- [45] V. Sukhovatkin, S. Hinds, L. Brzozowski, and E. H. Sargent, Colloidal quantum-dot photodetectors exploiting multiexciton generation, **324**, 1542 (2009).
- [46] D. V. Talapin and C. B. Murray, Pbse nanocrystal solids for n- and p-channel thin film field-effect transistors, **310**, 86 (2005).
- [47] V. I. Klimov et al., Optical gain and stimulated emission in nanocrystal quantum dots, **290**, 314 (2000).
- [48] R. Y. Wang et al., Enhanced thermopower in pbse nanocrystal quantum dot superlattices, **8**, 2283 (2008).
- [49] D. Wöhrle and D. Meissner, Organic solar cells, *Adv. Mater.* **3**, 129 (1991).
- [50] A. K. Ghosh, D. L. Morel, T. Feng, R. F. Shaw, and C. A. Rowe, Jr., Photovoltaic and rectification properties of al/mg phthalocyanine/ag schottky-barrier cells, *J. Appl. Phys.* **45**, 230 (1974).
- [51] A. K. Ghosh and T. Feng, Merocyanine organic solar cells, *J. Appl. Phys.* **49**, 5982 (1978).
- [52] D. L. Morel et al., High-efficiency organic solar cells, *Appl. Phys. Lett.* **32**, 495 (1978).

- [53] S. Sze, *Physics of Semiconductor Devices*, John Wiley & Sons, 1981.
- [54] C. W. Tang, Two-layer organic photovoltaic cell, *Applied Physics Letters* **48**, 183 (1986).
- [55] S. Karg, W. Riess, V. Dyakonov, and M. Schworer, Electrical and optical characterization of poly(phenylene-vinylene) light emitting diodes, *Synthetic Metals* **54**, 427 (1993).
- [56] R. N. Marks, J. J. M. Halls, D. D. C. Bradely, R. H. Friend, and A. B. Holmes, The photovoltaic response in poly(p-phenylene vinylene) thin-film devices, *Journal of Physics: Condensed Matter* **6**, 1379 (1994).
- [57] G. Yu, C. Zhang, and A. J. Heeger, Dual-function semiconducting polymer devices: Light-emitting and photodetecting diodes, *Applied Physics Letters* **64**, 1540 (1994).
- [58] H. Antoniadis, B. Hsieh, M. Abkowitz, S. Jenekhe, and M. Stolka, Photovoltaic and photoconductive properties of aluminum/poly(p-phenylene vinylene) interfaces, *Synthetic Metals* **62**, 265 (1994).
- [59] J. J. M. Halls, K. Pichler, R. H. Friend, S. C. Moratti, and A. B. Holmes, Exciton diffusion and dissociation in a poly(p-phenylenevinylene)/c60 heterojunction photovoltaic cell, *Applied Physics Letters* **68**, 3120 (1996).
- [60] N. S. Sariciftci et al., Semiconducting polymer-buckminsterfullerene heterojunctions: Diodes, photodiodes, and photovoltaic cells, *Applied Physics Letters* **62**, 585 (1993).
- [61] L. S. Roman, W. Mammo, L. A. A. Pettersson, M. R. Andersson, and O. Ingans, High quantum efficiency polythiophene, *Adv. Mater.* **10**, 774 (1998).
- [62] G. Yu, J. Gao, J. C. Hummelen, F. Wudl, and A. J. Heeger, Polymer photovoltaic cells: Enhanced efficiencies via a network of internal donor-acceptor heterojunctions, *Science* **270**, 1789 (1995).
- [63] C. Yang and A. Heeger, Morphology of composites of semiconducting polymers mixed with c60, *Synthetic Metals* **83**, 85 (1996).
- [64] J. Halls et al., Efficient photodiodes from interpenetrating polymer networks, *Nature* **376**, 498 (1995).
- [65] K. Tada et al., Donor polymer (pat6) – acceptor polymer (cnppv) fractal network photo-cells, *Synthetic Metals* **85**, 1305 (1997).
- [66] B. O'Regan and M. Gratzel, A low-cost, high-efficiency solar cell based on dye-sensitized colloidal tio2 films, *Nature* **353**, 737 (1991).
- [67] W. Shockley and H. J. Queisser, Detailed balance limit of efficiency of p-n junction solar cells, **32**, 510 (1961).
- [68] W. A. Tisdale et al., Hot-electron transfer from semiconductor nanocrystals, **328**, 1543 (2010).

- [69] J. B. Sambur, T. Novet, and B. A. Parkinson, Multiple exciton collection in a sensitized photovoltaic system, **330**, 63 (2010).
- [70] D. S. Ginger and N. C. Greenham, Photoinduced electron transfer from conjugated polymers to cdse nanocrystals, *Phys. Rev. B* **59**, 10622 (1999).
- [71] P. Reiss, E. Couderc, J. De Girolamo, and A. Pron, Conjugated polymers/semiconductor nanocrystals hybrid materials-preparation, electrical transport properties and applications, *Nanoscale* **3**, 446 (2011).
- [72] D. M. N. M. Dissanayake, R. A. H. T. Lutz, R. J. Curry, and S. R. P. Silva, Charge transfer between acenes and pbs nanocrystals, *Nanotechnology* **20**, 195205 (2009).
- [73] D. J. Gundlach, Y. Y. Lin, T. N. Jackson, S. F. Nelson, and D. G. Schlom, Pentacene organic thin-film transistors - molecular ordering and mobility, *IEEE Electron Device Letters* **18**, 87 (1997).
- [74] B. Kippelen, Efficient organic: Researchers use pentacene to develop next-generation solar power, *Science Daily* (2004).
- [75] S. Yoo, B. Domercq, and B. Kippelen, Efficient thin-film organic solar cells based on pentacene/C-60 heterojunctions, *Appl. Phys. Lett.* **85**, 5427 (2004).
- [76] B. Kippelen, Y. Seunghyp, B. Domercq, and W. Potscavage Jr., Efficient organic solar cells using polycrystalline pentacene films, *SPIE Newsroom* (2006).
- [77] R. Signerski, J. Gra&zdot;yna, and J. Godlewski, Photovoltaic properties of tetracene and pentacene layers, *Macromolecular Symposia* **212**, 357 (2004).
- [78] K. Harada, M. Riede, K. Leo, O. R. Hild, and C. M. Elliott, Pentacene homojunctions: Electron and hole transport properties and related photovoltaic responses, *Physical Review B (Condensed Matter and Materials Physics)* **77**, 195212 (2008).
- [79] Y.-F. Lim, Y. Shu, S. R. Parkin, J. E. Anthony, and G. G. Malliaras, Soluble n-type pentacene derivatives as novel acceptors for organic solar cells, *J. Mater. Chem.* **19**, 3049 (2009).
- [80] A. Benor, A. Hoppe, V. Wagner, and D. Knipp, Electrical stability of pentacene thin film transistors, *Organic Electronics* **8**, 749 (2007).
- [81] W. J. Potscavage, S. Yoo, B. Domercq, and B. Kippelen, Encapsulation of pentacene/c60 organic solar cells with alumina deposited by atomic layer deposition, *Applied Physics Letters* **90**, 253511 (2007).
- [82] H. Yang et al., Aging susceptibility of terrace-like pentacene films, *J. Phys. Chem. C* **112**, 16161 (2008).
- [83] F. De Angelis, M. Gaspari, A. Procopio, G. Cuda, and E. Di Fabrizio, Direct mass spectrometry investigation on pentacene thin film oxidation upon exposure to air, *Chemical Physics Letters* **468**, 193 (2009).

- [84] S. Verlaak, V. Arkhipov, and P. Heremans, Modeling of transport in polycrystalline organic semiconductor films, *Appl. Phys. Lett.* **82**, 745 (2003).
- [85] M. Tello, M. Chiesa, C. M. Duffy, and H. Sirringhaus, Charge trapping in intergrain regions of pentacene thin film transistors, *Adv. Func. Mater.* **18**, 3907 (2008).
- [86] J. Veres, S. Ogier, G. Lloyd, and D. De Leeuw, Gate insulators in organic field-effect transistors, *Chem. Mater.* **16**, 4543 (2004).
- [87] S. J. Konezny, M. N. Bussac, and L. Zuppiroli, Hopping and trapping mechanisms in organic field-effect transistors, *Phys. Rev. B* **81**, 045313 (2010).
- [88] R. Street, A. Salleo, and M. Chabinyk, Bipolaron mechanism for bias-stress effects in polymer transistors, *Phys. Rev. B* **68**, 85316 (2003).
- [89] J. H. Kang, D. da Silva, J. L. Bredas, and X. Y. Zhu, Shallow trap states in pentacene thin films from molecular sliding, *Appl. Phys. Lett.* **86**, 152115 (2005).
- [90] E. Tsiper and Z. Soos, Electronic polarization in pentacene crystals and thin films, *Physical Review B* **68**, 85301 (2003).
- [91] J. Northrup and M. Chabinyk, Gap states in organic semiconductors: hydrogen- and oxygen-induced states in pentacene, *Physical Review B* **68**, 41202 (2003).
- [92] D. Lang, X. Chi, T. Siegrist, A. Sergent, and A. Ramirez, Bias-dependent generation and quenching of defects in pentacene, *Physical Review Letters* **93**, 076601 (2004).
- [93] D. Knipp and J. E. Northrup, Electric-field-induced gap states in pentacene, *Adv. Mater.* **21**, 2511 (2009).
- [94] O. D. Jurchescu, J. Baas, and T. T. M. Palstra, Electronic transport properties of pentacene single crystals upon exposure to air, *Applied Physics Letters* **87**, 052102 (2005).
- [95] E. Muller and J. Marohn, Microscopic evidence for spatially inhomogeneous charge trapping in pentacene, *Adv. Mater.* **17**, 1410 (2005).
- [96] M. Jaquith, E. Muller, and J. Marohn, Time-resolved electric force microscopy of charge trapping in polycrystalline pentacene, *J. Phys. Chem. B* **111**, 7711 (2007).
- [97] M. Jaquith, *The kinetics of charge trapping in polycrystalline pentacene and ion migration in light emitting electrochemical cells studied by time- and temperature-resolved electric force microscopy*, PhD thesis, Cornell University, 2009.
- [98] C. Groves, J. C. Blakesley, and N. C. Greenham, Effect of charge trapping on geminate recombination and polymer solar cell performance, *Nano Letters* **10**, 1063 (2010).
- [99] L. Burgi, T. Richards, M. Chiesa, R. H. Friend, and H. Sirringhaus, A microscopic view of charge transport in polymer transistors, *Synth. Met.* **146**, 297 (2004).

- [100] A. Maurano et al., Recombination dynamics as a key determinant of open circuit voltage in organic bulk heterojunction solar cells: A comparison of four different donor polymers, *Adv. Mater.* **22**, 4987 (2010).
- [101] J. L. Luria, K. A. Schwarz, M. J. Jaquith, R. G. Hennig, and J. A. Marohn, Spectroscopic characterization of charged defects in polycrystalline pentacene by time- and wavelength-resolved electric force microscopy, *Adv. Mater.* **23**, 624 (2011).
- [102] B. Fraboni, A. Matteucci, A. Cavallini, E. Orgiu, and A. Bonfiglio, Photocurrent studies of stress and aging in pentacene thin film transistors, *Applied Physics Letters* **89**, 222112 (2006).
- [103] J. Gao and F. A. Hegmann, Bulk photoconductive gain in pentacene thin films, *Applied Physics Letters* **93**, 223306 (2008).
- [104] M. Panzer, C. Newman, and C. Frisbie, Low-voltage operation of a pentacene field-effect transistor with a polymer electrolyte gate dielectric, *Applied Physics Letters* **86**, 103503 (2005).
- [105] C. B. Park, T. Yokoyama, T. Nishimura, K. Kita, and A. Toriumi, Molecular ordering and interface state modification for reducing bias-induced threshold voltage shift in pentacene field-effect transistors., *Journal of the Electrochemical Society* **155**, H575 (2008).
- [106] E. A. Silinsh et al., Photoelectrical properties, energy level spectra, and photogeneration mechanisms of pentacene, *Physica Status Solidi (a)* **25**, 339 (1974).
- [107] S. G. J. Mathijssen et al., Revealing buried interfaces to understand the origins of threshold voltage shifts in organic field-effect transistors, *Adv. Mater.* **22**, 5105 (2010).
- [108] S. Mathijssen et al., Dynamics of threshold voltage shifts in organic and amorphous silicon field-effect transistors, *Advanced Materials* **19**, 2785 (2007).
- [109] D. Knipp and J. E. Northrup, Electric-field-induced gap states in pentacene, *Advanced Materials* **21**, 2511 (2009).
- [110] N. Geacintov and M. Pope, Low-lying valence band states and intrinsic photoconductivity in crystalline anthracene and tetracene, *The Journal of Chemical Physics* **50**, 814 (1969).
- [111] J. Genoe et al., Bias stress in pentacene transistors measured by four probe transistor structures, *Proceedings of the 34th European Solid-State Device Research Conference* , 413 (2004).
- [112] A. Salleo and R. Street, Kinetics of bias stress and bipolaron formation in polythiophene, *Physical Review B* **70**, 235324 (2004).
- [113] J. Godlewski, Currents and photocurrents in organic materials determined by the interface phenomena, *Advances in Colloid and Interface Science* **116**, 227 (2005).

- [114] O. Ostroverkhova et al., Bandlike transport in pentacene and functionalized pentacene thin films revealed by subpicosecond transient photoconductivity measurements, *Physical Review B* **71**, 035204 (2005).
- [115] Z. T. Zhu, J. T. Mason, R. Dieckmann, and G. G. Malliaras, Humidity sensors based on pentacene thin-film transistors, *Appl. Phys. Lett.* **81**, 4643 (2002).
- [116] Y. Qiu et al., H<sub>2</sub>O effect on the stability of organic thin-film field-effect transistors, *Appl. Phys. Lett.* **83**, 1644 (2003).
- [117] A. Maliakal, K. Raghavachari, H. Katz, E. Chandross, and T. Siegrist, Photochemical stability of pentacene and a substituted pentacene in solution and in thin films, *Chemistry of Materials* **16**, 4980 (2004).
- [118] C. Pannemann, T. Diekmann, and U. Hilleringmann, Degradation of organic field-effect transistors made of pentacene, *J. Mater. Res.* **19**, 1999 (2004).
- [119] G. Gu and M. G. Kane, Moisture induced electron traps and hysteresis in pentacene-based organic thin-film transistors, *Appl. Phys. Lett.* **92**, 053305 (2008).
- [120] C. Ambrosch-Draxl, K. Hummer, S. Sagmeister, and P. Puschnig, Excitonic effects in molecular crystals built up by small organic molecules, *Chemical Physics* **325**, 3 (2006).
- [121] A. Modelli and L. Mussoni, Rapid quantitative prediction of ionization energies and electron affinities of polycyclic aromatic hydrocarbons, *Chemical Physics* **332**, 367 (2007).
- [122] M. L. Tiago, J. E. Northrup, and S. G. Louie, Ab initio calculation of the electronic and optical properties of solid pentacene, *Phys. Rev. B* **67**, 115212 (2003).
- [123] T. M. Halasinski, D. M. Hudgins, F. Salama, L. J. Allamandola, and T. Bally, Electronic absorption spectra of neutral pentacene (c<sub>22</sub>h<sub>14</sub>) and its positive and negative ions in ne, ar, and kr matrices, *The Journal of Physical Chemistry A* **104**, 7484 (2000).
- [124] K. Hummer and C. Ambrosch-Draxl, Electronic properties of oligoacenes from first principles, *Phys. Rev. B* **72**, 205205 (2005).
- [125] M. Knupfer, Exciton binding energies in organic semiconductors, *Applied Physics A: Materials Science & Processing* **77**, 623 (2003).
- [126] P. Puschnig and C. Ambrosch-Draxl, Excitons in organic semiconductors, *Comptes Rendus Physique* **10**, 504 (2009).
- [127] S. Guenes, H. Neugebauer, and N. S. Sariciftci, Conjugated polymer-based organic solar cells, *Chem. Rev.* **107**, 1324 (2007).
- [128] B. C. Thompson and J. M. J. Frechet, Organic photovoltaics - Polymer-fullerene composite solar cells, *Angew. Chem. - Int. Edit.* **47**, 58 (2008).
- [129] T. M. Clarke and J. R. Durrant, Charge photogeneration in organic solar cells, *Chem. Rev.* **110**, 6736 (2010).

- [130] A. C. Arias et al., Vertically segregated polymer-blend photovoltaic thin-film structures through surface-mediated solution processing, *Appl. Phys. Lett.* **80**, 1695 (2002).
- [131] C. R. McNeill, S. Westenhoff, C. Groves, R. H. Friend, and N. C. Greenham, Influence of nanoscale phase separation on the charge generation dynamics and photovoltaic performance of conjugated polymer blends: Balancing charge generation and separation, *J. Phys. Chem. C* **111**, 19153 (2007).
- [132] C. Groves, O. G. Reid, and D. S. Ginger, Heterogeneity in polymer solar cells: Local morphology and performance in organic photovoltaics studied with scanning probe microscopy, *Acc. Chem. Res.* **43**, 612 (2010).
- [133] C. J. Brabec et al., Origin of the open circuit voltage of plastic solar cells, *Adv. Funct. Mater.* **11**, 374 (2001).
- [134] J. Liu, Y. Shi, and Y. Yang, Solvation-induced morphology effects on the performance of polymer-based photovoltaic devices, *Adv. Funct. Mater.* **11**, 420 (2001).
- [135] B. A. Gregg, Excitonic solar cells, *J. Phys. Chem. B* **107**, 4688 (2003).
- [136] H. Snaith, N. Greenham, and R. Friend, The origin of collected charge and open-circuit voltage in blended polyfluorene photovoltaic devices, *Adv. Mater.* **16**, 1640 (2004).
- [137] P. Peumans and S. R. Forrest, Separation of geminate charge-pairs at donor-acceptor interfaces in disordered solids, *Chem. Phys. Lett.* **398**, 27 (2004).
- [138] L. Koster, V. Mihailetschi, R. Ramaker, and P. Blom, Light intensity dependence of open-circuit voltage of polymer:fullerene solar cells, *Appl. Phys. Lett.* **86**, 123509 (2005).
- [139] B. P. Rand, D. P. Burk, and S. R. Forrest, Offset energies at organic semiconductor heterojunctions and their influence on the open-circuit voltage of thin-film solar cells, *Phys. Rev. B* **75**, 115327 (2007).
- [140] P. W. M. Blom, V. D. Mihailetschi, L. J. A. Koster, and D. E. Markov, Device physics of polymer : Fullerene bulk heterojunction solar cells, *Adv. Mater.* **19**, 1551 (2007).
- [141] S. Westenhoff et al., Charge recombination in organic photovoltaic devices with high open-circuit voltages, *J. Am. Chem. Soc.* **130**, 13653 (2008).
- [142] W. J. Potscavage, Jr., A. Sharma, and B. Kippelen, Critical interfaces in organic solar cells and their influence on the open-circuit voltage, *Acc. Chem. Res.* **42**, 1758 (2009).
- [143] K. Vandewal, K. Tvingstedt, A. Gadisa, O. Inganäs, and J. V. Manca, On the origin of the open-circuit voltage of polymer-fullerene solar cells, *Nat. Mater.* **8**, 904 (2009).
- [144] G. Garcia-Belmonte and J. Bisquert, Open-circuit voltage limit caused by recombination through tail states in bulk heterojunction polymer-fullerene solar cells, *Appl. Phys. Lett.* **96**, 113301 (2010).
- [145] O. Reid, H. Xin, S. Jenekhe, and D. Ginger, Nanostructure determines the intensity-dependence of open-circuit voltage in plastic solar cells, *J. Appl. Phys.* **108**, 084320 (2010).

- [146] T. M. Clarke et al., Analysis of charge photogeneration as a key determinant of photocurrent density in polymer: Fullerene solar cells, *Adv. Mater.* **22**, 5287 (2010).
- [147] C. W. Schlenker and M. E. Thompson, The molecular nature of photovoltage losses in organic solar cells, *Chem. Commun.* **47**, 3702 (2011).
- [148] R. Giridharagopal and D. S. Ginger, Characterizing morphology in bulk heterojunction organic photovoltaic systems, *J. Phys. Chem. Lett.* **1**, 1160 (2010).
- [149] R. Stevenson, A. Arias, C. Ramsdale, J. MacKenzie, and D. Richards, Raman microscopy determination of phase composition in polyfluorene composites, *Appl. Phys. Lett.* **79**, 2178 (2001).
- [150] Y. Xia and R. Friend, Phase separation of polyfluorene-based blend films and its influence on device operations, *Adv. Mater.* **18**, 1371 (2006).
- [151] R. Shikler, M. Chiesa, and R. H. Friend, Photovoltaic performance and morphology of polyfluorene blends: The influence of phase separation evolution, *Macromolecules* **39**, 5393 (2006).
- [152] S. Williams, D. Morrison, B. Thiel, and A. Donald, Imaging of semiconducting polymer blend systems using environmental scanning electron microscopy and environmental scanning transmission electron microscopy, *Scanning* **27**, 190 (2005).
- [153] D. W. Steuerman et al., Imaging the interfaces of conjugated polymer optoelectronic devices, *Adv. Mater.* **20**, 528 (2008).
- [154] C. McNeill et al., Nanoscale quantitative chemical mapping of conjugated polymer blends, *Nano Lett.* **6**, 1202 (2006).
- [155] C. R. McNeill et al., Evolution of laterally phase-separated polyfluorene blend morphology studied by x-ray spectromicroscopy, *Macromolecules* **42**, 3347 (2009).
- [156] H. Ade and H. Stoll, Near-edge x-ray absorption fine-structure microscopy of organic and magnetic materials, *Nat Mater* **8**, 281 (2009).
- [157] H. Ade and A. P. Hitchcock, Nexafs microscopy and resonant scattering: Composition and orientation probed in real and reciprocal space, *Polymer* **49**, 643 (2008).
- [158] A. Cadby, G. Khalil, A. M. Fox, and D. G. Lidzey, Mapping exciton quenching in photovoltaic-applicable polymer blends using time-resolved scanning near-field optical microscopy, *J. Appl. Phy.* **103**, 093715 (2008).
- [159] L. S. C. Pingree, O. G. Reid, and D. S. Ginger, Electrical scanning probe microscopy on active organic electronic devices, *Adv. Mater.* **21**, 19 (2009).
- [160] H. Hoppe et al., Kelvin probe force microscopy study on conjugated polymer/fullerene bulk heterojunction organic solar cells, *Nano Lett.* **5**, 269 (2005).
- [161] M. Chiesa et al., Correlation between surface photovoltage and blend morphology in polyfluorene-based photodiodes, *Nano Lett.* **5**, 559 (2005).

- [162] T. Glatzel, H. Hoppe, N. S. Sariciftci, M. C. Lux-Steiner, and M. Komiyama, Kelvin probe force microscopy study of conjugated polymer/fullerene organic solar cells, *Jap. J. Appl. Phys.* **44**, 5370 (2005).
- [163] V. Palermo et al., A kelvin probe force microscopy study of the photogeneration of surface charges in all-thiophene photovoltaic blends, *Adv. Funct. Mater.* **17**, 472 (2007).
- [164] A. Liscio et al., Photovoltaic charge generation visualized at the nanoscale: A proof of principle, *J. Am. Chem. Soc.* **130**, 780 (2008).
- [165] K. Maturova, M. Kemerink, M. Wienk, D. Charrier, and R. Janssen, Scanning kelvin probe microscopy on bulk heterojunction polymer blends, *Adv. Funct. Mater.* **19**, 1379 (2009).
- [166] O. G. Reid, G. E. Rayermann, D. C. Coffey, and D. S. Ginger, Imaging local trap formation in conjugated polymer solar cells: A comparison of time-resolved electrostatic force microscopy and scanning kelvin probe imaging, *J. Phys. Chem. C* **114**, 20672 (2010).
- [167] E. J. Spadafora, R. Demadrille, B. Ratier, and B. Grevin, Imaging the carrier photogeneration in nanoscale phase segregated organic heterojunctions by kelvin probe force microscopy, *Nano Letters* **10**, 3337 (2010).
- [168] M.-C. Wu et al., Correlation between nanoscale surface potential and power conversion efficiency of p3ht/tio2 nanorod bulk heterojunction photovoltaic devices, *Nanoscale* **2**, 1448 (2010).
- [169] D. C. Coffey and D. S. Ginger, Time-resolved electrostatic force microscopy of polymer solar cells, *Nat. Mater.* **5**, 735 (2006).
- [170] D. Coffey and D. Ginger, Patterning phase separation in polymer films with dip-pen nanolithography, *J. Am. Chem. Soc.* **127**, 4564 (2005).
- [171] A. Alexeev, J. Loos, and M. Koetse, Nanoscale electrical characterization of semiconducting polymer blends by conductive atomic force microscopy, *Ultramicroscopy* **106**, 191 (2006).
- [172] O. Douheret et al., Nanoscale electrical characterization of organic photovoltaic blends by conductive atomic force microscopy, *Appl. Phys. Lett.* **89**, 032107 (2006).
- [173] D. C. Coffey, O. G. Reid, D. B. Rodovsky, G. P. Bartholomew, and D. S. Ginger, Mapping local photocurrents in polymer/fullerene solar cells with photoconductive atomic force microscopy, *Nano Lett.* **7**, 738 (2007).
- [174] M. Dante, J. Peet, and T.-Q. Nguyen, Nanoscale charge transport and internal structure of bulk heterojunction conjugated polymer/fullerene solar cells by scanning probe microscopy, *J. Phys. Chem. C* **112**, 7241 (2008).
- [175] O. G. Reid, K. Munechika, and D. S. Ginger, Space charge limited current measurements on conjugated polymer films using conductive atomic force microscopy, *Nano Lett.* **8**, 1602 (2008).

- [176] T. A. Bull, L. S. C. Pingree, S. A. Jenekhe, D. S. Ginger, and C. K. Luscombe, The role of mesoscopic pcbm crystallites in solvent vapor annealed copolymer solar cells, *ACS Nano* **3**, 627 (2009).
- [177] L. S. C. Pingree, O. G. Reid, and D. S. Ginger, Imaging the evolution of nanoscale photocurrent collection and transport networks during annealing of polythiophene/fullerene solar cells, *Nano Lett.* **9**, 2946 (2009).
- [178] M. Guide, X.-D. Dang, and T.-Q. Nguyen, Nanoscale characterization of tetrabenzoporphyrin and fullerene-based solar cells by photoconductive atomic force microscopy, *Adv. Mater.* **23**, in press (2011).
- [179] B. Leever et al., spatially resolved photocurrent mapping of operating organic photovoltaic devices using atomic force photovoltaic microscopy, *Applied Physics Letters* (2008).
- [180] C. McNeill, H. Frohne, J. Holdsworth, and P. Dastoor, Near-field scanning photocurrent measurements of polyfluorene blend devices: Directly correlating morphology with current generation, *Nano Lett.* **4**, 2503 (2004).
- [181] C. McNeill and P. Dastoor, Photocurrent pattern formation in polymer/methanofullerene blends imaged by near-field scanning photocurrent microscopy, *J. Appl. Phys.* **99**, 033502 (2006).
- [182] A. P. Alivisatos, Perspectives on the physical chemistry of semiconductor nanocrystals, *The Journal of Physical Chemistry* **100**, 13226 (1996).
- [183] S. Kohtani, A. Kudo, and T. Sakata, Spectral sensitization of a tio2 semiconductor electrode by cds microcrystals and its photoelectrochemical properties, *Chemical Physics Letters* **206**, 166 (1993).
- [184] R. Vogel, P. Hoyer, and H. Weller, Quantum-sized pbs, cds, ag2s, sb2s3, and bi2s3 particles as sensitizers for various nanoporous wide-bandgap semiconductors, *The Journal of Physical Chemistry* **98**, 3183 (1994).
- [185] J. J. Choi et al., PbSe nanocrystal excitonic solar cells, *Nano Letters* **9**, 3749 (2009).
- [186] I. Robel, V. Subramanian, M. Kuno, and P. V. Kamat, Quantum dot solar cells. harvesting light energy with cdse nanocrystals molecularly linked to mesoscopic tio2 films, *Journal of the American Chemical Society* **128**, 2385 (2006).
- [187] A. Zaban, O. I. Micic, B. A. Gregg, and A. J. Nozik, Photosensitization of nanoporous tio2 electrodes with inp quantum dots, *Langmuir* **14**, 3153 (1998).
- [188] J. J. Choi et al., Photogenerated exciton dissociation in highly coupled lead salt nanocrystal assemblies, *Nano Lett.* **10**, 1805 (2010).
- [189] J. J. Choi et al., Solution processed nanocrystal quantum dot tandem solar cells, *Adv. Mater.* (accepted) (2011).

- [190] L. Kelvin, On electric machines founded on induction and convection, *Philosophical Magazine* **46**, 82 (1898).
- [191] G. Binnig, C. Quate, and C. Gerber, Atomic force microscope, *Physical Review Letters* **56**, 930 (1986).
- [192] Y. Martin, D. Abraham, and H. Wickramasinghe, High-resolution capacitance measurement and potentiometry by force microscopy, *Appl. Phys. Lett.* **52**, 1103 (1988).
- [193] M. Nonnenmacher, M. P. Oboyle, and H. K. Wickramasinghe, Kelvin probe force microscopy, *Applied Physics Letters* **58**, 2921 (1991).
- [194] T. Krauss and L. Brus, Charge, polarizability, and photoionization of single semiconductor nanocrystals, *Phys. Rev. Lett.* **83**, 4840 (1999).
- [195] M. Loiacono, E. Granstrom, and C. Frisbie, Investigation of charge transport in thin, doped sexithiophene crystals by conducting probe atomic force microscopy, *Journal of Physical Chemistry B* **102**, 1679 (1998).
- [196] K. Kobayashi et al., Surface potential measurement on organic ultrathin film by kelvin probe force microscopy using a piezoelectric cantilever, *Applied Physics A: Materials Science & Processing* **72**, S97 (2001).
- [197] L. Burgi, H. Sirringhaus, and R. Friend, Noncontact potentiometry of polymer field-effect transistors, *Applied Physics Letters* **80**, 2913 (2002).
- [198] V. Palermo et al., The relationship between nanoscale architecture and function in photovoltaic multichromophoric arrays as visualized by kelvin probe force microscopy, *J. Am. Chem. Soc.* **130**, 14605 (2008).
- [199] K. Seshadri and C. Frisbie, Potentiometry of an operating organic semiconductor field-effect transistor, *Applied Physics Letters* **78**, 993 (2001).
- [200] T. Kelley and C. Frisbie, Gate voltage dependent resistance of a single organic semiconductor grain boundary, *Journal of Physical Chemistry B* **105**, 4538 (2001).
- [201] A. Chwang and C. Frisbie, Temperature and gate voltage dependent transport across a single organic semiconductor grain boundary, *Journal of Applied Physics* **90**, 1342 (2001).
- [202] K. P. Puntambekar, P. V. Pesavento, and C. D. Frisbie, Surface potential profiling and contact resistance measurements on operating pentacene thin-film transistors by Kelvin probe force microscopy, *Appl. Phys. Lett.* **83**, 5539 (2003).
- [203] K. Maturov, M. Kemerink, M. M. Wienk, D. S. H. Charrier, and R. A. J. Janssen, Scanning kelvin probe microscopy on bulk heterojunction polymer blends, *Advanced Functional Materials* **19**, 1379 (2009).
- [204] M. Jaquith, E. Muller, and J. Marohn, Time-resolved electric force microscopy of charge trapping in polycrystalline pentacene, *J. Phys. Chem. B* **111**, 7711 (2007).

- [205] M. Jaquith, J. Anthony, and J. Marohn, Long-lived charge traps in functionalized pentacene and anthradithiophene studied by time-resolved electric force microscopy, *J. Mater. Chem.* **19**, 6116 (2009).
- [206] L. C. Teague et al., Surface potential imaging of solution processable acene-based thin film transistors, *Advanced Materials* **20**, 4513 (2008).
- [207] A. Liscio, V. Palermo, and P. Samori, Nanoscale quantitative measurement of the potential of charged nanostructures by electrostatic and kelvin probe force microscopy: Unraveling electronic processes in complex materials, *Acc. Chem. Res.* **43**, 541 (2010).
- [208] D. S. H. Charrier, M. Kemerink, B. E. Smalbrugge, T. de Vries, and R. A. J. Janssen, Real versus measured surface potentials in scanning Kelvin probe microscopy, *ACS Nano* **2**, 622 (2008).
- [209] T. Hallam, C. M. Duffy, T. Minakata, M. Aando, and H. Sirringhaus, A scanning Kelvin probe study of charge trapping in zone-cast pentacene thin film transistors, *Nanotech.* **20**, 025203 (2009).
- [210] T. N. Ng, J. Marohn, and M. Chabinyk, Comparing the kinetics of bias stress in organic field-effect transistors with different dielectric interfaces, *J. Appl. Phys.* **100**, 84505 (2006).
- [211] T. N. Ng, J. Marohn, and M. Chabinyk, Comparing the kinetics of bias stress in organic field-effect transistors with different dielectric interfaces, *J. Appl. Phys.* **100**, 84505 (2006).
- [212] T. D. Stowe, T. W. Kenny, D. J. Thomson, and D. Rugar, Silicon dopant imaging by dissipation force microscopy, *Appl. Phys. Lett.* **75**, 2785 (1999).
- [213] S. K. Park, T. N. Jackson, J. E. Anthony, and D. A. Mourey, High mobility solution processed 6,13-bis(triisopropyl-silylethynyl) pentacene organic thin film transistors, *Applied Physics Letters* **91**, 063514 (2007).
- [214] Y. Qi, J. Y. Park, B. L. M. Hendriksen, D. F. Ogletree, and M. Salmeron, Electronic contribution to friction on GaAs: An atomic force microscope study, *Phys. Rev. B* **77**, 184105 (2008).
- [215] I. Dorofeyev, H. Fuchs, G. Wenning, and B. Gotsmann, Brownian motion of microscopic solids under the action of fluctuating electromagnetic fields, *Phys. Rev. Lett.* **83**, 2402 (1999).
- [216] B. N. J. Persson and A. I. Volokitin, Comment on “brownian motion of microscopic solids under the action of fluctuating electromagnetic fields”, *Phys. Rev. Lett.* **84**, 3504 (2000).
- [217] I. Dorofeyev, H. Fuchs, and B. Gotsmann, Dorofeyev, fuchs, and gotsmann reply, *Phys. Rev. Lett.* **84**, 3505 (2000).
- [218] P. Grütter, Y. Liu, P. LeBlanc, and U. Dürig, Magnetic dissipation force microscopy, *Appl. Phys. Lett.* **71**, 279 (1997).

- [219] Y. Liu and P. Grütter, Theory of magnetoelastic dissipation due to domain wall width oscillation, *J. Appl. Phys.* **83**, 5922 (1998).
- [220] V. Nalladega, S. Sathish, K. V. Jata, and M. P. Blodgett, Development of eddy current microscopy for high resolution electrical conductivity imaging using atomic force microscopy, *Rev. Sci. Instrum.* **79**, 073705 (2008).
- [221] B. C. Stipe, H. J. Mamin, T. D. Stowe, T. W. Kenny, and D. Rugar, Magnetic dissipation and fluctuations in individual nanomagnets measured by ultrasensitive cantilever magnetometry, *Phys. Rev. Lett.* **86**, 2874 (2001).
- [222] T. Ng, N. Jenkins, and J. Marohn, Thermomagnetic fluctuations and hysteresis loops of magnetic cantilevers for magnetic resonance force microscopy, *IEEE Trans. Mag.* **42**, 378 (2006).
- [223] L. Cockins, Y. Miyahara, and P. Grutter, Spatially resolved low-frequency noise measured by atomic force microscopy, *Phys. Rev. B* **79**, 121309 (2009).
- [224] W. R. Silveira, E. M. Muller, T. N. Ng, D. H. Dunlap, and J. A. Marohn, High-sensitivity electric force microscopy of organic electronic devices and materials, in *Scanning Probe Microscopy: Electrical and Electromechanical Phenomena at the Nanoscale*, edited by S. V. Kalinin and A. Gruverman, volume II, pages 788 – 830, Springer Verlag, New York, 2007.
- [225] E. Muller, *Electric Force microscopy of charge trapping in thin-film Pentacene Transistors*, PhD thesis, Cornell University, 2005.
- [226] W. R. Silveira, *Microscopic view of charge injection in a model organic semiconductor*, PhD thesis, Cornell University, 2005.
- [227] E. M. Muller and J. A. Marohn, Microscopic evidence for spatially inhomogeneous charge trapping in pentacene, *Advanced Materials* **17**, 1410 (2005).
- [228] S. M. Yazdanian, *Scanned Probe Microscopy Studies of Thin organic Films using Cantilever Frequency Noise*, PhD thesis, Cornell University, 2009.
- [229] K. Bruland et al., Thermal tuning of a fiber-optic interferometer for maximum sensitivity, *Review of Scientific Instruments* **70**, 3542 (1999).
- [230] J. Siegel, J. Witt, N. Venturi, and S. Field, Compact large-range cryogenic scanner, *Review of Scientific Instruments* **66**, 2520 (1995).
- [231] W. Silveira and J. Marohn, A vertical inertial coarse approach for variable temperature scanned probe microscopy, *Rev. Sci. Instrum.* **74**, 267 (2003).
- [232] R. S. McLean and B. B. Sauer, Tapping-mode afm studies using phase detection for resolution of nanophases in segmented polyurethanes and other block copolymers, *Macromolecules* **30**, 8314 (1997).
- [233] A. Kikukawa, S. Hosaka, and R. Imura, Silicon pn junction imaging and characterization using sensitivity enhanced kelvin probe microscopy, *Appl. Phys. Lett.* **66**, 3510 (1995).

- [234] S. Kuehn, *Force-Gradient Detected Nuclear Magnetic Resonance and the Origins of Non-contact Friction*, PhD thesis, Cornell University, 2007.
- [235] A. Vollmer et al., The effect of oxygen exposure on pentacene electronic structure, *Eur. Phys. J. E* **17**, 339 (2005).
- [236] V. Bliznyuk et al., Electrical and photoinduced degradation of polyfluorene based films and light-emitting devices, *Macromolecules* **32**, 361 (1999).
- [237] L. J. Soltzberg et al., Identification of a quenching species in ruthenium tris-bipyridine electroluminescent devices, *J. Am. Chem. Soc.* **128**, 7761 (2006).
- [238] Material Research Society, *The Effect of Oxygen Exposure on Pentacene Thin Film Electronic Structure*, volume 871E, 2005.
- [239] C. C. Mattheus et al., A 2:1 cocrystal of 6,13-dihydro-pentacene and pentacene, *Acta Crystallogr., Sect. E: Struct. Rep. Online* **58**, o1229 (2002).
- [240] L. Roberson et al., Pentacene disproportionation during sublimation for field-effect transistors, *J. Amer. Chem. Soc.* **127**, 3069 (2005).
- [241] Y. Y. Lin, D. J. Gundlach, S. F. Nelson, and T. N. Jackson, Pentacene-based organic thin-film transistors, *IEEE Trans. Electron Devices* **44**, 1325 (1997).
- [242] J. E. Anthony, Functionalized acenes and heteroacenes for organic electronics, *Chemical Reviews* **106**, 5028 (2006).
- [243] R. A. Street, Thin-film transistors, *Adv. Mater.* **21**, 2007 (2009).
- [244] T. N. Ng, W. R. Silveira, and J. A. Marohn, Non-ideal behavior in a model system: Contact degradation in a molecularly doped polymer revealed by variable-temperature electric force microscopy, *Proc. SPIE* **6336**, 63360A (2006).
- [245] *Gaussian 09, Revision A.1; Gaussian Inc., Wallingford, CT.*
- [246] R. Bauernschmitt and R. Ahlrichs, Treatment of electronic excitations within the adiabatic approximation of time dependent density functional theory, *Chem. Phys. Lett.* **256**, 454 (1996).
- [247] A. D. Becke, Density-functional thermochemistry. 3. The role of exact exchange., *J. Chem. Phys.* **98**, 5648 (1993).
- [248] S. Miertus, E. Scrocco, and J. Tomasi, Electrostatic interaction of a solute with a continuum. A direct utilization of ab initio molecular potentials for the prevision of solvent effects, *Chem. Phys.* **55**, 117 (1981).
- [249] P. K. Nayak and N. Periasamy, Calculation of electron affinity, ionization potential, transport gap, optical band gap and exciton binding energy of organic solids using ‘solvation’ model and dft, *Org. Electronics* **10**, 1396 (2009).

- [250] W. R. Silveira, E. M. Muller, T.-N. Ng, D. H. Dunlap, and J. A. Marohn, High-sensitivity electric force microscopy of organic electronic devices and materials, in *Scanning Probe Microscopy: Electrical and Electromechanical Phenomena at the Nanoscale (Volume II)*, edited by S. V. Kalinin and A. Gruverman, pages 788 – 830, Springer Verlag, New York, 2007.
- [251] M. Breban, D. B. Romero, S. Mezheny, V. W. Ballarotto, and E. D. Williams, Photocurrent probe of field-dependent mobility in organic thin-film transistors, *Appl. Phys. Lett.* **87**, 203503 (2005).
- [252] A. Salleo and R. A. Street, Light-induced bias stress reversal in polyfluorene thin-film transistors, *J. Appl. Phys.* **94**, 471 (2003).
- [253] A. Salleo, F. Endicott, and R. A. Street, Reversible and irreversible trapping at room temperature in poly(thiophene) thin-film transistors, *Appl. Phys. Lett.* **86**, 263505 (2005).
- [254] C. Jundt et al., Excitation dynamics in pentacene thin-films studied by pump-probe spectroscopy, *Chem. Phys. Lett.* **241**, 84 (1995).
- [255] L. Sebastian, G. Weiser, and H. Bässler, Charge transfer transitions in solid tetracene and pentacene studied by electroabsorption, *Chem. Phys.* **61**, 125 (1981).
- [256] S. Grimme and M. Parac, Substantial errors from time-dependent density functional theory for the calculation of excited states of large  $\pi$  systems, *Chem. Phys. Chem.* **4**, 292 (2003).
- [257] E. S. Kadantsev, M. J. Stott, and A. Rubio, Electronic structure and excitations in oligoacenes from ab initio calculations, *J. Chem. Phys.* **124**, 134901 (2006).
- [258] O. D. Jurchescu, J. Baas, and T. T. M. Palstra, Effect of impurities on the mobility of single crystal pentacene, *Appl. Phys. Lett.* **84**, 3061 (2004).
- [259] B. R. Conrad et al., Effect of impurities on pentacene island nucleation, *Phys. Rev. B* **77**, 205328 (2008).
- [260] E. Gomar-Nadal, B. R. Conrad, W. G. Cullen, and E. A. Williams, Effect of impurities on pentacene thin film growth for field-effect transistors, *J. Phys. Chem. C* **112**, 5646 (2008).
- [261] I. Salzmann et al., Phase separation in vacuum codeposited pentacene/6,13-pentacenequinone thin films, *Phys. Rev. B* **75**, 174108 (2007).
- [262] C. Groves, R. A. Marsh, and N. C. Greenham, Monte carlo modeling of geminate recombination in polymer-polymer photovoltaic devices, *J. Chem. Phys.* **129**, 114903 (2008).
- [263] C. Ramsdale et al., The origin of the open-circuit voltage in polyfluorene-based photovoltaic devices, *J. Appl. Phys.* **92**, 4266 (2002).
- [264] S. M. Yazdaniyan, N. Hoepker, S. Kuehn, R. F. Loring, and J. A. Marohn, Quantifying electric field gradient fluctuations over polymers using ultrasensitive cantilevers, *Nano Lett.* **9**, 2273 (2009).

- [265] D. Ginger and D. Coffey, Time-resolved electrostatic force microscopy of polymer solar cells, *Nature Materials* **5**, 735 (2006).
- [266] C. Yin, B. Pieper, B. Stiller, T. Kietzke, and D. Neher, Charge carrier generation and electron blocking at interlayers in polymer solar cells, *Appl. Phys. Lett.* **90**, 133502 (2007).
- [267] T. Kietzke et al., A nanoparticle approach to control the phase separation in polyfluorene photovoltaic devices, *Macromolecules* **37**, 4882 (2004).
- [268] R. A. Segalman, B. McCulloch, S. Kirmayer, and J. J. Urban, Block copolymers for organic optoelectronics, *Macromolec.* **42**, 9205 (2009).
- [269] C. Tengstedt et al., Fermi-level pinning at conjugated polymer interfaces, *Appl. Phys. Lett.* **88**, 053502 (2006).
- [270] J. X. Tang, C. S. Lee, and S. T. Lee, Electronic structures of organic/organic heterojunctions: From vacuum level alignment to fermi level pinning, *J. Appl. Phys.* **101**, 064504 (2007).
- [271] H. Ishii et al., Kelvin probe study of band bending at organic semiconductor/metal interfaces: examination of fermi level alignment, *phys. stat. sol. (a)* **201**, 1075 (2004).
- [272] E. R. Bittner, J. G. S. Ramon, and S. Karabunarliev, Exciton dissociation dynamics in model donor-acceptor polymer heterojunctions. i. energetics and spectra, *J. Chem. Phys.* **122**, 214719 (2005).
- [273] A. C. Morteani, P. Sreearunothai, L. M. Herz, R. H. Friend, and C. Silva, Exciton regeneration at polymeric semiconductor heterojunctions, *Phys. Rev. Lett.* **92**, 247402 (2004).
- [274] A. Gonzalez-Rabade, A. C. Morteani, and R. H. Friend, Correlation of heterojunction luminescence quenching and photocurrent in polymer-blend photovoltaic diodes, *Advanced Materials* **21**, 3924 (2009).
- [275] H. Fukagawa et al., The role of the ionization potential in vacuum-level alignment at organic semiconductor interfaces, *Adv. Mater.* **19**, 665 (2007).
- [276] N. Koch and A. Vollmer, Electrode-molecular semiconductor contacts: Work-function-dependent hole injection barriers versus fermi-level pinning, *Appl. Phys. Lett.* **89**, 162107 (2006).
- [277] J. C. Scott and G. G. Malliaras, Charge injection and recombination at the metal-organic interface, *Chemical Physics Letters* **299**, 115 (1999).
- [278] Y. Zhang and P. W. M. Blom, Electron and hole transport in poly(fluorene-benzothiadiazole), *Appl. Phys. Lett.* **98**, 143504 (2011).
- [279] J. Marohn and D. H. Dunlap, *Mott-Gurney Law Tutorial*, 2003.
- [280] J. Marohn, *Mott-Gurney Heterojunction Notes*, 2011.

- [281] C. R. McNeill et al., X-ray microscopy of photovoltaic polyfluorene blends: Relating nanomorphology to device performance, *Macromolecules* **40**, 3263 (2007).
- [282] L. Kronik and Y. Shapira, Surface photovoltage phenomena: Theory, experiment, and applications, *Surf. Sci. Rep.* **37**, 1 (1999).
- [283] A. Carbone, C. Pennetta, and L. Reggiani, Trapping-detrapping fluctuations in organic space-charge layers, *Appl. Phys. Lett.* **95**, 233303 (2009).
- [284] A. Carbone, B. Kotowska, and D. Kotowski,  $f^\gamma$  current fluctuations in organic semiconductors: Evidence for percolation, *Eur. Phys. J. B* **50**, 77 (2006).
- [285] E. V. Russell and N. E. Israeloff, Direct observation of molecular cooperativity near the glass transition, *Nature* **408**, 695 (2000).
- [286] O. Cherniavskaya, L. Chen, V. Weng, L. Yuditsky, and L. E. Brus, Quantitative non electrostatic force imaging of nanocrystal polarizability, *J. Phys. Chem. B* **107**, 1525 (2002).
- [287] N. Hoepker, S. Lekkala, R. F. Loring, and J. A. Marohn, Quantifying dielectric fluctuations over polymer films using an atomic force microscope, *J. Phys. Chem. B* (2011).
- [288] J. A. Barker, C. M. Ramsdale, and N. C. Greenham, Modeling the current-voltage characteristics of bilayer polymer photovoltaic devices, *Phys. Rev. B* **67**, 075205 (2003).
- [289] L.-L. Chua et al., General observation of n-type field-effect behaviour in organic semiconductors, *Nature* **434**, 194 (2005).
- [290] L. Kronik and Y. Shapira, Surface photovoltage spectroscopy of semiconductor structures: At the crossroads of physics, chemistry and electrical engineering, *Surf. and Interface Analysis* **31**, 954 (2001).
- [291] M. Musser and S. C. Dahlberg, The surface photovoltage of an increasing series of pol-yarenes: Anthracene, tetracene, and pentacene, *J. Chem. Phys.* **71**, 2806 (1979).
- [292] M. Musser and S. C. Dahlberg, The surface photovoltage of polymethine semiconducting films, *J. Chem. Phys.* **72**, 4084 (1980).
- [293] N. J. Tremblay et al., Photovoltaic universal joints: Ball-and-socket interfaces in molecular photovoltaic cells, *ChemPhysChem* **11**, 799 (2010).
- [294] E. Clar and J. F. Stephen, Synthesis of 1:2,3:4,5:6,7:8,9:10,11:12-hexabenzocoronene, *Tetrahedron* **21**, 467 (1965).
- [295] S. Xiao et al., Molecular wires from contorted aromatic compounds, *Angew. Chem.* **44**, 7390 (2005).
- [296] S. Xiao et al., Transferring self-assembled, nanoscale cables into electrical devices, *J. Amer. Chem. Soc.* **128**, 10700 (2006).

- [297] Y. S. Cohen, S. Xiao, M. L. Steigerwald, C. Nuckolls, and C. R. Kagan, Enforced one-dimensional photoconductivity in core-cladding hexabenzocoronenes, *Nano Lett.* **6**, 2838 (2006).
- [298] K. D. Harris et al., High mobility, air-stable organic transistors from hexabenzocoronene/carbon nanotube bilayers, *J. Phys. Chem. C* **111**, 17947 (2007).
- [299] K. N. Plunkett et al., Expeditious synthesis of contorted hexabenzocoronenes, *Org. Lett.* **11**, 2225 (2009).
- [300] A. A. Gorodetsky et al., Reticulated heterojunctions for photovoltaic devices, *Angew. Chem.* **49**, 7909 (2010).
- [301] A. C. Whalley et al., Bending contorted hexabenzocoronene into a bowl, *Chem. Science* **2**, 132 (2011).
- [302] X. Guo et al., Photoresponsive nanoscale columnar transistors, *Proc. Natl. Acad. Sci.* **106**, 691 (2009).
- [303] O. Douheret et al., High-resolution morphological and electrical characterisation of organic bulk heterojunction solar cells by scanning probe microscopy, *Prog. in Photovoltaics* **15**, 713 (2007).
- [304] Z. Wang, Barton-kellogg olefination, page (2010).
- [305] G. Markovich et al., Architectonic quantum dot solids, **32**, 415 (1999).
- [306] A. J. Nozik, Quantum dot solar cells, **14**, 115 (2002).
- [307] A. J. Nozik, Nanoscience and nanostructures for photovoltaics and solar fuels, **10**, 2735 (2010).
- [308] J. Tang and E. H. Sargent, Infrared colloidal quantum dots for photovoltaics: Fundamentals and recent progress, **23**, 12 (2010).
- [309] S. W. Clark, J. M. Harbold, and F. W. Wise, Resonant energy transfer in pbs quantum dots, **111**, 7302 (2007).
- [310] R. Koole, P. Liljeroth, C. de Mello Donega, D. Vanmaekelbergh, and A. Meijerink, Electronic coupling and exciton energy transfer in cdte quantum-dot molecules, **128**, 10436 (2006).
- [311] I. Kang and F. W. Wise, Electronic structure and optical properties of pbs and pbse quantum dots, **14**, 1632 (1997).
- [312] R. W. Meulenbergh et al., Determination of the exciton binding energy in cdse quantum dots, **3**, 325 (2009).
- [313] F. W. Wise, Lead salt quantum dots: the limit of strong quantum confinement, **33**, 773 (2000).

- [314] K. J. Williams et al., Strong electronic coupling in two-dimensional assemblies of colloidal pbse quantum dots, **3**, 1532 (2009).
- [315] P. Liljeroth et al., Variable orbital coupling in a two-dimensional quantum-dot solid probed on a local scale, **97**, 096803 (2006).
- [316] I. S. Liu et al., Enhancing photoluminescence quenching and photoelectric properties of cdse quantum dots with hole accepting ligands, **18**, 675 (2008).
- [317] M. A. Hines and G. D. Scholes, Colloidal pbs nanocrystals with size-tunable near-infrared emission: Observation of post-synthesis self-narrowing of the particle size distribution, **15**, 1844 (2003).
- [318] L. Venkataraman, J. E. Klare, C. Nuckolls, M. S. Hybertsen, and M. L. Steigerwald, Dependence of single-molecule junction conductance on molecular conformation, **442**, 904 (2006).
- [319] A. M. Scheer, G. A. Gallup, and P. D. Burrow, Unoccupied orbital energies of 1,4-benzenedithiol and the homo-lumo gap, **466**, 131 (2008).
- [320] T. Hanrath, J. J. Choi, and D.-M. Smilgies, Structure/processing relationships of highly ordered lead salt nanocrystal superlattices, **3**, 2975 (2009).
- [321] M. C. Beard et al., Variations in the quantum efficiency of multiple exciton generation for a series of chemically treated pbse nanocrystal films, **9**, 836 (2009).
- [322] M. Sykora et al., Photoinduced charge transfer between cdse nanocrystal quantum dots and ru-polypyridine complexes, **128**, 9984 (2006).
- [323] A. Pandey and P. Guyot-Sionnest, Slow electron cooling in colloidal quantum dots, **322**, 929 (2008).
- [324] J. Slinker et al., Electroluminescent devices from ionic transition metal complexes, *Journal of Materials Chemistry* **17**, 2976 (2007).
- [325] W. R. Silveira and J. A. Marohn, Microscopic view of charge injection in an organic semiconductor, **93**, 116104 (2004).
- [326] J. Gilot, M. M. Wienk, and R. A. J. Janssen, Double and triple junction polymer solar cells processed from solution, **90**, 143512 (2007).
- [327] A. Hadipour, B. deBoer, and P. W. M. Blom, Organic tandem and multi-junction solar cells, **18**, 169 (2008).
- [328] Y. Kim, H. Song, D. Kim, T. Lee, and H. Jeong, Noise characteristics of charge tunneling via localized states in metal-molecule-metal junctions, *ACS Nano* **4**, 4426 (2010).
- [329] D. J. D. Moet, P. de Bruyn, and P. W. M. Blom, High work function transparent middle electrode for organic tandem solar cells, **96**, 153504 (2010).

- [330] A. S. Brown and M. A. Green, Detailed balance limit for the series constrained two terminal tandem solar cell, **14**, 96 (2002).
- [331] J. Gilot, M. M. Wienk, and R. A. J. Janssen, Measuring the external quantum efficiency of two-terminal polymer tandem solar cells, **20**, 3904 (2010).
- [332] A. Yakimov and S. Forrest, High photovoltage multiple-heterojunction organic solar cells incorporating interfacial metallic nanoclusters, **80**, 1667 (2002).
- [333] A. Kumar, S. Sista, and Y. Yang, Dipole induced anomalous s-shape i-v curves in polymer solar cells, **105**, 094512 (2009).
- [334] R. K. Swank, Surface properties of ii-vi compounds, **153**, 844 (1967).
- [335] H. B. Michaelson, The work function of the elements and its periodicity, **48**, 4729 (1977).
- [336] M. S. White, D. C. Olson, S. E. Shaheen, N. Kopidakis, and D. S. Ginley, Inverted bulk-heterojunction organic photovoltaic device using a solution-derived zno underlayer, **89**, 143517 (2006).
- [337] F. Verbakel, S. C. J. Meskers, and R. A. J. Janssen, Electronic memory effects in diodes from a zinc oxide nanoparticle-polystyrene hybrid material, **89**, 102103 (2006).
- [338] R. A. Marcus and N. Sutin, Electron transfers in chemistry and biology, **811**, 265 (1985).
- [339] A. Mart and G. L. Arajo, Limiting efficiencies for photovoltaic energy conversion in multi-gap systems, *Solar Energy Materials and Solar Cells* **43**, 203 (1996).
- [340] S. P. Bremner, M. Y. Levy, and C. B. Honsberg, Limiting efficiency of an intermediate band solar cell under a terrestrial spectrum, *Applied Physics Letters* DOI - 10.1063/1.2907493 **92**, 171110 (2008).